Towards Polarization Measurements of Laser-accelerated Helium-3 Ions

---

Inaugural Dissertation

submitted in fulfillment of the requirements for the doctoral degree
of the Faculty of Mathematics and Natural Sciences
at Heinrich-Heine-University Düsseldorf

Forschungszentrum Jülich

by

Ilhan Engin

born in Stolberg / Rhld.

Jülich

August 28, 2015

from the Institute for Laser and Plasma Physics
at Heinrich-Heine-University Düsseldorf

and the Institute for Nuclear Physics
at Forschungszentrum Jülich

Printed with permission of the
Faculty of Mathematics and Natural Sciences at
Heinrich-Heine-University Düsseldorf

1st reviewer:	Prof. Dr. Markus Büscher
2nd reviewer:	Prof. Dr. Dr. Carsten Müller

Date of oral examination: November 20, 2015

Declaration in Lieu of Oath

I hereby declare in lieu of oath that I have written this innaugural dissertation self-dependently and without any prohibited help from others in compliance with the "regulations and guidelines for safeguarding good scientific practice at Heinrich-Heine-University Düsseldorf".

Eidesstattliche Erklärung

Ich versichere an Eides Statt, dass die Dissertation von mir selbständig und ohne unzulässige fremde Hilfe unter Beachtung der "Grundsätze zur Sicherung guter wissenschaftlicher Praxis an der Heinrich-Heine-Universität Düsseldorf" erstellt worden ist.

Jülich, August 28, 2015 __________________________

Acknowledgment

First of all I want to thank my parents Dipl.-Psych. C. A. Engin and Dr.-Ing. K. Engin. They helped me building up a solid basis and always lighted me my way. This doctoral thesis is dedicated to them. May they rest in peace.

The studies required huge amount of work, scientific research and dedication and the implementation would not have been possible without the great support of many individuals. I would like to extend my deep appreciation to all of them.

I would like to express my sincere gratitude to Prof. Dr. R. Maier for accommodating me as a member of his institute and furthermore for all the possibilities concerning financial as well as professional issues, for all of his brilliant help as well as his wise advice I got for making this thesis possible. I am proud to be his last doctoral candidate.

I would like to express my great appreciation to Prof. Dr. M. Büscher as the first reviewer of this thesis and as one of my mentors during my time at Forschungszentrum Jülich. Not only according to scientific aspects of my work but also concerning other gains in experience, like supervising bachelor as well as master students or leading working groups at the Hadron Physics Summer Schools 2012 & 2014, I really learned for life.

I also want to sincerely thank Prof. Dr. Dr. C. Müller who became the second reviewer of this thesis and also my dedicated mentor at Heinrich-Heine-University Düsseldorf.

Prof. M. Bai as the acting head of IKP-4, Dr. D. Prasuhn and Prof. Dr. A. Lehrach supported me very much during the final stages of my doctoral studies. Prof. Lehrach and Dr. Prasuhn helped me to master some of the big challenges risen up on my way to the sight line. I am heartily thankful for their guidance.

For the mentoring concerning theoretical questions as well as computational physics I owe a very important debt to Prof. Dr. P. Gibbon. He escorted me through the final phases of my doctoral studies. Due to the important exchange with him and also to Dr. L. Di Lucchio and Dr. H. Zilken, I could gain a lot of experience - not only in scientific respects. I wish to thank them all for their good and friendly support.

I would like to heartily thank Prof. Dr. O. Willi for giving me the opportunity to work with his wonderful team and to gain important experience in the field of laser-plasma physics. In particular, I am deeply grateful to Dr. M. Cerchez. She showed me how to work in laser-plasma physics, taught me the tricks, and had always time to explain in a patient way. With her help, I was able to build up big parts of my own expertise, and thus, I was able to work autarkically. Thank you Mirela! Dipl.-Phys. M. Swantusch and Dr. Dipl.-Ing. J. Böker were (and are) good companions in many respects - two guys of good nature with a huge amount of power of endurance, good friends, colleagues, and roommates. I would like to offer my special thanks to them. Dipl.-Phys. S. Spickermann, Dipl.-Phys. F.(K.V.) Schlüter and Dipl.-Phys. T. Thiele, but also Dr. M. Cerchez, Dr. R. Prasad and Dipl.-Phys. M. Swantusch: together, we spent so many nights inside the bunker. I want to heartily thank them for their lifetime, for their good advice and true help, for their blood toll, for escorting me to the ophthalmic emergency clinic on Dec. 20th/21st 2013, and for their familiar friendship. T. Wowra B.Sc. consequently provided me with some high-intensity light inside the dark, and thus, helped me to gain some knowledge. Big thanks to him, and also to Dr. T. Toncian for helping me to search for energetic particles. I do not want to forget Dr. G. A. Lehmann, S. Brauckmann M.Sc., A.-M. Schroer M.Sc., and also C. Dingle, K. Lanzer, C. Helbig, C. Bolten, H. Borrmann, and S. Manderla. I wish to thank them all for their individual support.

I would particularly like to thank Prof. Dr. T. Stöhlker who gave me the chance to experimentally investigate on my topic also at GSI Darmstadt. I am deeply grateful to Dr. V. Bagnoud, Dr. B. Zielbauer, and the other nice colleagues from the PHELIX group at GSI Darmstadt who *illuminated* my precious helium-3 gas, in particular Dr. S. Götte, Dr. C. Brabetz, Dr. U. Eisenbarth, and Dr. D. Reemts. Special thanks go to Prof. Dr. M. Roth, O. Deppert M.Sc. (a great experimenter, good companion and friend), S. Frydrych M.Sc., A. Kleinschmidt M.Sc., and Dipl.-Phys. F.(K.V.) Schlüter (all of them very supportive and reliable natures), who supported me very much with preparing and conducting my final experiment and afterwards had always good advice for me. Furthermore, I want to thank the RCF-champion D. Jahn B.Sc., V. Schanz B.Sc., and Dr. F. Wagner.

I would like to express my very great appreciation to G. Roes. She always supported and helped me concerning administrative issues as well as general essential questions of life. With her, I gained a true friend. Thank you, Gisela! I would also like to extend my appreciation to P. Burgmer B.Eng., Dr. D. Deermann, especially to Dr. R.W. Engels, Dr. P. Fedorets, in particular to Dr. O. Felden and Prof. Dr. D. Gotta and Dr. M. Hartmann, Dr. A. Herten, Dr. V. Hejny, G. Khukhalashvili M.Sc., Dr. D. Lersch, Dr. M. Mikirtychyants, especially to Dr. S. Mikirtytchiants and Dr. A. Nass, Dr. H. Ohm, Dr. R. Schleichert, especially to Dr. H. Seyfarth and Dr. H.J. Stein, K. Strathmann, Dr. S. Trusov, especially to Dr. Y. Valdau, Dipl.-Phys. P. Weiß, Dr. P. Wurm, Dr. A. Zambanini, and all of the other good friends and colleagues of the IKP for the good discussions, for their open ears and for listening, for their good ideas and suggestions which forwarded my advancing in the implementation of my concepts. Special thanks go to my good fellows Dr. Dipl.-Ing. J. Böker, Dr. M. Gaisser, Dr. L. Kröll, and Dr. C. Weidemann for their remarkable commitment and their helpful suggestions. Dr. T. Sefzick, J. But, G. D'Orsaneo, R. Dosdall, A. Erben (may he rest in peace), W. Firmenich, T. Hahnraths - von der Gracht, M. Holona, S. Kistemann, M. Kremer, Dipl.-Ing. T. Krings, G. Sterzenbach, D. Spölgen and also the other colleagues from the machine shop as well as from the electronics lab were an important help to me. Many thanks to all of them. I wish to acknowledge the big help provided by Dipl.-Kfr. A. Kelleners and C. Müller concerning administrative issues.

Special thanks go to Dr. H. Glückler, Dr. H. Soltner, and Dipl.-Ing. U. Giesen, and Dipl.-Ing. K. Dahlhoff, Dipl.-Ing. P. Jansen, Dipl.-Ing. F. Klehr, J. Pfennings, Dipl.-Ing. M. Schmitt, and furthermore Dipl.-Ing. H. Feilbach and T. Leipold B.Eng. who provided me with very valuable expertise in many technical issues. Without their help, the realization of the experimental work would have been iffy. Big thanks to all of them.

My lovely sister Dipl.-Gyml. I. M. Engin-Doğanyılmaz and me together underwent some of the highs and lows of life and we could always lean on each other. It is dulcet to have her as a good and faithful companion by my side. May the winds of bliss always blow with her. And also with her good husband K. Doğanyılmaz M.B.A, who fortunately became a full member of my family - I was always able to count on him.

My lovely girlfriend and life partner G. Steinritz M.A. always supported me and I could - metaphorically speaking - base myself on her. I am glad that our ways crossed somehow and interfered with each other. Until now, we stood shoulder to shoulder, may it be the same in future.

Of particular importance to me are Dipl.-Psych. D. Krebber-Goossens, her husband Dr. B. Goossens and their lovely children H. Raindl and J. Goossens M.A. who were always present, who kept me grounded and really treated me as a loved one, even as their own son and brother. I do not want to forget the lovely family ”extensions”, Dipl.-Kfr. A. S. Goossens M.A. and M. K. Raindl. I am glad they are in my life.

Also Dr. med. H. Zahn, A. Schlüter-Janzen and her husband H. Schlüter, S. & D. Verhülsdonk, S. Padel M.A. & I. Schierstein B.A., M. Derieth, M. Palka, Dipl.-Phys. H. Kayan, Dipl.-Phys. M. Theisen, İ. Dinç B.A. walked with me through many important respects of my life. I would like to express my deep gratitude to them.

Last but not least I would like to thank all of my friends for standing by my side and motivating me. THANK YOU... !!! :)

Kurzfassung

Die vorliegende Arbeit umfasst vorbereitende Studien zur Spinpolarisationsmessung von ^{3}He-Ionen aus laserinduzierten Plasmen.

In diesem Kontext wurden Experimente an zwei Hochleistungslasern, dem Arcturus Laser der Heinrich-Heine-Universität Düsseldorf sowie PHELIX an der GSI Darmstadt, durchgeführt, um effizient Ionen laserinduziert aus einem ^{4}He-Gastarget zu beschleunigen. Das wissenschaftliche Ziel beider Experimente war, den Ionenbeschleunigungsmechanismus in unterdichten Plasmen zu untersuchen, indem die Ionenenergiespektren und die Winkelverteilung im Ionensignal rund um das Gasjettarget gemessen wurden. Laserbeschleunigte MeV-He-Ionen konnten erfolgreich detektiert werden. Hierbei wurde die Hauptbeschleunigungsrichtung bei großen Winkeln relativ zur Laserpropagationsrichtung bestimmt. Im zweiten Schritt wurde unpolarisiertes ^{3}He-Gas eingesetzt, um die hier erzielten experimentellen Resultate mit denen von ^{4}He zu vergleichen. Mit Hilfe der Daten zur erzielten Ionenausbeute konnten die erwarteten Raten der Fusionsreaktion D(^{3}He,p)^{4}He im polarisierten Falle abgeschätzt werden: Die gewonnenen Informationen bezüglich der Fusionsprotonenausbeute dieser Kernreaktion erlaubt eine experimentell gestützte Abschätzung für zukünftige Experimente mit vorpolarisiertem ^{3}He-Gas als Plasmatarget. Die experimentellen Daten stimmen mit begleitenden Particle-in-Cell (PIC) Simulationen auf den Jülicher Supercomputern überein. Hierbei wurde das simulierte Target als neutrales Gas definiert.

Der Einsatz von vorpolarisiertem ^{3}He-Gas stellt neue Anforderungen an den Versuchsaufbau für Laserbeschleunigungsexperimente. Bestandteil dieser Anordnung ist ein (externes) homogenes magnetisches Haltefeld (Feldstärke $\sim 1,4\,\mathrm{mT}$) für eine längerfristige Lagerung des vorpolarisierten Gases in der PHELIX Targetkammer. Zu diesem Zweck wurde eine präzise Halbachanordnung aus horizontal gelagerten Ringen mit Permanentmagneten entworfen, optimiert und in Hinblick auf eine hohe Homogenität und auf den verfügbaren Platz in der Vakuumkammer konstruiert. Zusammen mit zusätzlichen Helmholtzspulen innerhalb der Targetkammer (Durchmesser von 0,8 m) kann die Richtung des homogenen Magnetfeldes variiert werden.

Ferner musste ein neues Konzept einer Gasstrahlquelle bestehend aus einem schnellen Druckverdichter aus nichtmagnetisierbaren Materialien und einem schnellöffnenden nichtmagnetischen Ventil mit aufgeflanschter Überschalldüse entwickelt werden, um polarisierte Gasjets mit adäquatem Dichteprofil aufzubauen. Das vorpolarisierte Gas wird bei kleinem Druck (3 bar) angeliefert, was für eine effiziente laserinduzierte Ionenbeschleunigung nicht von Vorteil ist. Der ^{3}He-Gasdruck muss daher verzehnfacht werden. Herkömmliche Öffnungsmechanismen, welche in konventionellen Solenoidventilen Anwendung finden, eignen sich nicht für den Einsatz mit spinpolarisiertem Gas. Ein piezogetriebenes und ein druckgesteuertes Ventil in Kombination mit einem neuartigen Druckverdichter erfüllen die Anforderungen.

Abstract

In the framework of this thesis, preparatory investigations for the spin-polarization measurement of ^{3}He ions from laser-induced plasmas have been performed.
Therefore, experiments aiming at an efficient laser-induced ion acceleration out of a ^{4}He gas target were carried out at two high-intensity laser facilities: the Arcturus laser at Heinrich-Heine-Universität Düsseldorf as well as PHELIX at GSI Darmstadt. The scientific goal of both experiments was to investigate the ion-acceleration process in underdense plasmas by measuring the ion energy spectra and the angular distribution of the ion signal around the gas-jet target. Laser-accelerated MeV-He-ions could successfully be detected. The main acceleration direction at large angles with regard to the laser propagation direction was determined. In a second step, unpolarized ^{3}He gas was attached in order to cross-check the experimental results with those of ^{4}He. With the help of the achieved ion yield data, the expected rates of the fusion reaction D(^{3}He,p)^{4}He in the polarized case have been estimated: the information regarding the fusion proton yield from this nuclear reaction allows an experimentally based estimation for future experiments with pre-polarized ^{3}He gas as plasma target. The experimental data is in line with supporting Particle-in-Cell (PIC) simulations performed on the Jülich supercomputers. For this purpose, the simulated target was defined as a neutral gas.
The use of pre-polarized ^{3}He gas demands a special preparation of a polarized ^{3}He target for laser-acceleration experiments. This layout includes an (external) homogeneous magnetic holding field (field strength of $\sim 1.4\,\mathrm{mT}$) for storing the pre-polarized gas for long time durations inside the PHELIX target chamber. For this purpose, a precise Halbach array consisting of horizontally arranged rings with built-in permanent magnets had to be designed, optimized, and constructed to deliver high homogeneity and take into account the available amount of space inside the vacuum chamber. Together with additional Helmholtz coils inside the target chamber (diameter of 0.8 m) the direction of the homogeneous magnetic field can be varied.
Furthermore, a new concept of a proper gas source composed of a fast pressure booster made of non-magnetizable materials and a fast-opening non-magnetic valve with a supersonic nozzle attached had to be designed in order to produce polarized gas jets with adequate density profiles. The pre-polarized gas is delivered at a low pressure (3 bar) which is not suitable for an efficient laser-driven ion acceleration. Hence, the ^{3}He gas pressure has to be increased tenfold. Prevalent opening mechanisms being used in commercial solenoid valves are not applicable for spin-polarized gases. A piezo-driven and a pressure-driven valve in combination with a novel booster made of unprohibited materials fulfill the requirements.

Contents

List of Figures

List of Tables

1. Introduction and Motivation [1]

For many branches of modern science nuclear spin-polarized noble gases play an important role. Polarized ^{3}He is of particular importance for fundamental research since the spins of the two protons are oriented anti-parallel so that the resulting spin is carried by the neutron. That is why polarized ^{3}He [Kri09] can be used as an effective polarized neutron target for studying the neutron structure by scattering with polarized electrons (*e.g.* spin-structure function, electromagnetic form factors) [Tan98]. For many experiments in nuclear and particle physics, like experiments with stored particle beams, the use of polarized ^{3}He *beams* instead of targets would be advantageous. A long-term perspective would be to build up a tabletop spin-polarized ^{3}He ion source with high currents and high degrees of polarization. This goal is challenging. Until now, only a few approaches could be accomplished - but not with the desired particle current or an adequate beam-polarization degree [Fin69, Bur74, Slo81]. At Brookhaven National Lab's Relativistic Heavy Ion Collider (RHIC) attempts are now being made to develop a polarized ^{3}He ion beam source [Max14].

Conventional accelerators reach fundamental, technological, and, as one of the most important aspects, financial limits of the achievable particle energies. Some limitations essentially concerning cost-benefit relations do not apply to laser-induced particle acceleration. During the past 50 years the achievable laser intensities have been increased continuously. Since the invention of chirped pulse amplification (CPA) in 1985 [Str85], the new intensities offered new applications for laser-physics experiments. With a high-intensity laser pulse impinge on a target (*e.g.* solid foils or gas jets) a plasma is formed out of which charged particles can be accelerated to energies of several MeV or, depending on the accelerated particle species, GeV.

An unsolved question in this context is the influence of the strong laser fields on the spin-polarization of the created ion beams. Only a few publications regarding particle spins in high-intensity laser fields are available. In [Kla14] the spin dynamics and induced spin effects in relativistic ionization with highly charged ions in super-strong laser fields were investigated. Regarding laser-accelerated ions, two scenarios are possible: either the magnetic fields of the incoming laser beam or the produced plasma are able to change the spin direction of the accelerated beam particles, or the spins are too inert so that the short laser pulse has no effect on the spin alignment of a pre-polarized target, and the polarization is conserved. In the latter case, the polarization could be conserved during laser-acceleration processes, and also laser-induced polarized nuclear fusion with increased energy gains seems to be feasible: due to the use of polarized fuel, the cross-sections for nuclear fusion reactions may be enhanced which leads to higher energy yields compared to the case of unpolarized fuel.

---

[1] Some passages of the following text were taken *for* an abstract for the "Laser-Plasma" working group at the *Hadron Physics Summer School 2014* before publishing this PhD thesis [Eng14]. The author was the working group's lecturer.

For the laser-induced nuclear fusion reaction D(T,n)^{4}He with fully polarized fuel, for instance, the nuclear fusion cross-section is theoretically increased by a factor of 1.5, while the energy gain increases by about 45 % [Tem12]. Regarding the laser power needed for the induced nuclear fusion a decrease by about 20 % is expected. In [Hon91] the effect of nuclear spin-polarization for D-^{3}He fuel was investigated. Compared to unpolarized fusion, a reduction of the driver energy for ignition of about 60 % could be predicted in the polarized case. Therefore, the proof of nuclear spin-polarization conservation inside a (laser-induced) plasma is of high relevance for fusion science.

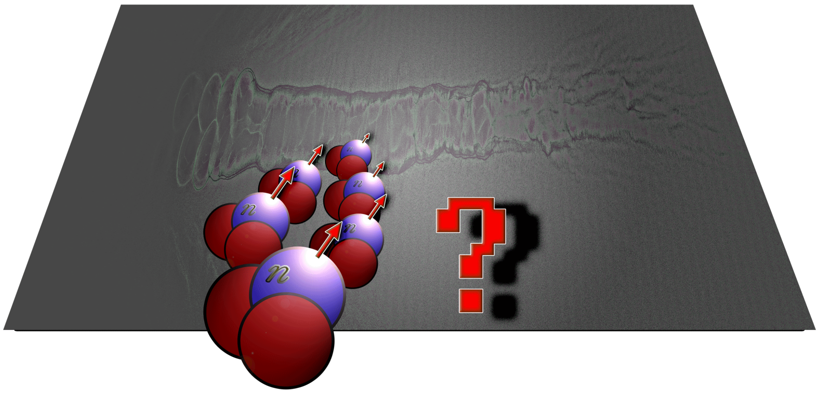

While the above mentioned first scenario (polarization *creation* by laser-particle interaction) has already been investigated with conventional foil targets by spin-dependent hadronic proton scattering off silicon nuclei [Raa14], for the second one (polarization conservation during laser-plasma interaction) pre-polarized ^{3}He gas can be used as production target. The relaxation rate of the polarization degree of ^{3}He is depending on several conditions, *e.g.* gas pressure or magnetic field gradients. Also the absence of one electron in the atomic shell leads to a rapid decrease of the polarization degree: the interaction time τ_{HF} for the coupling of the nuclear spins with the spin of the remaining electron is around 0.2 ns (GHz energy level). Thus, a full ionization of the pre-polarized ^{3}He has to be accomplished within a few picoseconds. This can be easily achieved with currently available laser intensities.

Of course, the *sine qua non* of a polarization measurement of laser-accelerated ^{3}He^{2+} ions is a successful laser-driven ion acceleration out of a ^{3}He gas-jet target. This includes the experimentally and computationally obtained knowledge about the main acceleration directions, the specific ion energies as well as the total ion number (*cf.* Chaps. 5 and 7). If all of these requirements are fulfilled, a layout of a polarized ^{3}He target for laser-acceleration experiments has to be planned and constructed, and finally manufactured and tested (*cf.* Chap. 8). Finally, when the single operation units have been completed, the final experiments can be conducted.

Science is fascinating: it can be frustrating and challenging, but also satisfying and quickening and good scientific practice requires time and resources.

2. Modern Lasers

In the framework of this thesis, laser-accelerated helium ions are investigated in terms of ion energy and acceleration direction. When talking about *laser-accelerated* ions, it is important to clarify the term *laser* first. Within this chapter, the laser principle as well as the technological development of lasers is described, while in the last section two examples of modern high-intensity lasers are presented.

2.1. The laser principle

Laser is an acronym for ***l**ight **a**mplification by **s**timulated **e**mission of **r**adiation*. Originally, this term described the physical principal of a special kind of light amplification. Later on, it became the name of the technical device which uses this principal and serves as a special radiation source.

Laser radiation features some specific characteristics which are due to the nature of its production: the laser principle which is based on the stimulated emission of radiation, first postulated by A. Einstein in 1917 [Ein17]. Together with the process of spontaneous emission as well as absorption, the three fundamental processes regarding the interaction of radiation with matter are given. According to quantum mechanics theory, atoms as the building blocks of matter can be excited from the ground state (state with the lowest possible energy) to higher quantized states with discrete energies. Discrete energies are also valid for a light field with certain frequency and intensity. The smallest energy possible, the light quantum, also known as the photon, is linearly dependent on the frequency ν or on the angular frequency $\omega = 2\pi\nu$: $\mathcal{E}_{\text{ph}} = h\nu = \hbar\omega$, with the Planck's constant $h = 2\pi\hbar$. The intensity I can be derived from an ensemble of n_{ph} photons propagating through a certain area within a certain time. It is given in units of an energy flux: $[I] = 1\ {}^{\text{W}}\!/_{\text{m}^2}$.

If light impinges on matter, some of the photons are absorbed, *i.e.* the photon number decreases, and the atoms are excited to a higher discrete energy level given by the photon energy: $h\nu = \mathcal{E}_i - \mathcal{E}_j$, with $\mathcal{E}_{i,j}$ as the energy levels of the atom ($\mathcal{E}_i > \mathcal{E}_j$) [Kul11, p. 6]. While the excited atom does not remain in the higher energetic state, it drops back to a lower level and emits a light quantum with an energy equal to the energy gap. In contrast to spontaneous emission which occurs without extraneous cause and is a random process (*e.g.* thermic radiation emitted isotropically), the emitted photons from the stimulated emission have the same frequency, phase, polarization, and propagation direction as the incident light quanta. Thus, the photon number is increased with uniform photons and the incident light is amplified. Since all processes (absorption, spontaneous emission, and stimulated emission) occur simultaneously in a certain medium, for a proper light amplification the stimulated emission has to be the dominant process.

For media in thermal equilibrium, the number of emitted photons n_{ph} is Bose-Einstein distributed: $n_{\text{ph}} = \left(\exp\left({}^{h\nu}\!/_{k_{\text{B}}T}\right) - 1\right)^{-1}$, while the occupation number of excited atoms follows the Boltzmann equation: $N_n = N_0 \exp\left(-{}^{h\nu}/_{k_B T}\right)$, with $h\nu = (\mathcal{E}_n - \mathcal{E}_0) > 0$. Here, $\mathcal{E}_{n,0}$ is the energy in the n^{th} energy level or ground state, respectively, and $N_{n,0}$ is the occupation number for the n^{th} energy level or ground state, respectively ($\sum_{N=0}^{\infty} = N_{\text{total}}$) [Kul11, p. 17]. The number of atoms in the ground state is usually larger than the one in an excited state. Therefore, absorption is the dominant process.

Active laser media exhibit the so-called population inversion, meaning that the occupation number of atoms being in a certain energy state $\mathcal{E}_{L,2} > \mathcal{E}_0$ with a desired transition is larger than the number of atoms in the energy level $\mathcal{E}_{L,1} < \mathcal{E}_{L,2}$. These energy states $\mathcal{E}_{L,i}$ are called laser levels which determine the desired frequency of the output laser radiation (each laser medium provides only a few discrete frequencies). Here, the index $i = 1, 2$ stands for the lower and the upper laser level given by the laser medium. Population inversion is built up by extraneous cause [Kul11, p. 18], the laser pumping, which is a process of energy transfer into the laser medium (*e.g.* by gas discharge, flash lamp or diode pump laser excitement). With population inversion, stimulated emission becomes the dominant process leading to light amplification. Nevertheless, there is still an amount of photons being spontaneously emitted isotropically in 4π and being amplified. *Amplified spontaneous emission* (ASE) dissipates population inversion without amplifying the incident light. A proper active laser medium has to have adequate laser levels with large lifetimes and has to be pumped efficiently, so that population inversion can be conserved during operation.

Real lasers cannot operate with a 2-level-system only, since a stationary population inversion cannot be realized. This can only be achieved with multiple-level-systems. Common lasers can be approximated by 3-level- or 4-level-systems [Ber04, p. 827]. In a 4-level-system like a He-Ne laser, atoms are excited from the ground state $\mathcal{E}_0$ to the pump level $\mathcal{E}_3$ with a short lifetime (*cf.* Fig. 2.1). The following transfer to the upper laser level $\mathcal{E}_{L,2} < \mathcal{E}_3$ is performed quickly leading to a fast build up of population inversion between the upper and lower laser level. The laser transition from $\mathcal{E}_{L,2}$ with a longer lifetime to the lower $\mathcal{E}_{L,1}$ laser level causes the emission of the desired photons. $\mathcal{E}_{L,1}$ also has a short lifetime so that the lower laser level is emptying fast in order to conserve population inversion. The intensity or photon number, respectively, of the emitted laser light is Poisson distributed, *i.e.* only small fluctuations around a high mean value are given.

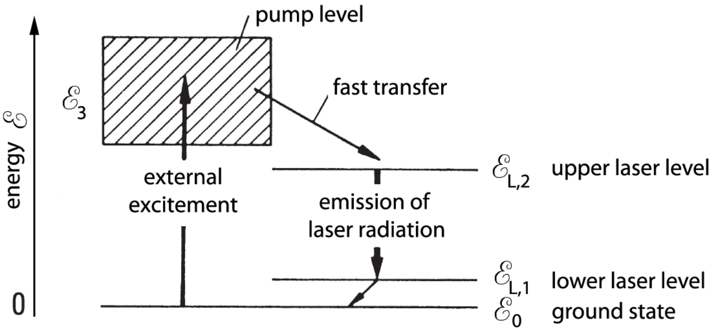

Figure 2.1.: Schematic drawing of a 4-level-system (*cf.* [Ber04, p. 827]).

The active laser medium together with the pumping process is an efficient amplifying system for light. In order to realize a fully functioning light source, a laser resonator is necessary. This self-excitation device is, generally speaking, an oscillator which can be excited by an input signal of a certain frequency. This signal is amplified, partially coupled back and amplified again. The outcoupled light serves as output signal with desired characteristics. The resonator can be simplified by two mirrors with the active laser medium in between. One of the mirrors has to be partially transparent to enable outcoupling of light (with desired properties). Inside the resonator electromagnetic resonance frequencies, *i.e.* the eigenmodes, can be built up, while other non-desired frequencies are suppressed. Hence, only frequencies similar to the laser transition frequency are amplified. Important for an outcoupled monochromatic low-divergent light beam is a nearly pure single-mode amplification. But still, a small amount of light from ASE processes can be present.

2.2. High-intensity lasers

In 1960, the first functional laser was built by T.H. Maiman. A solid-state flash lamp-pumped synthetic ruby crystal was used to produce pulsed red laser light [Mai60]. The available laser intensities increased rapidly to values of around $10^{15}\ {}^{\mathrm{W}}\!/_{\mathrm{cm}^2}$ until ∼1970 [Gib05, p. 2]. Henceforward, higher intensities in the TW or PW regime could not be generated since nonlinear effects cause damages in the amplifier media. This stagnation lasted for around two decades until 1985 when D. Strickland and G. Mourou invented the chirped pulse amplification (CPA) technique [Str85].

With the CPA technique, ultra-short laser pulses can be amplified up to the PW regime by temporally and spatially stretching the laser pulse before entering the main amplifier. Therefore, the pulse peak intensity is reduced to values below the damage threshold in the amplifier medium. After the amplification, the pulse is coupled out into the evacuated compressor, where the long pulse is re-compressed to the desired (original) pulse duration. Vacuum is necessary due to the high intensities $> 10^{18}\ {}^{\mathrm{W}}\!/_{\mathrm{cm}^2}$ which immediately would ionize air. The compression is performed with the help of dispersing elements such as gratings or prisms. Long-wavelength parts of the stretched amplified laser pulse propagate larger distances than short-wavelength components. This principle is called negative dispersion, *i.e.* components with higher frequencies take less time for passing the compressor than components with lower frequencies. The stretcher device in front of the main amplifier works with positive dispersion. Thus, compressor- and stretcher-based dispersion are compensated in the end.

Modern lasers can be characterized by several properties, like *e.g.* laser power P, peak intensity I_{peak}, pulse energy in the focus $\mathcal{E}_{\mathrm{fok}}$, pulse duration τ, wavelength λ, repetition rate, etc. - to mention but a few. Table 2.1 exemplifies five multi-TW/PW laser facilities with their current properties. In the framework of this thesis, the PHELIX laser of GSI Darmstadt as well as the Arcturus laser of ILPP Düsseldorf are of particular interest since the experimental work (*cf.* Sec. 7, p. 105) has been performed at these laser facilities. In the following, both laser facilities are described in detail.

	VULCAN	*Ju*SPARC [1]	PHELIX	ARCTURUS	POLARIS
amplifier	Nd:glass	Ti:Sa	Nd:glass	Ti:Sa	Yb-doped glass
P [TW]	1000	≥ 1000	500	300	25
I_{peak} [$^{\text{W}}/_{\text{cm}^2}$]	$\geq 10^{21}$	- -	2×10^{21}	4.5×10^{19}	6×10^{20}
τ [ps]	≥ 0.5	$0.025 - 0.04$	$0.4 - 20\,\text{k}$	0.025	0.165
$\mathcal{E}_{\text{fok}}$ [J]	2.6 k	40	$250 - 1\,\text{k}$	7.5	> 4
λ [nm]	1054	800	1053	800	1030
rep. rate [Hz]	single shot	$0.1 - 1\,\text{k}$	single shot	10	$^1/_{40}$

Table 2.1.: Examples for today's multi-TW/PW laser systems with current properties

2.2.1. PHELIX laser

The **P**etawatt **H**igh-**E**nergy **L**aser for heavy **I**on e**X**periments (PHELIX) is operated at GSI Darmstadt. PHELIX is a flash lamp pumped neodym-doped glass (Nd:glass) laser system which delivers peak powers up to 0.5 PW (central wavelength of 1053 nm). PHELIX consists of two separate front-ends (the "fs" as well as the "ns" front-end for short and long pulses, respectively), the pre-amplifier, the main amplifier, and the grating compressor. Since the experiments at PHELIX were performed with the short pulses, only the fs front-end will be described in detail.

The fs front-end can be used for ion acceleration experiments. Its commercial titanium-doped sapphire (Ti^{3+}:Al_2O_3 or "Ti:Sa") oscillator, the *Mira 900 Coherent*, generates fs pulses with a pulse duration of 100 fs and an energy of 2 nJ at a repetition rate of 72 MHz. Since the attached laser medium is Ti:Sa with a maximum cross section around 800 nm, the spectrum has to be shifted to 1053 nm in order to match the cross sections of the glass amplifiers [Wag13]. Before entering the stretcher unit, the pulses can be optionally injected into a contrast-boosting ultrafast optical parametric amplifier (uOPA). Here, highest-contrast pulses in the order of 10^{10-11} can be produced (the contrast is explained on p. 19). Within the stretcher, the pulse duration can be enlarged by a factor of 190 $^{\text{ps}}/_{\text{nm}}$ to a value of 2.4 ns. With the stretcher unit the pulse duration is adjusted, the compressor grating configuration stays fix. Behind the stretcher, two 10 Hz Ti:Sa amplifiers amplify the pulse energy to a value of 20 mJ. The pulses are directed into the pre-amplification stage which consists of three flash lamp pumped Nd:glass amplifiers. Between each amplifier, the beam has to be expanded with Keppler telescopes in order to keep the intensity below the damage threshold of the beam line optics. In case of the short pulses, the output pulse energy is 5 J before entering the main amplifier.

Within the main amplification stage in double-pass configuration, the pulse is amplified by five flash lamp pumped Nd:glass amplifiers. In case of the short pulses, the maximum output beam energy is 250 J. The stretched and amplified pulse enters the grating compressor where it can be recompressed to minimal pulse durations of 500 fs and exit powers of up to 500 TW. Both optical dielectric gratings (1740 lines per mm) have a dimension of width × heigth = $480 \times 350\,\text{mm}^2$ and are operated in single-pass configuration.

---

[1] the *Ju*SPARC project of FZJ is in planning stage

The recompressed amplified pulse with elliptical beam profile (width × heigth = $280 \times 140\,\mathrm{mm}^2$) can be focused by a 90° off-axis parabola with a focal length of 1500 mm to a spot size of typically $15 \times 20\,\mu\mathrm{m}^2$. In Fig. 2.2, a 3D model of the PHELIX vacuum target chamber is illustrated [PHE]. It has an approximately rectangular base area. The inner dimensions are $1950 \times 1200\,\mathrm{mm}^2$ (*cf.* Fig. 2.3 [Zie14]). The laser beam is focused at a height of 360 mm above the chamber breadboard. There are two designated locations for the focus spot, given by the two deviation pots next to the chamber for housing the parabolic mirrors or turning mirrors if needed.

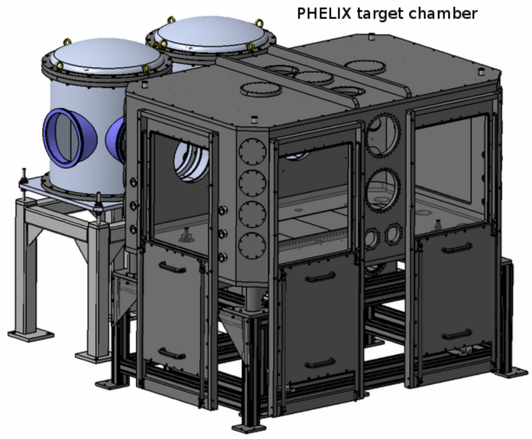

Figure 2.2.: 3D model of the PHELIX target chamber [PHE].

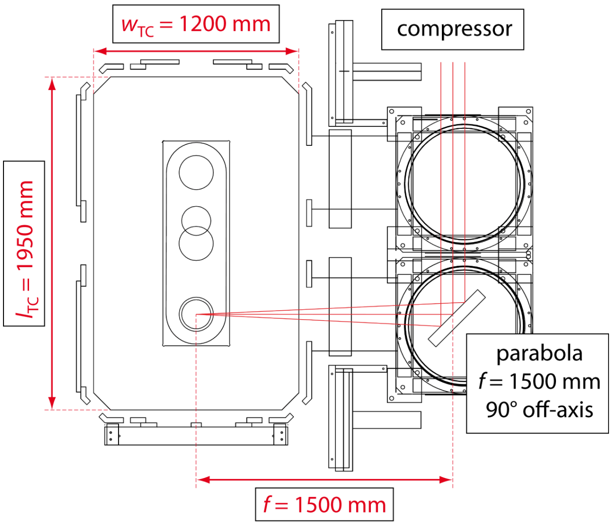

Figure 2.3.: Top view of the PHELIX target chamber [Zie14].

2.2.2. Arcturus laser

The Arcturus laser is operated by the institute for laser and plasma physics (ILPP) at Heinrich-Heine-University Düsseldorf. It is a compact CPA laser produced by *Amplitude Technologies* / France which delivers peak powers of several 100 TW at minimal pulse durations of 25 fs and a central wavelength of 800 nm. The laser system consists of the front-end (oscillator, booster, grating stretcher, and pre-amplifier units), the main amplifiers, and the grating compressors for two main beam lines.

The front-end oscillator (Ti:Sa) is pumped by a CW diode laser (power 5 W, central wavelength 790 nm, bandwidth 96 nm). The generated pulses have a pulse duration of 23 fs and an energy of 5 nJ at a repetition rate of 75 MHz. Behind the oscillator, the booster amplifies the pulses to energies in the order of μJ at a reduced repetition rate of 10 Hz. The multipass amplifier contains a frequency doubled Nd:YAG pump laser: *CRF Ultra*. Furthermore, ASE fractions in the pulses are cleaned by a saturable absorber. Behind the booster, the pulses are stretched ($\sim 500\,\mathrm{ps}$) and subsequently guided into the regenerative amplifier (Ti:Sa, Nd:YAG pump laser: *CRF Ultra*). Here, the pulses are amplified to energies of 1 mJ.

The first part of the main amplifier system is a 5-multipass unit with a Nd:YAG pump laser: *CRF 200* with an energy of 120 mJ. The energy of the outgoing amplified pulses is increased to 23 mJ. The beams are expanded before entering the next amplifier. Here, in the second 4-multipass amplifier unit (frequency doubled Nd:YAG pump laser with an energy of 2 J) the pulse energy again is intensified to a value of 600 mJ. A separated part of these pulses (15 mJ, compressible to 25 fs) serves as probe beam, *e.g.* for visualization of laser-plasma interaction. The desired timing for this purpose is established with the help of several delay stages within the probe line. Regarding the main beams, there are two main amplifiers with separate grating compressors.

Beam line no. 1 consists of a 4-multipass main amplifier with a $5 \times 5 \times 3\,\mathrm{cm}^3$ cryogenically cooled Ti:Sa crystal. By pumping the pulses with four frequency doubled Nd:YAG lasers ($4 \times 2\,\mathrm{J}$), the amplified beam has an energy of 3.1 J and is expanded to 8 cm beam diameter before entering the compressor. Here in vacuum, two gratings (gold coating) are aligned parallelly. With a compression to 23 fs and a compressor transmission in the order of 60%, focus energies of around 2 J or peak intensities of $10^{20}\,{}^{\mathrm{W}}/_{\mathrm{cm}^2}$ ($f/2$ off-axis parabola) are reachable for laser-plasma experiments.

Beam line no. 2 consists of a 4-multipass amplifier (Nd:YAG pump laser with an energy of 1.2 J) before the main amplifier stage. Five frequency doubled pump lasers (each 2.5 J) amplify the pulses to an energy of 4 J before entering the compressor.

The compressed amplified pulses are guided into the radiation shielded target area, the so-called *bunker*. Here, three vacuum target chambers, *viz.* the gas-target, the solid-target, as well as the medical chamber, are placed in order to conduct different laser-plasma experiments. In the framework of this thesis, the experiments were performed in the gas-target chamber (TC-1), *cf.* Fig. 2.4 [Wil11]. TC-1 has an octagonal base area. Each lateral plane is endowed with a window with a height of $h_{\mathrm{win}} = (475 \pm 1)\,\mathrm{mm}$ and a width of $w_{\mathrm{win}} = (275 \pm 1)\,\mathrm{mm}$. For housing additional diagnostic systems which do not fit inside the chamber (a Thomson parabola inside a separate vacuum chamber, *e.g.*) extension boxes can be mounted at each window. In a height of $h_{\mathrm{gr}} = (39.98 \pm 0.01)\,\mathrm{mm}$ above the footprint a ground plate, *i.e.* an optical breadboard, is mounted. The distance between the laser axis and the ground plate is $h_\mathrm{L} = 170\,\mathrm{mm}$. Beneath the target-chamber center, the so-called TCC which defines the shooting position in the experiment, a solenoid valve of the *Parker Hannifin series 9* with a supersonic Laval nozzle attached is installed. The laser beam propagating in z-direction crosses over the nozzle in a desired height and is focused into the gas jet. In order to avoid damage in the nozzle material, the minimal distance between laser focus and the nozzle edge is $\sim 500\,\mu\mathrm{m}$. The focus diagnostics, an optical lens system to image the focus shape in laser propagation direction, is an important tool for a precise focus adjustment. During the experiments, a parabolic mirror with a focal length of 1000 mm focused the laser beam to a circular spot with $15\,\mu\mathrm{m}$ in diameter ($^1/_{\mathrm{e}^2}$ width).

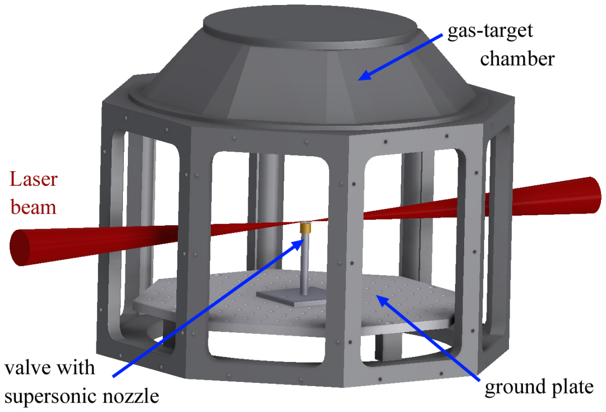

Figure 2.4.: 3D model of the Arcturus gas-target chamber [Wil11].

3. High-Intensity Laser-Plasma Interactions

After the previous insight into the laser principle and its technological implementation, the physical background on laser radiation interacting with matter is discussed shortly. The following chapter provides a digression in laser-plasma physics and serves to help understand the acceleration mechanisms in laser-induced plasmas. At first, the general characteristics of laser optics are described, while the last section deals with the influence of high-intensity laser radiation on matter.

3.1. Physics of laser optics

A monochromatic laser wave propagating in a medium with refractive index η can be described by a vector potential $\boldsymbol{A}$ which is (in case of a monochromatic plane wave) given by:

$$\boldsymbol{A} = \boldsymbol{A}_0 \exp\left(\mathrm{i}\, \boldsymbol{k}_\mathrm{L} \cdot \boldsymbol{r} - \mathrm{i}\, \omega_\mathrm{L} t\right) \,, \tag{3.1}$$

with $\boldsymbol{A}_0$ as the amplitude of the vector potential, $\boldsymbol{k}_\mathrm{L} = k_\mathrm{L}\, \boldsymbol{e}_k = ({}^{2\pi\eta}/_{\lambda_\mathrm{L}})\, \boldsymbol{e}_k$ as the wave number and $\omega_\mathrm{L} = 2\pi\, \nu_\mathrm{L}$ as the angular frequency of the laser pulse. In the following, ω_L will be called *laser frequency*. The dispersion relation for light propagating in vacuum connects ω_L and k_L as follows: $\omega_\mathrm{L}^2 = k_\mathrm{L}^2\, c^2$. Equation (3.1) is written as a complex formula. The real part of the vector potential $\Re(\boldsymbol{A})$ describes the physical vector potential, yielding the electric and magnetic fields according to the Maxwell equations

$$\boldsymbol{E} = -\frac{\partial \boldsymbol{A}}{\partial t} - \nabla \Phi_\mathrm{elec} \,, \tag{3.2}$$

$$\boldsymbol{B} = \nabla \times \boldsymbol{A} \,. \tag{3.3}$$

In the absence of a scalar electrostatic potential ($\nabla \Phi_\mathrm{elec} = 0$ in vacuum) the electric and magnetic field of the laser wave as well as the laser intensity I_L can be written as:

$$\boldsymbol{E}_\mathrm{L} = \mathrm{i}\, \omega_\mathrm{L} \boldsymbol{A} \,, \quad \boldsymbol{B}_\mathrm{L} = \mathrm{i}\, \boldsymbol{k}_\mathrm{L} \times \boldsymbol{A} \,, \quad \text{and} \quad I_\mathrm{L} = \langle |\boldsymbol{S}| \rangle = \frac{1}{\mu_0} \langle |\boldsymbol{E}_\mathrm{L} \times \boldsymbol{B}_\mathrm{L}| \rangle \,, \tag{3.4}$$

where $\langle |\boldsymbol{S}| \rangle$ is the time-averaged Poynting vector, *i.e.* an energy flux. The speed of light in vacuum is given by $c_0^2 = (\varepsilon_0 \mu_0)^{-1}$, where ε_0 is the vacuum permittivity and μ_0 is the vacuum permeability. With the first equation in (3.4), the magnetic field $\boldsymbol{B}_\mathrm{L}$ can also be transformed to: $\boldsymbol{B}_\mathrm{L} = {}^{\mathrm{i}}\!/_{\mathrm{i}\omega_\mathrm{L}}\, \boldsymbol{k}_\mathrm{L} \times \boldsymbol{E}_\mathrm{L} = {}^{1}\!/_{\omega_\mathrm{L}}\, \boldsymbol{k}_\mathrm{L} \times \boldsymbol{E}_\mathrm{L}$, and hence, $\boldsymbol{B}_\mathrm{L} \perp \boldsymbol{E}_\mathrm{L}$. Taking Eq. (3.1) into account, the following relations can be deduced:

$$\begin{aligned} \boldsymbol{E}_\mathrm{L} &= \boldsymbol{E}_0 \exp\left(\mathrm{i}\,\boldsymbol{k}_\mathrm{L}\cdot\boldsymbol{r} - \mathrm{i}\,\omega_\mathrm{L} t\right)\ , \\ \text{thus, } \Re(\boldsymbol{E}_\mathrm{L}) &= \boldsymbol{E}_0\ \cos\left(\boldsymbol{k}_\mathrm{L}\cdot\boldsymbol{r} - \omega_\mathrm{L} t\right)\ , \end{aligned} \tag{3.5}$$

$$\begin{aligned} \boldsymbol{B}_\mathrm{L} &= \boldsymbol{B}_0 \exp\left(\mathrm{i}\,\boldsymbol{k}_\mathrm{L}\cdot\boldsymbol{r} - \mathrm{i}\,\omega_\mathrm{L} t\right)\ , \\ \text{thus, } \Re(\boldsymbol{B}_\mathrm{L}) &= \boldsymbol{B}_0\ \cos\left(\boldsymbol{k}_\mathrm{L}\cdot\boldsymbol{r} - \omega_\mathrm{L} t\right)\ , \end{aligned} \tag{3.6}$$

$$I_\mathrm{L} = \frac{\varepsilon_0 c}{2}\, E_0^2\,, \tag{3.7}$$

Strictly speaking, a plane wave has an infinite latitude perpendicular to the propagation direction (*i.e.* along the $\boldsymbol{k}_\mathrm{L}$-direction), while real laser fields are spatially bounded. Along the propagation direction, a laser pulse is similar to a plane wave with a constant amplitude (*cf.* Eq. (3.5)). On the other hand, similarities to spherical or dipole waves are given: the amplitude decreases radially with increasing distance to the laser source ($E_0(\boldsymbol{r},t) \propto |\boldsymbol{kr}|^{-1}$). Therefore, the theoretical description of laser pulses as plane waves is an approximation.

In optics, Gaussian beams serve as a good description of focused laser waves. The transverse electric field as well as the intensity are Gaussian distributed. Hence, the laser device emits fundamental transverse modes of the resonator, the so-called TEM$_{00}$ modes which are solutions of the paraxial Helmholtz equation $(\Delta_\perp + 2\mathrm{i}k\partial_z)\,A = 0$ [Kul11, p. 104], with A as the wave amplitude and $\Delta_\perp = \partial_x^2 + \partial_y^2 = {}^{\partial^2}\!/_{\partial x^2} + {}^{\partial^2}\!/_{\partial y^2}$ as the Laplace operator regarding the plane perpendicular to the laser propagation direction (here: z-direction). Spatially, the electric field is given by

$$E(r,z) = E_0\,\frac{w_0}{w(z)} \times \mathrm{e}^{-\left(\frac{r}{w(z)}\right)^2} \times \mathrm{e}^{-\mathrm{i}k_\mathrm{L}\left(\frac{r^2}{2R(z)}\right)} \times \mathrm{e}^{\mathrm{i}(\zeta(z)-k_\mathrm{L}z)}\ \text{[Kog66]}\,. \tag{3.8}$$

In the following, the constituents of Eq. (3.8) are described in detail. For a better understanding, Fig. 3.1 illustrates the contour of a Gaussian beam: in Fig. 3.1 (a) an EPOCH simulation [1] of the electric field E_y of a focused Gaussian laser pulse is given, while Fig. 3.1 (b) is a schematic drawing of the focal region.

Assume a Gaussian beam propagating in z-direction in a medium with refractive index η, r is the radial distance from the center axis, $w(z)$ is the Gaussian beam radius at which the electric field or the laser intensity drops to ${}^{1}\!/_{\mathrm{e}}$ or ${}^{1}\!/_{\mathrm{e}^2}$, respectively, and $z_0 = 0$ is the location of the beam waist with a diameter of $2\,w_0 = 2\,w(z_0)$.

---

[1] EPOCH is a PIC simulation code, where the dynamics of charged particles in electromagnetic fields are solved with regard to the Maxwell equations and the particle's equation of motion [Bra14, Bra13], *cf.* Ch. 5 on p. 47

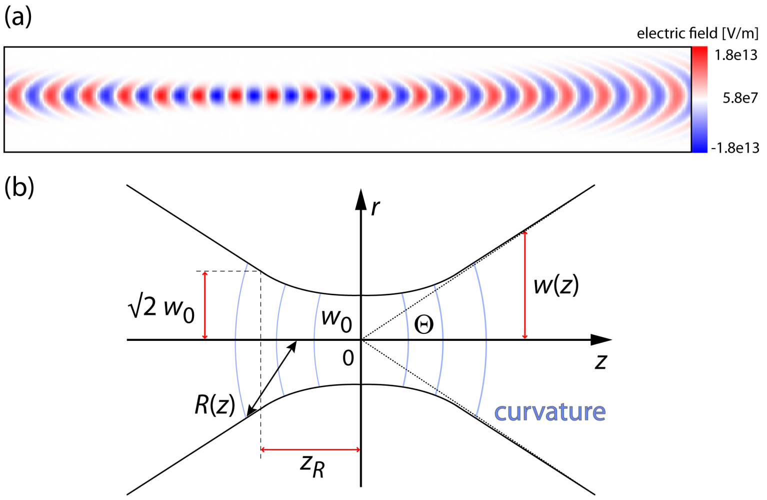

Figure 3.1.: Contour of a focused Gaussian beam: (a) EPOCH simulation of a laser pulse with Gaussian beam profile, and (b) schematic drawing of a focused Gaussian beam propagating in z-direction with the beam radius $w(z)$ which has a minimum, the focus, at $z_0 = 0$, the so-called beam waist with a diameter of $2\,w_0$, as well as the Rayleigh length z_{R} and the radius of curvature $R(z)$ (*cf.* [Kog66]).

Now, the beam radius, the so-called spot size, $w(z)$ as well as the focal radius w_0 can be calculated by [Kog66]

$$w(z) = w_0 \sqrt{1 + \left(\frac{z}{z_{\mathrm{R}}}\right)^2}\,, \tag{3.9}$$

$$\text{and} \qquad w_0^2 = 2\,\frac{z_{\mathrm{R}}}{k_{\mathrm{L}}} = \frac{\lambda\, z_{\mathrm{R}}}{\pi\,\eta}\,, \tag{3.10}$$

Here, $z_{\mathrm{R}} = {}^{\pi\eta}/_{\lambda}\, w_0^2$ is the Rayleigh length. In the region $z_0 \pm z_{\mathrm{R}}$, the so-called Rayleigh region with a width of $b = 2\,z_{\mathrm{R}}$, the laser pulse undergoes its biggest change, which will be described in the following. The Rayleigh region b is also called confocal parameter and depends on the focusing of the laser pulse. Within the near field of the focus (for $z \ll |z_{\mathrm{R}}|$), the wave fronts are changing marginally and the laser pulse can be described by a plane wave. For $z \gg |z_{\mathrm{R}}|$ (far field) the similarity to spherical or dipole waves is given. At the crossover $z = |z_{\mathrm{R}}|$, the spot size w is equal to $w(|z_{\mathrm{R}}|) = \sqrt{2}\,w_0$, while in the far field an approximately linear dependence between w and z is given, with $w(z) = {}^{w_0}/_{z_{\mathrm{R}}}\, z$ as the asymptote for $z \to \infty$. All in all, z_{R} is a measure of how far a laser pulse is collimated.

The bending of the wave fronts, *i.e.* the phase delay at locations far away from the axis, can be calculated by the radius of curvature $R(z) = z\left(1 + ({}^{z_{\mathrm{R}}}/_{z})^2\right)$ [Kog66]. While within the near field the radius of curvature can be approximated by an infinitive value (*i.e.* plane wave fronts), it is approximately equal to z in the far field (*i.e.* spherical wave front). The intensity perpendicular to the propagation direction is Gaussian distributed:

$$I(r,z) = \frac{\varepsilon_0 c}{2}\,|E_0|^2 \left(\frac{w_0}{w(z)}\right)^2 \times \mathrm{e}^{-2\left(\frac{r}{w(z)}\right)^2}\,, \tag{3.11}$$

$$I_z = I(0,z) = \underbrace{\frac{\varepsilon_0 c}{2}\,|E_0|^2 \left(\frac{w_0}{w(z)}\right)^2}_{I_0\left(1+(\frac{z}{z_\mathrm{R}})^2\right)^{-1}}\,, \tag{3.12}$$

with I_z as the axial Lorentz distributed intensity $\propto (1 + (z/z_\mathrm{R})^2)^{-1}$. In the focus $(r_0 = 0, z_0 = 0)$ the intensity reaches its maximum value, the focus peak intensity [2] given by $I_0 = I_\mathrm{peak} = I(0,0) = \varepsilon_0\, c/2\; |E_0|^2$. Its FWHM value is given at $z = z_\mathrm{R}$.

Due to the Gaussian intensity distribution, the beam is diverging behind the Rayleigh region and the wave fronts bend. At the crossover, at $z = z_\mathrm{R}$, the radius of curvature is given by $R(z_\mathrm{R}) = 2\,z_\mathrm{R}$. Regarding the Rayleigh region, a Gaussian laser wave is slightly more bent compared to a plane wave where a linear development of the phase is given. This additional phase as a function of z is called Gouy phase $\zeta(z) = \arctan\left(z/z_\mathrm{R}\right)$ [Kog66] leading to a phase shift of π $(-\pi/2 \leq \zeta(z) \leq \pi/2)$ in the laser wave when passing through its focus.

The divergence Θ of the laser beam behind the focal spot is equal to the angle between the asymptotic linearly propagating outer beam boundary (the far field part) relative to the z-axis. For small z it can be defined by $\Theta \approx \tan\Theta = w_0/z_\mathrm{R} = \lambda/\pi\eta w_0 = \sqrt{\lambda/\pi\eta\, z_\mathrm{R}}$, while for the far field $(z \gg 2\,z_\mathrm{R})$ it is given with $\Theta(z)_{|z\to\infty} = w(z)/z$ (for $z \to \infty$).

Regarding the constituents of Eq. (3.8), it can be concluded that the first factor stands for the transversal distribution of the wave amplitude, the second one (the transverse phase factor) describes the spherical bending of the wave fronts, and the latter (the longitudinal phase factor) includes the oscillating phase distribution along the propagation direction. Hence, the amplitude of the electric field distribution $\boldsymbol{C}(r,z)$ as well as the phase factor $\mathit{\Phi}(r,z)$ are given by

$$\begin{aligned} \boldsymbol{C}(r,z) &= \boldsymbol{E}_0\,\frac{w_0}{w(z)} \times \exp\left(-\frac{r^2}{w^2(z)}\right) \\ \mathit{\Phi}(r,z) &= \exp\left(-\mathrm{i}\left(\frac{k_\mathrm{L}\,r^2}{2R(z)} + \zeta(z) - k_\mathrm{L} z\right)\right)\,. \end{aligned} \tag{3.13}$$

Regarding the temporal evolution, the laser pulse is Gaussian in time, as well. The pulse shape in time, *i.e.* the envelope of the electric field, is given by $\boldsymbol{E}_\mathrm{env}(t) = \boldsymbol{E}_0\,\exp(-\,(t - t_0/w_\mathrm{t})^2)$. The electric field itself can be calculated by $\boldsymbol{E}_\mathrm{env}(t) \times \cos(\omega_\mathrm{L} t + \varphi(t))$, with $\varphi(t)$ as a time-dependent phase. Furthermore, $w_\mathrm{t} = 1/\mathrm{e}\, E_0$ is the Gaussian

---

[2] example: in Fig. 3.1 (a) the maximum electric field amplitude has a value of 1.8×10^{13} V/m leading to a peak intensity of 4.3×10^{19} W/cm²

width and $\Delta t_E = 2 w_\mathrm{t} \sqrt{\ln 2}$ is the FWHM of the electric field strength. According to Eq. (3.7), the time-dependent Gaussian intensity can be derived to:

$$I(t) = \frac{\varepsilon_0\, c}{2}\, E_0^2 \times \mathrm{e}^{\left(-4\,\ln(2)\left(\frac{t-t_0}{\Delta t_E}\right)^2 = -2\,\ln(2)\left(\frac{t-t_0}{\Delta t_I}\right)^2\right)}\,, \tag{3.14}$$

where the FWHM of the electric field Δt_E was substituted by the FWHM of the intensity, *i.e.* $\sqrt{2}\,\Delta t_I = \Delta t_E$.

Figure 3.2 illustrates a simulation of a Gaussian ultra-short high-intensity laser pulse (wavelength of $\lambda_\mathrm{L} = 800\,\mathrm{nm}$, FWHM pulse duration of $\Delta t_I = 26\,\mathrm{fs}$, peak intensity $I_\mathrm{peak} = 4.35 \times 10^{19}\ \mathrm{W/cm^2}$): the electric field E is plotted along the laser propagation axis. Note: for light in vacuum, a length of $5\,\mu\mathrm{m}$ corresponds to a propagation time of approximately $16.7\,\mathrm{fs}$. It becomes obvious, that the amplitude of the oscillating electric field is not a constant value, but Gaussian distributed in time. Therefore, the envelope of the pulse shows a characteristic Gaussian shape.

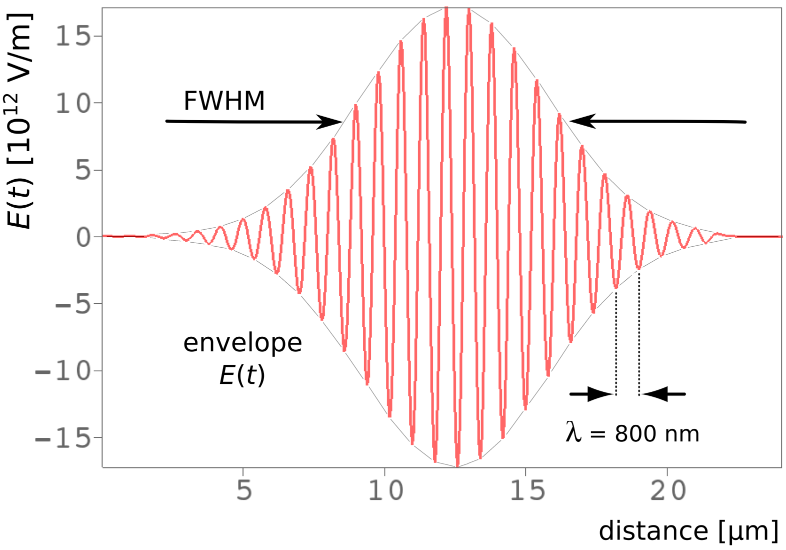

Figure 3.2.: Simulated Gaussian laser pulse: the electric field. The envelope of the electric field $\boldsymbol{E}(t)$ is symbolized by the gray dashed line. In the simulation, the laser pulse had a wavelength of $\lambda_\mathrm{L} = 800\,\mathrm{nm}$, a FWHM pulse duration of $\Delta t_I = 26\,\mathrm{fs}$, and a peak intensity of $I_\mathrm{peak} = 4.35 \times 10^{19}\ \mathrm{W/cm^2}$.

The peak power P_peak of the Gaussian laser beam (for $r \to \infty$) can be derived by integrating the radial intensity distribution (*cf.* Eq. (3.11) and (3.12)) over the full beam area:

$$\begin{aligned} P_{\text{peak}} &= \int_0^\infty \mathrm{d}r\, 2\pi r\, I(r,z) = \frac{\varepsilon_0\, c}{2} \int_0^\infty \mathrm{d}r\, 2\pi r\, E_0^2\, \frac{w_0^2}{w^2(z)}\, \mathrm{e}^{-2\left(\frac{r}{w(z)}\right)^2} \\ &= \frac{\pi\, w^2(z)}{2}\, I_z = \frac{\pi w_0^2}{2}\, I_0\,. \end{aligned} \tag{3.15}$$

3.2. Laser-matter interaction

When interacting with matter, an energy-transfer from the incident laser pulse to atoms or molecules occurs. If the intensity of the incident laser pulse is high enough, a plasma can be generated by ionization processes (*cf.* Sec. 3.2.1), so that in a (fully) ionized medium "free" electrons and heavier ions are present. Furthermore, the laser pulse loses energy by an excitation of plasma waves (*cf.* Sec. 3.2.2), and also by inducing electromagnetic fields which can accelerate the plasma components (*cf.* Sec. 3.2.4). In the following, the interaction processes of laser radiation with matter will be described.

3.2.1. Ionization processes

In order to accelerate charged particles by laser-plasma interaction, first of all the aggregation state of the target material (solid, liquid, gaseous) has to be changed into plasma state. Here, the atomic or molecular bonds, *i.e.* the binding force which prevents matter from decay, have to be overcome by an incident laser pulse. When talking about an *intense* laser, the emphasis is placed on a force which is strong enough to compete against the binding force inside the atom or molecule and leads to ionization of the target.

A good example is the hydrogen atom: an electron with charge $-e$ and a mass of m_e being in the first Bohr orbit with radius a_B experiences an attractive electric force $\boldsymbol{F}_\mathrm{el} = -e\boldsymbol{E}_\mathrm{a}$ (Coulomb attraction) which is due to the proton's positive charge in the nucleus. Here, $\boldsymbol{E}_\mathrm{a}$ is the atomic electric field with the scalar field strength E_a ,

$$E_\mathrm{a} = |\boldsymbol{E}_\mathrm{a}| = \frac{1}{4\pi\varepsilon_0}\, \frac{e}{a_\mathrm{B}^2}\,, \tag{3.16}$$

where a_B is the Bohr radius defined by $a_\mathrm{B} = 4\pi\varepsilon_0\,\left(\hbar^2/m_\mathrm{e}e^2\right) = 5.30 \times 10^{-11}\,\mathrm{m}$. Thus, the electric field between the electron and the proton in hydrogen is $E_\mathrm{a,H} = 5.13 \times 10^{11}\ \mathrm{V/m}$ which is equivalent to an atomic intensity $I_\mathrm{a,H}$ (*cf.* Eq. (3.7)) given with $3.49 \times 10^{16}\ \mathrm{W/cm^2}$. For helium, they can be calculated to $E_\mathrm{a,He} = 1.03 \times 10^{12}\ \mathrm{V/m}$ and $I_\mathrm{a,He} = 1.40 \times 10^{17}\ \mathrm{W/cm^2}$, respectively. A laser intensity I_L exceeding this atomic intensity is able to overcome the binding energy for hydrogen or helium, and hence, expel the bound electron to the free continuum. Compared to sunlight propagating to the surface of earth with the solar constant of approximately 1367 $\mathrm{W/m^2}$, this threshold intensity $I_\mathrm{L} > I_\mathrm{a}$ seems to be enormous. But compared to today's laser facilities which reach intensities of up to $10^{22}\ \mathrm{W/cm^2}$, it is a "moderate" value. Also lower intensities

$< I_\mathrm{a}$ cause high ionization rates. This is due to the fact that the electric field of the incident laser pulse affects the atomic potential (*cf.* paragraph "tunneling ionization", p. 17) [Bet77, p. 235 f.].

Depending on the properties of the incident laser pulse, like *e.g.* peak intensity, focus energy, pulse duration, or wavelength, several ionization processes can occur during laser-matter interaction, which are described in the following.

Multi-photon ionization (MPI) In order to expel out an electron from the Coulomb potential of the parent atom or ion, external energy input is necessary. This can be realized by absorbing single high-frequency photons or simultaneously multiple low-frequency photons with an energy $\mathcal{E}_\mathrm{ph} = \hbar\omega_\mathrm{L}$ [Mai91]. If the binding energy $\mathcal{E}_\mathrm{ion}$ (*i.e.* the ionization energy) of the bound electrons in the atom is lower than the photon energy, the atom can be photo-ionized. The kinetic energy of the released electron is $\mathcal{E}_\mathrm{kin} = \hbar\omega_\mathrm{L} - \mathcal{E}_\mathrm{ion}$. This ionization process is called *single photon ionization.* Otherwise, if the energy of a single photon is lower than the binding energy, several photons are required for an ionization of the atom. A multiple absorption of n photons proceeds until the absorbed energy $n\,\hbar\omega_\mathrm{L}$ is higher than $\mathcal{E}_\mathrm{ion}$ (*multi-photon ionization*). The energy gain of the electron is $\mathcal{E}_\mathrm{kin}^\mathrm{mpi} = n\,\hbar\omega_\mathrm{L} - \mathcal{E}_\mathrm{ion}$.

Figure 3.3 illustrates a schematic drawing of different ionization mechanisms (*cf.* [Jun07]). In Fig. 3.3 a), the MPI process is shown. The electron with binding energy $\mathcal{E}_\mathrm{ion}$ is kept in the Coulomb potential of the parent ion (indicated by the wave packet). Due to an incident laser pulse with $I_\mathrm{L} = 10^{12}\ \mathrm{W/cm^2}$, the electron simultaneously absorbs n photons, and thus, it is able to escape the atomic potential, *cf.* Fig. 3.3 b). MPI was observed by [Vor65, Ago68] for the first time. For MPI a high photon flux density propagating through a certain surface area is necessary in order to increase the probability for photon-matter interaction, *i.e.* for an absorption of an incoming photon.

A special case of MPI is *above-threshold ionization* (ATI). Here, an additional number of m photons is absorbed although this extra amount of energy would not be required for releasing the bound electron [Ago79, Bur93]. The additional energy is transferred to the parent ion in terms of momentum. Now, the kinetic energy of the electron is given by the extended Einstein's formula $\mathcal{E}_\mathrm{kin}^\mathrm{ati} = (n+m)\,\hbar\omega_\mathrm{L} - \mathcal{E}_\mathrm{ion}$. Both MPI and ATI processes mainly occur for intensities $> 10^{10}\ \mathrm{W/cm^2}$, short wavelengths, and long pulse durations.

Tunneling ionization (TI) With increasing laser intensities I_L, *i.e.* strong fields, the binding Coulomb potential $\mathcal{V}_\mathrm{C}$ of the parent atom or ion is deformed by the laser potential $\mathcal{V}_\mathrm{L}$. Due to this superposition, a decreased potential barrier is formed [Per66, Amm86, Bur93]. The effective potential $\mathcal{V}_\mathrm{eff}(x) = \mathcal{V}_\mathrm{C} + \mathcal{V}_\mathrm{L}$, with $\mathcal{V}_\mathrm{L} = -eE_0\,x$, has a saddle point at a critical distance x_s which is above the binding energy of the electron $\mathcal{E}_\mathrm{ion}$ [Bet77, p. 235 f.] (*cf.* Fig. 3.3 c)). Electrons are able to tunnel through this barrier and are subsequently accelerated by the laser field (TI). A special case of TI is given with higher intensities I_L, and thus, stronger electric fields: the saddle point decreases with increasing electric fields until, at a critical electric field E_cr, the binding energy is reached. At this point, *i.e.* for $\mathcal{V}_{\mathrm{eff}_\mathrm{s}} = -\mathcal{E}_\mathrm{ion}$, *over-the-barrier ionization* (OTBI) is the

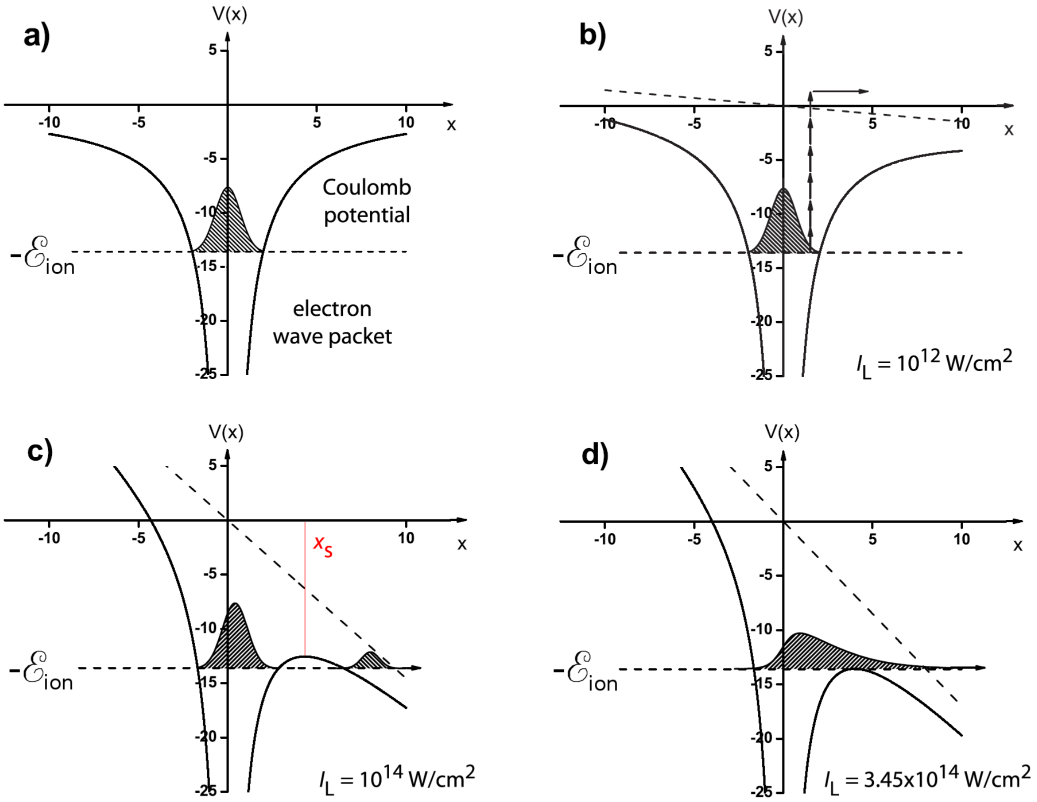

Figure 3.3.: Schematic drawing of ionization processes (*cf.* [Jun07]): a) electrostatic Coulomb potential $\mathcal{V}(x)$ of an ion ($Z = 1$) without external electric fields. The bound electron with binding energy $\mathcal{E}_{\mathrm{ion}}$ inside the potential barrier is indicated by the wave packet. In b)-d) the external electric field of the laser pulse is present. The dashed line indicates the linear laser potential $\mathcal{V}_{\mathrm{L}} \propto -x$. Dependent on the field strength, the atomic potential is deformed. Ionization mechanisms: b) MPI ($I_{\mathrm{L}} = 10^{12}\ \mathrm{W/cm^2}$), c) TI ($I_{\mathrm{L}} = 10^{14}\ \mathrm{W/cm^2}$), d) BSI ($I_{\mathrm{L}} = 3.45 \times 10^{14}\ \mathrm{W/cm^2}$).

dominant ionization process. OTBI is also called *barrier suppression ionization* (BSI). Now, electrons have enough energy to follow the laser field directly without need for tunneling, *cf.* Fig. 3.3 d). Regarding laser intensities comparable to those of the Arcturus or the PHELIX laser, BSI is the prevailing ionization mechanism. The critical electric field E_{cr} for the case $\mathcal{V}_{\mathrm{eff_s}} = -\mathcal{E}_{\mathrm{ion}}$ yields an effective appearance intensity, *i.e.* the minimal laser intensity needed in order to reach the BSI regime:

$$E_{\mathrm{cr}} = \frac{\pi \varepsilon_0}{Z e^3} \mathcal{E}_{\mathrm{ion}}^2 , \tag{3.17}$$

$$I_{\mathrm{app}} = \frac{\pi^2 \varepsilon_0^3 c}{2 Z^2 e^6} \mathcal{E}_{\mathrm{ion}}^4 \approx 4 \times 10^9 \left(\frac{\mathcal{E}_{\mathrm{ion}}}{\mathrm{eV}} \right)^4 Z^{-2} \frac{\mathrm{W}}{\mathrm{cm}^2} . \tag{3.18}$$

In context of the present thesis, ^{4}He as well as ^{3}He served as plasma target and were ionized by high-intensity laser irradiation. The energies for the first and second ionization stages for helium are 24.59 eV and 54.42 eV, respectively. Thus, the appearance intensities needed to ionize helium gas can be calculated to $I_{\mathrm{app,He^+}} = 3.7 \times 10^{14}\ {}^{\mathrm{W}}\!/_{\mathrm{cm}^2}$ and $I_{\mathrm{app,He^{2+}}} = 8.8 \times 10^{15}\ {}^{\mathrm{W}}\!/_{\mathrm{cm}^2}$, respectively. This value is significantly lower than the predicted intensity I_{a} (*cf.* p. 16) in case that only the undisturbed ionization potential is taken into account. Knowing the certain appearance intensities is important since the intensity distribution of the incoming laser pulse indeed has a Gaussian shape, but due to ASE there is a certain amount of "low"-intensity radiation temporally before the main pulse. This so-called *pedestal* or *prepulse* is able to pre-ionize target material if the relation between the peak intensity of the main pulse I_{peak} and the pedestal intensity I_{ped}, *i.e.* the *contrast (ratio)* of the laser system, is unfavorable. For laser-acceleration experiments, a possible pre-ionization can be disadvantageous. The contrast in dB can be calculated by $10\,\lg({}^{I_{\mathrm{peak}}}\!/_{I_{\mathrm{ped}}})$. The PHELIX laser, *e.g.*, offers a contrast of down to $100 - 110\,\mathrm{dB}$ in case of the short pulse - the relation ${}^{I_{\mathrm{peak}}}\!/_{I_{\mathrm{ped}}} = 10^{10-11}$ indicates a pedestal intensity in the order of $\sim 10^{10-11}\ {}^{\mathrm{W}}\!/_{\mathrm{cm}^2}$. Within the experimental studies at PHELIX, a contrast of 10^7, and hence, a pedestal intensity of $10^{12}\ {}^{\mathrm{W}}\!/_{\mathrm{cm}^2}$ was given. Thus, a possible high pre-ionization of the helium gas due to a high prepulse is not expected.

Ionization processes can be characterized by the dimensionless Keldysh parameter γ_{K} [Kel65]. It is a quantitative indicator of the certain regime in which the different ionization processes might occur. It can be understood as the relation between the classical circulation time of a bound electron and the characteristic time for tunneling through a potential barrier, *i.e.* the tunnel probability of the electron through the (modified) Coulomb wall. This probability increases with the presence of external quasi-static electric fields. Attendant calculations were performed by [Kel65, Per66, Per67]. The Keldysh parameter [3] is given by

$$\gamma_{\mathrm{K}} = \omega_{\mathrm{L}}\,\frac{\sqrt{2\,m_{\mathrm{e}}\,\mathcal{E}_{\mathrm{ion}}}}{e\,E_0} = \omega_{\mathrm{L}}\,\sqrt{\frac{\varepsilon_0\,m_{\mathrm{e}}c\,\mathcal{E}_{\mathrm{ion}}}{e^2\,I_{\mathrm{L}}}}\,, \tag{3.19}$$

where E_0 is the peak electric field, I_{L} is the laser peak intensity, ω_{L} is the laser frequency, and $\mathcal{E}_{\mathrm{ion}}$ is the binding energy of the electrons. For $\gamma_{\mathrm{K}} < 1$, TI is the dominant ionization process. Here, strong electric fields and long wavelengths are present. The BSI regime is given for $\gamma_{\mathrm{K}} \ll 1$, while ATI occurs for $\gamma_{\mathrm{K}} > 1$. In case of ATI, the tunneling time of the electron is larger than the laser period.

3.2.2. Interaction with single electrons

After a high-intensity laser ionizes the target material, the freed electrons start to oscillate due to the strong electromagnetic fields. The equation of motion for a single electron with mass m_{e} and charge $-e$ in high-intensity electromagnetic laser fields is given by the Lorentz equation:

---

[3] note: γ_{K} also depends on the plasma frequency $\omega_{\mathrm{p}} = \sqrt{{}^{e^2\,n_{\mathrm{e}}}\!/_{(\varepsilon_0\,\bar{\gamma} m_{\mathrm{e}})}}$ (defined on p. 24)

$$\frac{\mathrm{d}\boldsymbol{p}_\mathrm{e}}{\mathrm{d}t} = \frac{\mathrm{d}}{\mathrm{d}t}\gamma m_\mathrm{e}\,\boldsymbol{v}_\mathrm{e} = -e\left(\boldsymbol{E}_\mathrm{L} + \boldsymbol{v}_\mathrm{e}\times\boldsymbol{B}_\mathrm{L}\right)\,, \tag{3.20}$$

with the relation $\boldsymbol{B}_\mathrm{L} = {}^{1}\!/_{c}\,\boldsymbol{E}_\mathrm{L}$, *cf.* Eq. (3.4), $\boldsymbol{v}_\mathrm{e}$ as the electron velocity, $\boldsymbol{p}_\mathrm{e} = \gamma m_\mathrm{e}\,\boldsymbol{v}_\mathrm{e}$ as the relativistic electron momentum, $\gamma = (1-\beta^2)^{-.5}$ as the relativistic Lorentz factor, $\beta = {}^{v_\mathrm{e}}\!/_{c}$ as the dimensionless relativistic parameter, *cf.* Eq. (3.23) and (3.24), which can be defined by the laser parameters. For different values of β two cases can occur: $\beta \ll 1$ is the non-relativistic case, while for $\beta \approx 1$ the motion of the plasma electrons has to be described relativistically.

Non-relativistic regime In the non-relativistic case, *i.e.* $\beta \ll 1$ or $\gamma \approx 1$, the influence of the magnetic field on the motion of the electron can be neglected: the vector product $\boldsymbol{v}_\mathrm{e}\times\boldsymbol{B}_\mathrm{L}$ becomes small since $\boldsymbol{B}_\mathrm{L} = {}^{1}\!/_{c}\,\boldsymbol{E}_\mathrm{L}$. Thus, only the electric force, $\dot{\boldsymbol{p}}_\mathrm{cl} = m_\mathrm{e}\dot{\boldsymbol{v}}_\mathrm{q} = \boldsymbol{F}_\mathrm{el} = -e\boldsymbol{E}_\mathrm{L}$, determines the equation of motion of the oscillating electron, leading to the electron quiver velocity given by $\boldsymbol{v}_\mathrm{q} = ({}^{e}\!/_{m_\mathrm{e}\omega_\mathrm{L}})\,\boldsymbol{E}_\mathrm{L}$ (with $\boldsymbol{v}_\mathrm{q} \parallel \boldsymbol{E}_\mathrm{L}$).

The quiver energy $\mathcal{U}_\mathrm{pon}$, the so-called *ponderomotive potential*[4] of the laser field, which is stored in the electron oscillation can be calculated by time-averaging the kinetic energy of the electron, $\mathcal{U}_\mathrm{pon} = \left\langle {}^{1}\!/_{2}\, m_\mathrm{e} v_\mathrm{q}^2 \right\rangle = {}^{1}\!/_{2}\,\mathcal{E}_\mathrm{kin}^\mathrm{max}$:

$$\begin{aligned}
\mathcal{U}_\mathrm{pon} &= \frac{e^2}{4\,m_\mathrm{e}\,\omega_\mathrm{L}^2}\,E_\mathrm{L}^2 \quad [\mathrm{Gib05, p.\,20}] \\
&= \frac{e^2}{8\,\pi^2\varepsilon_0\,m_\mathrm{e}\,c^3}\,I_\mathrm{L}\,\lambda_\mathrm{L}^2 \qquad\qquad (3.21) \\
\mathcal{U}_\mathrm{pon} &\approx 1.498\times10^{-24}\,\mathrm{s}\;\times\; I_\mathrm{L}\,\lambda_\mathrm{L}^2\,.
\end{aligned}$$

This classical ansatz is only valid for certain intensity-wavelength products of up to $\sim 10^{18}\,\mathrm{W}\,{}^{\mu\mathrm{m}^2}\!/_{\mathrm{cm}^2}$. Then the ponderomotive potential is nearly equal to the rest energy of the electron. Since the intensity of the incident laser pulse has a Gaussian contour in time and space, the intensity is not a constant: an intensity gradient is present perpendicular to the beam propagation axis. Therefore, the quiver motion of the electrons occurs in radial direction, *i.e.* in the direction of decreasing intensity or simply out of the laser focus.

This motion is due to the *ponderomotive force* $\boldsymbol{F}_\mathrm{pon}$ given by:

$$F_\mathrm{pon} = |\boldsymbol{F}_\mathrm{pon}| = -\frac{e^2}{4\,m_\mathrm{e}\,\omega_\mathrm{L}^2}\,\frac{\partial E_0^2}{\partial y}\quad [\mathrm{Gib05}, p.38]\,. \tag{3.22}$$

---

[4] example: the PHELIX laser, *e.g.*, delivers pulses with an intensity of $I_\mathrm{L} = 2\times10^{21}\,{}^{\mathrm{W}}\!/_{\mathrm{cm}^2}$ at a wavelength of $\lambda_\mathrm{L} = 1053\,\mathrm{nm}$. Here, the ponderomotive potential is equal to $207.673\,\mathrm{MeV} \gg \mathcal{E}_\mathrm{e}^\mathrm{rest} = 0.511\,\mathrm{MeV}$ (rest energy of the electron). The classical ansatz is no longer valid

Comparing Eq. (3.22) to (3.21), it is clear that the ponderomotive force can be calculated by the negative gradient of the ponderomotive potential: $\boldsymbol{F}_{\text{pon}} = -\nabla\mathcal{U}_{\text{pon}} \propto -\nabla I_{\text{L}}$. Therefore, an intensity gradient has to be present in order to properly accelerate electrons in a laser field. In case of a plane wave (*i.e.* constant intensity distribution), the electron will oscillate due to the electromagnetic field of the laser pulse. The electric field of a plane wave has a constant amplitude which fluctuates periodically between the maximal values. As soon as the laser pulse has left the interaction region, the electron will not follow the pulse, but it will remain on its original location. Averaged in time, acceleration and deceleration of the electrons due to the certain value of the electric field strength cancel each other out. But, in case of a focused Gaussian laser pulse, the electric field amplitude is Gaussian distributed, *cf.* Fig. 3.2. The electron being on the laser axis "sees" the oscillating electric field with increasing amplitude. It is radially accelerated to outer regions. At this location, the repelling force is smaller, and therefore, the electron cannot return to its original position, it is displaced. With the following half-cycles, it is re-accelerated outwards. Hence, it starts to oscillate and with each turn it gains more kinetic energy. This repetitive process is sustainable until the appealing electric field amplitude starts to decrease again. Then, the kinetic energy of the electron is high enough to exit the interaction region because the decelerating force due to the (decreased) electric field strength cannot compete against the motion of the electron. All in all, the given intensity gradient forces the electron to be irreversibly expelled out of regions with higher intensity.

Relativistic regime With stronger electric fields and therefore increasing laser intensities, the electron oscillation in y-direction becomes faster and faster, and hence, the magnetic component in the Lorentz equation (*cf.* Eq. (3.20)) is no longer neglectable. The electron motion along y and the magnetic field alignment along x result in a z-component of the appearing force. This magnetic component does not contribute in the acceleration of the electron, but the propagation direction of the charged particle is changed in forward direction.

The relation between the quiver velocity $v_{\text{q}} = v_{\perp}$ perpendicular to the laser propagation direction and the speed of light c is given by the relativistic dimensionless parameter β_{q}[5]:

$$\beta_{\text{q}} = \frac{v_{\text{q}}}{c} = \frac{eE_0}{m_{\text{e}}\omega_{\text{L}}c} = \frac{eA_0}{m_{\text{e}}c} \equiv a_0 \,. \tag{3.23}$$

Regarding a laser-induced motion of charged particles, a_0 can be understood as a normalized vector potential, which can be written as a function of the laser intensity as well as the wavelength:

---

[5] note: in theoretical laser-plasma physics, the notation for the normalized vector potential, a_0, is common

$$
\begin{aligned}
a_0 &= \sqrt{\frac{e^2}{2\pi^2\,\varepsilon_0\,m_\mathrm{e}^2\,c^5}\,\lambda_\mathrm{L}^2\,I_\mathrm{L}} \\
&\approx \sqrt{7.324\times 10^{-11}\,\mathrm{s/J}} \times \sqrt{\lambda_\mathrm{L}^2\,I_\mathrm{L}}\;.
\end{aligned}
\tag{3.24}
$$

For $a_0 \approx 1$, *i.e.* $v_\mathrm{q} \to c$, nonlinear dynamics occur due to the magnetic force $-e\,\boldsymbol{v} \times \boldsymbol{B}_\mathrm{L}$. The limit regarding the given laser properties is approximately $\lambda_\mathrm{L}^2\,I_\mathrm{L} \gtrsim 1.37 \times 10^{18}\,\mathrm{W\,\mu m^2/cm^2} = 1.37 \times 10^{10}\,\mathrm{W}$.

The relativistic equations of motion for electrons in electromagnetic fields were investigated by [San65, Ebe68, Bar89]. The electron momenta in each x, y, z-direction in the laboratory frame are (in case of a linearly polarized laser pulse)

$$
\frac{\boldsymbol{p}}{m_\mathrm{e}c} = \frac{1}{m_\mathrm{e}c}\begin{pmatrix} p_x \\ p_y \\ p_z \end{pmatrix} = \begin{pmatrix} 0 \\ a_0\,\cos\psi \\ \frac{a_0^2}{4}\,[1+\cos(2\psi)] \end{pmatrix}\,, \tag{3.25}
$$

with $\psi = \omega_\mathrm{L}t - k_\mathrm{L}z$ (for other laser polarizations *cf.* [Gib05, p. 31 f.]). Next to the quiver motion along y, in forward direction the electron gets a z-momentum p_z. Thus, the electron starts to drift with an average momentum $p_\mathrm{d} = \bar{p}_z = {}^{a_0^2}\!/_4\,m_\mathrm{e}c$ (note: the overscore indicates the average over the rapidly varying phase ψ) [Gib05, p. 33]. The average drift velocity $\boldsymbol{v}_\mathrm{d}$ in z-direction can be calculated by

$$
\boldsymbol{v}_\mathrm{d} = \frac{\bar{\boldsymbol{p}}_z}{\bar{\gamma}}\,c = \frac{a_0^2}{4+a_0^2}\,c\,\boldsymbol{e}_z\,. \tag{3.26}
$$

Following [Bau95, Sta97, Que98], the relativistic ponderomotive potential $\mathcal{U}_\mathrm{pon}$ as well as the relativistic ponderomotive force $\boldsymbol{F}_\mathrm{pon}$ can be derived to

$$
\mathcal{U}_\mathrm{pon} = \frac{e^2\,E_0^2}{4\,\bar{\gamma}m_\mathrm{e}\,\omega_\mathrm{L}^2} = \frac{m_\mathrm{e}\,c^2}{4\,\bar{\gamma}}\,\beta^2\;, \tag{3.27}
$$

$$
\boldsymbol{F}_\mathrm{pon} = -\nabla\mathcal{U}_\mathrm{pon} = -\frac{e^2}{4\,\bar{\gamma}m_\mathrm{e}\,\omega_\mathrm{L}^2}\,\nabla E_0^2\;, \tag{3.28}
$$

$$
\text{with } \bar{\gamma} = \langle\gamma\rangle \approx \sqrt{1+\frac{a_0^2}{2}} \tag{3.29}
$$

as the cycle-averaged Lorentz factor of an oscillating free electron in case of a linearly polarized laser pulse.

The derived equations above describe the influence of laser radiation only on quasi-free single electrons - not included are additional electrostatic potentials which are due to laser-induced charge-separation after the laser-electron interaction. But next to electrons as plasma constituents, heavier ions are present. Compared to the mass of an electron, ions are massive particle compounds: a proton as the lightest ion species has a mass of almost 2000 times the electron mass, $m_\mathrm{p} = 1836\, m_\mathrm{e}$. Since the quiver velocity, and thus the ponderomotive potential, and subsequently also the ponderomotive force, as well as the relativistic parameter β are proportional to $\propto m_i^{-1}$ of the given particle, it becomes obvious that for a nearly 2000 times (in case of heavy ions even more) heavier particle the laser-generated forces are too weak to induce a relativistic ion motion. In order to reach an $a_0 \approx 1$ (relativistic) regime for ions, intensity-wavelength products of several $10^{24}\,\mathrm{W}\,{}^{\mu\mathrm{m}^2}\!/_{\mathrm{cm}^2}$ would be needed in order to accelerate ions directly with an incident ultra-intensity laser pulse. However, this lower limit is beyond today's achievable laser intensities. Therefore, laser-induced ion acceleration has to be accomplished in a different (indirect) way (*cf.* Sec. 3.2.4).

3.2.3. Laser-plasma interaction

The term *plasma*, which stands for the *fourth state of matter*, was adopted by I. Langmuir (1928) in order to signify the properties of ionized gas [Lan28]. For plasma in thermodynamic equilibrium, the relevant quantity to describe plasma and its conditions is the temperature T. The plasma constituents are electrons and ions. While the negatively charged plasma electrons can be described by their density distribution $n_\mathrm{e}(\boldsymbol{r}, t)$ as well as by their velocity distribution $v_\mathrm{e}(\boldsymbol{r}, t)$, the inert plasma ions form a positively charged background (n_i). In plasma physics, the electron density is referred to as the *plasma density.* Depending on the ionization degree also neutral atoms or molecules can be given (n_n). In that case, the plasma is not fully ionized. One of the plasma characteristics is quasi neutrality, *i.e.* the positive and negative charges nearly counterbalance each other, and thus, leading to a nearly neutral plasma. The quasi-neutrality condition can be written as $n_\mathrm{e} = Z n_\mathrm{i}$ (Z is the charge state).

A test charge being at rest which is brought into plasma leads to a polarization of the surrounding plasma. Hence, this test charge is shielded by the opposite charge carriers: its potential $\Phi \propto \exp\left(-{}^{r}\!/_{\lambda_\mathrm{D}}\right)$ decreases to ${}^{1}\!/_{\mathrm{e}}$ of the Coulomb potential within a certain range λ_D around this charge, the so-called Debye length [Gol95, p. 15], given by

$$\lambda_\mathrm{D} \equiv \sqrt{\frac{\varepsilon_0\, k_\mathrm{B}\, e^{-2}}{\frac{n_\mathrm{e}}{T_\mathrm{e}} + \sum_j Z_j^2 \frac{n_{\mathrm{i},j}}{T_{\mathrm{i},j}}}}\,, \tag{3.30}$$

with k_B as the Boltzmann constant, $n_\mathrm{e,i}$ and $T_\mathrm{e,i}$ as the electron and ion densities and temperatures, respectively, and $(Z)e$ as the electron (and ion) charge. In case that the ion mobility can be neglected (in comparison to the physics' timescale), the ion term in Eq. (3.30) often is not included in the Debye length: $\lambda_\mathrm{D} = \sqrt{\varepsilon_0\, k_\mathrm{B}\, T_\mathrm{e}\, (n_\mathrm{e}\, e^2)^{-1}}$.

The number N_D of particles of species i inside the so-called Debye sphere (volume of $V_\mathrm{D} = {}^{4}\!/_{3}\, \pi\, \lambda_\mathrm{D}^3$) is referred to as the plasma parameter Λ_p given by

$$N_{\mathrm{D}} \equiv \Lambda_{\mathrm{p}} = \frac{4\pi}{3}\,\lambda_{\mathrm{D}}^{3}\,n_i\,. \tag{3.31}$$

Effective Debye shielding is only given if the number of surrounding particles is high enough. For $N_{\mathrm{D}} \gg 1$, the plasma constituents exhibit collective behavior. Example: for plasma electrons with $T_{\mathrm{e}} = 100\,\mathrm{eV}$ and $n_{\mathrm{e}} = 10^{19}\,\mathrm{cm}^{-3}$, *e.g.*, the Debye length is $\lambda_{\mathrm{D,e}} \approx 23.5\,\mathrm{nm}$, and the Debye sphere with a volume of $V_{\mathrm{D,e}} \approx 54.4 \times 10^{3}\,\mathrm{nm}^{3}$ is filled with $N_{\mathrm{D,e}} \approx 544$ electrons.

As described above, an incoming high-intensity laser wave creates a plasma with oscillating relativistic electrons. Plasma can be seen as a dielectric medium with the dispersion relation $\omega^2 = \omega_{\mathrm{p}}^2 + c^2 k_{\mathrm{L}}^2$ and a refractive index $\eta_{\mathrm{p}} = \sqrt{\varepsilon} = \Re(\eta_{\mathrm{p}}) + \mathrm{i}\Im(\eta_{\mathrm{p}})$. Here, ε is the dielectric function. The eigenfrequency of the collective electron motion against the plasma ion background is called (electron) *plasma frequency* $\omega_{\mathrm{p,e}} = \omega_{\mathrm{p}}$. It is influenced by the electron density n_{e} and also by the relativistic electron mass $\bar{\gamma} m_{\mathrm{e}}$. Similar to the definition of the Debye length, the ion plasma frequencies $\omega_{\mathrm{p,i}}$ can be neglected in case of a more or less immobile ion background. The plasma frequency as well as the v_{ph}-dependent refractive index are defined in the following Eq. ($v_{\mathrm{ph}} = \omega_{\mathrm{L}} k_{\mathrm{L}}^{-1}$ is the wave's phase velocity) [Puk03]:

$$\omega_{\mathrm{p}} = \sqrt{\frac{e^2\,n_{\mathrm{e}}}{\varepsilon_0\,\bar{\gamma} m_{\mathrm{e}}}}\,, \tag{3.32}$$

$$\eta^2(r) = \varepsilon = \left(\frac{c}{v_{\mathrm{ph}}}\right)^2 = \left(\frac{c k_{\mathrm{L}}}{\omega_{\mathrm{L}}}\right)^2 = 1 - \frac{\omega_{\mathrm{p}}^2(r)}{\omega_{\mathrm{L}}^2}\,. \tag{3.33}$$

In laser-induced plasmas nonlinear processes result in a relativistic *self-focusing* of the laser beam [Cum70, Max74, Spr87, Bor92, Mon95]. For low laser intensities, *i.e.* in the absence of nonlinear effects, a Gaussian laser beam will diverge behind the focus spot (divergence Θ, *cf.* p. 14). But for a high-intensity laser beam propagating through an ionized medium with refractive index η, beam spreading effects due to diffraction vanish. This means that the laser beam stays focused for several Rayleigh lengths z_{R}. Thus, a plasma channel in electron density can be generated. The important parameter for self-focusing is not the laser peak intensity, but the initial laser power P_{in}, *cf.* Eq. (3.15) [Cou07]. According to [Mar75], beam diffraction is only overcome if the input peak power exceeds a critical threshold power P_{c}, which is dependent on the laser wavelength as well as on the refractive index of the medium (which can be increased in the presence of high-intensity laser radiation). A usual value for the critical power is given by $P_{\mathrm{c}} \simeq 17.5\,({}^{\omega_{\mathrm{L}}}\!/_{\omega_{\mathrm{p}}})^2\,\mathrm{GW}$ [Puk03, Gib05, p. 105].

Next to relativistic self-focusing, also ponderomotive self-focusing can occur. This mechanism can be explained by the ponderomotive force $\boldsymbol{F}_{\mathrm{pon}}$: the plasma electrons are expelled out of regions with higher intensity, because here $\boldsymbol{F}_{\mathrm{pon}}$ (pointing out of the direction of the maximum intensity gradient) is stronger than in a distance r to the optical axis with lower intensity. This ponderomotive displacement of the electrons occurs until an equilibrium of forces between the attractive Coulomb force (between the inert ions and the electrons) and the repulsive ponderomotive force is established. In this case, near the focus as the location with the highest laser intensity I_{peak} the electron density $n_{\mathrm{e},0} = n_{\mathrm{e}}(r=0)$, and thereby also the plasma frequency $\omega_{\mathrm{p},0} = \omega_{\mathrm{p}}(r=0)$, are lower than in a certain distance r from the center: $n_{\mathrm{e}}(0) < n_{\mathrm{e}}(r)$ and $\omega_{\mathrm{p}}(0) < \omega_{\mathrm{p}}(r)$, respectively. The ponderomotive displacement of the relativistic electrons causes an inhomogeneous distribution of the refractive index according to the laser intensity $I_{\mathrm{L}}(r)$, *i.e.* $\eta_{\mathrm{p}}(0) > \eta_{\mathrm{p}}(r)$: in the core, η_{p} is greater than in the fringes of the laser beam. Therefore, these changes in the refractive index resemble a focusing lens for the incident laser pulse, resulting in a ponderomotive self-focusing of the laser pulse. The surface wave front is bent inwards and the laser beam converges.

The r-dependence of the laser intensity causes an r-dependence of the relativistic parameter $\beta(r) = a_0(r)$ and also of the cycle-averaged Lorentz factor $\bar{\gamma}(r) \approx \sqrt{1 + a_0^2(r)/2}$. For relativistic electrons with a mass $\bar{\gamma}(r) m_{\mathrm{e}}$ the plasma frequency ω_{p}^2 changes to $\omega_{\mathrm{p}}^2/\bar{\gamma}(r)$ which influences the refractive index as follows:

$$\eta(r) = \sqrt{1 - \frac{\omega_{\mathrm{p}}^2}{\bar{\gamma}(r)\omega_{\mathrm{L}}^2}} \; . \tag{3.34}$$

Close to the focus, the cycle-averaged Lorentz factor is larger than in a certain distance r from the main laser axis, so that the refractive index declines with larger distances: $\gamma(0) > \gamma(r) \Rightarrow \eta(0) > \eta(r)$, resulting in a self-focusing effect on the laser pulse in the medium.

The relation between plasma and laser frequency determines whether a laser pulse is able to propagate through plasma or not: an incoming laser bullet can propagate through plasma until the plasma frequency (*cf.* Eq. (3.32)) is equal to the frequency of the electromagnetic wave: $\omega_{\mathrm{p}} \overset{!}{=} \omega_{\mathrm{L}}$. This limiting case occurs for a critical plasma density n_{c}, which is given by

$$n_{\mathrm{c}}\left(\omega_{\mathrm{L}}\right) = \frac{\varepsilon_0 \, \bar{\gamma} m_{\mathrm{e}}}{e^2} \, \omega_{\mathrm{L}}^2 \; . \tag{3.35}$$

With the aid of Eq. (3.35), the refractive index η_{p} can also be written as

$$\eta_{\mathrm{p}}(r) = \sqrt{1 - \left(\frac{\omega_{\mathrm{p}}(r)}{\omega_{\mathrm{L}}}\right)^2} = \sqrt{1 - \frac{n_{\mathrm{e}}(r)}{n_{\mathrm{c}}}} \; . \tag{3.36}$$

Laser-plasma interactions generally can be categorized in *overdense* or *underdense* interactions depending on the electron density in the plasma target. If the plasma density is higher than the critical density ($n_{\mathrm{e}} > n_{\mathrm{c}}$, *i.e.* $\omega_{\mathrm{p}} > \omega_{\mathrm{L}}$), the refractive index becomes complex, which is referred to as an overdense plasma. Here, propagation is inhibited. The laser beam cannot (completely) propagate through the medium and is partially reflected on the target surface. The skin depth $l_\mathrm{s} = {}^{c}/_{\omega_\mathrm{p}}$ is the maximum depth the laser pulse can penetrate plasma. The electric field decays exponentially inside plasma: $E = E_0 \times \exp(-{}^{r}/_{l_\mathrm{s}})$. In the opposite case of an underdense plasma, as it is valid for the most gaseous targets ($n_\mathrm{e} < n_\mathrm{c}$, *i.e.* $\omega_\mathrm{p} < \omega_\mathrm{L}$), the medium is optically transparent - the laser pulse is able to propagate through plasma without significant absorption.

In case that the input peak power is larger than the critical power for self-focusing effects, also *filamentation* can occur in plasmas [Vid96, Bar00, Kum06, Cou07]. Due to this instability, the laser beam breaks up which causes a splitting of the high-intensity laser pulse into a large number $N_\mathrm{fil} \propto {}^{P_\mathrm{in}}/_{P_\mathrm{c}}$ of so-called filaments. As described above, due to the laser's Gaussian intensity profile and the acting ponderomotive force, plasma electrons are displaced and the refractive index changes in radial direction. Therefore, self-focusing is directly due to the changed electron density profile: the laser is focused into regions where the electron density is minimized, *i.e.* where a perturbation in particle density is given. As a result, the transversal intensity profile is sharpened and consequently the ponderomotive force increases. Subsequently as a feedback effect, the perturbation in density is increased and a channel is formed. If the density perturbation is smaller than the focal spot size, the filamenting pulse can be divided and channeled into multiple filaments which propagate independently from the main pulse. At the filament borders the electron density is larger than in between. This density gradient acts on unfilamented parts of the pulse. Hence, multiple independent filaments are created and the beam energy of the parent pulse is split. The number of filaments N_fil decreases with increasing propagation length inside plasma since energy losses by absorption lead to less energy to feed new narrow filaments. In order to investigate the full dynamics of filamentation by numerically simulating the propagation within plasma, it is recommended to consider 3 (spatial) + 1 (time) dimensions [Cou07, p. 64]. However, within this thesis the current simulations (*cf.* Sec. 5.3) are performed in 2D (+ time). This is due to the fact that a large domain had to be defined and a large number of pseudoparticles had to interact with the simulated laser pulse which consumes a lot of computing power.

3.2.4. Ion-acceleration mechanisms in gaseous targets

As it is deduced in the prior Secs., intensity-wavelength products of several $10^{24}\,\mathrm{W}\,{}^{\mu\mathrm{m}^2}/_{\mathrm{cm}^2}$ are required in order to accelerate ions directly with an incident ultra-intensity laser pulse. Nowadays, the achievable laser intensities are beyond this limit. Therefore, ions have to be laser-accelerated indirectly due to the presence of secondary electric fields inside laser-induced plasmas. For this instance, charge separation due to electron acceleration is necessary.

When a high-intensity laser pulse hits on a target, an energy transfer from the incident laser pulse to the plasma occurs. Such a process is called *heating* and can be characterized by several absorption mechanisms. Which absorption regime will dominate, is dependent on the applied laser parameters (the peak intensity or also the laser contrast as well as the pulse duration), and furthermore, on the target properties (to be more precise: the particle density). The mechanisms can be categorized in collisional absorption regimes (*e.g. inverse Bremsstrahlung*) and collisionless absorption regimes (*e.g. vacuum heating* and $\boldsymbol{j} \times \boldsymbol{B}$ *heating*) and are summarized *e.g.* in [Dai12]. The term *heating* means an energy increase of the plasma electrons which are accelerated by the incoming laser pulse. There are different electron acceleration mechanisms like *Laser-Wakefield-Acceleration (LWA)* for underdense plasmas with electron densities in the order of $n_\mathrm{e} \sim \mathcal{O}(10^{18}\,\mathrm{cm}^{-3})$ [Taj79], *Direct Laser Acceleration (DLA)* for $n_\mathrm{e} \sim \mathcal{O}(10^{20}\,\mathrm{cm}^{-3})$ [Puk99] or the prior discussed ponderomotive acceleration (PA) as the most important mechanism regarding ion acceleration. A detailed review regarding the different ion acceleration mechanisms from various targets, like the *Target Normal Sheath Acceleration (TNSA)* for solid foil targets or the *Radiation Pressure Acceleration (RPA)* scheme are summarized in [Tik10]. In the following, the laser-driven ion acceleration processes from gas-jet targets shall be considered.

In underdense plasma targets, relativistic self-focusing and channeling occur which results in the fact that the laser pulse stays focused over several Rayleigh lengths. Thus, an energy transfer to the electrons can remain for longer interaction times, *i.e.* the high-intensity interaction length is enlarged. Due to the maintained laser-plasma interaction, electrons are accelerated by various acceleration mechanisms (LWA, DLA, PA) and the electron density within the interaction region decreases more and more. Simultaneously, the quasistatic potential increases since it is influenced by the ponderomotive pressure. The arising Coulomb forces $\boldsymbol{F}_\mathrm{C} = e\boldsymbol{E}$ and the given ponderomotive forces $\boldsymbol{F}_\mathrm{pon} = -m_\mathrm{e}c^2\,\nabla\sqrt{1+0.5\,a_0^2}$ compete against each other until the potential causes a *Coulomb explosion* in which the remaining ions are accelerated radially outwards from the location of highest ion density. The ion movement takes place during the laser propagation time through the plasma region and maintains even after the laser pulse has exited into vacuum. This is due to the fact, that the inert ions do not lose their gained kinetic energy quickly. The radial acceleration occurs if the pulse length $c\tau_\mathrm{L}$ is larger than the pulse radius (which is the fact for both the Arcturus laser as well as for PHELIX). According to [Sar99], out of the equilibrium of forces $\boldsymbol{F}_\mathrm{pon} = \boldsymbol{F}_\mathrm{C}$ the radial ion acceleration $a_\mathrm{i,rad}$, the radial ion velocity $v_\mathrm{i,rad}$, and the ion energy $\mathcal{E}_\mathrm{i}$ (in case of short laser pulses) can be deduced to

$$
\begin{aligned}
a_\mathrm{i,rad} &= \frac{Zm_\mathrm{e}}{m_\mathrm{i}}\,c^2\;\nabla\sqrt{1+\frac{a_0^2}{2}}\,,\\
v_\mathrm{i,rad} &= -\frac{Zm_\mathrm{e}}{m_\mathrm{i}}\,c^2\;\partial_r\int \mathrm{d}t\,\sqrt{1+\frac{a_0^2}{2}}\,,\\
\mathcal{E}_\mathrm{i,rad} &= \frac{1}{2}\,m_\mathrm{i}v_\mathrm{i,rad}^2\,.
\end{aligned}
\tag{3.37}
$$

A predicted high-energy cut-off for the energy spectrum in the range of $0 \leq \mathcal{E}_\mathrm{i} \leq \mathcal{E}_\mathrm{i,max}$ ca be approximated by the following Eq.:

$$\begin{aligned}\mathcal{E}_{\mathrm{i,max}} &\approx \frac{(Zm_{\mathrm{e}})^2\,c^4}{16\,m_{\mathrm{i}}\,r_{\mathrm{ch}}^2} \times \frac{a_{0^*}^2\,\tau_{\mathrm{L}}^2}{1+\frac{a_{0^*}^2}{2}} \\ &\approx 3\,\frac{Z^2}{A_{\mathrm{i}}}\,\frac{\tau_{\mathrm{L}}^2}{r_{\mathrm{ch}}^2} \times \frac{a_{0^*}^4}{1+\frac{a_{0^*}^2}{2}}\ [\mathrm{MeV}]\,, \\ \text{with } a_{0^*} &\approx 3.6\,\frac{\lambda_{\mathrm{L}}}{r_{\mathrm{ch}}}\sqrt{\frac{\mathcal{E}_{\mathrm{L,tr}}}{\tau_{\mathrm{L}}}}\,.\end{aligned} \tag{3.38}$$

Here, a_{0^*} is the maximum vector potential of the laser, $\mathcal{E}_{\mathrm{L,tr}}$ is the laser energy (in J) which is trapped inside the channel of radius r_{ch} (in μm), τ_{L} is the pulse duration (in ps), λ_{L} is the laser wavelength (in μm), and A_{i} is the ion mass number. The trapped laser energy can be calculated with the on-axis laser intensity $I_0 = \pi^{-1.5}\,\tau_{\mathrm{L}}^{-1}\,r_{\mathrm{ch}}^{-2} \times \mathcal{E}_{\mathrm{L,tr}}$.

Finally, the total ion energy per unit length along the longitudinal channel axis in x, $\mathrm{d}\mathcal{E}_{\mathrm{tot}}\,\mathrm{d}x^{-1}$ (in $\mathrm{J\,cm^{-1}}$), can be approximated by $\sim 0.08\,n_{\mathrm{i}}\,r_{\mathrm{ch}}^2 \times \mathcal{E}_{\mathrm{i,max}}$ [Sar99]. The ion density (in $10^{19}\,\mathrm{cm^{-3}}$) is equal to the intrinsic atomic density inside the gas jet. The units of the cut-off energy and the channel radius are in MeV and in μm. With the help of this Eq., the radius of the channel can be estimated with the experimentally obtained ion energies.

3.2.5. Former experiments with ^{4}He gas targets

In 1999, ^{4}He ions from underdense plasmas could be accelerated to MeV energies with the VULCAN (Nd:glass) laser at Rutherford Appleton Laboratory for the first time [Kru99]. Here, a high-intensity laser beam ($\mathcal{E} \sim 50\,\mathrm{J}$, $\lambda = 1054\,\mathrm{nm}$, $\tau = 0.9\,\mathrm{ps}$) was focused into a ^{4}He gas jet out of a nozzle with $d_{\mathrm{noz}} = 4\,\mathrm{mm}$ in diameter ($n_{\mathrm{e}} = 5 \times 10^{19}\,\mathrm{cm^{-3}}$). The focus peak intensity was approximately $6 \times 10^{19}\,\mathrm{W/cm^2}$. ^{4}He ions could be detected by CR-39 solid-state nuclear track detectors (*cf.* Sec. 6.2.6 on p. 96) which were placed at different positions around the target. An energy measurement was performed with the help of a Thomson parabola spectrometer (TP) (*cf.* Sec. 6.2 on p. 84) and CR-39 as ion detector. At an angle of approximately 90° relative to the laser propagation direction ^{4}He ions with energies larger than 300 keV up to 2 MeV could be observed, while in forward direction no signal could be detected. Figures 3.4 (a) and (b) illustrate the energy spectra for both ion species at an emission angle of 90° relative to the laser propagation direction, as well as the angular emission of energetic ions. Next to $^4\mathrm{He}^{2+}$ ions also high-energetic $^4\mathrm{He}^{1+}$ ions were generated due to recombination processes inside the rest gas. The inset in Fig. 3.4 (a) shows the corresponding TP signal. Regarding the angular distribution plot, it becomes obvious that ions could be detected at larger angles ($\sim 90°$) relative to the laser axis (note: the dashed lines in Fig. 3.4 (b) serve only to guide the eye).

In 2004, another laser-acceleration experiment with a ^{4}He gas target was performed with the VULCAN PW laser ($\mathcal{E} = 180\,\mathrm{J}$, $\lambda = 1054\,\mathrm{nm}$, $\tau = 0.5 - 0.7\,\mathrm{ps}$) [Wei04]. A supersonic

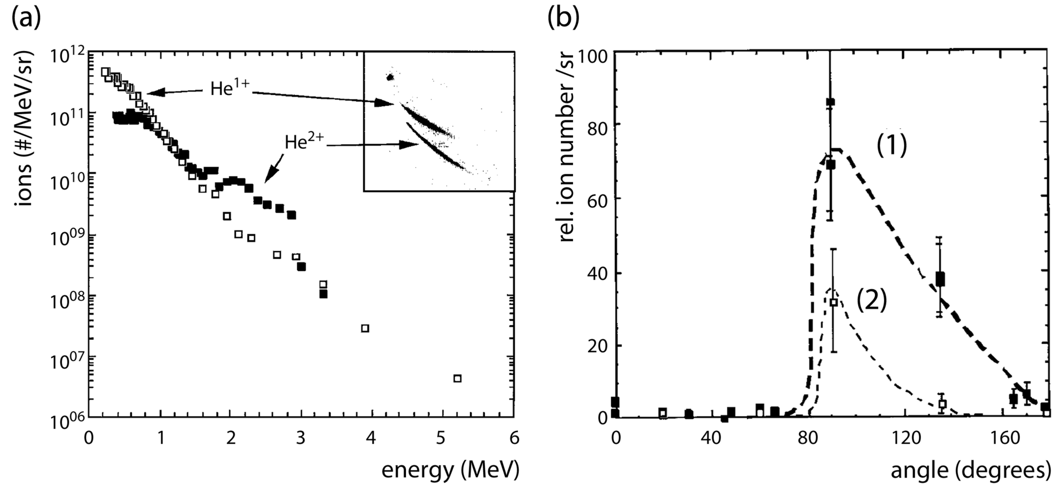

Figure 3.4.: (a) ^{4}He ion energy spectra and the corresponding TP signal (inset) for an emission angle of 90° relative to the laser axis. (b) ^{4}He ion angular distribution for different ion energies: $\mathcal{E} > 400\,\mathrm{keV}$ in (1), and in (2) $\mathcal{E} > 2\,\mathrm{MeV}$ (shown ×10). The dashed lines serve as visual aid [Kru99].

^{4}He gas jet with $n_\mathrm{e} = (0.004 - 1.4) \times 10^{20}\,\mathrm{cm}^{-3}$, $d_\mathrm{noz} = 2\,\mathrm{mm}$, was used. The focus peak intensity had a value of $3 \times 10^{20}\ {}^{\mathrm{W}}\!/_{\mathrm{cm}^2}$. The influence of the particle density inside the plasma target on the energy of the accelerated ^{4}He ions was investigated. The energy spectrum of the ^{4}He ions being accelerated at an angle of 100° to the laser propagation direction was measured with a TP and CR-39 detector plates (*cf.* Fig. 3.5 (a)), while the ^{4}He ion angular distribution could be recorded with stacks of radiochromic films (RCF) (*cf.* Sec. 6.2.6 on p. 102) which were positioned next to the target (*cf.* Fig. 3.5 (b)).

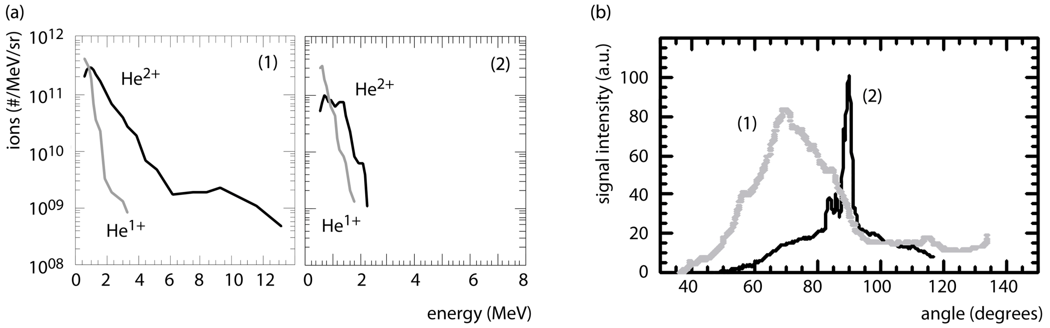

Figure 3.5.: (a) ^{4}He ion energy spectra for different particle densities n_e: (1) $1.4 \times 10^{20}\,\mathrm{cm}^{-3}$, and (2) $1.7 \times 10^{19}\,\mathrm{cm}^{-3}$. (b) ^{4}He ion angular distribution for different particle densities n_e: $1.4 \times 10^{20}\,\mathrm{cm}^{-3}$ ($\mathcal{E} > 3.5\,\mathrm{MeV}$) in (1), and in (2) $10^{19}\,\mathrm{cm}^{-3}$ ($\mathcal{E} > 2\,\mathrm{MeV}$) [Wei04].

As shown by Fig. 3.5 (a), a higher particle density leads to a higher maximum ion energy and also to a higher ion yield as in the low-density case. As also shown in the 1999 experiment, next to ^{4}He^{2+} ions also ^{4}He^{1+} ions are accelerated (recombination processes). In case of the higher density (Fig. 3.5 (a) (1)), the energy spectrum shows a plateau at higher energies (approximately 6-10 MeV). The maximum ion energy for $^4\mathrm{He}^{2+}$ is 13.2 MeV. The total number of $^4\mathrm{He}^{2+}$ ions with an energy >680 keV is 3.8×10^{11}. In the low-density case (*cf.* Fig. 3.5 (a) (2)) the maximum ion energies and also the total number of ions with energies >590 keV are reduced to values of 2.3 MeV and 7.4×10^{10}, respectively. It is important to note that for particle densities below $4 \times 10^{18}\,\mathrm{cm}^{-3}$ no ^{4}He ions with energies $>100\ ^{\mathrm{keV}}\!/_{\mathrm{nucleon}}$ (threshold energy for ions to be detected with CR-39) could be detected at all.

Figure 3.5 (b) illustrates the angular distribution of the accelerated ^{4}He ions for both particle densities. In case of the lower density the ions mainly are accelerated at an angle of 90° to the laser propagation direction. A sharp peak (4° angular spread) is given for ion energies >2 MeV. For higher densities the peak widens (angular spread of 27°) and is shifted to smaller angles.

In 2006, 40 MeV $^4\mathrm{He}^{2+}$ ions could be accelerated in laser propagation direction for the first time [Wil06]. The emitted ion beam featured a divergence angle of 10°. The measurements were carried out at the VULCAN PW laser. The laser parameters were $\mathcal{E} = 340\,\mathrm{J}$, $\lambda = 1054\,\mathrm{nm}$, $\tau = 1\,\mathrm{ps}$, $I_{\mathrm{peak}} = 5.5 \times 10^{20}\ ^{\mathrm{W}}\!/_{\mathrm{cm}^2}$, $2w_0 = 7\,\mu\mathrm{m}$, and the target parameters: supersonic ^{4}He gas jet, $d_{\mathrm{noz}} = 2\,\mathrm{mm}$, $n_{\mathrm{e}} = (0.7 - 4) \times 10^{19}\,\mathrm{cm}^{-3}$. The energy spectra of the laser-accelerated ^{4}He ions were measured at different angles (0°, 10°, 45°, and 90°) to the laser propagation direction. In both forward directions magnetic spectrometers with CR-39 detectors were placed, while for the 45° and 90° directions a Thomson parabola was attached. Below a plasma density of $2 \times 10^{19}\,\mathrm{cm}^{-3}$ no ions could be detected in forward direction, while for higher densities ($4 \times 10^{19}\,\mathrm{cm}^{-3}$) longitudinally accelerated $^4\mathrm{He}^{2+}$ and $^4\mathrm{He}^{1+}$ ions had a maximum energy of 40 MeV and 10 MeV, respectively (*cf.* Fig. 3.6). In the transverse direction (90°) both ion species showed a maximum energy of 7.8 MeV and 3.4 MeV, respectively. At an angle of 45° to the laser propagation direction the ion energies and also the number of accelerated ^{4}He ions are less than in the transverse and longitudinal directions.

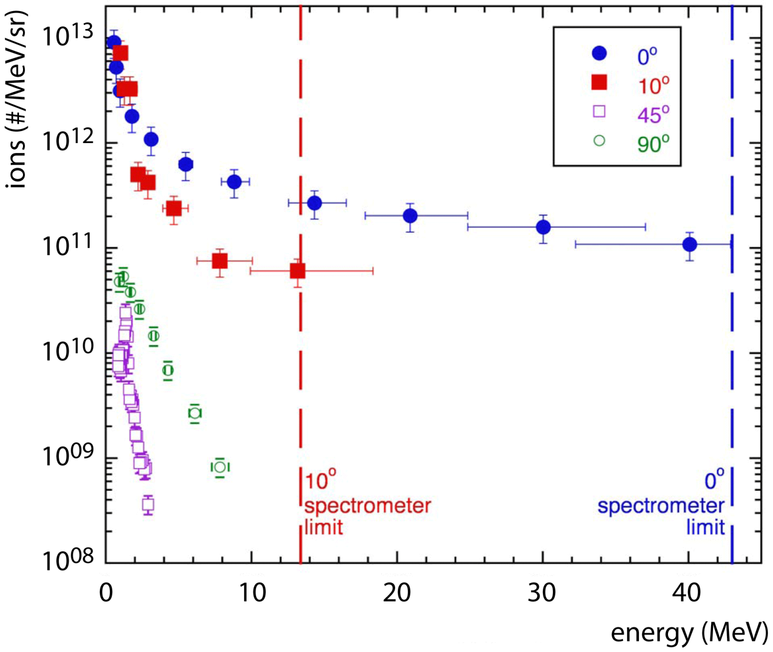

Figure 3.6.: $^4\text{He}^{2+}$ ion energy spectra for different angles [Wil06].

In [Lif14], ^{4}He ions were accelerated with the Salle Jaune (Ti:Sa) laser at Laboratoire d'Obtique Appliquée ($\mathcal{E} = 0.8\,\text{J}$, $\lambda = 800\,\text{nm}$, $\tau = 35\,\text{fs}$, $I_\text{peak} = 1.3 \times 10^{19}\,{}^\text{W}/_{\text{cm}^2}$, $2w_0 = 20\,\mu\text{m}$) from a supersonic He gas jet with $n_\text{e} = (0.8 - 5.6) \times 10^{19}\,\text{cm}^{-3}$ ($d_\text{noz} = 700\,\mu\text{m}$). In forward direction, no ^{4}He ion signal could be detected at all. At an angle of 80° relative to the laser propagation direction the energy spectrum of laser-accelerated ^{4}He ions showed a maximum ion energy of about 200 keV.

Conclusions From the above described studies it can be concluded that the helium ion energy as well as the number of laser-accelerated ^{4}He ions scale with the attached laser-pulse energy. Hence, energies similar to the ones provided by the PHELIX laser at GSI Darmstadt are required in order to accelerate helium ions with adequate energies ($\sim$ a few MeV) as well as with an adequate number of ions out of the laser-induced plasma.

4. Spin and Polarization of Particle Beams

The planned experiments with accelerated $^{3}\mathrm{He}^{2+}$ ions aim at investigating the influence of high-intensity laser fields on nuclear spin-polarized target particles. This chapter helps to get a better understanding of particle spins. Firstly, the spin and its basic principles are presented, while the following section is about manipulating particle spins. Finally, the spin-polarization of a particle beam as well as the measurement of this polarization are described, followed by a digression about $^{3}\mathrm{He}$ as a pre-polarized laser-plasma target and its properties.

4.1. Spin formalism

Quantum-mechanically the spin can be described by the spin-operator $\boldsymbol{S} = (S_x, S_y, S_z)$ [Nol06], which couples with the orbital angular momentum operator $\boldsymbol{L}$ to the total angular momentum $\boldsymbol{J}$. The $\boldsymbol{S}$-operator obeys the commutator equation $[S_i, S_j] = \epsilon_{ijk}\, S_k$, with ϵ_{ijk} as the Levi-Civita tensor. While the single components of spin-operators do not commutate, $\boldsymbol{S}^2 = S_x^2 + S_y^2 + S_z^2$ does. With a given direction z as quantization axis (*e.g.* defined by an external magnetic field), the system can be described by the projection S_z on this axis together with $\boldsymbol{S}^2$. The corresponding eigenfunctions $|s\, m\rangle$ are eigenfunctions to S_z as well as to $\boldsymbol{S}^2$ with eigenvalues m and $s(s+1)$, respectively:

$$S_z\, |s\, m\rangle = m\, |s\, m\rangle \quad \text{and} \quad \boldsymbol{S}^2\, |s\, m\rangle = s(s+1)\, |s\, m\rangle \ . \tag{4.1}$$

Here, s denotes the spin quantum number and $m \in \{-s, -s+1, ..., s-1, s\}$ is the magnetic spin quantum number. A spin-s particle has $2s+1$ possible values m. For the simplest case of a spin-$1/2$ particle like the proton p or the electron e there exist two possible values $m = \pm 1/2$ along the z-axis. The quantum states are $m = +1/2$ for spin projection "up" and $m = -1/2$ for spin projection "down". With the aid of the Pauli matrices σ_i (*cf.* Eq. (A.4), p. 157) the spin operators for spin-$1/2$ particles can be written as $S_i = 1/2\, \hbar\, \sigma_i$ (with $i = x, y, z$).

4.2. Manipulation of particle spins

The spin is associated with a magnetic dipole moment $\boldsymbol{\mu}$ which can interact with an external magnetic field B_{ext}. Thus, it is possible to influence the spin and also the trajectory of a particle. The magnetic dipole moment is given by

$$\boldsymbol{\mu} = \gamma_{\mathrm{gy}}\, \boldsymbol{S} = g \frac{q}{2m}\, \boldsymbol{S}\,, \tag{4.2}$$

where $\gamma_{\mathrm{gy}} = g\mu\hbar^{-1}$ is the gyromagnetic ratio, $\mu = {}^{q}\!/\!_{2m}\,\hbar$ is the magneton, g is the dimensionless magnetic moment (g-factor), q is the charge, and m is the mass of the particle with spin $\boldsymbol{S}$. For protons and electrons the g-factor is $g_{\mathrm{p}} = 5.586$ and $g_{\mathrm{e}} = 2.002$ (the so-called Landé g-factor), respectively. The projection of the spin as well as the magnetic dipole moment is defined by the projection direction of the magnetic field as quantization axis.

The potential energy $\mathcal{U}$ of a spin magnetic moment in an external magnetic field, given by the scalar product of $\boldsymbol{\mu}$ and $\boldsymbol{B}_{\mathrm{ext}}$, is quantized:

$$\mathcal{U} = -\boldsymbol{\mu} \cdot \boldsymbol{B}_{\mathrm{ext}} = \mp\mu_{\mathrm{B,N}}\, B_{\mathrm{ext}}\,, \tag{4.3}$$

with $\mu_{\mathrm{B,N}}$ as a special case of the magneton μ: the nuclear magneton with $\mu_{\mathrm{N}} = {}^{e\hbar}\!/\!_{2m_{\mathrm{p}}} \approx 3.152 \times 10^{-8}\ {}^{\mathrm{eV}}\!/\!_{\mathrm{T}}$, and the Bohr magneton for electrons given with $\mu_{\mathrm{B}} = {}^{e\hbar}\!/\!_{2m_{\mathrm{e}}} \approx 5.788 \times 10^{-5}\ {}^{\mathrm{eV}}\!/\!_{\mathrm{T}}$.

The two spin states differ by an energy $\Delta\mathcal{U}$. If this difference $\Delta\mathcal{U}$ is larger than the thermal energy of the spin carriers, the orientation of the spins can effectively be changed with an external magnetic field. In the thermal equilibrium and for an ensemble of particles with N_+ particles being in spin-up state and N_- particles with spin-down state, the relation between both numbers is Boltzmann distributed:

$$\frac{N_+}{N_-} = \exp\left(-\frac{\Delta\mathcal{U}}{k_{\mathrm{B}}T}\right)\,, \tag{4.4}$$

with k_{B} as the Boltzmann constant, and T as the temperature, so that the thermal energy can be defined as $k_{\mathrm{B}}T$.

In 1922, the spin of bound electrons was discovered by O. Stern and W. Gerlach by deflection of neutral silver atoms in an inhomogeneous magnetic field [Ste22]. Instead of a homogeneous distribution of the silver atoms after propagating through the magnet, two discrete lines were detected. In 1925, this observation could be explained theoretically by [Uhl25]. Electrons were associated with an intrinsic degree of freedom similar to an angular momentum, the *spin*. Due to the effective direction of the resulting force $\boldsymbol{F} = -g_{\mathrm{e}}\,\mu_{\mathrm{B}}\,m \times \partial_z\boldsymbol{B}$, the atoms are deflected up- or downwards, respectively.

Due to the spin as a quantum number, particles can be categorized in two classes: fermions and bosons. While fermions, like electrons, protons, or neutrons, have a half-integer spin and obey the Fermi-Dirac statistics, bosons, like mesons or photons obeying the Bose-Einstein statistics, have an integer spin.

4.3. Polarization of a particle beam

For an ensemble of particles composed of several spin carriers, the probability $p_\pm$ for beam particles with $m = \pm{}^{1}\!/\!_{2}$ is given by $p_\pm = {}^{N_\pm}\!/\!_{N}$, where $N_\pm$ is the occupation number for particles with up and down state, and $N = N_+ + N_-$ is the number of all particles (N is proportional to the intensity I of the incoming particle beam). With the help of this relation and for a magnetic field aligned in z-direction, the polarization P_z of such an ensemble can be defined as (*cf.* App. A.1.1)

$$P_z = p_+ - p_- = \frac{N_+ - N_-}{N_+ + N_-} \text{ [Fic91]} . \tag{4.5}$$

The possible values for the polarization P_z vary between $-1 \leq P_z \leq 1$. If the probability p_+ for particles with the quantum state $|{}^1\!/_2, +{}^1\!/_2\rangle$ is equal to the one for particles with the quantum state $|{}^1\!/_2, -{}^1\!/_2\rangle$, *i.e.* $p_+ = p_-$, the occupation numbers $N_\pm$ for $m = \pm{}^1\!/_2$ are equal, too. In this case, the polarization of the particle beam is zero, $P_z = 0$.

With the aid of Eq. (4.4) and for $\mu B_\text{ext} \ll k_\text{B} T$, P_z can also be written as the Boltzmann equilibrium polarization:

$$P_z = \frac{1 - \exp\left(-\frac{\Delta\mathcal{U}}{k_\text{B}T}\right)}{1 + \exp\left(-\frac{\Delta\mathcal{U}}{k_\text{B}T}\right)} \approx \frac{\mu B_\text{ext}}{k_\text{B}T} . \tag{4.6}$$

Thus, P_z is proportional to ${}^{B_\text{ext}}\!/_T$ $\left(P_z \approx 0.366 \times 10^{-3}\, {}^{B_\text{ext}}\!/_T\right)$, with $\mu = \mu_\text{N}$ for protons, B_ext in T and T in K. Apart from this special case, in general it becomes obvious that for room ambient temperature ($T = 293\,\text{K}$) huge magnetic fields of several hundreds of kT are required to result in a polarization with significant values. Even with superconductive magnets this is not feasible at the moment. On the other hand, if the temperature is cooled down to magnitudes of several mK, smaller magnetic fields $B_\text{ext} \approx 1 \cdots 10\,\text{T}$ are required to establish a proper polarization.

In a laser-induced plasma, as it is present in the planned experiment with pre-polarized ^{3}He gas, laser-induced magnetic field strengths of well above 10^3 T can be reached for short time durations. For such conditions, the potential difference $\Delta\mathcal{U}$ is approximately 10^{-4} eV. At the same time, the temperatures in laser-induced plasmas rise to magnitudes of several 10^3 K in equilibrium. However, in the beginning of the ionization processes (non-equilibrium states), the ion temperatures are lower [McK11]. The influence of these extreme constraints concerning temperature and magnetic field strength on the spin-alignment of the ^{3}He ions will be investigated in the planned experiment.

4.4. Measurement of nuclear spin-polarization

If a particle beam interacts with the field of atomic nuclei, the beam is scattered (*cf.* App. A.1.2). The direction in which each particle is deflected depends on the polarization, as a property of the incoming beam, as well as on the analyzing powers $A_i = A_i(\mathcal{E}, \vartheta)$, with $i = x, y, z$, $\mathcal{E}$ as the beam energy, and ϑ as the angle between incoming and scattered particles [Fic91]. A_i describes the influence of the polarization on the reaction, and thus, on the differential cross section. The analyzing power is a measure for the asymmetry of the angular distribution in ϕ (as azimuthal angle of the detected ejected or scattered particles) for a given transversal beam polarization P_y. In the following, the scattering of a transversely polarized spin-$^1\!/_2$ particle beam on an unpolarized target shall be considered.

Both polarization and analyzing power are observables which depend on the coordinate system. In spin physics, it is common to use the Madison convention [Mad71]: the axes of the coordinate system of the incoming particles are given with: $\boldsymbol{z} = {}^{\boldsymbol{k}_\mathrm{in}}\!/_{|\boldsymbol{k}_\mathrm{in}|} = \boldsymbol{e}_\mathrm{z}$, while $\boldsymbol{x}$ and $\boldsymbol{y}$ are free to choose if the scattering experiment is not a double scattering experiment. The axes of the coordinate system of the outgoing particles (x', y', z') are defined by: $\boldsymbol{z}' = \boldsymbol{z}$, $\boldsymbol{y}' = \boldsymbol{n} = {}^{(\boldsymbol{k}_\mathrm{in} \times \boldsymbol{k}_\mathrm{out})}\!/_{|\boldsymbol{k}_\mathrm{in} \times \boldsymbol{k}_\mathrm{out}|}$, and $\boldsymbol{x}' = \boldsymbol{y}' \times \boldsymbol{z}'$. A rotation around the z-axis by an azimuth angle ϕ transforms (x, y, z) to (x', y', z') (*cf.* Fig. 4.1).

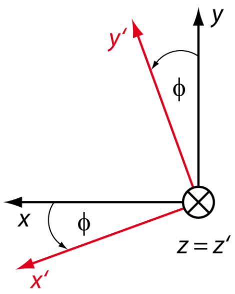

Figure 4.1.: Madison convention (*cf.* [Raa11]).

Given the magnetic field pointing along the y-direction. Due to the parity conservation of the strong interaction, the only non-vanishing component of the analyzing power $A_i \neq 0$ is $A_{\mathrm{y}'}$. For the y'-component of the polarization $P_{y'}$ the following Eq. applies:

$$P_{y'} = \boldsymbol{P} \cdot \boldsymbol{e}_{y'} = -\sin\phi\, P_x + \cos\phi\, P_y\,. \tag{4.7}$$

If the y-axis of (x, y, z) is aligned parallel to the polarization of the particle beam, the differential cross section (*cf.* Eq. (A.15)) can be written as

$$\left(\frac{d\sigma}{d\Omega}\right)_\mathrm{pol} = \left(\frac{d\sigma}{d\Omega}\right)_\mathrm{unpol} \left(1 + A_{y'} P_y \cos\phi\right) \;\; \text{[Fic91]}\,. \tag{4.8}$$

The polarization of a particle beam can be measured with the help of a scattering experiment: the probe beam with unknown beam polarization is scattered on a certain target. If the analyzing power for the scattering process (*cf.* Eq. (4.8)) is known from former investigations, the angular distribution of the scattered particles is a measure of the polarization.

If particles with a certain spin state are mainly deflected in a certain direction, an asymmetrical distribution ϵ of scattered particles can be observed. For the number of particles deflected in contrary directions, the following Eq. apply:

$$N_{\phi=0} = N\,\rho_{\text{target}}\;\Delta\Omega\;D\;\left(\frac{d\sigma}{d\Omega}\right)_{\text{unpol}}\left(1 + A_{y'}P_y\right)\;, \tag{4.9}$$

$$N_{\phi=\pi} = N\,\rho_{\text{target}}\;\Delta\Omega\;D\;\left(\frac{d\sigma}{d\Omega}\right)_{\text{unpol}}\left(1 - A_{y'}P_y\right)\;, \tag{4.10}$$

with N as the number of incoming particles, ρ_{target} as the density of the target material, $\Delta\Omega$ as the solid angle which is covered by one detector, and D as the detector-efficiency. Now, the asymmetry ϵ can be defined by the relation

$$\epsilon = \frac{N_{\phi=0} - N_{\phi=\pi}}{N_{\phi=0} + N_{\phi=\pi}} = P_y A_{y'}\;. \tag{4.11}$$

For a better understanding of the resulting effects, Figs. 4.2 and 4.3 illustrate a simulation of scattered particles for each an unpolarized and polarized spin-$^1\!/_2$ particle beam. In Fig. 4.2 the value for the polarization is set to zero. A symmetrical distribution in ϕ is observed as it is predicted by the differential cross section for the unpolarized case. In Fig. 4.3 the values for both analyzing power and polarization are set to 1. The result is an asymmetrical distribution in ϕ, $\left({}^{d\sigma}\!/_{d\Omega}\right)_{\text{pol}} = \left({}^{d\sigma}\!/_{d\Omega}\right)_{\text{unpol}}(1+\cos\phi)$ with a maximized $\epsilon = 100\%$.

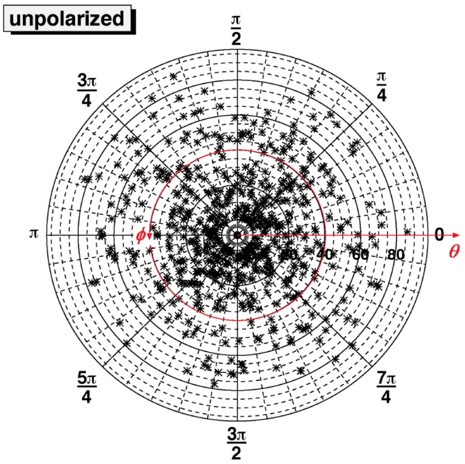

Figure 4.2.: $P_y = 0$, symmetric distribution in ϕ, $\epsilon = 0\%$.

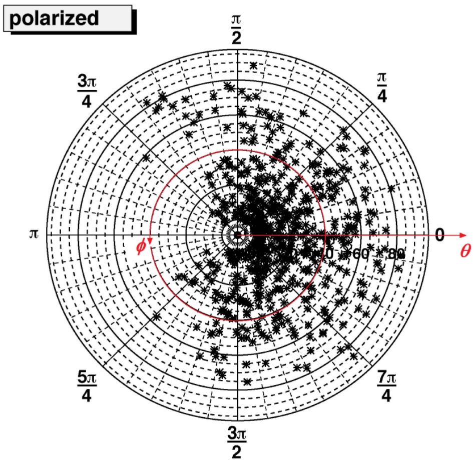

Figure 4.3.: $P_y = 1$, $A_{y'} = 1$, asymmetric distribution in ϕ, $\epsilon = 100\%$.

4.5. Spin-polarized ^{3}He as possible polarized ^{3}He ion source

The ^{3}He gas being deployed in the planned experiments is spin-polarized by the study group Helium-3 at Johannes Gutenberg University Mainz [Hei]. Low temperatures as well as high magnetic fields are not a good solution for building up a high polarization degree of ^{3}He gas. Instead, the polarization has to be established by optical pumping. Optical pumping is a technique which was firstly reported in 1960 [Col60]: ^{4}He atoms were excited into the 2^3S_1 metastable state. The metastable atoms were produced at low pressure by an RF discharge. Later, in 1963, measurements with ^{3}He gas were accomplished [Col63]. By optical pumping of the 2^3S_1 state an orientation of the nuclear spins of the ground state could be detected.

Nowadays at Mainz, a circular polarized laser excites the ^{3}He atoms indirectly. An optical pumping directly from the atomic ground state for noble gases, like ^{3}He, *e.g.*, is not possible, because the excited states are too high (approximately 20 eV). For an indirect transfer of the laser's angular momentum to the atoms two possible techniques are available: spin exchange optical pumping (SEOP), and *metastable exchange optical pumping* (MEOP). The latter is used at Mainz (for a detailed description of MEOP of ^{3}He gas, *cf.* App. A.2). Polarization degrees of up to 85% can be achieved.

4.5.1. Relaxation of the ^{3}He polarization

Once the ^{3}He nuclei are polarized, their polarization P decays exponentially towards thermal equilibrium in time:

$$P(t) = P_0\, \mathrm{e}^{-\Gamma_{\mathrm{rel}} t} = P_0\, \mathrm{e}^{-\frac{t}{T_{\mathrm{rel}}}} \,. \tag{4.12}$$

The total relaxation rate $\Gamma_{\mathrm{rel}} = T_{\mathrm{rel}}^{-1}$ as the reciprocal relaxation time T_{rel} is the sum of several single relaxation rates $\Gamma_{\mathrm{rel},i}$ which describe different relaxation processes. For a long conservation of the polarization and, of course, for building up maximal polarization degrees, the relaxation has to be minimized. In the following, the most important relaxation mechanisms are presented (for more relaxation mechanisms, which are important for MEOP, *cf.* App. A.2).

Relaxation of the nuclear spin by field gradients The nuclear spin of the polarized ^{3}He is oriented along the quantization axis of the external magnetic field. If spin-polarized ^{3}He propagates through a transversal magnetic field gradient, a time-varying field with fluctuating amplitude and frequency is given thereby. Magnetic dipole transfers are induced which lead to spin-flips. Thus, the polarization decreases [Sch65, Cat88a, Cat88b, Has90]. The magnetic field gradient relaxation rate $\Gamma_{\mathrm{rel}}^{\nabla}$ can be described by [Hie10]:

$$\Gamma_{\mathrm{rel}}^{\nabla} = D \left(\frac{\partial_r B_r}{B_0} \right)^2 , \tag{4.13}$$

where D is the diffusion constant of the aligned spins which is proportional to the inverse gas pressure p, B_0 is the central magnetic field strength, and ${}^{\partial_r B_r}/_{B_0}$ is the relative transverse field gradient of the static magnetic field. According to [Cat88a, Hie10], Eq. (4.13) holds for the following relation between the average diffusion time τ_diff (required for the spins to diffuse across a reservoir, *e.g.* a spherical cell, with characteristic length R), the Larmor period as the characteristic precession time $\tau_\text{Larmor} = \omega_\text{Larmor}^{-1}$, and the gas kinetic collision time τ_coll:

$$\begin{aligned} \tau_\text{diff} \approx \frac{R^2}{D} &\gg \frac{1}{\omega_\text{Larmor}} \gg \tau_\text{coll} \\ i.e.\ \frac{\tau_\text{diff}}{\tau_\text{Larmor}} &= \frac{R^2}{D}\,\omega_\text{Larmor} \gg 1 \end{aligned} \tag{4.14}$$

The Larmor frequency of the ^{3}He spins in a magnetic field $B_0 = 1\,\text{mT}$ is given by $\omega_\text{Larmor} = \gamma_\text{gy} B_0 \approx 0.2\,\text{MHz}$, with $\gamma_{\text{gy},^3\text{He}} \approx 2\pi \times 32.4\ ^\text{MHz}/_\text{T}$ as the gyromagnetic ratio of ^{3}He gas [Flo93]. With a pressure of 2.7 bar being at room ambient temperature the diffusion constant D of ^{3}He gas has a value of $0.7\,\text{cm}^2\text{s}^{-1}$ [Hie10]. Assuming a relative field gradient of $10^{-3}\,\text{cm}^{-1}$, a lower limit for the relaxation time can be derived to $T_\text{rel}^\nabla \gtrsim 400\,\text{h}$.

The homogeneity of the magnetic field $\boldsymbol{B}_\text{ext}$ is of great importance for long relaxation times. Thus, a precise magnetic holding field (*cf.* Sec. 8.1, p. 143) has to be built for storing polarized ^{3}He in a vacuum chamber for large time durations (several days). Furthermore, inside $\boldsymbol{B}_\text{ext}$ additional magnetic fields have to be avoided. The gas supply has to be made of non-magnetic materials and the opening mechanism of the valve has to be non-electromagnetic (conventional solenoid valves cannot be used). Moreover, magnetic fields of electric motors, *e.g.* linear step motors in mirror supports for the laser focus adjustment, have to be removed. Otherwise, the homogeneity of the magnetic field is locally distorted and the field gradients increase.

Dipolar relaxation Due to the magnetic dipole-dipole interaction between two ^{3}He nuclei, the nuclear spins couple while losing their orientation. According to [New93, Kri09] the dipolar relaxation rate $\Gamma_\text{rel}^\text{dip}$ for room ambient temperature (23 °C) can be written as:

$$\Gamma_\text{rel}^\text{dip} = {T_\text{rel}^\text{dip}}^{-1} = \frac{p}{817}\,\frac{1}{\text{h bar}} \propto p\,, \tag{4.15}$$

with p (in bar) as the pressure inside the storage cell. With rising pressures the relaxation time decreases. For the planned experiment storage cells with a maximum ^{3}He gas pressure of approximately 3 bar are available. The relaxation time for these conditions is $T_\text{rel}^\text{dip} \approx 270\,\text{h}$.

Relaxation by impurities Due to additive paramagnetic molecular oxygen as a possible impurity inside the gas supply system, the relaxation rate $\Gamma_\text{rel}^{\text{O}_2}$ decreases as follows [Saa95, Den99, Den00, Hie06]:

$$\Gamma_{\mathrm{rel}}^{\mathrm{O}_2} \approx 4.8 \times 10^6 \times p_{\mathrm{O}_2}\, T^{-1.42}\, \frac{\mathrm{K}^{1.42}}{\mathrm{h\,bar}}\,, \tag{4.16}$$

with the partial pressure p_{O_2} (in bar) for oxygen. For the planned experiment it is important to evacuate all supply pipes from the storage cell to the piezo valve, so that no paramagnetic oxygen will destroy the polarization.

Surface relaxation The surface relaxation $\Gamma_{\mathrm{rel}}^{\mathrm{W}}$ is proportional to the relation between the surface A and the volume V of the storage cell. Adsorption effects on the surface as well as diffusion processes into the cell material cause the surface relaxation rate [Den06, Sch06]:

$$\Gamma_{\mathrm{rel}}^{\mathrm{W}} = \Gamma_{\mathrm{rel}}^{\mathrm{ads}} + \Gamma_{\mathrm{rel}}^{\mathrm{diff}} = \rho\, \frac{A}{V} \propto \frac{A}{V}\,, \tag{4.17}$$

with the matter constant $\rho \approx 1...10^{-3}$ cm/h as the specific relaxation coefficient. Uncoated storage cells made of glass lead to relaxation times of a few hours. At Mainz special storage cells made of Cs layered glass are applied, so that relaxation times of $430 - 570$ h can be reached [Den06, Sch06, Ric02]. These storage cells will be transferred from Mainz in special transport boxes with implemented permanent magnets, which build up a homogeneous magnetic storage field [Hie10].

With the relaxation times given above, it is possible to estimate the total relaxation rate for these processes as follows. Assuming that the gas supply system was evacuated so that no paramagnetic oxygen is present, and thus, $\Gamma_{\mathrm{rel}}^{\mathrm{O}_2} = 0$ and taking the mean surface relaxation time of 500 h into account, then Γ_{rel} can be calculated to: $\Gamma_{\mathrm{rel}} = \Gamma_{\mathrm{rel}}^{\nabla} + \Gamma_{\mathrm{rel}}^{\mathrm{dip}} + \Gamma_{\mathrm{rel}}^{\mathrm{W}}$. Hence, the total relaxation time has a value of approximately $T_{\mathrm{rel}} \approx 121$ h, or 5 days, respectively. This relaxation time is a theoretical value which does not include additional local conditions like the effective magnetic field gradients inside the target chamber or the pressure booster valve combination to build up a proper gas jet.

4.5.2. Interaction with a high-intensity laser pulse

In the planned experiment the polarized ^{3}He gas will be ionized by a high-intensity laser pulse. In this case, an unsolved question is whether the laser-gas interaction destroys the nuclear spin-polarization of the ^{3}He during the ionization process. If the electrons would be expelled out too slowly so that one of both electrons would remain in the atomic shell, the influence of this remaining electron on the nuclear spin would change its orientation. Figure 4.4 illustrates the time profile of the Arcturus laser intensity I_{L} [Wil11]. The time t_{ion} for fully ionizing ^{4}He gas is included in this plot: t_{ion} has values of several hundreds of fs. It is assumed that the ionization time is the same for ^{4}He and ^{3}He. This time has to be compared to the hyperfine interaction time for the coupling of nuclear and electronic spin in ^{3}He: $\tau_{\mathrm{HF}} \sim 0.1$ ns $\gg t_{\mathrm{ion}}$. Hence, one can assume that the electrons are expelled out too quickly for establishing a coupling of the electronic with the inert nuclear spins.

The second question depends on the huge time-varying secondary magnetic field strengths that can be produced by the plasma. Figure 4.5 illustrates a simulated laser-foil interaction at a time of 120 fs after the laser pulse hit a solid target: the huge magnetic field gradient $\partial_y B_z \sim \mathcal{O}(10^{10})$ $^{\mathrm{T}}/_{\mathrm{m}}$ along the horizontal x-axis in a height of $y = 32.5\,\mu\mathrm{m}$ (foil center) is apparent. The inset illustrates the magnetic field distribution $B_z(x, y)$. The magnetic field strength has a peak value of about $\mid B_0 \mid = 5 \times 10^3$ T. According to [Raa14], it can be speculated that the huge magnetic field gradients have no effect on the alignment of the nuclear spins.

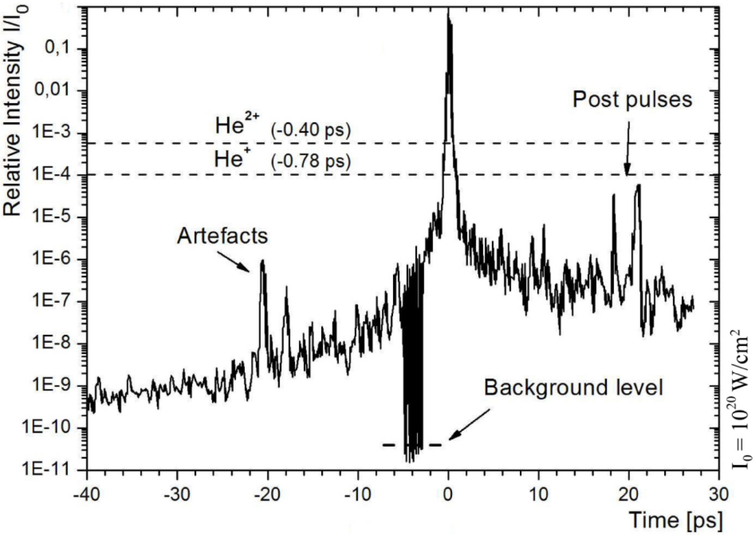

Figure 4.4.: Time profile of the Arcturus laser intensity [Wil11].

4.5.3. Fusion reactions with ^{3}He

In the planned experiment, the spin-polarization of laser-accelerated ^{3}He ions from a pre-polarized helium-3 gas target shall be investigated. As described in Sec. 4.4, for this purpose an appropriate detection reaction is needed.

A method to measure the polarization degree of spin-$^1/_2$ particles was developed and successfully adopted by [Raa14]. Here, laser-accelerated protons from gold foils were scattered on a silicon foil: Si(p, p')Si. For this nuclear scattering reaction the cross-sections as well as the analyzing powers are known. The angular distribution in ϕ of the scattered protons is sensitive to the spin-polarization of the incoming proton beam: no polarization was observed for the laser-accelerated protons, $P_y = 0$.

In case of a laser-accelerated ^{3}He ion beam, the polarization degree can be measured in a nuclear reaction if the differential cross sections as well as the analyzing powers are known from former experiments: the fusion reactions D(^{3}He,p)^{4}He with a Q-value of

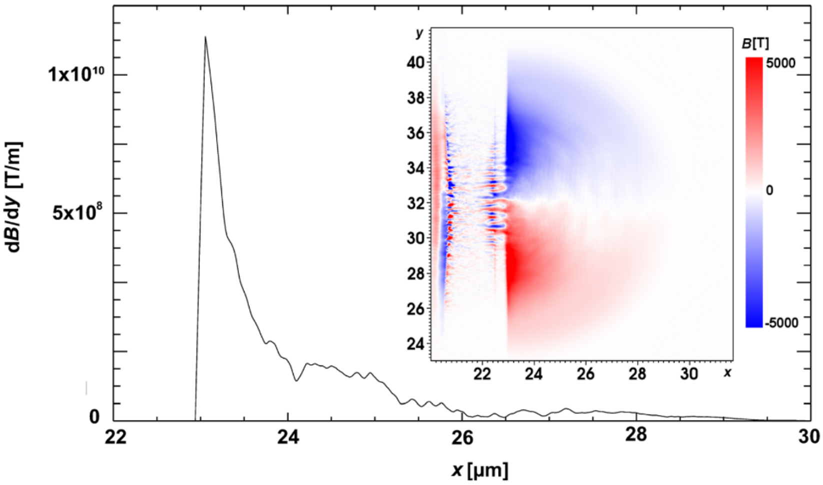

Figure 4.5.: Simulation of the magnetic field gradient at a time of 140 fs after the laser pulse hit the foil target [Raa14].

18.35 MeV as well as ^{3}He(^{3}He,2p)^{4}He with a Q-value of 12.86 MeV serve as detection reactions for the ion's spin-polarization degree. Both fusion reactions are described in [Hol14]. With a measured asymmetry of the ejected protons out of the nuclear reaction, the polarization of the incoming ^{3}He ions can be determined. The cross sections for the fusion reactions can be found in [Dwa71, Bos92, Ali05, KLO05] (*cf.* Fig. 4.6).

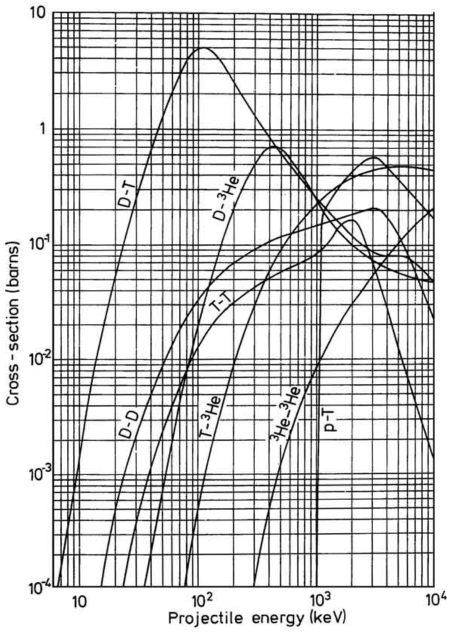

Figure 4.6.: Cross sections for different fusion reactions including ^{3}He [KLO05]: D-^{3}He and ^{3}He-^{3}He are of great importance for the planned experiment.

If the spin-polarization of the ^{3}He gas can be conserved during the laser-target interaction, it is important to investigate whether the polarization is preserved only inside the plasma or also after the acceleration process. Therefore, two different approaches are planned which are presented in the following.

Fusion reaction ^{3}He-^{3}He inside the plasma target

The polarized gas is stored in an external homogeneous magnetic field. The laser-accelerated ^{3}He ions propagate through plasma and gas regions until they exit into vacuum. There is a certain probability for the fusion reaction ^{3}He(^{3}He,2p)^{4}He inside the plasma. In case of an unpolarized ^{3}He gas as underdense plasma target, the protons will be emitted symmetrically into 4π. If for a pre-polarized ^{3}He gas target and a conserved spin-polarization the angular distribution of the protons will show an asymmetry in ϕ relative to the quantization axis given by the direction of the external homogeneous magnetic field the fusion protons can be detected with CR-39 detector plates[1] placed around the gas jet.

Estimation of the fusion proton yield The particle density inside the gas jet is assumed[2] to be in the order of several $10^{19}\,\mathrm{cm}^{-3}$. If a mm nozzle is attached, the width of the gas jet is assumed to be in the order of approximately one mm. Thus, the plasma channel, *i.e.* the region of the acceleration process, also has a length of one mm. This leads to an areal density of $\rho_A = 10^{18}\,\mathrm{cm}^{-2}$. Regarding the experimental results of [Kru99] (laser energy of 50 J), [Wei04] (180 J on target), and [Wil06] (340 J on target), *cf.* Sec. 3.2.5 on p. 28, and taking into account that the energy range of the PHELIX laser at GSI Darmstadt for short pulses lies in between those values, the total number of ^{3}He ions being accelerated out of the plasma is $10^{10} - 10^{12}$ per MeV and Sr. The cross section for the fusion reaction ^{3}He(^{3}He,2p)^{4}He for ^{3}He energies of 1 MeV is in the order of $\sigma = 10\,\mathrm{mb}$ [Dwa71]. With $n_p = 2\ L \times \sigma = 2\ \rho_A\, j \times \sigma$ for the number of fusion protons per laser shot, the proton yield can be estimated to be within 200 and 20000 protons per laser shot, respectively. The emitted protons show a continuous energy spectrum up to 10.7 MeV [Jun98, Bon99].

First of all, unpolarized ^{3}He gas will serve as underdense plasma target in order to get a zero-measurement of the emitted proton signal. In a second step, the same measurement will be performed with pre-polarized ^{3}He gas as plasma target. If the spin-polarization of the accelerated ^{3}He ions will be conserved during the laser-plasma interaction, an asymmetry in ϕ for the emitted protons is expected. The direction of the magnetic holding field will be turned by an angle of 180° in a third step in order to verify the asymmetry effect.

Since there are no analyzing powers given for the current fusion reaction, the asymmetry can be measured, but the polarization of the laser-accelerated ^{3}He ions is not determinable. For this purpose, the second fusion reaction D(^{3}He,p)^{4}He will be investigated. If thereby the degree of polarization could be measured, a first rough estimation of the

---

[1] *cf.* Sec. 6.2.6, p. 96

[2] based on interferometric characterizations of the gas-jet density profiles, *cf.* Sec. 6.1.4 on p. 74

analyzing powers given at the ^{3}He(^{3}He,2p)^{4}He fusion reaction for a broad ^{3}He energy range would be possible.

Fusion reaction D-^{3}He after the acceleration process

(Pre-polarized) ^{3}He gas will serve as underdense plasma target in order to accelerate ^{3}He ions out of the plasma. A CD$_2$ foil (deuterized polyethylene foil given with various thicknesses) will be placed close to the gas jet at the pre-determined main emittance angle (determined within the Jan. 2015 PHELIX experiment i009). When a beam of laser-accelerated ^{3}He ions hits the CD$_2$ foil, there is a given probability for the fusion of ^{3}He with deuterium, depending on the incident ^{3}He energy, while the fusion proton yield also depends on the number of incoming beam particles. In the unpolarized case, the MeV protons as ejected fusion products will propagate out of the CD$_2$ foil and a symmetric distribution of fusion protons in the azimuthal range ϕ results. If, in the second case, the incoming ^{3}He ion beam is spin-polarized, the proton distribution will be asymmetric in ϕ.

Estimation of the fusion proton yield The number of protons from the fusion reaction D(^{3}He,p)^{4}He in the secondary scattering target can be estimated by $n_\mathrm{p} = \mathcal{L} \times {}^{\mathrm{d}\sigma}\!/_{\mathrm{d}\Omega}\, \Delta\Omega$. Here, the luminosity $\mathcal{L}$ is the number of laser-accelerated ^{3}He ions times the areal density ρ_A of the CD$_2$ foil, ${}^{\mathrm{d}\sigma}\!/_{\mathrm{d}\Omega}$ is the differential cross section and $\Delta\Omega$ is the solid angle.

The number and the energy of ^{3}He ions being accelerated out of the underdense plasma can be estimated by the given experimental data for laser-accelerated ^{4}He ions in [Kru99, Wei04, Wil06], *cf.* Figs. 3.4 to 3.6. Similar to the previous case a lower and an upper limit for the number of laser-accelerated ^{3}He ions can be estimated. Starting with the lower limit, the estimation of the proton yield leads to the following number per laser shot: assuming a gas jet density in the order of $10^{19}\,\mathrm{cm}^{-3}$ and a maximum ^{3}He^{2+} ion energy of $\sim 2\,\mathrm{MeV}$, *cf.* Fig. 3.5 (a)-(2) on p. 29. Here, the total number of ions was in the order of 10^{10} per MeV and Sr. In the angular distribution for the lower density case in Fig. 3.5 (b)-(2), a sharp peak at 90° relative to the laser direction was detected. The number of ^{3}He^{2+} ions at this emittance angle roughly can be estimated to a value of approximately 10^9 per MeV and Sr. This ion number again is reduced: in an assumed distance of $d = 5\,\mathrm{cm}$ from the laser-target interaction region a 1 mm pinhole ($r = 0.5\,\mathrm{mm}$) extracts a part of this ^{3}He ion beam. This leads to a cone with an opening angle of approximately 1.15° which corresponds to a solid angle of ${}^{\pi r^2}\!/_{d^2} = 3.1\,\mathrm{mSr}$. Thus, only 3.1×10^5 ^{3}He ions per MeV will pass the pinhole in order to hit on the CD$_2$ foil with an areal density of $\rho_A = 2.7 \times 10^{20}\,\mathrm{cm}^{-2}$. The differential cross section for the fusion reaction has a maximum value of approximately 60 ${}^{\mathrm{mb}}\!/_{\mathrm{Sr}}$ for an incident ^{3}He ion energy of 0.69 MeV [Ali05]. The thickness of the CD$_2$ foil is chosen such that all of the incoming ^{3}He ions will be stopped inside the foil. Thus, the probability for fusion reactions is increased. The fusion protons will be detected with CR-39 detector plates with a cross-section area of $9\,\mathrm{cm}^2$ at a distance of around 2 cm from the CD$_2$ foil. This corresponds to a solid angle of 2.25 Sr. Hence, in total up to 23 protons per laser shot are expected as a lower limit. For the upper limit, the number of ^{3}He ions (also with an energy of 2 MeV) can be assumed to 10^{12} ions per MeV and Sr (*cf.* Fig. 3.6). A proton yield of approximately 23000 protons per laser shot per CR-39 detector can be estimated as an upper limit.

In a first step, unpolarized ^{3}He will serve as underdense plasma target in order to get a zero-measurement of the emitted proton signal. In a second step, the same measurement will be performed with pre-polarized ^{3}He gas which is stored in an external homogeneous magnetic holding field. If the spin-polarization of the accelerated ^{3}He ions will be conserved during the laser-plasma interaction, an asymmetry in ϕ for the emitted protons is expected. The direction of the magnetic holding field will be turned by an angle of 180° in a third step in order to verify the asymmetry effect. The CD_2 foil is mounted in a cage next to the plasma target. The CR-39 detectors will be placed relatively to the position of the CD_2 foil: front, back, left, right, top, and bottom. A stack of apertures serves as an entrance into the cage in order to minimize $^3He^{2+}$ side-scattering effects.

Estimation of the asymmetries Assuming a possible yield of 1000 protons per laser shot on each CR-39 detector, an analyzing power of $A_y = 0.1$, an assumed maximized polarization of $P_y = 1$, and a given direction of the magnetic field as quantization axis, then the number of fusion protons on the single detectors will be: $N_{\mathrm{det,r}} = 900$, $N_{\mathrm{det,l}} = 1100$, $N_{\mathrm{det,t}} = 1000$, $N_{\mathrm{det,b}} = 1000$ (the indices $i = \mathrm{r, l, t, b}$ indicate the position of the CR-39 detector plate relative to the CD_2 foil, *i.e.* relative to the incident ion beam). The resulting asymmetry of $\epsilon = 0.1$ will be visible and can be cross-checked by rotating the magnetic field.

5. Simulations of Ion Acceleration from Gas-Jet Plasmas

Computer simulations are a helpful tool to gain an insight into the physics of laser-plasma interactions. This chapter describes computations of laser-induced ion acceleration from an underdense plasma target. First of all, the used infrastructure, *i.e.* the Jülich supercomputers, are described, the basics of Particle-in-Cell algorithms are presented and the EPOCH code which was used for the current simulations is described. The simulations were performed with different parameters regarding laser and target properties. The last part of this chapter deals with the simulation results.

5.1. Jülich supercomputers

The Jülich Supercomputing Centre (JSC) at FZJ is, inter alia, in charge of the operation and development of high performance supercomputers and with JUROPA (*Jülich Research on Petaflop Architectures*) and JUQUEEN (*Jülich Blue Gene/Q*) it is one of the most powerful computer centers in the world.

In the framework of this thesis, laser-plasma simulations mainly were performed on JUQUEEN. According to the TOP500 list for today's most powerful computer systems, JUQUEEN is on rank 8 (status: November 2014, [TOP]). JUQUEEN is a BlueGene/Q system, a supercomputer design in the BlueGene series. The Processor is an IBM PowerPC A2 (16 GHz, 16 cores per node). It is equipped with 16 GB SDRAM-DDR3 memory per node. In total, 28 672 nodes are given in 28 racks, *i.e.* 458 752 cores build up the whole processing unit. Within the LINPACK Benchmark, a tool to characterize the performance of computing systems by solving a dense system of linear equations, JUQUEEN achieved a performance of $R_{\mathrm{max}} = 5008.86\,$Tera-FLOPS. The theoretical peak performance is $R_{\mathrm{peak}} = 5872.03\,$TFLOPS. Here, FLOPS (also denoted as FLOP/s) is the abbreviation for *floating point operations per second.* After the shutdown of JUQUEEN in Jun. 2015, the successor JURECA (Jülich Research on Exascale Cluster Architectures) could be used for the final simulations. JURECA will be upgraded to peak performances of 1.8 PFLOPS. Two Intel Xeon E5-2680 v3 Haswell CPUs (2×12 cores per CPU, 2.5 GHz) build the basis of the new system. Regarding the memory technology, DDR4 memory is equipped: 1605 compute nodes with 128 GB, 128 compute nodes with 256 GB, and 64 compute nodes with 512 GB. For visualization issues, next to two Intel Xeon E5-2680 v3 Haswell CPUs per node also two NVIDIA K40 GPUs per node (2×12 GB GDDR5 memory) are available.

The General Parallel File System (GPFS), a high-performance clustered file system by IBM, consists of three file systems with individual data policies: `$HOME`, `$WORK`, and `$ARCH`. The first one is a repository for compiling programs (here: EPOCH-2D), for storing source code or libraries. `$WORK` is a file system for temporarily storing data with large size and high Input/Output demands (I/O bandwidth 160 GB/s) during or after simulation runs. This file system is cleaned frequently: data older than 90 days is deleted in order to keep the file system uncongested, while empty directories are purged after three days. Simulated data has to be stored within the `$ARCH` file system.

5.2. Particle-in-Cell algorithm

In theoretical laser-plasma physics, Particle-in-Cell (PIC) codes are used to calculate the behavior of different particle species (*e.g.* electrons, ions, neutral atoms or molecules) interacting with electromagnetic fields [Bir85, Tsk07]. The Lorentz equation of motion together with the Maxwell's equations form the core of PIC algorithms. The particles are arranged, *i.e.* mapped, on a discrete spatial grid upon which the simulated particles can travel freely. On each grid point the positions x_i and the velocities v_i of the particles are translated into a charge density ρ_j as well as into a current density J_j (note: i, j represent particle and grid indices, respectively). By solving the Maxwell's equations, the electric and magnetic fields, E_j and B_j, are calculated and localized to each discrete grid point. These updated values for the fields serve as an input for the Lorentz equation, and thus, the particle's motion (*i.e.* the new positions and velocities) is determined by the Lorentz forces F_i. The iteration is completed after Δt and the described cycle restarts (mapping of the particles, solving the Maxwell's equations and subsequently calculating the new equations of motion). Figure 5.1 is a flow chart of the subsequent steps for one cycle Δt of a PIC algorithm (*cf.* [Nak12]). The single operations are described in the following paragraphs.

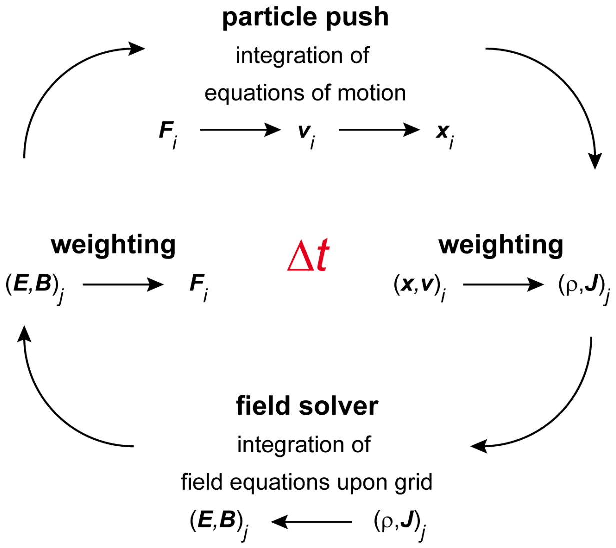

Figure 5.1.: Flow chart of the subsequent operations for one cycle Δt of a PIC algorithm (*cf.* [Nak12]).

Particle pusher The velocity and position of simulated particles can be derived by integrating the equations of motion. The simulation time is discretized: $t \to t^0 + k\,\Delta t$, with $t^0 = 0$, $k \in \mathbb{N}$, and Δt as the time for one iteration. According to the *leapfrog* method [Bor70], both position and velocity are calculated every Δt, but with a time lag of $\nicefrac{1}{2}\,\Delta t$ to each other. The equations of motion (for the non-relativistic case) can be written as:

$$\begin{aligned}\boldsymbol{v}^{k+1/2} &= \frac{\boldsymbol{x}^{k+1}-\boldsymbol{x}^{k}}{\Delta t}\,,\\ \boldsymbol{x}^{k+1} &= \boldsymbol{x}^{k}+\Delta t\,\boldsymbol{v}^{k+1/2}\,,\\ \boldsymbol{F}_{\mathrm{L}}^{k} = m\,\frac{\boldsymbol{v}^{k+1/2}-\boldsymbol{v}^{k-1/2}}{\Delta t} &= q\left(\boldsymbol{E}^{k}+\frac{\boldsymbol{v}^{k+1/2}+\boldsymbol{v}^{k-1/2}}{2}\times\boldsymbol{B}^{k}\right)\,.\end{aligned} \tag{5.1}$$

An easy way to solve Eq. (5.1) is the use of Boris rotation [Bor70] where electric and magnetic forces are separated via $\boldsymbol{u}=\boldsymbol{v}^{k-1/2}+\tilde{q}\boldsymbol{E}^{k}$, $\boldsymbol{h}=\tilde{q}\boldsymbol{B}^{k}$, $\boldsymbol{s}=\nicefrac{2\boldsymbol{h}}{1+h^2}$, and $\tilde{q}=\nicefrac{q}{2m}\,\Delta t$, leading to

$$\boldsymbol{v}^{k+1/2}=\boldsymbol{u}+(\boldsymbol{u}+(\boldsymbol{u}\times\boldsymbol{h}))\times\boldsymbol{s}+\tilde{q}\boldsymbol{E}^{k}\,. \tag{5.2}$$

Field solver Similar to the discretization above, also the Maxwell's equations are solved at discrete points on the grid:

$$\frac{\boldsymbol{B}^{k+1/2}-\boldsymbol{B}^{k-1/2}}{\Delta t}=-\nabla\times\boldsymbol{E}^{k}\,, \tag{5.3}$$

$$\frac{\boldsymbol{E}^{k+1}-\boldsymbol{E}^{k}}{\Delta t}=\frac{1}{\varepsilon_0\mu_0}\,\nabla\times\boldsymbol{B}^{k+1/2}-\frac{1}{\varepsilon_0}\boldsymbol{J}^{k+1/2}\,, \tag{5.4}$$

where $\boldsymbol{J}=nq\boldsymbol{v}$ is the current density which can be calculated by the sum over the particle charges q_i times the particle velocities $\boldsymbol{v}_i^{k+1/2}$:

$$\boldsymbol{J}_j^{k+1/2}=\sum_i q_i\boldsymbol{v}_i^{k+1/2}\,\frac{S(\boldsymbol{X}_j-\boldsymbol{x}_i^{k})+S(\boldsymbol{X}_j-\boldsymbol{x}_i^{k+1})}{2}\,. \tag{5.5}$$

Here, the indices i,j denote the number of a particle and a grid point, respectively, $\boldsymbol{X}_j$ is the position of the grid points, and S is a weighting term which depends on the shape function of the particles (*cf.* the next paragraph "weighting").

Within the PIC algorithm, analytically only Faraday's and Ampère's laws are needed, since Gauss's law as well as $\nabla\cdot\boldsymbol{B}=0$ indirectly are handled initially by choosing the initial conditions wisely (Gauss's law is satisfied when charge conservation is provided, $\partial_t\rho=-\nabla\cdot\boldsymbol{J}\rightarrow\nabla\cdot\boldsymbol{E}=\nicefrac{\rho}{\varepsilon_0}$).

Weighting In the framework of this thesis, the interaction of a high-intensity laser pulse with a helium gas jet are investigated. The real particle density inside such a gas jet is in the order of several $10^{18} - 10^{19}$ particles per cm^3. Thus, a simulation of this huge amount of single particles, each being influenced by the electromagnetic fields of an incident laser bullet, nowadays is not possible in an appropriate time. A lot of computing power would be needed - even if a supercomputer like JUQUEEN or JURECA is used for the calculations. The state-of-the-art limit is $\sim 10^{12}$ particles.

In PIC algorithms this problem is solved by introducing so-called *super-* or *pseudoparticles*. Each pseudoparticle is not a single point placed on the grid, but a region with a certain size that can move in the simulation box. A pseudoparticle represents a large number of real particles, a so-called *particle cloud*. Hence, a pseudoparticle represents real particles in the form of a charge and mass distribution in space: here, the charge and the mass of a pseudoparticle might vary depending on the number of represented real particles, but the species' charge-to-mass ratio q/m is constant. Within the current simulations, the number of pseudoparticles is in the order of $N_\mathrm{p} \sim 10^8$, which would lead to N_p^2 equations of motion to be solved. In a PIC algorithm the number of calculations is reduced: first of all, the particle density and the charge current density are derived ($\propto N_\mathrm{p}$), followed by the calculation of the electromagnetic fields on N_cell ($\ll N_\mathrm{p}$) grid points. Finally, the Lorentz force for every particle is calculated ($\propto N_\mathrm{p}$). The number of FLOPS needed for the whole simulation is given by $\alpha N_\mathrm{p} + \beta N_\mathrm{cell}$.

As mentioned above, the calculated fields are localized to discrete grid points while particles are able to propagate freely within the simulation box. An allocation of particle properties to certain grid points can be performed by *weighting*: charge and mass of particles are no longer punctual given, *i.e.* $\{q, m\}\, \delta(\boldsymbol{X}_j - \boldsymbol{x}_i)$. Instead, they are distributed with the previously mentioned weight function $S(\boldsymbol{X}_j - \boldsymbol{x}_i)$. When traveling on the grid, the particle's contribution to each grid point is its weight function which is the integral of the particle shape function. Here, the shape function stands for the effective shape of the particles: it can be a tophat (less accuracy), triangle, or spline function (more accurate). Note: the weight function is often called shape function, *cf.* [Bir85]. The weight as the fraction of pseudoparticles in the j^th cell at position $\boldsymbol{X}_j$ is dependent on the particle's shape as well as on its position $\boldsymbol{x}_i$. Example: the charge density at the j^th grid point or the electric field which acts on the i^th particle, for instance, can be set as follows:

$$\rho_j = \rho(\boldsymbol{X}_j) = \sum_i q_i\, S(\boldsymbol{X}_j - \boldsymbol{x}_i)\,, \tag{5.6}$$

$$\boldsymbol{E}_i = \sum_j \boldsymbol{E}_j\, S(\boldsymbol{X}_j - \boldsymbol{x}_i) \tag{5.7}$$

Possible weight functions are the Nearest-Grid-Point (NGP) or the Cloud-in-Cell (CIC) method. While the first one allocates the i^th particle to the nearest grid point, the latter assigns only a certain part of the particle's mass or charge to neighboring grid points.

5.3. EPOCH code

In the framework of this thesis, the 2D open-source *Extendable PIC Open Collaboration* (EPOCH) code v.4.3 [Bra14, Bra13] developed by the Collaborative Computational Projects (CCP) was used. EPOCH is a relativistic electromagnetic {1,2,3}D PIC code written in `Fortran` source code language. It implements parallelization via message passing interface (MPI) [Gab04]. The origin of EPOCH and the core algorithm (field updates and particle push routines) can be found in the older Plasma Simulation Code (PSC) [Ruh]. On this basis, in EPOCH modern features like a complete ionization tool were implemented in order to make simulations more realistic. Furthermore, the code was structured efficiently so that future upgrades can be performed easily. EPOCH is entirely written in SI units although some quantities have to be set in more convenient units. Charges, *e.g.*, are always multiples of the electron charge. Also particle or ionization energies can be given in eV.

For running an EPOCH simulation, input parameters are required. These have to be defined in the `input.deck` file, a text file saved in the output directory (for the structure *cf.* App. A.3). Here, the desired simulation parameters can be added without editing the whole source code or recompiling it. With the input deck the parameters are passed to the main program. An input deck contains the information about the size of the simulation box including the number of grid points, the boundary conditions, the particle species with certain physical properties, the laser parameters, the desired output settings, to mention but a few. All these parameters are arranged in separate blocks which gives the input deck a more or less fix structure, similar to an *unit assembly system.* Indeed, the order of the blocks is not important. Each block has a specified structure of *input deck directive* commands: blocks are initiated and closed by `begin:` and `end:`, respectively. In between both lines simple constants and complex mathematical functions can be defined. EPOCH uses a *maths parser*, *i.e.* a certain section in the core code which reads the input deck. This tool includes mathematical functions, physical as well as simulation constants, and considers mathematical operators. In Tab. 5.1 some examples for predefined constants, functions, and operators are summarized. The following code exemplifies the basic structure of an input deck:

```
#____________________________EPOCH_input_deck_structure______________

begin:BLOCK                # begin the block named BLOCK

  parameter = ...

  # the hash key '#' introduces...

  # ...a comment line

end:BLOCK                  # end the block named BLOCK

#____________________________EPOCH_input_deck_structure______________
```

The different block types (used in the current 2D simulations) are:

- `control` block: here, the number of grid points `n{x,y}`, the final time of simulation `t_end`, the size of the domain `{x,y}_{min,max}`, as well as the ionization mechanism `field_ionisation` are defined
- `boundaries` block: the boundary conditions (regarding the reflection/transmission behavior of particles at the box borders), as well as laser sources are defined `bc_{x,y}_{min,max} = {simple_laser,simple_outflow}`
- `constant` block: here, self-defined functions and constants are implemented and can be used later on
- `species` block(s): each species gets an individual block where the particle properties like `name`, `charge`, `mass`, `density`, `ionisation_energies`, or `temp_ev` (initial particle temperature in case of a fully ionized plasma as target) are defined
- `laser` block: here, the laser parameters like `lambda`, `intensity_w_cm2`, `phase`, `t_profile`, or `profile` are defined
- `output` block: `dt_snapshot` defines at which times simulated data shall be written into the output files; furthermore the desired particle and electromagnetic field properties which should be saved are chosen

constants		functions		operators	
`pi`	π	`sqrt()`	square root	`+`	addition
`nano`	10^{-9}	`if(a,b,c)`	conditional fn.	`-`	subtraction
`me`	electron mass	`sin()`	sine	`*`	multiplication
`qe`	electron charge	`exp()`	exponential	`/`	division
`c`	speed of light	`loge()`	natural logarithm	`^`	power raise
`x,y,z`	grid coordinates	`gauss()`	Gaussian	`e`	power of 10

Table 5.1.: Examples for predefined constants, functions, and operators in EPOCH

After the EPOCH simulation is terminated, the output data is saved in `.sdf` container files. Here, SDF stands for *structure-data file*. Each desired particle as well as electromagnetic field properties are written as an individual data field inside the SDF file. For data analysis, the different data fields can be read out with the help of visualization software, like *e.g. VisIt* [Chi11] or *IDL* or by self-coded programs, *e.g.* in `Python` programming language. In order to import the SDF files, a SDF reader provided by EPOCH has to be compiled.

5.3.1. Input parameters

The experiments were carried out at two laser facilities: the Arcturus laser at Heinrich-Heine-University Düsseldorf and the PHELIX laser at GSI Darmstadt (*cf.* Sec. 2.2 for the given laser properties). As underdense plasma target a helium gas jet was attached.

In order to simulate the experimental conditions as realistic as possible, they have to be transferred into the input deck. As mentioned before, the input deck is a structured text file with specific blocks as core components. In the following, the significant parameters are summarized according to their association with thematic blocks (roughly structured in domain, laser, and target blocks).

The domain

Within the `control` block the domain parameters are set, while in the `boundaries` block the domain borders are specified (*cf.* App. A.3, lines 5 to 33).

In the current simulations, a 2D simulation box with 2500 µm in x and 250 µm in y was defined (`x_min = 0.0`, `x_max = 2.5e-3`, `y_min = 0.0`, `y_max = 0.25e-3`). This box is filled with a number of grid points in each direction. The simulation resolution is determined by the grid point density in x, y, *i.e.* the number of grid points per µm. In the first simulations the number of grid points in both x- and y-direction was set to `nx = 50000` and `ny = 5000`, respectively, leading to a resolution of $\Delta x = \Delta y = 0.05$µm. Compared to the wavelength of the attached laser, in case of the PHELIX laser with a wavelength of $\lambda_{\mathrm{L,PH}} = 1.053$ µm a resolution of approximately 21 grid points per wavelength is given in both dimensions, while for the Arcturus laser with $\lambda_{\mathrm{L,Arc}} = 0.8$ µm the resolution is 16 grid points per wavelength.

The boundaries of the simulation box have to be chosen carefully regarding the reflection as well as transmission characteristics. In the current simulations the laser pulse propagates in positive x-direction in a height of $^1/_2$ `y_max`. Hence, it enters the box at the left boundary `bc_x_min`. Here, an electromagnetic source has to be attached. The reflection characteristics of impinging electromagnetic waves have to be minimized while incoming particles have to be fully transmitted. The boundary condition is `simple_laser`. The other boundaries (`bc_x_max`, `bc_y_min`, and `bc_y_max`) are defined by the `simple_outflow` condition: no electromagnetic waves are attachable, and furthermore, the inflowing characteristics are set to zero, *i.e.* particles are fully removed when reaching the boundary.

Laser block

Since the focused laser pulse is Gaussian distributed in time and space, the simulated laser with predefined wavelength `lambda` and peak intensity `intensity_w_cm2` is assigned to a temporal and spatial Gauss function `gauss(d,d0,w)` $\rightarrow f(x) = \exp\{-\,({}^{d\,-\,d_0}/_{w})^2\}$. The corresponding commands for the temporal and spatial Gauss profiles are `t_profile` and `profile`, respectively. The Gauss function leads to a Gaussian profile in variable d which is centered around d_0. The characteristic width w can be substituted by the variable's FWHM, *i.e.* FWHM $= 2w\sqrt{\ln 2}$.

Regarding the temporal evolution of the pulse, the simulation parameters are $d_t =$ `time`, $d_{0,t} =$ `3*wtlaser`, and $w_t =$ `wtlaser`, with `wtlaser` as the FWHM of the laser's pulse duration τ over $2\sqrt{\ln 2}$. In space, the Gauss function in `y` is centered around `ym` $= {}^1/_2$ `y_max`. The characteristic width is `ylaser0` as the laser beam radius at the left boundary of the simulation box (*cf.* Eq. (3.9), p. 13: beam spot size evolution $w(z)$).

Here, the FWHM of the beam waist has to be divided by $2\sqrt{\ln 2}$, also for defining the Rayleigh length. By defining the `phase` and the normalization of the intensity `norm`, the Gaussian beam-optics are satisfied. Without defining the temporal characteristics, the laser pulse will be simulated as shown in Fig. 3.1 (a) on p. 13.

In the input deck (*cf.* App. A.3), the `laser` block can be found within lines 119 and 130. Table 5.2 summarizes the simulated laser parameters of the PHELIX as well as the Arcturus laser:

parameter	PHELIX	Arcturus
`intensity_w_cm2` [Wcm^{-2}]	1.38×10^{19}	4.35×10^{19}
`lambda` [µm]	1.053	0.8
`tlaser` [ps]	0.8	0.026
`waist` [µm]	12.85	15
focus energy [J]	40	2

Table 5.2.: Laser parameters of the PHELIX and the Arcturus laser

Species properties

During the experimental studies, two supersonic de Laval nozzles with different minimal opening diameter were attached in order to form a gas jet (*cf.* Sec. 6.1.2). The diameters were 167 µm and 0.5 mm. The influence of the nozzle geometry on the shape of the gas jet as well as on the particle density profile was determined prior (*cf.* Sec. 6.1.4).

There are two possibilities for defining an underdense plasma target: either, the target is supposed to be pre-ionized before the laser pulse enters the box, or in the more realistic case, the target is assumed to be a neutral helium gas (for the latter *cf.* App. A.3, lines 88 to 117). In both cases, the particle density has to be set according to prior interferometrical characterizations of the *real* gas-jet's density profile. In the experiment, the laser focus is adjusted in a certain height above the nozzle edge. Therefore, it is important to know the gas-jet properties for this location. Along the x-direction the particle density is assumed to be superGaussian distributed (to be more precise: in case of the 0.5 mm de Laval nozzle, the distribution is a superposition of two 6$^{\text{th}}$-order superGaussians). In y-direction a constant density is set. This approximation is tolerable since the decrease in particle density in height along a distance comparable to the laser focus dimension is neglectable. In the following, the superGaussian distribution is exemplified according to the interferometrical characterizations of the 0.5 mm de Laval nozzle at a pressure of $p = 26$ bar (*cf.* Sec. 6.1.4, p. 74).

The position of the gas jet inside the simulation box was chosen thus that it is surrounded by vacuum on the left ($x <$ `xl`) and right side ($x >$ `xr`). Hence, the laser pulse propagates through vacuum after it entered the domain and hits on the left gas-jet border at `xl` - before being fully focused. The focus is positioned between `xl` and the central gas-jet axis (at `xm`). This is due to the fact, that during laser-plasma experiments a totally fix shooting position at the target's "front side", *e.g.*, cannot be achieved with (sub-)micron accuracy (pointing of the laser). Furthermore, the density distribution of a gas-jet target is not a completely plateau-like saltus function with sharp density ramps as it is given for foil targets. Moving from vacuum into the gas jet, the particle density increases smoothly. Therefore, it is advantageous to adjust the laser focus somewhere inside the gas target to be sure that nearly the whole peak intensity can act on the target. Of course, if the focus position is chosen too deep inside the gas then a tight focusing will not occur and no efficient particle acceleration can be expected. In the upper half of Fig. 5.2, a neutral ^{4}He gas jet inside the simulation box is illustrated in pseudo colors. The laser pulse has not entered the simulation box, yet, *i.e.* no laser-target interaction has occurred. The lineout of the superGaussian particle density along the laser axis (*i.e.* in a height of $y = \mathtt{ym}$) can be regarded in the lower half of the image.

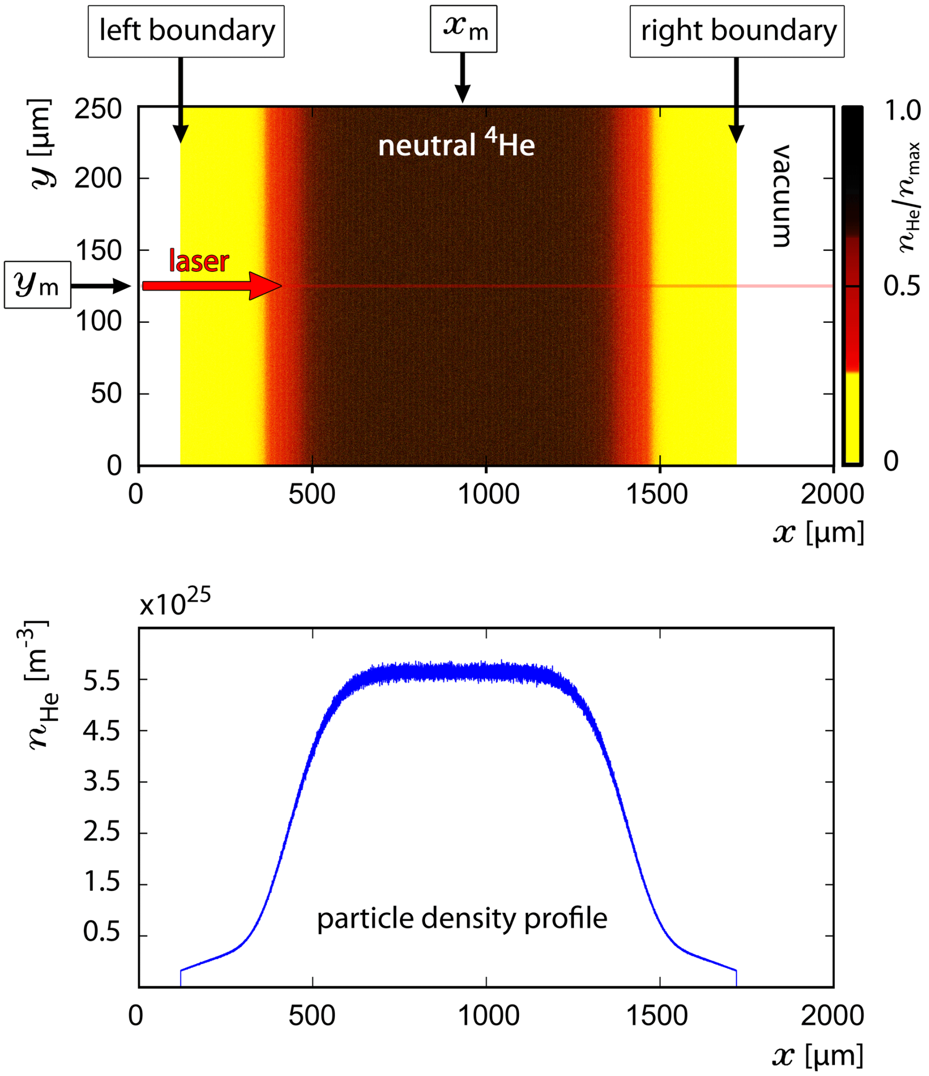

Figure 5.2.: *Top*: example of a simulated neutral ^{4}He gas jet inside the simulation box, and *bottom*: lineout of the superGaussian particle density along the laser axis in x (indicated by the semitransparent red line). On each side, the gas jet is surrounded by vacuum.

In case of a neutral ^{4}He gas target, the particle species `Helium` is defined with a `mass` of $2m_\mathrm{p} + 2m_\mathrm{n} + 2m_\mathrm{e}$ and a `charge` equal zero (note: the masses m_i $(i = \mathrm{p}, \mathrm{n}, \mathrm{e})$ are defined in multiples of the electron mass)[1]. The superGaussian density distribution in x (centered around `xm` with the characteristic widths `c1 = 0.502e-3` and `c2 = 0.8e-3`, in units of m), as it is exemplified in Fig. 5.2, is set with `density = (4.75e25 * supergauss(x,xm,c1,6) + 8e24 * supergauss(x,xm,c2,6))`, in units of m^{-3}. The condition function `density = if((x lt xl) or (x gt xr), 1e-11, density(Helium))` defines the vacuum regions next to the gas-jet borders (`xl`, `xr`) and assigns the beforehand defined superGaussian density distribution to the regions within these borders.

Since the gas has to be ionized by the incident laser pulse (note: `field_ionisation` is enabled within the `control` block), the ionization energies for both ionization stages of ^{4}He (or ^{3}He) have to be defined. This is accomplished by adding the command lines `ionisation_energies = (54.4*ev,24.6*ev)` and `electron = (Electron1, Electron2)`. The first line defines the number of ionization stages as well as the specific binding energies of the simulated species, while the second one introduces the number and the name of ionization electrons. The physical properties of both electron species have to be set individually within their particular `species` block (`name = Electron{1,2}`, `charge = -1.0`, `mass = 1.0`, `rho = 0.0` [since at the beginning no electron species is given]). The number of `Helium` pseudoparticles is determined by the number of grid points inside the gas-jet region times N_part particles per cell. Within the simulations, N_part was set to 1.0. Thus, in case of the PHELIX simulations in total 1.6×10^8 pseudoparticles were simulated.

5.3.2. Simulation results

The current EPOCH simulation were conducted in order to support two laser-acceleration experiments at different high-intensity lasers, the Arcturus laser and PHELIX. The scientific reason for performing both simulations was different: while the Arcturus-related calculations were executed to confirm experimental results of an already terminated beamtime, the PHELIX-related simulations were necessary in order to predict the main acceleration directions of laser-accelerated helium ions. The corresponding beamtime was planned according to the simulated outcome. In the framework of this thesis, (for both experiments necessary) ion-emission parameters are mainly investigated.

Arcturus laser

As already said, the EPOCH simulations for the Arcturus experiments were conducted *after* the experimental beamtime (*cf.* Sec. 7.1). Former EPOCH simulations as well as preliminary experimental data from a preceding Faraday cup measurement on laser axis predicted a sharp ion-emission angle of 0° [Hol14]. The Arcturus beamtime was scheduled in order to verify those predictions and to investigate the laser-induced ion-

---

[1] For the other case that the target is assumed to be fully ionized, only two particle species have to be defined ($^{4,3}\mathrm{He}^{2+}$, e^-). Each can be assembled with a superGaussian density distribution, their individual mass and charge. Next to this, the plasma electrons have to gain an intrinsic temperature of *e.g.* 100 eV.

acceleration mechanism in gaseous targets. But since the experiments disproved the former simulated output, own simulations were prepared.

The simulation box was defined with `nx = 37500` and `nx = 6250` global grid points arranged over 1500 µm in x and 250 µm in y. This leads to a resolution of 25 grid points per micron, *i.e.* 40 nm, in both spatial dimensions. The gas-jet parameters (neutral ^{4}He gas @25 bar) were set according to Eq. (6.13) on p. 81. In total, 156.25×10^6 neutral helium atoms were set in the domain between `xl = 0.12e-3` [m] and `xr = 1.12e-3` [m]. The laser parameters were adapted from the experiment: `intensity_w_cm2 = 4.353e19` [W cm^{-2}], `lambda = 0.8*micron` [m], `tlaser = 26*femto` [s], `dfocus = 15*micron` [m] (focus diameter FWHM), `ncrit = 1.743e27` [m^{-3}], leading to a normalized vector potential of $a_0 \approx 5.9$. The laser focus was positioned at $(x_\mathrm{F}, y_\mathrm{F}) = (520\,\mu\mathrm{m}, 125\,\mu\mathrm{m})$, *i.e.* 400 micron inside the gas jet. Simulation output was written every 0.5 ps.

In Fig. 5.3 the electron and ion densities are illustrated for two different times t after the simulation started[2]: $t = 1.5$ ps (from the 0003.sdf data) and $t = 6.5$ ps (from the 0013.sdf data). The densities are normalized to the intrinsic maximum neutral He particle density $n_\mathrm{max} = 10^{19}\,\mathrm{cm}^{-3} \approx 0.006\,n_\mathrm{c}$. In the top and center row, the electron and ion densities are plotted in pseudo colors, while in the bottom of the image lineouts of the particle densities can be regarded: in blue the normalized ^{4}He^{2+} ion density, in red the normalized electron density.

At $t = 1.5$ ps, the focusing laser pulse already has entered the simulation box and started to ionize the neutral ^{4}He gas (the left density ramp arises at `xl = 0.12e-3` [m]). The particle densities for both electrons and ions arise. In case of electrons, bubble structures with increased particle density at their rear sides (with respect to the laser propagation direction) are formed behind the laser pulse. Within the inset, an enlarged image section of the bubble region can be regarded. At the bubble locations, the corresponding lineout of the arising electron density (red color) shows sharp peaks with values up to about $13 \times n_\mathrm{max} \approx 0.07\,n_\mathrm{c}$. In contrast to this, the ion density exhibits only a smooth increase. 5 ps later, at $t = 6.5$ ps, the laser pulse has already passed the original gas-jet borders and exited the whole simulation box (vacuum propagation in 6.5 ps: $\sim$ 1950 µm). A channel both in electron and ion density has developed. The focusing/defocusing of the laser pulse and the focal waist at $x \sim x_\mathrm{F}$ becomes obvious. Here, both species' densities are rapidly increased: the lineouts of the densities indicate sharp peaks up to $\sim 2\,n_\mathrm{max}$ (electrons) or $\sim n_\mathrm{max}$ (ions), respectively. The outer diameter of the channels is about 25 µm. In total, the laser pulse propagates about 800 µm into the gas jet and disperses (at $x \sim 900$ µm). Regarding both simulation times, self-focusing and ponderomotive self-focusing occur. Behind the focal region, the channels expand following the diverging laser pulse. The high-density regions (dark green/orange, thickness of approximately $1 - 2$ µm) inside the channel sheath can clearly be regarded. At the target's rear side, "filigrees" of high number density are extended into rest gas regions.

In order to observe the simulated emission of laser-accelerated ^{4}He^{2+} ions, a distribution function was defined in the input.deck: the ion energies in MeV and the corresponding

---

[2] Note: to simplify matters, in the following "a time t after the simulation started" will be called "a time t".

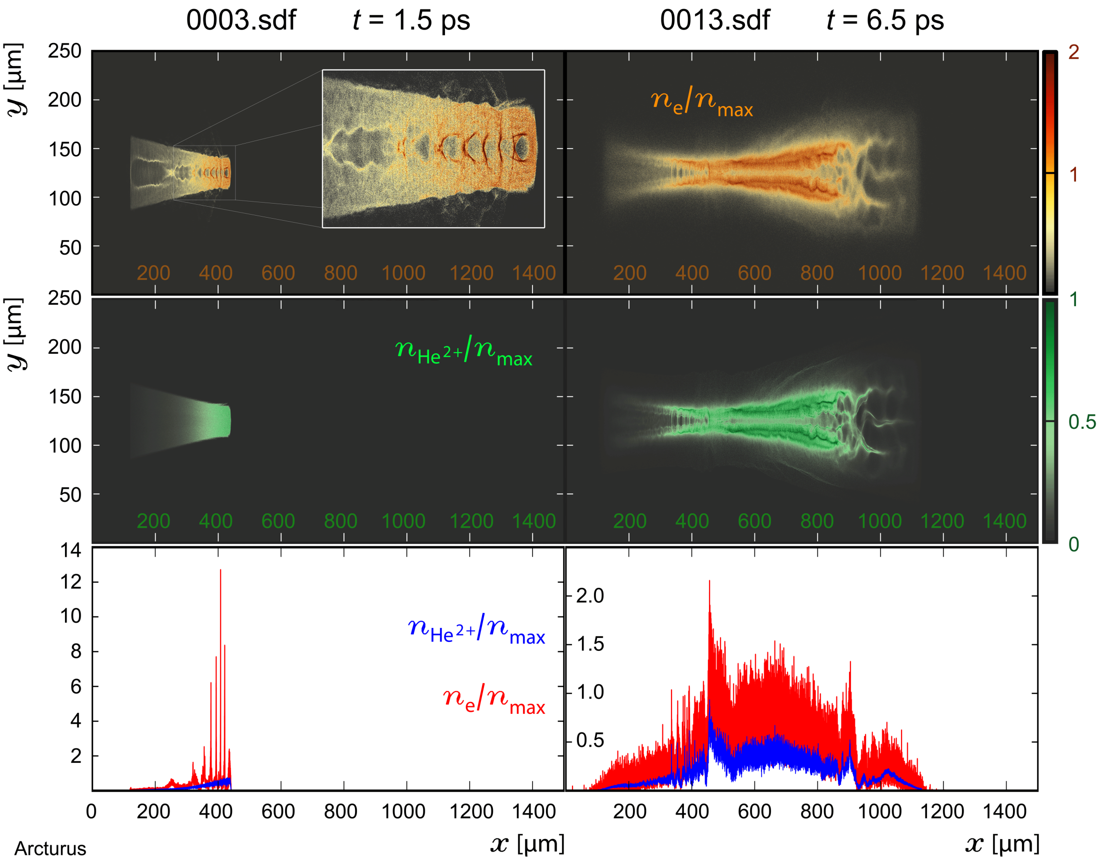

Figure 5.3.: Temporal evolution of the electron and ^{4}He^{2+} ion number densities for $t = 1.5\,\mathrm{ps}$ (*left column*) and $t = 6.5\,\mathrm{ps}$ (*right column*) after the simulation start. *Top*: normalized electron density, *center*: normalized ion density, and *bottom*: lineout of the normalized particle densities (*blue*: ions, *red*: electrons) along the laser axis in x.

angles in rad were directly written into the output files. Figure 5.4 illustrates the angular-energy distribution of accelerated helium ions at $t = 6.5\,\mathrm{ps}$. Within the plot, the ion number npart/cell is added in pseudo colors. Furthermore, six angles were substituted from rad to degree: $\pm\{80°, 90°, 100°\}$. Around $\pm 90°$ relative to the laser axis ($= 0°$) two peaks were originated. The maximal achieved energy around $90°$ is about $2.5\,\mathrm{MeV}$ while the energy peak on the contrary side is slightly less energetic ($\sim 2.25\,\mathrm{MeV}$). Furthermore, around $0°$ a thin forward signal with energies up to $0.9\,\mathrm{MeV}$ is striking (like predicted in the former simulations in [Hol14]).

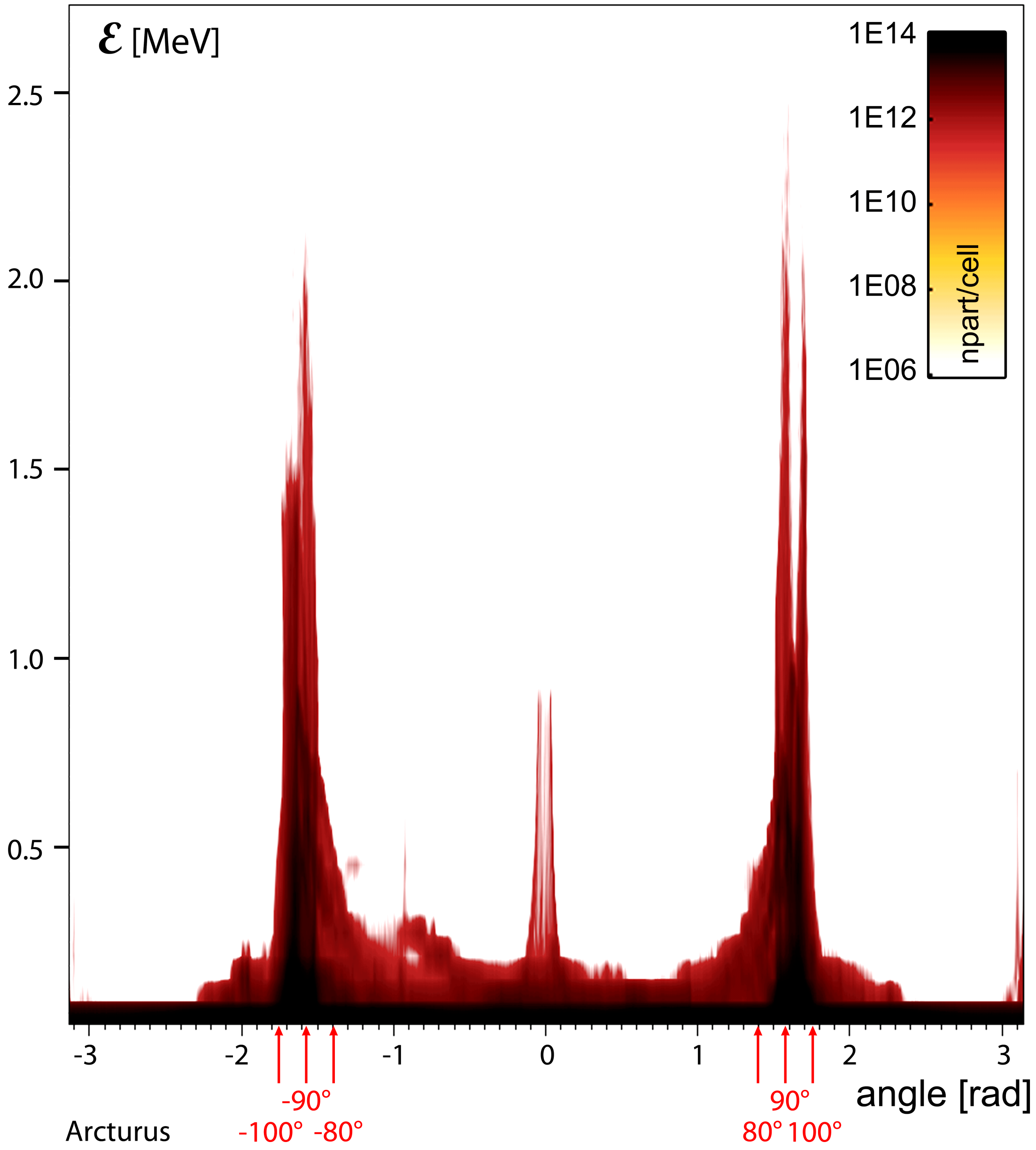

Figure 5.4.: Angular $^4\mathrm{He}^{2+}$ ion energy distribution for $t = 6.5\,\mathrm{ps}$ (Arcturus simulation).

When considering the signal intensities for the observed energy peaks, *i.e.* the corresponding npart/cell, it becomes obvious that the color strength or ion density decreases rapidly for higher energies. By generating lineouts over the full angular range for a fix ion energy, the total number of "monoenergetic" ions can be extracted. In Fig. 5.5, two lineouts for 0.5 MeV (blue curve) and 1 MeV (red curve) are plotted.

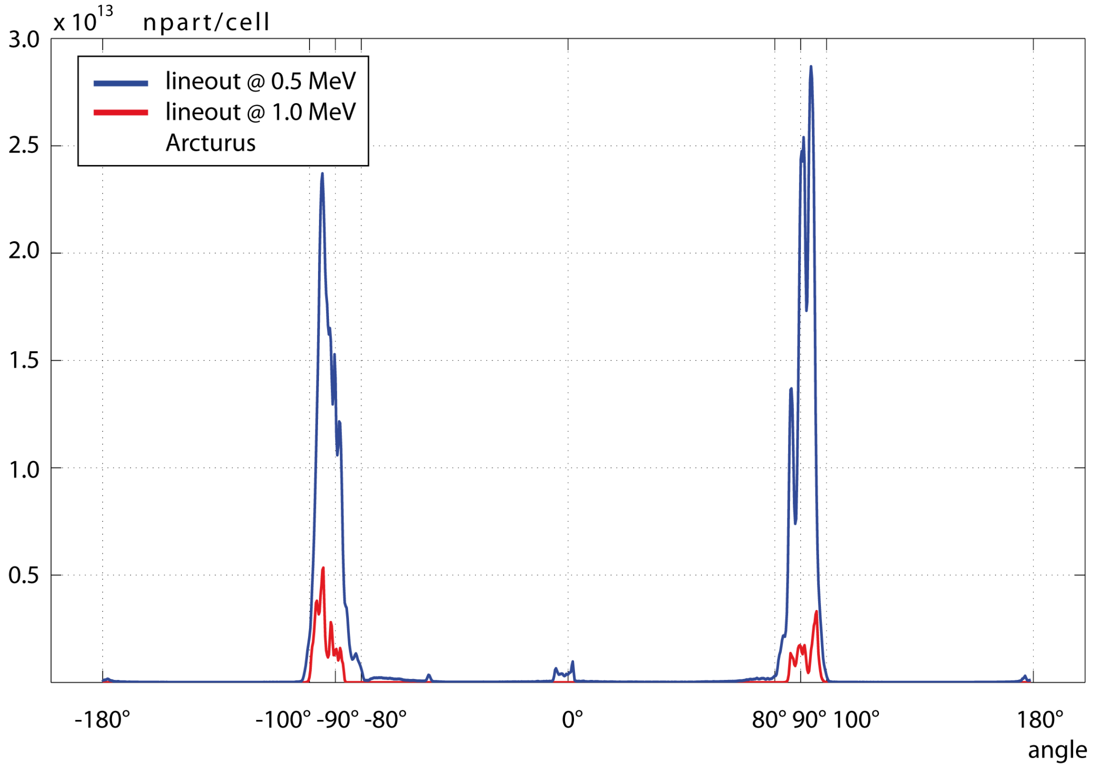

Figure 5.5.: Lineout of the angular energy distribution for $^4He^{2+}$ ion energies of 0.5 MeV (blue curve) and 1 MeV (red curve) (Arcturus simulation).

In case of 500 keV $^4He^{2+}$ ions, the maximal npart/cell at $-95°$ and $+94°$ is 2.37×10^{13} and 2.87×10^{13}, respectively. In contrast to these values, for an ion energy of 1 MeV the ion numbers are reduced by a factor of $\times 0.22$ to a value of 5.23×10^{12} at $-95°$ and by $\times 0.05$ to 1.50×10^{12} in the opposite direction. Regarding the "visible" forward signal in Fig. 5.4, it can be summarized that it is only given for the 0.5 MeV lineout between $-6.2°$ and $2.5°$. Within this range two peaks arise with a maximal ion number of 9.66×10^{11} at $1.8°$, and 6.54×10^{11} located at $-4.6°$. In comparison to the maximum transversely emitted ion number for the 500 keV case, a decrease in signal of nearly 97% is given. Within the Arcturus experiments, the ion diagnostics were precisely adjusted at 0° (on laser axis) and no ion signal could be recorded during the whole beamtime. If the above described simulated data would have been available before the Arcturus beamtime, then the investigations would have been conducted differently, *i.e.* by concentrating on the transversal signals.

Since the angular-energy distribution showed a huge ion signal in transverse direction, for a fix angle of $-90°$ a lineout along the energy axis, *i.e.* an energy spectrum for a specific ion emission angle, is plotted in Fig. 5.9 on p. 65. This plot also contains the simulated PHELIX data. Therefore, it can be regarded (and will be described) later on.

PHELIX laser

The following simulations of the experimental PHELIX conditions included neutral helium-4 as plasma target. This is due to the fact that helium-4 served as reference gas target for feasibility investigations at PHELIX. The EPOCH calculations were performed in order to determine the main ion-acceleration direction. The experimental setup of the PHELIX i009 beamtime was planned according to the simulated outcome.

The simulation box was filled with `nx = 50000` $\times$ `ny = 6250` grid points distributed over an area of 2000 micron in x and 250 micron in y. The resolution again was 25 grid points per micron or 40 nm. The gas-jet parameters were set according to the 0.5 mm de Laval nozzle characterizations (*cf.* Figs. 6.11 and 6.15 on p. 78 and p. 80, respectively). The gas-jet borders were `xl = 0.12e-3` [m] and `xr = xl + 1.6e-3` [m]. In total, 150×10^6 neutral He atoms were distributed within the gas-jet region. The laser parameters were defined as: `intensity_w_cm2 = 1.38e19` [$\mathrm{W\,cm^{-2}}$], `lambda = 1.053*micron` [m], `tlaser = 0.8*pico` [s], `dfocus = 25.7*micron` [m] (focus diameter FWHM), `ncrit = 1.0e27` [$\mathrm{m^{-3}}$], leading to a normalized vector potential of $a_0 \approx 3.3$. The laser focus was positioned at $(x_\mathrm{F}, y_\mathrm{F}) = (800\,\mu\mathrm{m}, 125\,\mu\mathrm{m})$, *i.e.* 680 micron inside the gas jet. Simulation output was written every 0.5 ps.

Similar to the prior Arcturus simulation, Fig. 5.6 illustrates the temporal evolution of the normalized electron and $^4\mathrm{He}^{2+}$ ion densities for $t = 3.5\,\mathrm{ps}$ and $t = 6.5\,\mathrm{ps}$. A channel in ion and electron density is generated. The simulated data predicts strong self-focusing effects followed by filamentation. For larger times, the channel widens and the sharp structures smear due to the presence of several filaments. Here, approximately at the location of the gas-jet center (at $x \approx 900\,\mu\mathrm{m}$), the laser pulse starts to disperse in the underdense plasma regions. The laser pulse changes its initial direction by hosing and bending [Spr92, Dud99]: the main filament is bent downwards. The sheath of the channel in both densities is characterized by a concentrated particle density. The corresponding lineouts for $n_\mathrm{e,i}\, n_\mathrm{max}^{-1}$ show sharp peaks around $x = 1000\,\mu\mathrm{m}$ and broader density distributions around $1250\,\mu\mathrm{m}$.

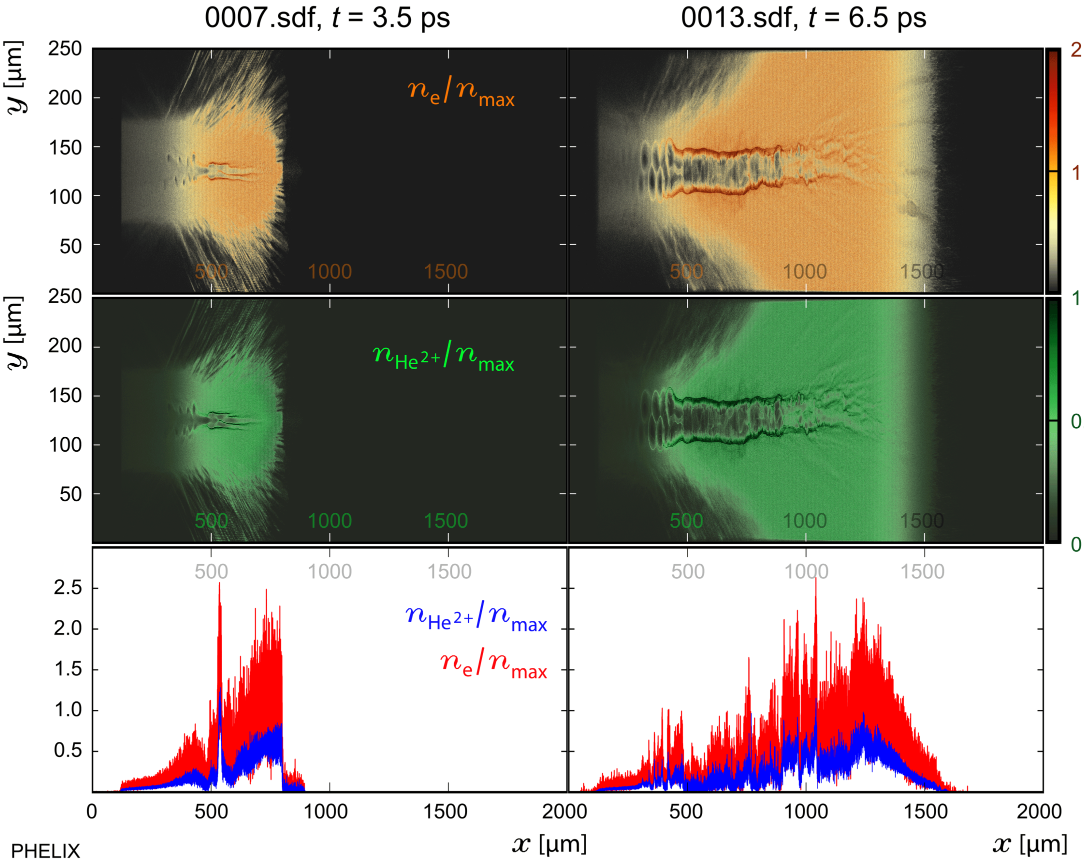

Figure 5.6.: Temporal evolution of the electron and $^4\mathrm{He}^{2+}$ ion number densities for $t = 3.5\,\mathrm{ps}$ (*left column*) and $t = 6.5\,\mathrm{ps}$ (*right column*) after the simulation start (PHELIX simulation). *Top*: normalized electron density, *center*: normalized ion density, and *bottom*: lineout of the normalized particle densities (*blue*: ions, *red*: electrons) along the laser axis in x.

The ion angular-energy distribution at $t = 6.5\,\mathrm{ps}$ can be regarded in Fig. 5.7. Similar to the prior Arcturus case, around $\pm 90°$ relative to the laser direction two energy peaks up to 12 MeV arise. But again, the npart/cell values are low for higher energies. Dense regions within both peaks are indicated by dark pseudo colors. A sharp peak in forward direction is not visible although in the angular range of $\sim \pm 20°$, *i.e.* $\sim \pm 0.35\,\mathrm{rad}$, a few particles are also accelerated to energies up to 3.5 MeV.

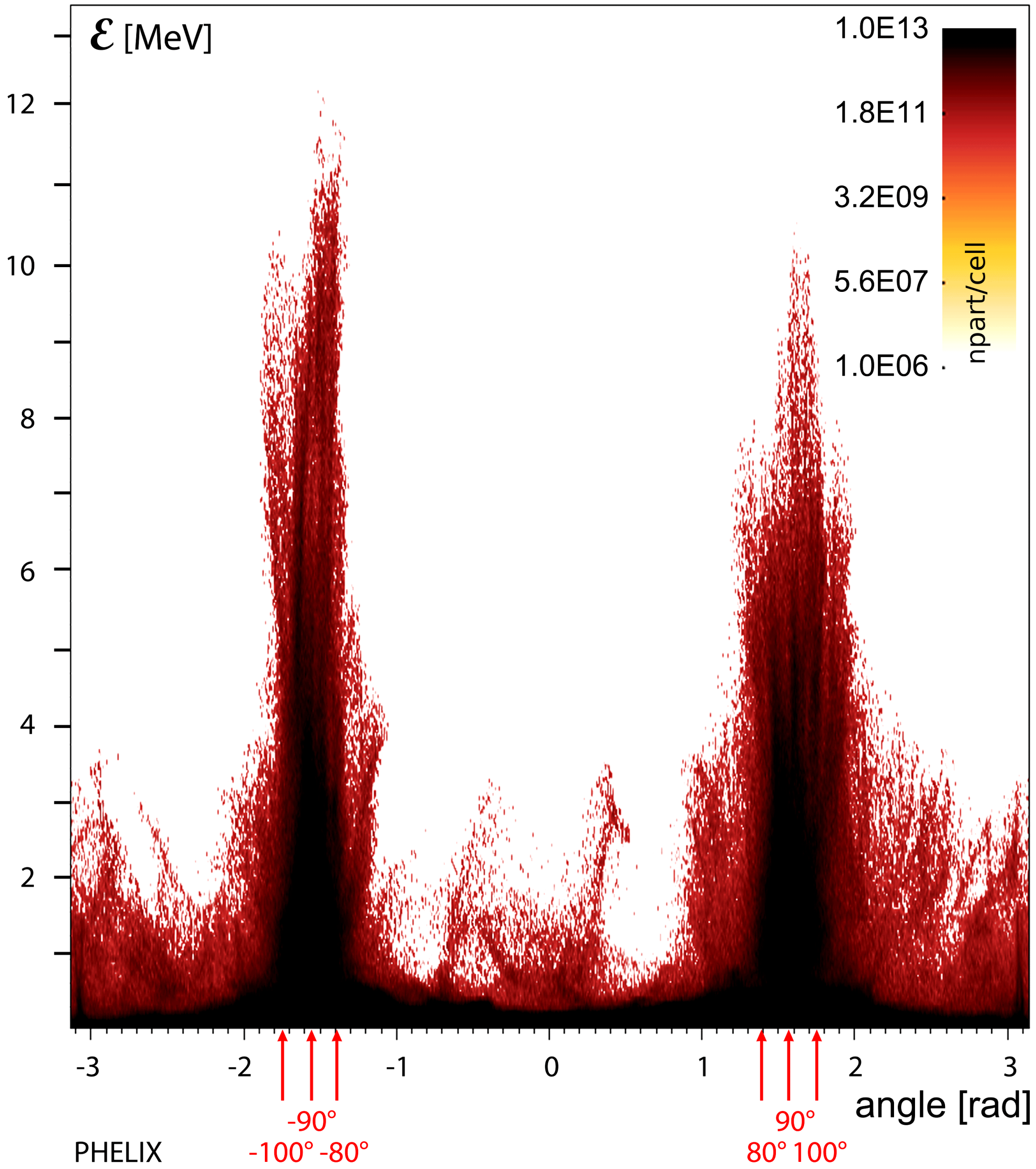

Figure 5.7.: Angular $^4\mathrm{He}^{2+}$ ion energy distribution for $t = 6.5\,\mathrm{ps}$ (PHELIX simulation).

A lineout for a fix ion energy of 2 MeV is plotted in Fig. 5.8. The two sharp peaks in ion number are centered around $-89.6°$ and $+88.6°$. A maximal particle number similar to the Arcturus case (but for an ion energy of 0.5 MeV) is given with 2.03×10^{13} (for $-89.6°$). At $-90°$ a npart/cell of 1.98×10^{13} is reached. The FWHM of this peak is ranged between $-94.82°$ and $-86.17°$, *ergo* a FWHM of 8.65° is given. In the opposite direction, the peak number is slightly reduced to 1.34×10^{13} and at 90° it is 1.05×10^{13}. Here, the FWHM is 11.45°, ranged over 82.78° to 94.23°.

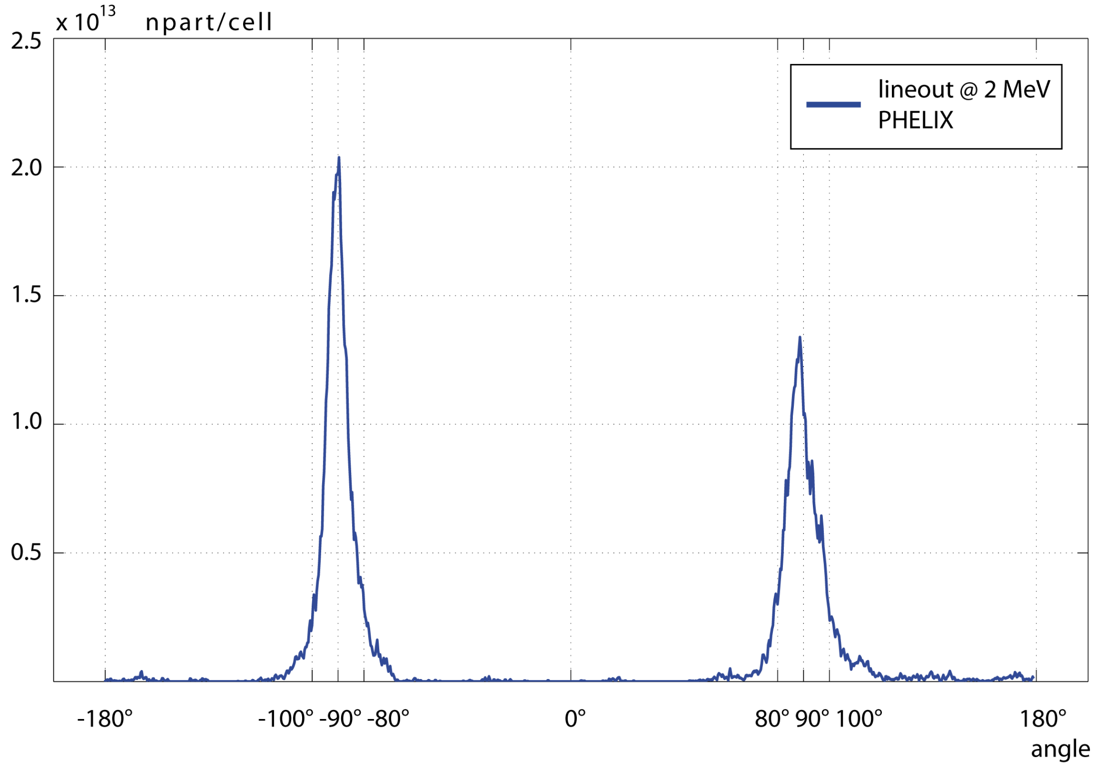

Figure 5.8.: Lineout of the angular energy distribution for a $^4He^{2+}$ ion energy of 2 MeV (PHELIX simulation).

Simulated ion energy spectra at $-90°$ For both the Arcturus and the PHELIX simulation, an energy lineout for a fix emission angle of $-90°$ was extracted in order to get an impression of the simulated ion energy spectra. The corresponding plot is illustrated in Fig. 5.9: the blue curve represents the simulated PHELIX data and the red curve belongs to the Arcturus case. The scale of the ordinate is $\log_{10}$ and the energies are given in units of MeV. Thermal spectra with a saddle structure can be regarded for both cases. The simulated high-energy cut-off for the PHELIX-related data is 9.84 MeV and for the Arcturus run it is 2.28 MeV. The corresponding npart/cell is 2.26×10^{10} (PHELIX) and 7.33×10^{10} (Arcturus), respectively. Assuming that an npart/cell of $\mathcal{O}(10^{12})$ would be comparable to a minimal detectable experimental ion number, then the related high-energy cut-offs would be 5.68 MeV for PHELIX and 1.05 MeV for Arcturus.

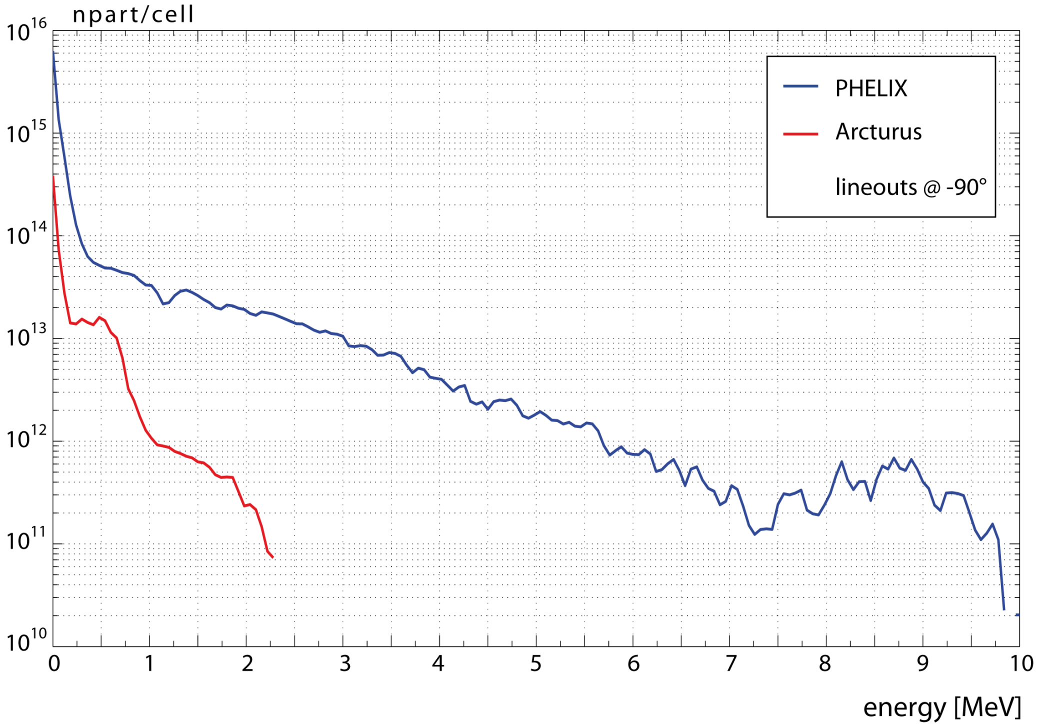

Figure 5.9.: Simulated $^{4}\mathrm{He}^{2+}$ ion energy spectra for an emission angle of $-90°$ (Arcturus and PHELIX simulation).

It has to be considered, that each the laser and also the gas-jet parameters in both simulations are defined totally different to each other. Therefore, a direct comparison between both energy spectra is not possible. The plots serve as a theoretical prediction or *hint* regarding the central planning of laser-acceleration experiments at PHELIX as well as at Arcturus.

Since the Arcturus experiment in Feb. 2014 did not yield any measurable ion signal exclusively in forward direction and since the current EPOCH simulations are in agreement with the experimental outcome, it is highly recommended to investigate the transversal direction around the gaseous target within a future experiment at Arcturus.

6. Targetry and Diagnostics for Laser-accelerated Ions

6.1. Gas jets as laser targets

A gas-jet target for laser-induced ion acceleration experiments consists of a gas source (*i.e.* a gas supply and an attached valve) and a nozzle to shape the gas jet as desired. Since laser-acceleration experiments are performed in vacuum, the response time of the valve has to be short and its opening time needs to be adjustable in the ms regime. This is important to maintain a good vacuum especially in the compressor.

6.1.1. Solenoid valve

Within the experiments at the Arcturus and the PHELIX laser, a fast-opening solenoid pulse valve, the *Parker Hannifin series 9* valve, was used [Parb]. It can be operated at repetition rates of up to 12 Hz and backing pressures of up to 86 bar. It is controlled by a *IOTA ONE pulse driver* [Para]. An external trigger can serve as input signal for the controller box where the opening time of the valve can be adjusted. The response time of the controller box was experimentally determined to 80^{+4}_{-2} µs relative to the incoming trigger signal. A typical opening time of a valve in a laser-acceleration experiment is 10 ms.

Figure 6.1 illustrates a schematic drawing of the used solenoid valve [Parb]. An electromagnet, *i.e.* a coil, is integrated in the valve body. When the valve is triggered, a magnetic field is built up and an armature in the center of the valve is pulled downwards. Thus, a teflon poppet being attached at the end of the armature unblocks the gas outlet and the valve is opened.

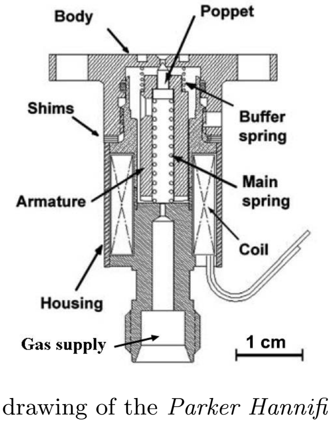

Figure 6.1.: Schematic drawing of the *Parker Hannifin series 9* valve [Parb].

Due to the presence of time-varying magnetic fields during valve operation, the *Parker*

Hannifin series 9 cannot be used in future laser-acceleration experiments with spin-polarized ^{3}He gas as plasma target: the large field gradients lead to a depolarization of the gas. For this purpose, a fast piezo valve is currently being planned and constructed (*cf.* Sec. 8.2). But, in order to demonstrate the general feasibility of laser-induced ion acceleration out of an underdense plasma target (unpolarized helium gas) the fast solenoid valve is a reliable device.

6.1.2. Supersonic nozzles

The shape of the gas jet, *i.e.* the particle-density profile, mainly is determined by the nozzle geometry. Furthermore, the order of magnitude achievable in the particle density-distribution, *i.e.* the initial neutral gas density, can be influenced by the attached backing pressure. As it can be concluded from [Wei04], below a certain particle density ($4\times10^{18}\,\mathrm{cm}^{-3}$) no ions could be laser-accelerated for a given set of laser/target parameters (*cf.* Sec. 3.2.5). Therefore, the maximum particle density for the experiments was chosen to be in the order of $10^{19}\,\mathrm{cm}^{-3}$.

According to [Sem01], a proper particle-density profile can be generated by using supersonic nozzles attached to the valve flange. In this context, a "proper" density profile means a broad plateau-like density distribution with sharp rising density ramps. Thus, when the incoming focusing laser pulse starts to interact with the gas, a more or less strong density gradient is present and the laser does not deplete too much energy in low-dense regions.

The desired nozzle geometry will be explained in the following. The Mach number M can be defined by the ratio of the gas-flow velocity v and the sound speed a inside the gas: $M = {}^{v}\!/_{a}$. The sound speed as the maximum velocity at which pressure disturbances are transported in the gas is given by $a = \sqrt{\kappa R_\mathrm{s} T}$. Here, T is the temperature, while $R_\mathrm{s} = {}^{R}\!/_{M_\mathrm{mol}}$ is the specific gas constant, with $R = 8.3144621(75)\ {}^{\mathrm{J}}\!/_{\mathrm{mol\,K}}$ as the molar gas constant and M_mol as the molar mass. For ^{3,4}He, *e.g.*, the specific gas constants are $R_\mathrm{s}^{^3\mathrm{He}} = 2757\ {}^{\mathrm{J}}\!/_{\mathrm{kg\,K}}$ and $R_\mathrm{s}^{^4\mathrm{He}} = 2077\ {}^{\mathrm{J}}\!/_{\mathrm{kg\,K}}$, respectively. The isentropic expansion factor κ (*i.e* the specific heat ratio) is given by $\kappa = {}^{c_\mathrm{p}}\!/_{c_\mathrm{v}}$, with c_i ($i = \mathrm{p}, \mathrm{v}$) as the specific heat capacities at constant pressure and constant volume, respectively. κ is dependent on the degrees of freedom f of the molecules, $\kappa = 1 + {}^{2}\!/_{f}$. For a monoatomic gas the following relations are given: $c_\mathrm{p} = {}^{5}\!/_{2}\,R$, $c_\mathrm{v} = {}^{3}\!/_{2}\,R$, and $\kappa = {}^{5}\!/_{3} = 1.\bar{6}$. Hence, the number of the degrees of freedom is $f = 3$.

Depending on the Mach number, the flow is called sub-sonic for $M < 1$, sonic for $M = 1$, and supersonic for $M > 1$, respectively. A de Laval nozzle has a minimal entry cross-section area $A^* = \pi\,({}^{d^*}\!/_{2})^2$ through which the gas flow enters the nozzle. The diameter d increases until the gas leaves the nozzle through an exit cross-section area A. The ratio of A to A^* depends on the Mach number, *cf.* Eq. (6.1) [Sem01, Sch12]. When solving this Eq. by calculating the Mach number for a given nozzle geometry there are two solutions: the sub-sonic solution M_sub before passing the nozzle throat, and the supersonic one M_super after having passed it. Furthermore, at the bottleneck with diameter d^*, *i.e.* for $A = A^*$, a sonic flow with $M = 1$ is given.

$$\begin{aligned}\frac{A}{A^*} &= \frac{1}{M}\left[\frac{2}{\kappa+1}\left(1+\frac{\kappa-1}{2}\,M^2\right)\right]^{\frac{\kappa+1}{2(\kappa-1)}}_{|\kappa=\frac{5}{3}} \\ &= \frac{(3+M^2)^2}{16\,M}\end{aligned} \tag{6.1}$$

The isentropic flow inside the nozzle can be defined by the following property ratios [Sem01, Sch12]:

$$\begin{aligned}\frac{T_0}{T} &= \left(1+\frac{\kappa-1}{2}\,M^2\right)_{|\kappa=\frac{5}{3}} = \left(1+\frac{M^2}{3}\right)\,, \\ \frac{p_0}{p} &= \left(1+\frac{\kappa-1}{2}\,M^2\right)^{\frac{\kappa}{\kappa-1}}_{|\kappa=\frac{5}{3}} = \left(1+\frac{M^2}{3}\right)^{\frac{5}{2}}\,, \\ \frac{n_0}{n} &= \left(1+\frac{\kappa-1}{2}\,M^2\right)^{\frac{1}{\kappa-1}}_{|\kappa=\frac{5}{3}} = \left(1+\frac{M^2}{3}\right)^{\frac{3}{2}}\,,\end{aligned} \tag{6.2}$$

with the temperature T, the gas pressure p, and the particle density n at any point of interest. The index "0" represents the initial conditions given in the gas reservoir. In the future experiment with spin-polarized ^{3}He gas, the reservoir is a glass vessel for ^{3}He being at a pressure of $p_0 = 3\,\mathrm{bar}$ inside a volume of $V_0 = 1.1\,\mathrm{l}$. The particle density inside the storage cell can be calculated to $n_0 \approx 7.4 \times 10^{19}\,\mathrm{cm}^{-3}$.

Within the Arcturus experiment, a de Laval nozzle with a minimal inner diameter of 167 µm was used. It was constructed within [Hol14]: due to the former simulation results, it was assumed that laser-induced ion acceleration (in forward direction) out of an underdense plasma target is only possible at the Arcturus laser facility if the target dimensions are minimized. Therefore, a thin gas jet with a width (FWHM value) $< 1\,\mathrm{mm}$ had to be attached as target.

For the PHELIX experiment, a de Laval nozzle with a larger inner diameter, a nozzle throat of 0.5 mm, was built in order to provide a thicker target, *i.e.* more target medium for the interaction and higher particle densities inside the jet. Figure 6.2 is a technical drawing of the PHELIX nozzle [Kle14]. The base body made of brass (CuZn alloy Ms58/Ms63) has a circular shape with an outer diameter of 35 mm and a wall thickness of 3 mm. In its center, the nozzle geometry is milled in the base body. The opening angle was set to 15.26° so that the nozzle diameter at the exit (nozzle tip) is $d_{\mathrm{exit}} = 1\,\mathrm{mm}$. This leads to a Mach number of $M_{\mathrm{super}} \approx 3.44$ and $M_{\mathrm{sub}} \approx 0.14$. The nozzle tip has an outer diameter of 2 mm and a height of 1 mm. For a proper target alignment this chimney-like structure is helpful regarding orientation issues. Furthermore, and even more important, it has to be ensured that the focusing laser pulse will not be clipped by the nozzle or the holder. But, the particle density inside the gas jet decreases with increasing height above the nozzle edge. In order to maximize the present particle density without clipping the laser pulse and also endangering the nozzle material, the nozzle tip has to be adjusted as near as possible to the laser focus. Therefore, the de Laval nozzle was also constructed with cone-shaped cut-outs (*pockets*) along the laser axis: dispensable blocking material is reduced by this technique.

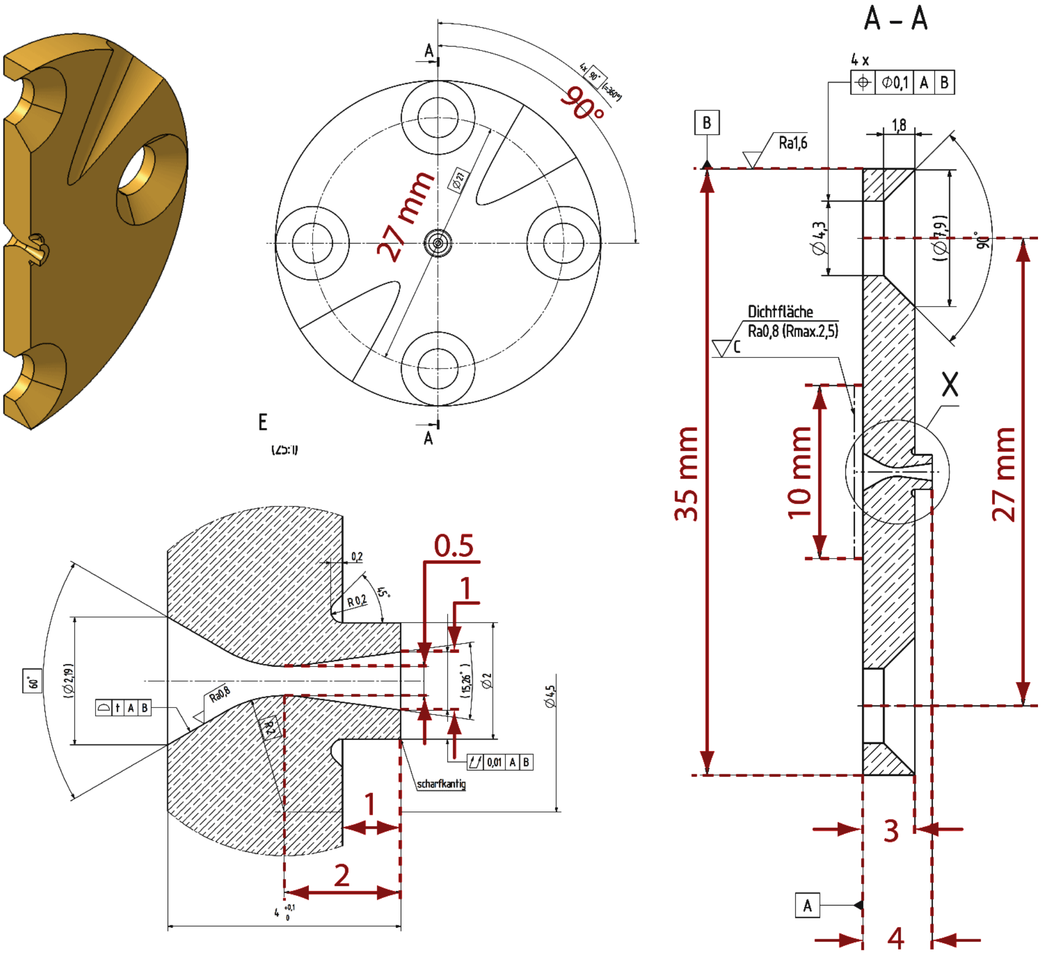

Figure 6.2.: Technical drawing of the de Laval nozzle ($d^* = 0.5\,\mathrm{mm}$) [Kle14]. *From left to right:* slice through the 3D model, top view, cross section through the middle plane, and cutaway view to an enlarged scale (nozzle geometry).

With the defined parameters, one can calculate the mass flow through the nozzle's minimal cross-section area A^*. The isentropic mass flow rate $\dot{m}$ is proportional to the attached backing pressure p_0 and A^*. Since in the future experiment with spin-polarized ^{3}He the gas is delivered at a pressure of $p_0 = 3\,\mathrm{bar}$, the intrinsic gas pressure cannot be handled as a variable parameter to regulate the target density. But, as it can be deduced from [Wei04], laser-induced ion acceleration is feasible if the target density has a proper value. Therefore, a fast pressure booster is currently being planned and constructed (*cf.* Sec. 8.2) to increase the intrinsic ^{3}He gas pressure tenfold for each laser shot. In order to plan the dimensions of the pressure booster, the isentropic mass flow rate for ^{3}He gas through the 0.5 mm nozzle is calculated as follows:

$$\dot{m} = \frac{\mathrm{d}m}{\mathrm{d}t} = \sqrt{\frac{\kappa}{R_\mathrm{s}\,T_0}}\,\left(\frac{2}{\kappa+1}\right)^{\frac{\kappa+1}{2(\kappa-1)}}_{|\kappa=\frac{5}{3}}\,p_0\,A^* \,. \tag{6.3}$$

With $T_0 = 293\,\mathrm{K}$, $\kappa = 1.\bar{6}$, $R_s^{^3\mathrm{He}} = 2757\ {}^{\mathrm{J}}\!/_{\mathrm{kg\,K}}$, $A^* = {}^{1}\!/_{4}\,\pi\,d^{*2} \approx 0.2\,\mathrm{mm}^2$, and a desired increased ^{3}He pressure of 30 bar (after compression with the planned pressure booster), the mass flow rate can be calculated to $\dot{m} \approx 4.8478 \times 10^{-4}\ {}^{\mathrm{kg}}\!/_{\mathrm{s}}$. Within the experiments, the valve is opened for 10 ms. Thus, in total 4.8478×10^{-3} g of gas will flow through the nozzle during this time. Using $pV = nRT = mR_\mathrm{s}T$, this corresponds to a volume of approximately 1.3 ml after compression. Since $pV = \mathrm{const}$, the volume of ^{3}He being at an intrinsic pressure of $p_0 = 3\,\mathrm{bar}$ can be calculated to about 13 ml. Hence, the pressure booster needs to have a minimal volume of 13 ml in order to tenfold increase the intrinsic gas pressure for the laser-acceleration experiment.

6.1.3. Interferometry of gas jets

The particle-density distribution in the gas jet as well as the temporal response of the valve can be investigated by a time-resolved interferometrical characterization. For this purpose, a Mach-Zehnder interferometer was built up which is based on superposition of two beamlets. If both beamlets with the same phase propagate through media with different refraction indices η (the *probe*) and finally are brought together, they interfere. Depending on the optical path difference, a phase difference results and an interference pattern is formed. With the help of this technique, the refraction index, and also changes of the refraction index, can be calculated.

Mach-Zehnder interferometer For the Mach-Zehnder interferometer (*cf.* Fig. 6.3), a linearly polarized HeNe laser beam (beam power of the intrinsic unexpanded laser 15 mW, wavelength $\lambda_\mathrm{HeNe} = 632.8\,\mathrm{nm}$, polarization ratio $> 500 : 1$, beam diameter (${}^{1}\!/_{\mathrm{e}^2}$) 1 mm, divergence 1 mrad) was widened and cleaned with a 25× beam expander system with attached spatial filter (aspheric lens, pinhole with a diameter of 20 μm). The clean Gaussian laser beam was split into two beamlets by a 50:50 non-polarizing beam splitter cube.

One of these beamlets was aligned such, that it propagated through a window into a vacuum chamber where the valve was installed (vacuum of 10^{-3} mbar). The beamlet illuminated the nozzle tip (*i.e.* the gas region when the valve is opened) and left the vacuum chamber through a second window. The second beamlet served as a *reference* beam: it propagated through air the same distance as the *probe* beam, but outside the vacuum chamber. Behind the vacuum chamber, a second beam splitter cube superposed both beamlets: an interference pattern was formed by slightly adjusting the path lengths of each beamlet. The interference fringes were horizontally aligned parallel to the nozzle edge. In this setup, the beam split occurred before passing the probe source. The advantage of this technique is that one beamlet *only* serves as a reference and the other one was *only* carrying the gas information: the full beamlets can be used when superposing them instead of separating gas regions and vacuum regions in the case that the beam split occurs after passing the probe (both beamlets carry the same information).

For a proper magnification of the nozzle region, an aspheric lens ($f_1 = 300\,\text{mm}$) and a plano-convex lens ($f_2 = 200\,\text{mm}$) were used. The magnified beam was imaged with a *SpeedCam MegaVis* CCD camera by *High Speed Vision GmbH*: high speed APS CMOS chip with a pixel size of $11\,\mu\text{m} \times 11\,\mu\text{m}$, a chip dimension of 22.18 mm (horizontally and vertically), a resolution of 2016×2016 pixel @ 1.279 fps, 12 bit [Hig].

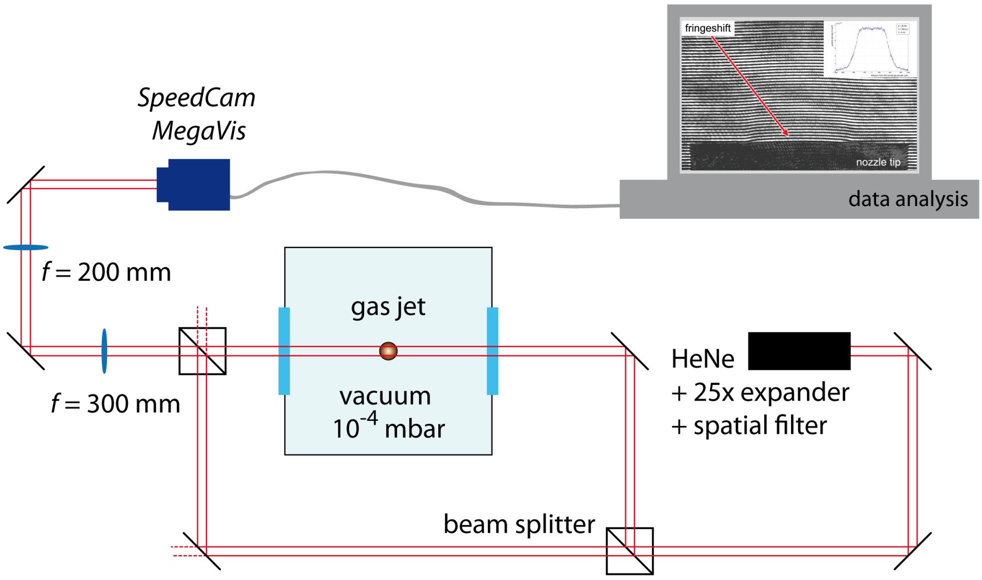

Figure 6.3.: Schematic drawing of the Mach-Zehnder interferometer.

Interferometrical characterization The CCD camera recorded the magnified region around the nozzle within the horizontally aligned interference pattern. A spatial resolution of $s_{\text{res}} = 1.079\,{}^{\mu\text{m}}/_{\text{pixel}}$ could be reached: on the CCD images, the nozzle tip with 2 mm in diameter corresponded to 1854 pixel. If the valve is opened and a gas jet is built up, local changes in particle density, *i.e.* a varying refractive index, result in a local fringe displacement due to a phase shift $\Delta\Phi$. The phase is proportional to the integral of the refractive index η along the optical propagation length [Mal00]. The refractive index η_{gas} of the gas and the given particle density follow the Clausius-Mosotti relation (Eq. (6.4)) which can be transformed into the Gladstone-Dale relationship (Eq. (6.5)) [Sch12]:

$$\frac{1}{3}\underbrace{\frac{N_\mathrm{A}\,\rho_\mathrm{gas}}{M_\mathrm{m}}}_{n_\mathrm{gas}}\frac{\alpha_\mathrm{gas}}{\varepsilon_0} = \frac{1}{3}\frac{\alpha_\mathrm{gas}}{\varepsilon_0}\,n_\mathrm{gas} = \frac{\eta_\mathrm{gas}^2-1}{\eta_\mathrm{gas}^2+2} \approx \frac{2}{3}\left(\eta_\mathrm{gas}-1\right) \tag{6.4}$$

$$\Leftrightarrow \qquad \eta_\mathrm{gas}-1 = K\,n_\mathrm{gas}\,, \tag{6.5}$$

with η_gas as the index of refraction, $n_\mathrm{gas} = N_\mathrm{A}\,\rho_\mathrm{gas}\,M_\mathrm{m}^{-1}$ as the particle density in cm^{-3}, N_A as the Avogadro constant, ρ_gas as the density in $\mathrm{g\,cm^{-3}}$, M_m as the molar mass in $\mathrm{kg\,mol^{-1}}$, α_gas as the gas' polarizability in $\mathrm{A^2\,s^4\,kg^{-1}}$, and $K = {}^1\!/_2\,\alpha_\mathrm{gas}\,\varepsilon_0^{-1}$ being the Gladstone-Dale constant [And67].

As probe gas argon was chosen because of its larger refractive index: the refractive indices of argon and helium are $\eta_\mathrm{Ar}-1 = 2.8168\times10^{-4}$ and $\eta_\mathrm{He}-1 = 0.3488\times10^{-4} \approx {}^1\!/_8(\eta_\mathrm{Ar}-1)$ (@ $p = 1.01325\,\mathrm{bar}$, $T = 273\,\mathrm{K}$, and for a wavelength of $\lambda_\mathrm{HeNe} = 632.8\,\mathrm{nm}$), respectively [Pol]. It becomes obvious, that in case of helium as probe gas the obtained phase shift will be approximately a factor of 8 smaller than an argon phase shift.

Figure 6.4 introduces the coordinates for the calculation of the phase shift $\Delta\Phi$ along the z-axis. The gas flow is directed out of the image plane. The color gradient indicates the particle-density distribution (in the center it is higher than in the border regions). As mentioned above, the phase can be deduced by integrating the refractive index along the optical path. During the measurements, the CCD camera had a fix side view on the nozzle region. Therefore, only the projection of the accumulated phase shift along the z-direction can be calculated. Since the knowledge about the refractive index in the whole medium is important, the gas jet is assumed to be cylindrically symmetrical which allows to calculate the radial refraction index distribution from the 2D measurement. This method is called *Abel inversion* (or *Abel transformation*).

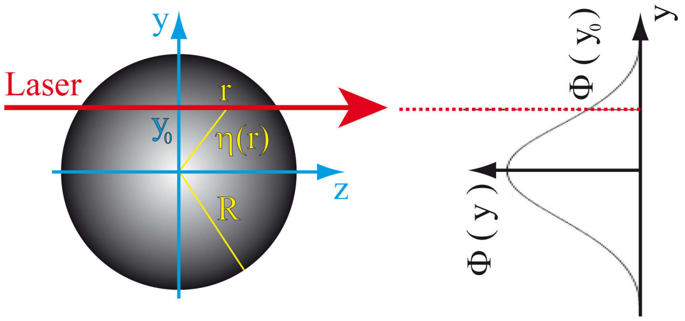

Figure 6.4.: Coordinates used for Abel inversion: the laser beam propagates in z-direction, the gas flow is directed out of the image plane [Eng11]. On the right side, the phase distribution along y is drawn.

According to [Mal00, Sch12], the measured projected phase difference $\Delta\Phi(y)$ from the propagation through gas regions can be calculated by the following Eq. (note: the substitutions $r^2 = y^2 + z^2 \;\Leftrightarrow\; z = \sqrt{r^2 - y^2}$ and $\mathrm{d}z = \mathrm{d}r\, r \sqrt{r^2 - y^2}^{\,-1}$ transform from Cartesian to cylindrical coordinates):

$$\Delta\Phi(y) = \frac{4\pi}{\lambda_{\mathrm{HeNe}}} \int_0^{z_\mathrm{r}} \mathrm{d}z \;\; (\eta(r(z)) - 1) \tag{6.6}$$

$$\Leftrightarrow \qquad \Delta\Phi(y) = \frac{4\pi}{\lambda_{\mathrm{HeNe}}} \int_y^{R} \mathrm{d}r \; r \, \frac{\eta(r) - 1}{\sqrt{r^2 - y^2}} \,, \tag{6.7}$$

with R chosen such that phase contributions at regions $> R$ can be neglected. Mathematically expressed, $F(y) = \Delta\Phi(y)$ in Eq. (6.7) is an Abel transform of a function $f(r) \propto \eta(r) - 1$. The inverse Abel transform is given by:

$$F(y) = 2 \int_y^{\infty} \mathrm{d}r \; \frac{r f(r)}{\sqrt{r^2 - y^2}} \qquad \longleftrightarrow \qquad f(r) = -\frac{1}{\pi} \int_r^{\infty} \mathrm{d}y \; \frac{\mathrm{d}F}{\mathrm{d}y} \; \frac{1}{\sqrt{y^2 - r^2}} \tag{6.8}$$

In this case, the Abel inversion leads to

$$\frac{2\pi}{\lambda_{\mathrm{HeNe}}} \;\; (\eta(r) - 1) = -\frac{1}{\pi} \int_r^{R} \mathrm{d}y \; \frac{\mathrm{d}\Delta\Phi(y)}{\mathrm{d}y} \; \frac{1}{\sqrt{y^2 - r^2}} \,. \tag{6.9}$$

Finally, the radial refractive-index distribution $\eta(r)$ can be derived. Together with Eq. (6.5), the radial particle-density distribution $n_{\mathrm{gas}}(r)$ can be calculated. In order to convert the unit in Eq. (6.9) from pixel^{-1} (coming from the CCD image) to cm^{-3} as a unit of particle density, Eq. (6.9) has to be multiplied with a factor S_{scal} [Sch12],

$$S_{\mathrm{scal}} = \frac{1}{2\pi} \, \frac{\lambda_{\mathrm{HeNe}}}{s_{\mathrm{res}}\, K} \,, \tag{6.10}$$

with $s_{\mathrm{res}} = 1.079\ {}^{\mu\mathrm{m}}/_{\mathrm{pixel}}$ as the spatial resolution of the recorded images, K as the Gladstone-Dale constant, and $\lambda_{\mathrm{HeNe}} = 632.8\,\mathrm{nm}$ as the wavelength of the attached HeNe laser.

6.1.4. Particle-density profiles

During the measurements, a movie was taken during the opening-closure time of the valve (10 ms). The movie was split into single video frames (each 0.83 ms one image) in order to analyze the temporal response of the valve, *i.e.* the temporal development of the gas flow. In order to gain knowledge about the maximal achievable particle densities as a function of the backing pressure, a pressure scan was conducted. The extracted

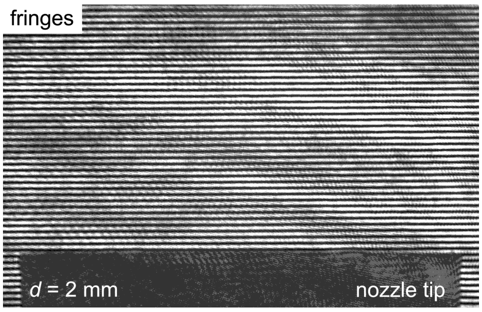

Figure 6.5.: Interferogram: reference image ($t = 0\,\text{ms}$).

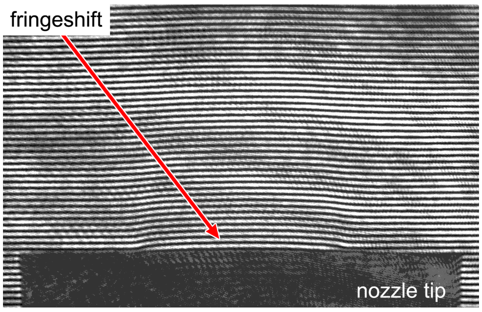

Figure 6.6.: Interferogram: gas image ($t = 5\,\text{ms}$).

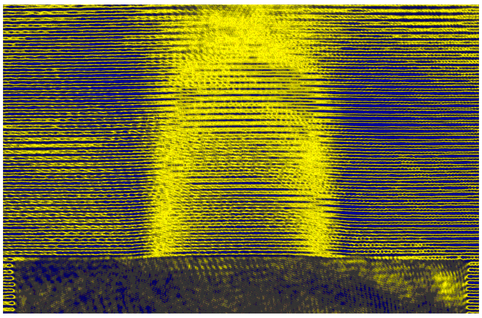

Figure 6.7.: Interferogram: visible gas jet.

frames served as input for a *Matlab* routine [Fen11]. Figures 6.5 to 6.7 exemplify the measured interferograms.

The shadow of the 500 µm nozzle can be regarded in the bottom of the images. The interference pattern is characterized by horizontally aligned fringes which are shifted due to the presence of an argon gas flow (*cf.* Fig. 6.6). The gas image was taken 5 ms after the valve was triggered. From the analysis it can be concluded that a stable gas jet already is built up 3 ms after the opening process was initialized. In Fig. 6.7, the reference image and the gas image are overlaid in order to make the fringe shift more visible. For further data analysis, the reference as well as the gas image were loaded into a first *Matlab* code where the phase shift could be extracted. Finally, with the obtained phase-shift data the Abel inversion was performed in order to get the particle-density distribution above the nozzle tip. Interesting for laser-acceleration experiments is the knowledge about the density profile in a certain height above the nozzle edge: during the experiments, a focus height of $\geq 500\,\mu\text{m}$ was a reasonable compromise between approaching the nozzle not too much and experiencing a lower gas density. The gas-jet analysis contains a 2D density plot of the gas jet in pseudo colors, a lineout of the particle density for a certain height above the nozzle edge, and a "height scan", *i.e.* a lineout of the particle density along the vertical central gas-jet axis. This analysis can be performed for different times after the valve was triggered (in order to gain information about the response time of the valve) as well as for different argon backing pressures. The following Figs. illustrate these plots for a time of 5 ms after triggering the valve with attached 0.5 mm de Laval nozzle for the PHELIX experiment and two different backing pressures (in Figs. 6.8 to 6.9: $p = 26\,\mathrm{bar}$, and in Figs. 6.12 to 6.13: $p = 15\,\mathrm{bar}$).

0.5 mm de Laval nozzle, $p = 26$ bar The 2D pseudo-color image in Fig. 6.8 illustrates the shape of the gas jet above the nozzle exit for a backing pressure of $p = 26\,\mathrm{bar}$. The particle density decreases with increasing height above the nozzle. In Fig. 6.9, the lineout of the particle density along the central gas-jet axis can be regarded. Right at the nozzle edge, a value of about $7.7 \times 10^{19}\,\mathrm{cm}^{-3}$ is given which decreases by about 30 % at a height of 500 µm to approximately $5.4 \times 10^{19}\,\mathrm{cm}^{-3}$. The corresponding density profile is displayed in Fig. 6.10. The density distribution can be characterized by a superposition of two 6^{th}-order superGaussian functions $f(x)$ and $g(x)$ which are dependent on the distance x around the central gas-jet axis ($x = 0$): Eq. (6.11) is the fit function and Fig. 6.11 is a plot of the fit on the experimental data.

$$\begin{aligned} n_{\mathrm{gas}}^{26\,\mathrm{bar}}(x) &= f(x) + g(x) \\ &= 4.75 \times 10^{19}\ \exp\left[-\left(\frac{x}{502.03\,\mu\mathrm{m}}\right)^6\right]\ {}^{1}\!/_{\mathrm{cm}^3} \\ &\quad + 0.8 \times 10^{19}\ \exp\left[-\left(\frac{x}{800\,\mu\mathrm{m}}\right)^6\right]\ {}^{1}\!/_{\mathrm{cm}^3}\,. \end{aligned} \tag{6.11}$$

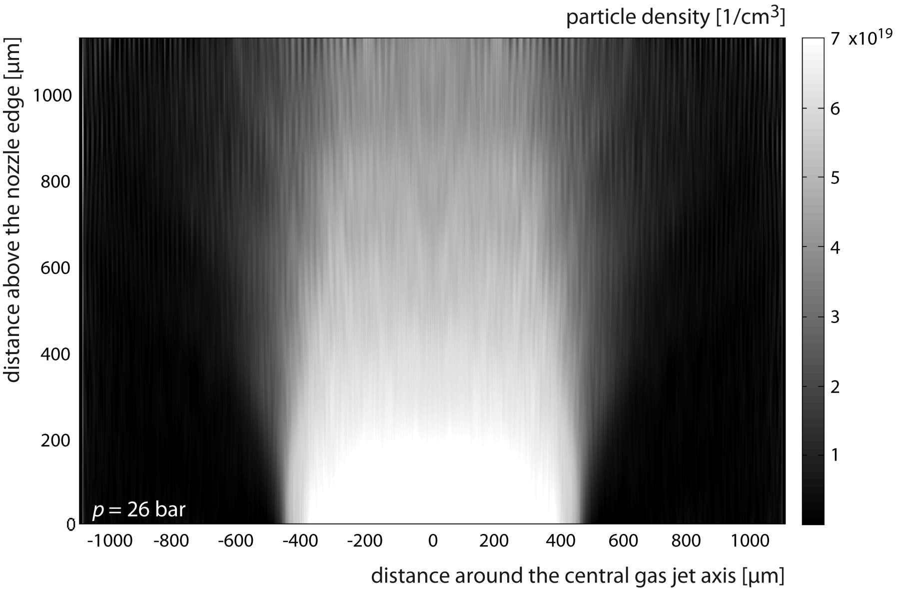

Figure 6.8.: 2D pseudo-color plot of the gas jet, at a backing pressure of $p = 26\,\mathrm{bar}$ ($d_{\mathrm{noz}} = 0.5\,\mathrm{mm}$).

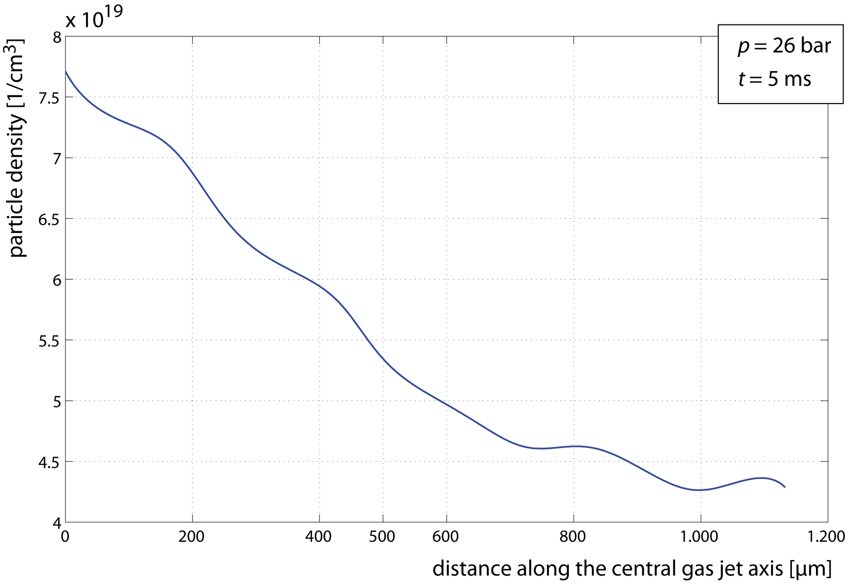

Figure 6.9.: Vertical lineout of the particle density along the central gas-jet axis, at a backing pressure of $p = 26\,\text{bar}$ ($d_{\text{noz}} = 0.5\,\text{mm}$).

0.5 mm de Laval nozzle, $p = 15$ bar The 2D pseudo-color image in Fig. 6.12 illustrates the shape of the gas jet above the nozzle exit for a backing pressure of $p = 15\,\text{bar}$. The particle density decreases with increasing height above the nozzle. In Fig. 6.13, the lineout of the particle density along the central gas-jet axis can be regarded. Right at the nozzle edge, a value of about $4.55 \times 10^{19}\,\text{cm}^{-3}$ is given which decreases by about 27 % at a height of 500 µm to approximately $3.35 \times 10^{19}\,\text{cm}^{-3}$. The density profile is plotted in Fig. 6.14. Similar to the last plots, the density distribution can be characterized by a superposition of two 6th-order superGaussian functions, given in Eq. (6.12) and plotted in Fig. 6.15:

$$
\begin{aligned}
n_{\text{gas}}^{15\,\text{bar}}(x) &= f(x) + g(x) \\
&= 2.45 \times 10^{19}\ \exp\left[-\left(\frac{x}{488.447\,\mu\text{m}}\right)^6\right]\ {}^1\!/\!_{\text{cm}^3} \\
&\quad + 0.8 \times 10^{19}\ \exp\left[-\left(\frac{x}{730\,\mu\text{m}}\right)^6\right]\ {}^1\!/\!_{\text{cm}^3}\,.
\end{aligned}
\tag{6.12}
$$

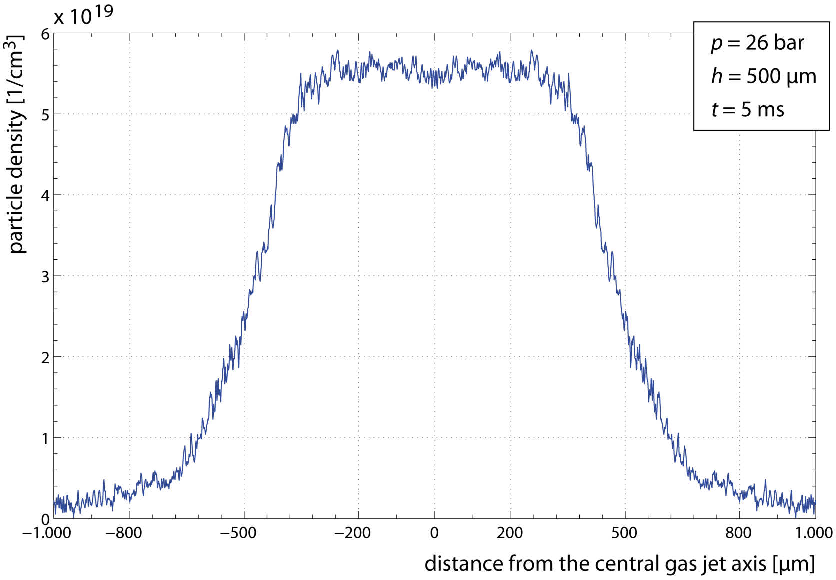

Figure 6.10.: Particle-density profile at a height of 500 µm above the nozzle edge, at a backing pressure of $p = 26\,\text{bar}$ ($d_{\text{noz}} = 0.5\,\text{mm}$).

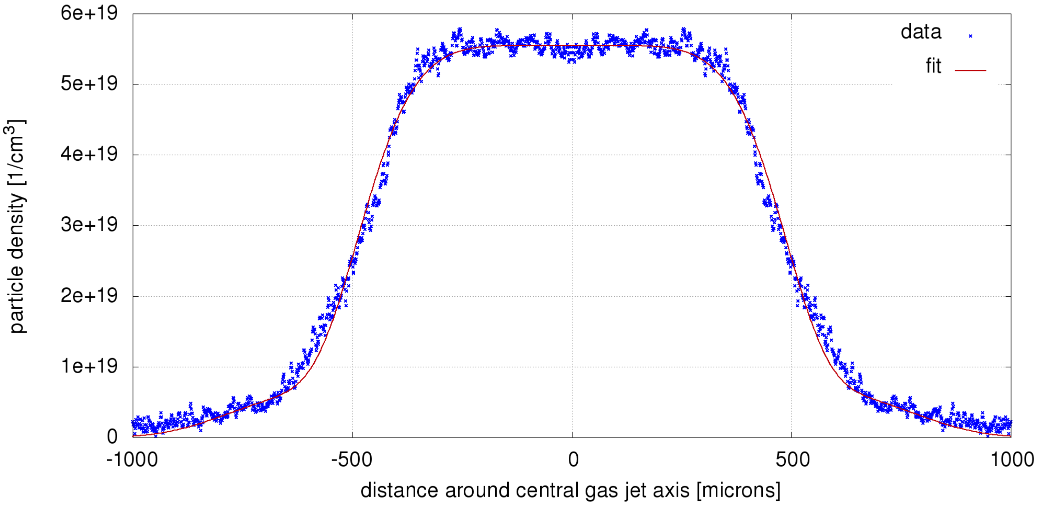

Figure 6.11.: SuperGaussian fit function $f(x) + g(x)$ for the particle-density distribution at a height of 500 µm above the nozzle edge and for a pressure of $p = 26\,\text{bar}$ ($d_{\text{noz}} = 0.5\,\text{mm}$).

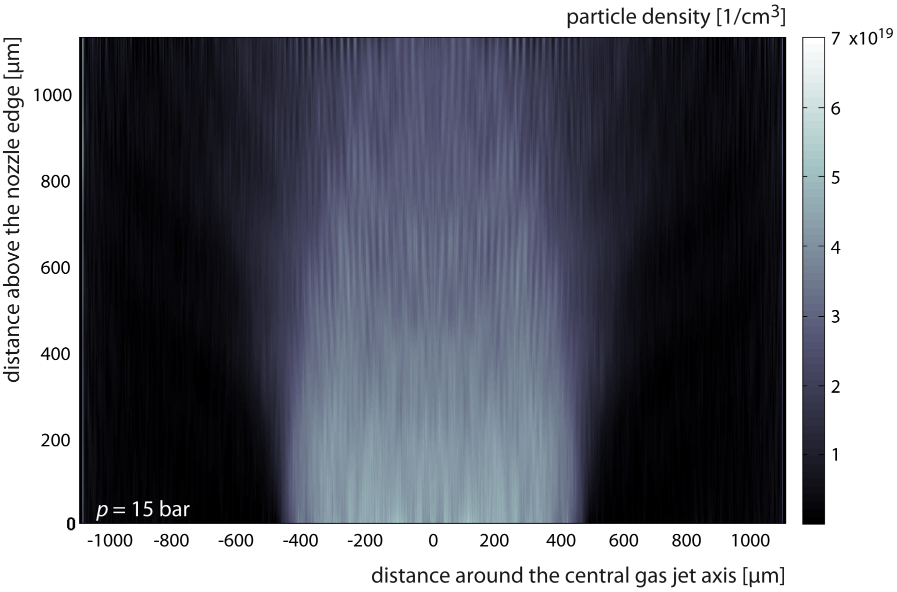

Figure 6.12.: 2D pseudo-color plot of the gas jet, at a backing pressure of $p = 15\,\text{bar}$ ($d_{\text{noz}} = 0.5\,\text{mm}$).

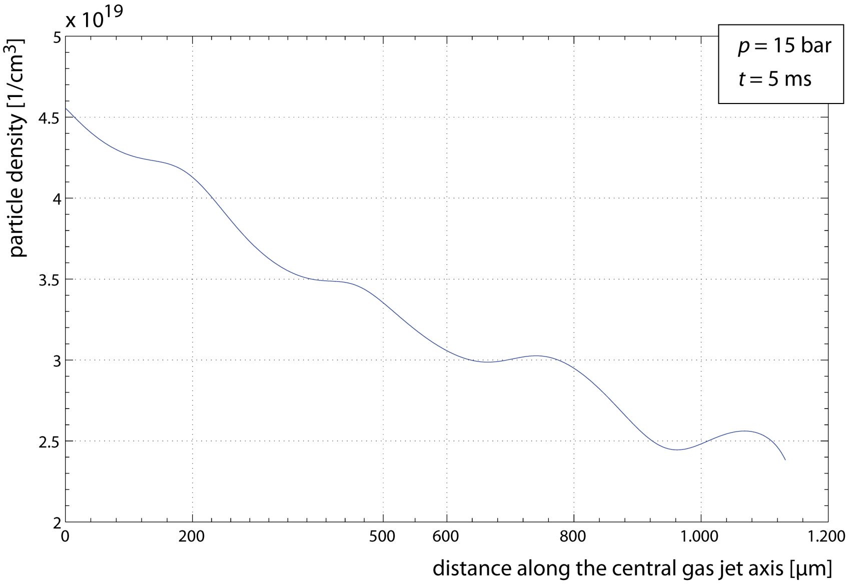

Figure 6.13.: Lineout of the particle density along the central gas-jet axis, at a backing pressure of $p = 15\,\text{bar}$ ($d_{\text{noz}} = 0.5\,\text{mm}$).

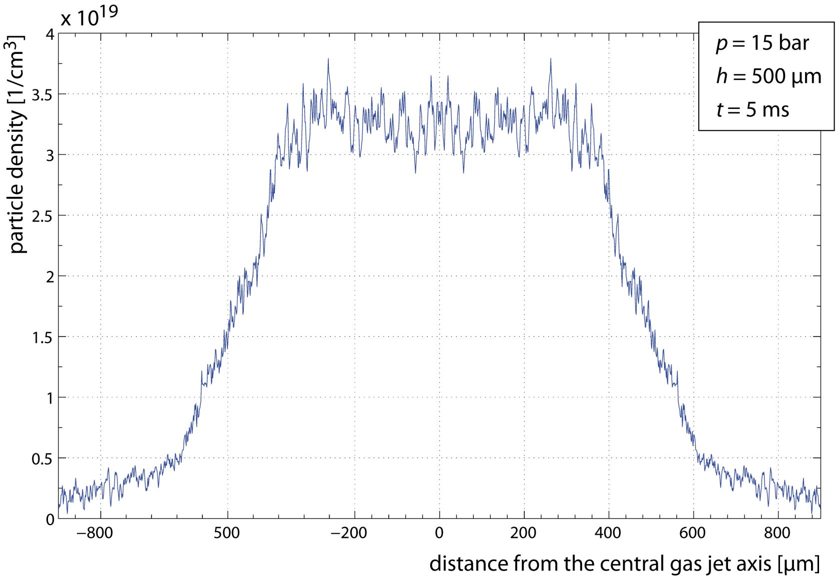

Figure 6.14.: Particle-density profile at a height of 500 µm above the nozzle edge, at a backing pressure of $p = 15\,\mathrm{bar}$ ($d_{\mathrm{noz}} = 0.5\,\mathrm{mm}$).

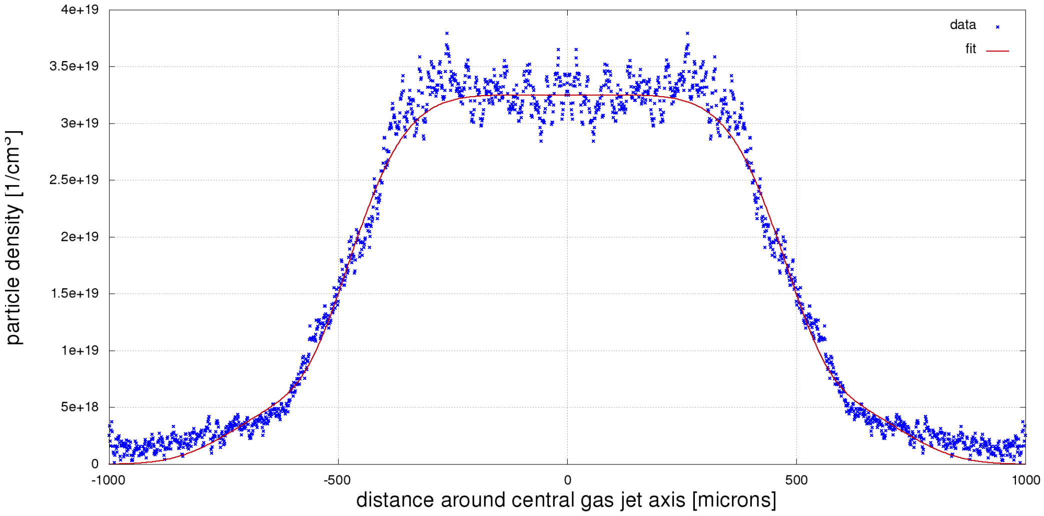

Figure 6.15.: SuperGaussian fit function $f(x) + g(x)$ for the particle-density distribution at a height of 500 µm above the nozzle edge and for a pressure of $p = 15\,\mathrm{bar}$ ($d_{\mathrm{noz}} = 0.5\,\mathrm{mm}$).

167 µm de Laval nozzle, $p = 25$ bar Within the Arcturus experiments, the 167 µm de Laval nozzle was used. The best laser-target interaction could be achieved with a backing pressure of 25 bar. Therefore, the interferometrical characterization was analyzed for this certain pressure. The 2D pseudo-color image in Fig. 6.16 illustrates the shape of the gas jet above the nozzle exit for a backing pressure of $p = 25\,\text{bar}$. The particle density decreases with increasing height above the nozzle. In Fig. 6.17, the lineout of the particle density along the central gas-jet axis can be regarded. Right at the nozzle edge, a value of $> 1.9 \times 10^{19}\,\text{cm}^{-3}$ is given which decreases by about 42 % at a height of 500 µm to approximately $1.1 \times 10^{19}\,\text{cm}^{-3}$. Here, the corresponding density profile is illustrated in Fig. 6.18. Similar to the last plots, the density distribution can be characterized by a superposition of two 4th-order superGaussian functions, given in Eq. (6.13) and plotted in Fig. 6.19:

$$\begin{aligned} n_{\text{gas}}^{25\,\text{bar}}(x) &= f(x) + g(x) \\ &= 0.85 \times 10^{19}\ \exp\left[-\left(\frac{x}{260\,\mu\text{m}}\right)^4\right]\ {}^1\!/_{\text{cm}^3} \\ &\quad + 0.2 \times 10^{19}\ \exp\left[-\left(\frac{x}{450\,\mu\text{m}}\right)^4\right]\ {}^1\!/_{\text{cm}^3}\,. \end{aligned} \tag{6.13}$$

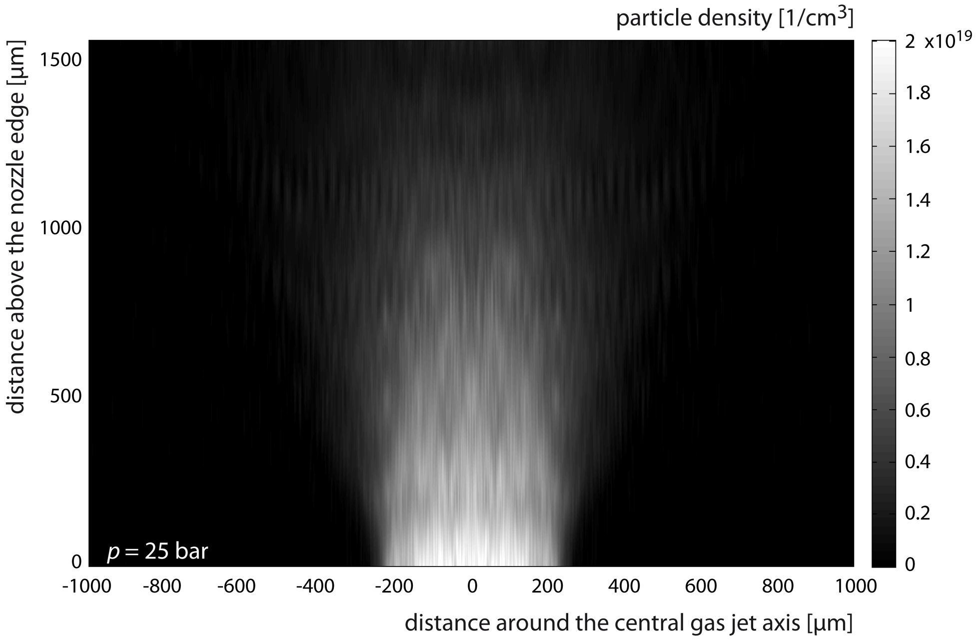

Figure 6.16.: 2D pseudo-color plot of the gas jet, at a backing pressure of $p = 25\,\text{bar}$ ($d_{\text{noz}} = 167\,\mu\text{m}$).

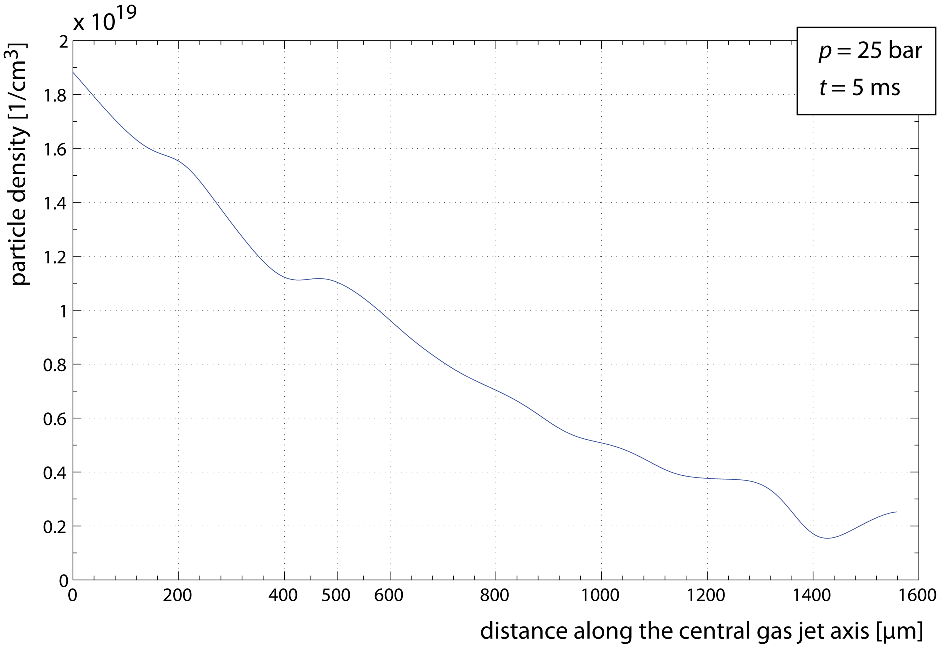

Figure 6.17.: Lineout of the particle density along the central gas-jet axis, at a backing pressure of $p = 25\,\mathrm{bar}$ ($d_{\mathrm{noz}} = 167\,\mu\mathrm{m}$).

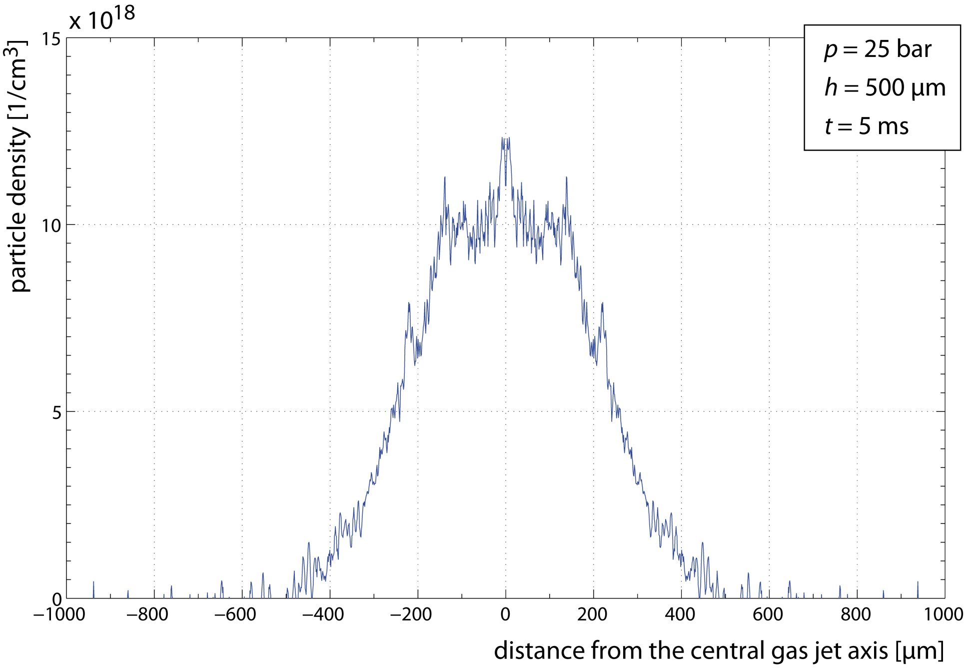

Figure 6.18.: Particle-density profile at a height of 500 µm above the nozzle edge, at a backing pressure of $p = 25\,\mathrm{bar}$ ($d_{\mathrm{noz}} = 167\,\mu\mathrm{m}$).

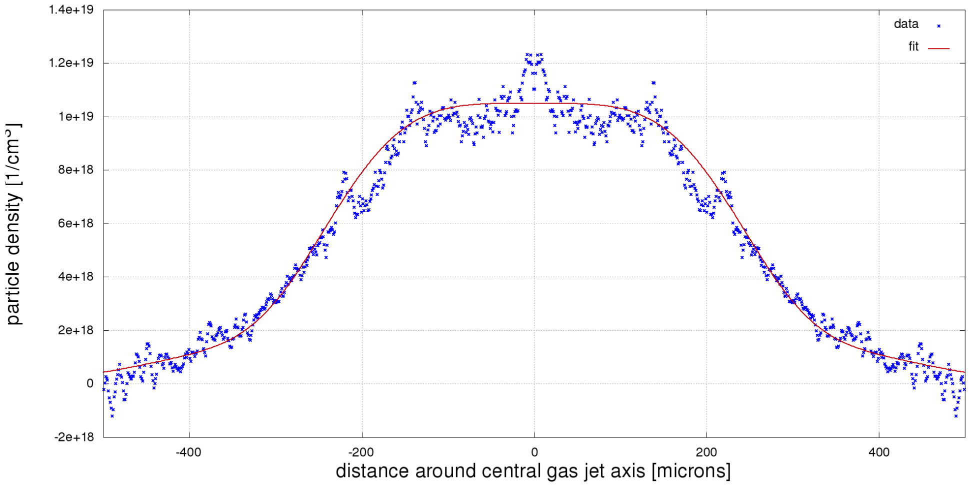

Figure 6.19.: SuperGaussian fit function $f(x) + g(x)$ for the particle-density distribution at a height of 500 µm above the nozzle edge and for a pressure of $p = 25\,\mathrm{bar}$ ($d_{\mathrm{noz}} = 167\,\mu\mathrm{m}$).

6.2. Thomson parabola spectrometer (TP)

The detection of laser-accelerated charged particles is challenging due to high particle fluxes, *i.e.* high particle intensities ($\geq 10^6\,\mathrm{cm}^{-2}$), together with small time scales given by the laser-target interaction time. The PHELIX or the Arcturus laser can provide pulse durations of a few ps or a few tens of fs, respectively. Ion fluxes of up to $10^{11-12}\,\mathrm{fs}^{-1}$ being generated in the laser-target interaction point are an usual order of magnitude. The divergence, *i.e.* the emission angles of laser-accelerated particles are large. Another important issue is the reproducibility of the achieved laser-generated ion pulses: shot to shot fluctuations in the ion signals are common. Furthermore, the laser-generated background signal in general, regarding huge EMP (depending on the laser pulse energy as well as on the attached plasma target), X-ray (primary from the interaction as well as secondaries from the vacuum chamber materials), and electron signals make it nearly impossible to setup conventional unshielded electronic ion-detection systems without endangering the hardware [Mea04, Sto06].

Detection systems therefore have to resolve ultra-fast laser-induced ion pulses in order to obtain ion-energy spectra depending on the laser and target parameters without being "blinded" by the isochronic radiation background. Hence, non-electronic ion detectors *e.g.* in combination with electromagnetic energy filters, like a Thomson parabola spectrometer, are reliable ion diagnostics tools in the field of laser-plasma acceleration.

6.2.1. TP design

A Thomson parabola spectrometer (TP) is a device to filter charged particles with regard to their kinetic energy as well as their specific charge-to-mass ratio $^q/_m$. It was invented by Sir J. J. Thomson in 1911 [Tho11]. Incoming particles enter the TP through a pinhole of proper size. The pinhole diameter has to be chosen according to the desired energy resolution as well as to the number of initial particles being accelerated in a certain solid angle. Inside the TP, a magnetic and an electric field are aligned (anti-)parallel. Hence, a charged particle propagating through these fields experiences two superposing forces which act perpendicular to each other: the particle is deflected both horizontally and vertically. The trajectory for a certain particle is dependent on the particle's energy. Since laser-accelerated particle bunches (in general) are not monoenergetic and often have a broad energy spread, the projection of all particle trajectories on a detector plane perpendicular to the initial propagation direction inside the TP is a $^q/_m$-specific parabolic curve, the so-called *Thomson parabola.* To be more precise: the direction in which a particle is deflected in electric or magnetic fields depends on its charge, and therefore, for a specific $\pm^q/_m$-ratio only the particular parabolic branch[1] will be given (and not the whole parabola). However, *(Thomson) parabola* is the historically evolved term.

The easiest way for setting up a TP, is to mount a dipole magnet (*e.g.* two permanent magnets with a yoke) and two parallel capacitor plates back-to-back behind the entrance pinhole. With such a setup, incoming particles will be deflected upwards, *e.g.*, by a

---

[1] note: in German, the term *Parabelast* describes only one part of the parabola with regard to the symmetry axis (an explicit translation in English could not be found).

horizontally aligned magnetic field and subsequently sidewise by the (anti-)parallel aligned electric field of the capacitor, respectively: with this basic setup, both spatial deflections are separated from each other. A disadvantage of such a layout can be seen in the amount of space which is used for each field component. With increasing distance between the magnetic and the electric fields, the particle beam expands more and more. Thus, due to the geometry of the yoke and the capacitor plates, slower particles will be clipped and more signal in the lower energy range is lost (slow particles are deflected more than the fast ones). Indeed, if only one particle species has to be investigated, the high voltage (HV) for building up the electric field can be reduced. Now, the particle parabola will be widened. But, in case that several ion species with varying energies have to be investigated simultaneously, it can occur that some ions are completely clipped or that single particle parabolas get so close to each other that they merge. Therefore, it can be advantageous to set the TP as compact as possible in order to use all space to full capacity.

Within the PHELIX experiment, a modified TP was used. This TP is based on a novel TP design presented in [Ban06, Car10] [2]. In contrast to the conventional concept, a wedge-shaped capacitor replaces the (commonly used) parallel aligned electric plates. By applying HV to the modified capacitor, a gradient electric field is built up which results in an increased particle deflection. Furthermore, for the sake of a compact design, the wedge-shaped capacitor is inserted into the magnetic field. Figure 6.20 illustrates the modified TP: in (a), a 3D model of the PHELIX TP can be regarded [Aur15], while in (b), a schematic of the modified TP is given.

TP fields The magnetic-deflection field is built up by two NdFeB permanent magnets (quadratic cross-section area with a feed size of $l_\mathrm{B} = 50\,\mathrm{mm}$) with a pole separation of $s_\mathrm{B} = 20\,\mathrm{mm}$. Each magnet has a remanescence of about 1.1 T. An iron yoke (length of $l_\mathrm{Y} = 70\,\mathrm{mm}$) around the magnets entails a return path for magnetic flux lines so that fringe fields at the entrance/exit of the dipole magnet are reduced. In the center of the magnetic field, a peak field strength of $B_z^\mathrm{max} = 0.6\,\mathrm{T}$ is given. The electric gradient field is built up by applying HV between the capacitor electrodes (length of $l_\mathrm{E} = 200\,\mathrm{mm}$, height of $h_\mathrm{E} = 75\,\mathrm{mm}$, thickness of $t_\mathrm{E} = 2\,\mathrm{mm}$). At the entrance an inter-electrode separation gap of $s_\mathrm{min} = 2.3\,\mathrm{mm}$ is given. This separation increases to a distance of $s_\mathrm{max} = 22.5\,\mathrm{mm}$ at the end of the capacitor which leads to an opening angle of $\sin\theta_\mathrm{E} = (s_\mathrm{max} - s_\mathrm{min})\, l_\mathrm{E}^{-1} \Leftrightarrow \theta_\mathrm{E} \approx 5.8^\circ$ between the electric field plates. In a distance of l_off behind the rear side of the capacitor plates (drift region), detectors can be placed to record the desired Thomson parabolas. The geometrical parameters are summarized in Tab. 6.1.

6.2.2. Ion deflection

In order to describe the equation of motion of charged particles inside the TP, a coordinate system has to be defined (*cf.* Fig. 6.21). Assume z_tp to be the initial propagation direction

---

[2] note: the novel TP concept was developed at the *Central Laser Facility (CLF)* at *RAL, STFC*, UK

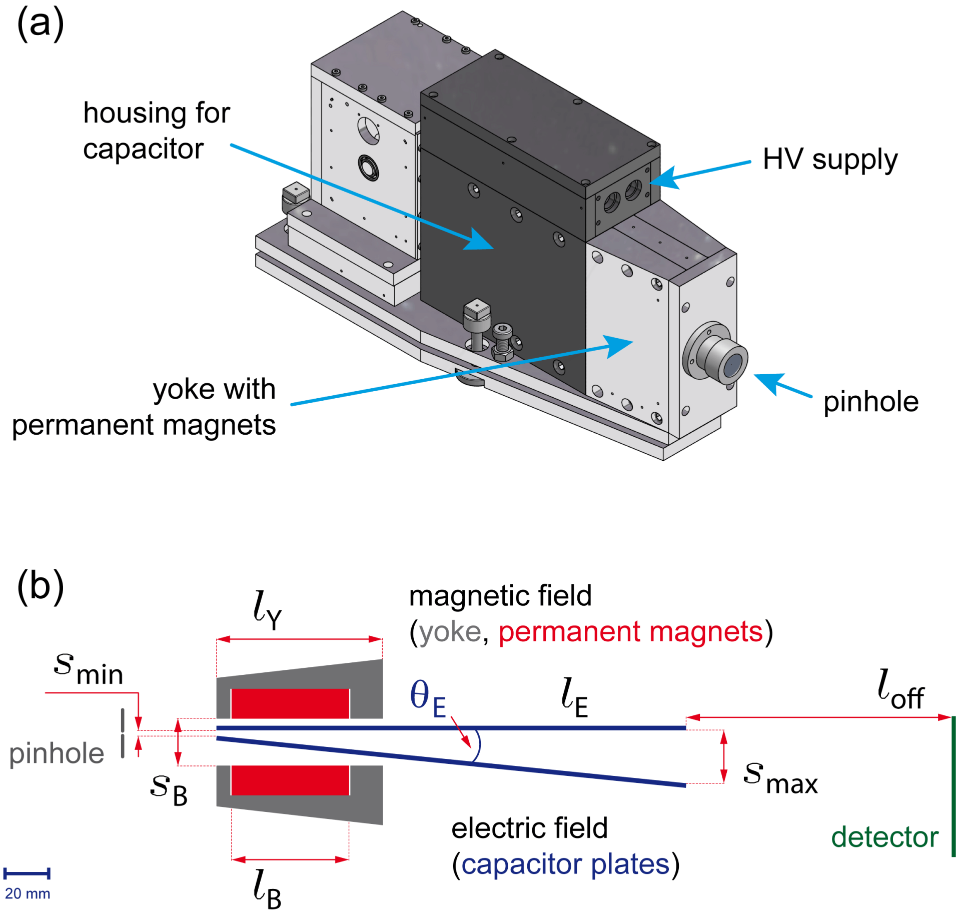

Figure 6.20.: PHELIX TP: (a) 3D model [Aur15], (b) schematic of the modified TP.

electric field		
capacitor-plate length	l_E [mm]	200
capacitor-plate height	h_E [mm]	75
capacitor-plate thickness	t_E [mm]	2
min. electrode gap	s_{min} [mm]	2.3
max. electrode gap	s_{max} [mm]	22.5
opening angle	θ_E	5.8°
magnetic field		
yoke length	l_Y [mm]	70
yoke height	h_Y [mm]	124
magnet length	l_B [mm]	50
yoke gap	s_B [mm]	20

Table 6.1.: General parameters of the PHELIX TP

of incoming particles (in this case: ions) of velocity $\boldsymbol{v} = v_0\, \boldsymbol{e}_z$. Then, x_{tp} is the direction in which positively charged ions are deflected horizontally, and y_{tp} is the one in which they are deflected vertically. The origin of the coordinate system is referred to the pinhole center.

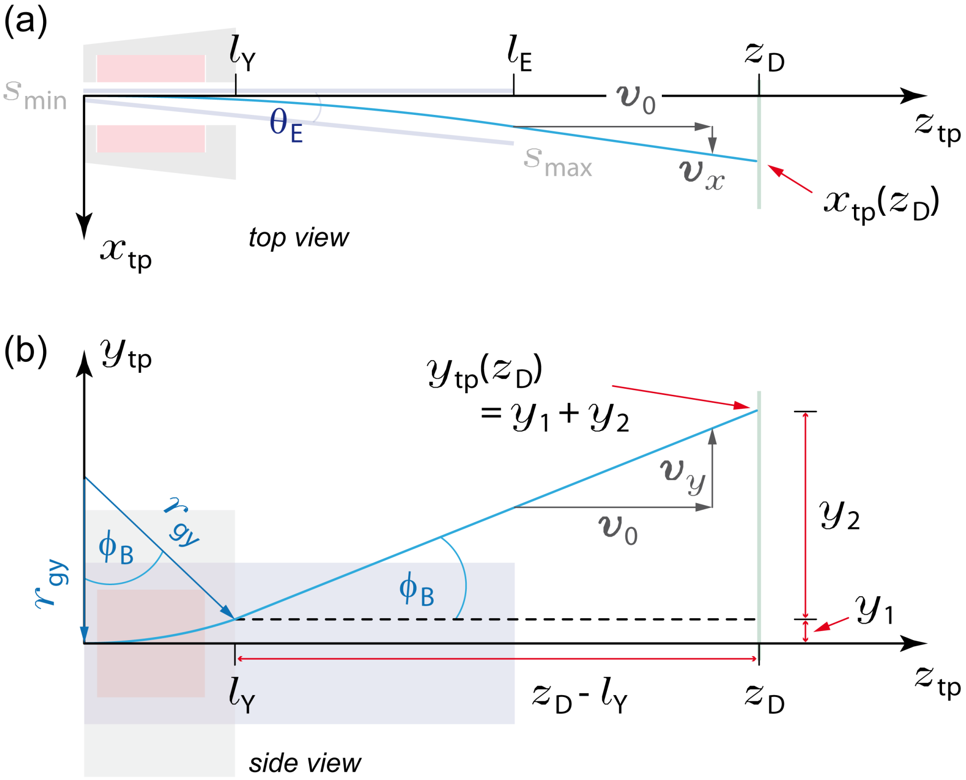

Figure 6.21.: Coordinate system for the PHELIX TP: (a) top view (x_{tp}-z_{tp}), (b) side view (y_{tp}-z_{tp}).

The electric-field deflection can be deduced from Newton's second law. The equation of motion for charged particles (mass m, charge $q = Ze$) within the TP is given by: (I) $\ddot{x}_{\text{tp}} = {}^{q}\!/_{m}\, E(z_{\text{tp}})$, (II) $\ddot{y}_{\text{tp}} = {}^{q}\!/_{m}\, v_0\, B$, and (III) $z_{\text{tp}} = v_0 t$. Assume that the initial conditions at $t = 0$ are set to: $\{x_{\text{tp}}, \dot{x}_{\text{tp}}, \ddot{x}_{\text{tp}}, y_{\text{tp}}, \dot{y}_{\text{tp}}, \ddot{y}_{\text{tp}}\} = 0$, $\dot{z}_{\text{tp}} = v_0$, and $\ddot{z}_{\text{tp}} = 0$.

Regarding (I), $E(z_{\text{tp}})$ is the gradient electric field along the z_{tp}-direction which arises after applying HV of, *e.g.*, $U_{\text{E}} = 3\,\text{kV}$ between the capacitor plates. The electric field can be approximated by $E(z_{\text{tp}}) = {}^{U_{\text{E}}}\!/_{s(z_{\text{tp}})}$, where $s(z_{\text{tp}})$ is the z_{tp}-dependent capacitor-plate separation $s(z_{\text{tp}}) = s_{\text{min}} + z_{\text{tp}}\, \sin\theta_{\text{E}}$. Temporal integration of (I) yields

$$x_{\mathrm{tp}}(z_{\mathrm{tp}}) = \frac{q}{m}\,\frac{U_{\mathrm{E}}}{v_0^2\,\sin\theta_{\mathrm{E}}} \times \left[z_{\mathrm{tp}}\,\ln\left(1 + \frac{\sin\theta_{\mathrm{E}}}{s_{\mathrm{min}}}\,z_{\mathrm{tp}}\right) + \right.$$
$$\left. - z_{\mathrm{tp}} + \frac{s_{\mathrm{min}}}{\sin\theta_{\mathrm{E}}}\,\ln\left(1 + \frac{\sin\theta_{\mathrm{E}}}{s_{\mathrm{min}}}\,z_{\mathrm{tp}}\right) \right]. \tag{6.14}$$

After having left the electric field at $z_{\mathrm{tp}} = l_{\mathrm{E}}$, the particle propagates uniformly linearly in the (x_{tp}-z_{tp})-plane and hits on the detector plane at $x_{\mathrm{tp}}(z_{\mathrm{D}})$ (here, fringe fields are negligible). The coordinate on the detector plane is given by (*cf.* also [Ban06, Mor11])[3]

$$x^*(z_{\mathrm{D}}) = \frac{q}{m}\,\frac{U_{\mathrm{E}}}{v_0^2\,\sin\theta_{\mathrm{E}}} \times$$
$$\times \left[\left[z^*\ln\left(1 + \frac{\sin\theta_{\mathrm{E}}}{s_{\mathrm{min}}} z^*\right) - z^* + \frac{s_{\mathrm{min}}}{\sin\theta_{\mathrm{E}}}\ln\left(1 + \frac{\sin\theta_{\mathrm{E}}}{s_{\mathrm{min}}} z^*\right)\right] + \right. \tag{6.15}$$
$$\left. + (z_{\mathrm{D}} - z^*)\,{}^{\mathrm{d}}\!/_{\mathrm{d}z^*}\left[z^*\ln\left(1 + \frac{\sin\theta_{\mathrm{E}}}{s_{\mathrm{min}}} z^*\right) - z^* + \frac{s_{\mathrm{min}}}{\sin\theta_{\mathrm{E}}}\ln\left(1 + \frac{\sin\theta_{\mathrm{E}}}{s_{\mathrm{min}}} z^*\right)\right]\right]_{|z^* = l_{\mathrm{E}}}$$

Due to the presence of a magnetic field B, a non-relativistic ion (mass m, charge $q = Ze$) is forced on a circular orbit with gyroradius $r_{\mathrm{gy}} = {}^{mv_0}\!/_{qB}$ (*cf.* Fig. 6.21 (b)). If the magnetic field is bordered (fringe fields outside the magnets are assumed to be negligible), the ion exits the field tangentially to its orbit and propagates with constant velocity to the detector (positioned at z_{D}). The angle of magnetic deflection ϕ_{B} can be calculated by $\sin\phi_{\mathrm{B}} = {}^{l_{\mathrm{Y}}}\!/_{r_{\mathrm{gy}}}$. Along the y_{tp}-direction, the equation of motion can be deduced by considering some geometrical relations. The total displacement on the detector plane due to the magnetic-force component is given by $y_{\mathrm{tp}}(z_{\mathrm{D}}) = y_1 + y_2$. The vertical displacement y_1 at the exit point of the magnetic field can be calculated by $\cos\phi_{\mathrm{B}} = (r_{\mathrm{gy}} - y_1)\,r_{\mathrm{gy}}^{-1} \Leftrightarrow y_1 = r_{\mathrm{gy}}\,(1 - \cos\phi_{\mathrm{B}})$. The second displacement y_2 after the uniform linear motion in the (y_{tp}-z_{tp})-plane can be deduced by $\tan\phi_{\mathrm{B}} = y_2\,(z_{\mathrm{D}} - l_{\mathrm{Y}})^{-1} \Leftrightarrow y_2 = \tan\phi_{\mathrm{B}}\,(z_{\mathrm{D}} - l_{\mathrm{Y}})$. As stated above, the angle of magnetic displacement is given by $\phi_{\mathrm{B}} = \arcsin {}^{l_{\mathrm{Y}}}\!/_{r_{\mathrm{gy}}}$. Using trigonometric identities, the magnetic displacement in y_{tp} can be calculated to [Mor11]:

---

[3] note: in order to shorten Eq. (6.15) a little bit, $\{x, z\}_{\mathrm{tp}}$ is abbreviated with $\{x, z\}^*$

$$
\begin{aligned}
y_{\mathrm{tp}}(z_{\mathrm{D}}) &= y_1 + y_2 \\
&= r_{\mathrm{gy}}\,\left(1 - \cos\phi_{\mathrm{B}}\right) + \tan\phi_{\mathrm{B}}\,\left(z_{\mathrm{D}} - l_{\mathrm{Y}}\right) \\
&= r_{\mathrm{gy}}\left(1 - \sqrt{1 - \left(\frac{l_{\mathrm{Y}}}{r_{\mathrm{gy}}}\right)^2}\right) + \frac{z_{\mathrm{D}} - l_{\mathrm{Y}}}{\sqrt{\left(\frac{r_{\mathrm{gy}}}{l_{\mathrm{Y}}}\right)^2 - 1}}\,, \qquad (6.16) \\
&\text{with} \quad \cos t = \frac{\sin t}{\tan t} \\
&\text{and} \quad \tan\left(\arcsin u\right) = \frac{u}{\sqrt{1-u^2}}\,.
\end{aligned}
$$

Next to this geometrical approach, the displacement in y_{tp} can also be deduced by integrating the equation of motion (II) $\ddot{y}_{\mathrm{tp}} = {}^{q}\!/_{m}\, v_0\, B$ on p. 87:

$$
\begin{aligned}
y_{\mathrm{tp}}(z_{\mathrm{D}}) &= y_1 + y_2 \\
&= \frac{1}{2}\,\underbrace{\frac{q}{m}\,\frac{B}{v_0}}_{r_{\mathrm{gy}}}\left[z_{\mathrm{tp}}^2 + \left(z_{\mathrm{D}} - z_{\mathrm{tp}}\right)\,{}^{\mathrm{d}}\!/_{\mathrm{d}z_{\mathrm{tp}}}\,\left(z_{\mathrm{tp}}^2\right)\right]_{|z_{\mathrm{tp}} = l_{\mathrm{Y}}} \qquad (6.17) \\
&= \frac{\varsigma}{v_0}\,,\ \ \varsigma = \mathrm{const}\,.
\end{aligned}
$$

Substituting the intrinsic ion velocity v_0 in Eq. (6.17) with the energy $\mathcal{E}$, *i.e.* $v_0 = \sqrt{{}^{2\mathcal{E}}\!/_{m}}$, yields the energy-displacement dependency $\mathcal{E} \propto y_{\mathrm{tp}}^{-2}$ which, later on, can be used for determining the energy resolution of the TP:

$$
\mathcal{E} = \frac{1}{2}\,m\varsigma^2 \times \frac{1}{y_{\mathrm{tp}}^2} \qquad (6.18)
$$

Since due to reasons of a compact TP design both capacitor plates are inserted into the dipole magnet, incoming particles do not enter the magnetic field on the plane of symmetry: the above mentioned approximation of negligible fringe fields cannot be made and the deduced equations for the ion's deflection in $\{x, y\}_{\mathrm{tp}}$ are not accurate enough. Therefore, ion trajectories for various energies had to be simulated with *CST (Computer Simulation Technology) Particle Studio* [cst].

6.2.3. Simulation of the PHELIX TP

With *CST Particle Studio* electromagnetic fields and charged particle dynamics can be modeled. Electromagnetic components can be defined according to the given hardware used in the experiments. For this purpose, a simulation box with vacuum as background material was defined in x, y, z. A mesh with a smallest mesh step of 0.05 led to approximately 8×10^5 meshcells in the simulated volume. With the *E-&M-Static Solver*, the electromagnetic fields are calculated for a given TP geometry, and the *Particle Tracking* tool allows to simulate charged particle trajectories within the simulated fields. For particle tracking, the following parameters were set: maximum number of timesteps performed by the tracking algorithm of "3×10^6", spatial sampling rate of the trajectories of minimal "5 pushes per cell", temporal sampling rate of calculated time steps of "10", particle sampling rate for the monitored particle tracking result of "1".

For the current simulations, an existing *.cst*-file [Sch15, Dep15] was modified regarding the simulated magnetic field, the simulated particles, as well as the simulation mesh. In *CST*, the TP was defined according to the technical drawings for the given PHELIX TP [Aur15]. Figure 6.22 illustrates a 3D model of the simulated TP. The angled electrodes are inserted in the magnetic field which is built up by two magnets being placed in a yoke. A HV of 3 kV was applied to the capacitor plates (each plate was supplied with ±1.5 kV, respectively).

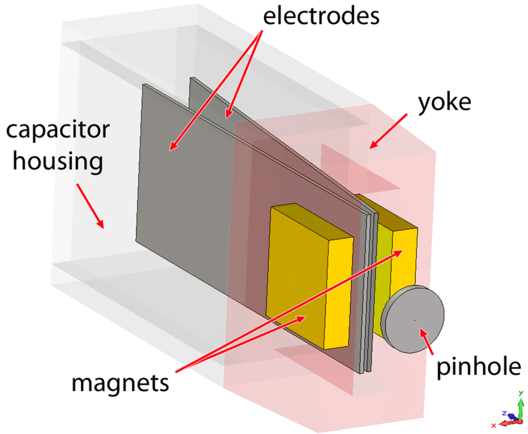

Figure 6.22.: *CST*-modeled PHELIX TP.

The resulting electric field E_x is plotted in Fig. 6.23 (a) and (b) in $^{\mathrm{V}}/_{\mathrm{m}}$. In (a), a 2D pseudo-color plot illustrates the electric field in the (y_{tp}-z_{tp})-plane in a distance of 1 mm from the parallel electrode (applied potential of +1.5 kV). Next to this in (b), a lineout of the electric field along the z_{tp}-axis, *i.e.* the pinhole axis, is given. The pinhole position as entrance into the TP as well as the borders of the positively charged capacitor plate are marked on the horizontal axis. Furthermore, a gray color patch highlights the position of the electric plate. A peak value of approximately $-1.25\ ^{\mathrm{MV}}/_{\mathrm{m}}$ is given at about 3.5 mm behind the front capacitor boundary. 24 mm inside the capacitor, this peak value is bisected to $-0.625\ ^{\mathrm{MV}}/_{\mathrm{m}}$, and in the center the electric field strength decreases to a value of $-0.240\ ^{\mathrm{MV}}/_{\mathrm{m}}$. Regarding fringe fields, it becomes obvious that the simulated electric field arises directly behind the pinhole position and reaches a value of about $1\ ^{\mathrm{MV}}/_{\mathrm{m}}$ at the left capacitor boundary. Right in front of the electrode end, a saltus in E_x is given. This behavior is not included in the above deduced equations. A *CST*-simulation considers not only ideally approximated field assumptions which makes the simulated outcome more realistic.

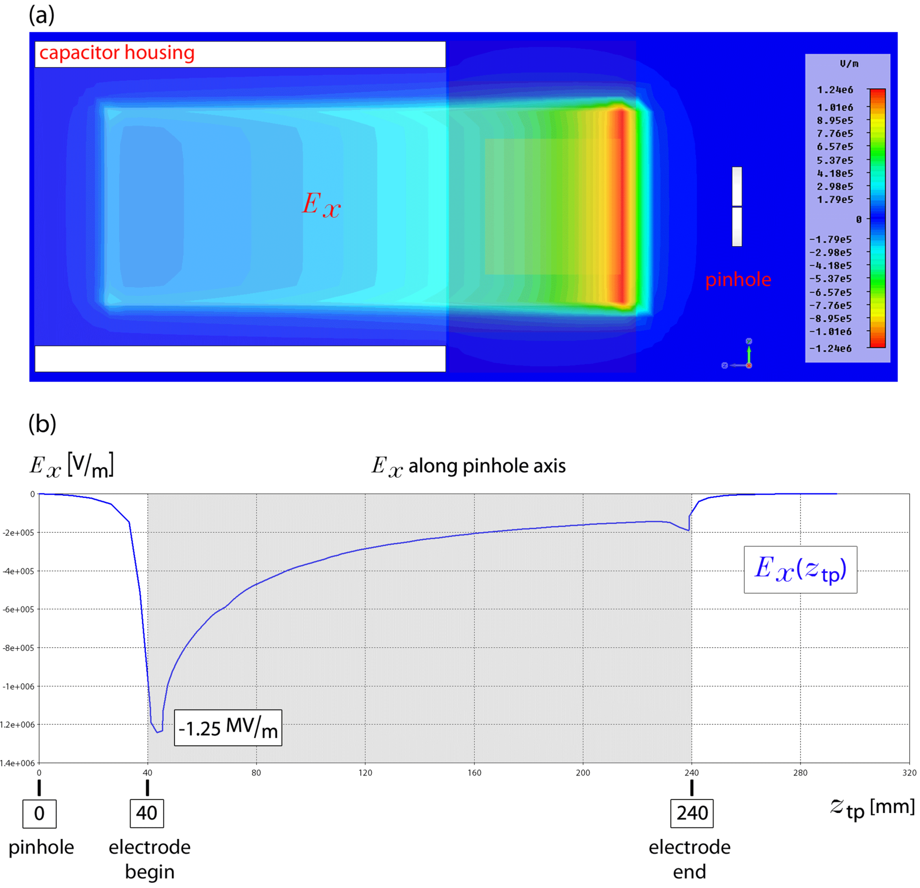

Figure 6.23.: *CST*-simulated electric field E_x: (a) 2D pseudo-color plot in the (y_{tp}-z_{tp})-plane, (b) lineout along the pinhole axis z_{tp}.

Figure 6.24 illustrates the *CST*-simulated magnetic field B_x in T. In (a), a 2D pseudo-color plot of B_x in the (y_{tp}-z_{tp})-plane is given. It can be regarded, that the magnetic field lines are oriented thus, that within the magnets they are pointing out of the image plane (positive values, red-yellow color grading), while within the yoke the magnetic field lines are returning and pointing into the image plane (negative values, pale- to dark-blue color grading). The B_x lineout in (b) illustrates the magnetic field along the z_{tp}-direction. The yoke as well as the magnet regions are symbolized by gray color patches. The particular borders are also marked on the horizontal axis. It becomes obvious, that the magnetic field marginally arises at a distance of 25 mm behind the pinhole. Due to the yoke, fringe fields could be reduced. In a depth of the magnet's center, the field strength becomes maximal: 0.58 T. The FWHM is given with 43.8 mm, starting at 3.5 mm behind the left magnet boundary (or about 9 mm behind the left yoke boundary) and ending 2.7 mm in front of the right magnet boundary.

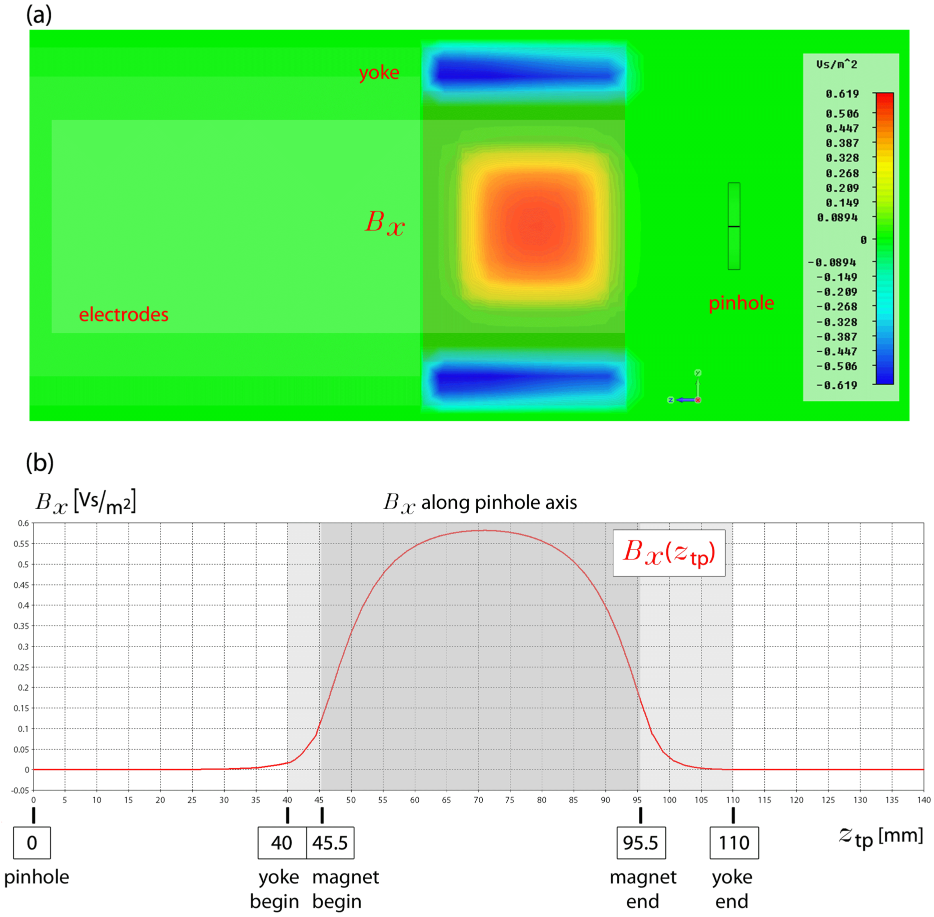

Figure 6.24.: *CST*-simulated magnetic field B_x: (a) 2D pseudo-color plot in the (y_{tp}-z_{tp})-plane, (b) lineout along the pinhole axis z_{tp}.

6.2.4. Simulated ion trajectories inside the TP

Ion trajectories were simulated for both ^{3,4}He ions. For each species, also both ionization degrees were implemented. The ion mass and charge had to be defined for every ion species. Furthermore, the kinetic energy could be set in eV with an energy spread of up to 200 %. Predefined particle monitors recorded the $\{x, y\}_{\text{tp}}$-displacement as well as the corresponding ion energies. Also the ion trajectories within the TP could be visualized. From the simulation output, energy-displacement dependencies could be extracted. They are important for the analysis of the experimental TP data.

In order to spare much calculation time, the particle source was placed directly in front of pinhole. A memory-consuming simulation (on a PC with a core i-7 CPU, 8 cores, 12 GB memory) with a source-pinhole distance comparable to the one from the experiments ($400 - 500$ mm) lasted 11 h. Most of the calculation time was spent for the ion propagation from their source to the TP entrance and the size of the simulation output became huge (~ 30 GB). Above all, the visualization of the ion trajectories was not possible due to memory issues.

Figure 6.25 exemplifies *CST*-simulated $^4\mathrm{He}^{2+}$ and $^4\mathrm{He}^{1+}$ ion trajectories for an initial ion energy of 1.5 MeV and 200 % energy spread. The ions enter the TP through a 200 µm pinhole. Depending on their energy as well as their specific q/m-ratio, they are deflected with varying strength due to the electric and the magnetic fields. The energy dispersion is symbolized with the 3D pseudo-color plot. It can be regarded that a few low-energy ions are trapped within the yoke since they are deflected too strong to escape the fields. The amount of ions which are able to leave the fields are detected with particle monitors behind the TP. Figures 6.26 to 6.28 illustrate the Thomson parabolas for both helium ions as well as their energy-x_{tp} and -y_{tp} dependencies. The particle monitors were placed in a distance of 354.7 mm from the pinhole (the same distance as in the PHELIX experiments).

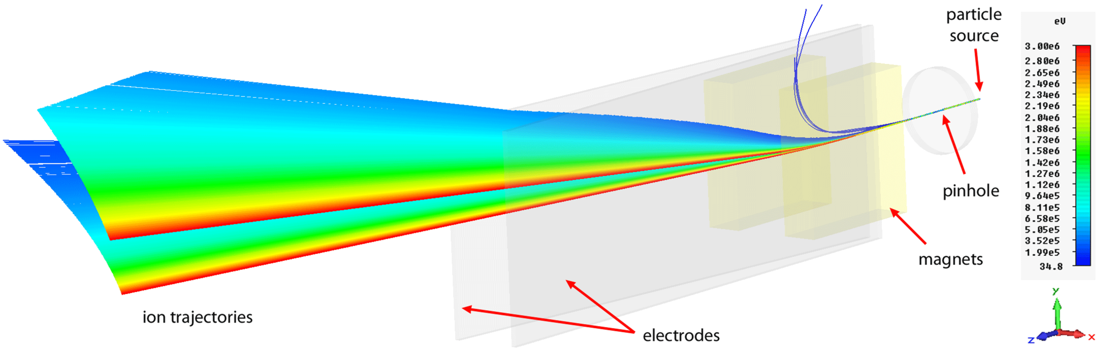

Figure 6.25.: *CST*-simulated $^4\mathrm{He}^{1+,2+}$ ion trajectories. The initial energy was set to 1.5 MeV with an energy spread of 200 %.

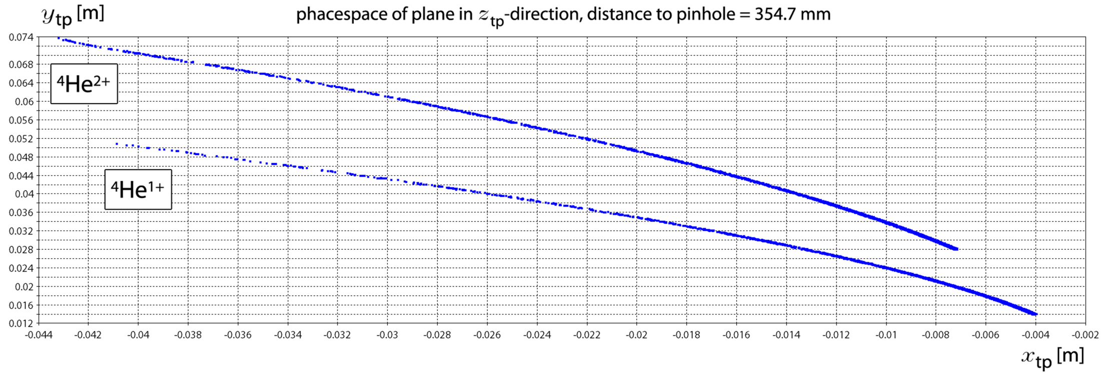

Figure 6.26.: *CST*-simulated $^4He^{1+,2+}$ Thomson parabola for. The initial energy was set to 1.5 MeV with an energy spread of 200 %.

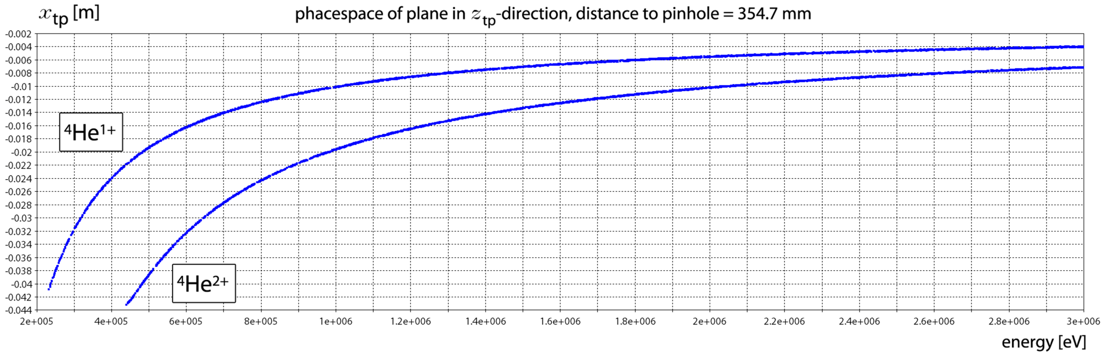

Figure 6.27.: *CST*-simulated energy-x_{tp} plot for $^4He^{1+,2+}$ ions.

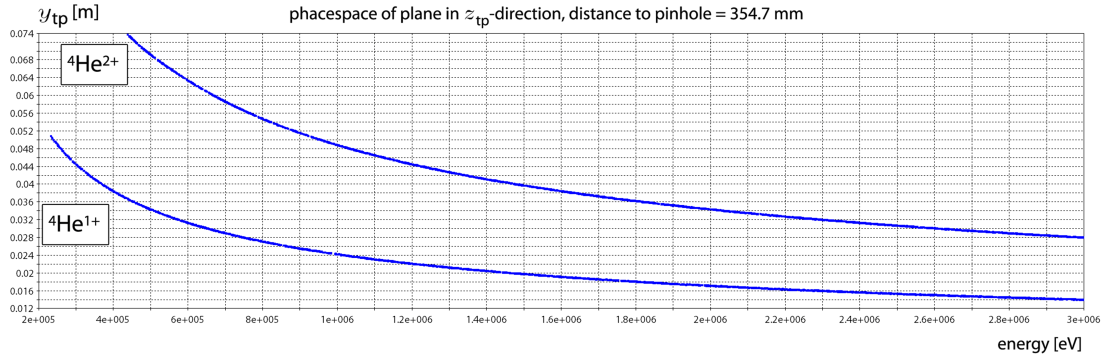

Figure 6.28.: *CST*-simulated energy-y_{tp} plot for $^4He^{1+,2+}$ ions.

6.2.5. Energy resolution

As it is indicated in Fig. 6.26, the electric-field deflection (in x_{tp}-direction) is smaller than the magnetic one. In actual fact, the horizontal deflection mainly serves to distinguish between different q/m-ratios: without an applied electric field, all ions would be deflected in y_{tp} only, and thus, *only* one straight trace would be given on the detector plane. A separate *CST*-simulation with single monoenergetic $^4\mathrm{He}^{2+}$ ions with and without electric field showed that the achieved height on the detector varied about a few tens of microns. Example: for $^4\mathrm{He}^{2+}$ ions with an energy of 1.5 MeV the reproducible y_{tp}-deflection with attached electric field was 39.6520 mm, while in the other case with only the magnetic deflection it was 39.6620 mm. Thus, the above mentioned energy error is only valid if the ion energies are extracted manually out of the the experimental raw data. But considering that this difference of 10 µm would cause an energy deviation of about ±2 keV, *i.e.* a neglectable value for TP-data evaluation, it is adequate to take only the magnetic displacement into account. Nevertheless, the *CST*-simulated output always considers the electric-deflection component.

As shown in Eq. (6.18) on p. 89, the ion energy is proportional to the inverse squared magnetic deflection. From the simulated data, *e.g.* in Fig. 6.28, an energy-fit function $\mathcal{E}(y_{\mathrm{tp}}) \propto y_{\mathrm{tp}}^{-2}$ can be extracted. In case of $^4\mathrm{He}^{2+}$ ions and an energy range of $0.4\,\mathrm{MeV} \leq \mathcal{E} \leq 3\,\mathrm{MeV}$ this fit function is given by:

$$\begin{aligned}\mathcal{E}(y_{\mathrm{tp}})_{|^4\mathrm{He}^{2+},\mathrm{TP-90}} &= \frac{a}{y_{\mathrm{tp}}^2} + b \\ &= \frac{2.317}{y_{\mathrm{tp}}^2}\,\mathrm{keV\,m^2} + 24.57\,\mathrm{keV}\end{aligned} \tag{6.19}$$

Another issue to be considered is the broadening in width δ_{tp} of the Thomson parabolas which induces an ambiguity in energy, *i.e.* in total deflection. This broadening is directly caused by the experimental setup. Between the laser-plasma interaction region and the pinhole of diameter d_{ap} a distance of l_{pre} is given, and from here, in a distance of l_{tp}, the ion detector is placed. The ion "imaging" through the pinhole influences the TP resolution. The Thomson parabola width can be calculated by $\delta_{\mathrm{tp}} = d_{\mathrm{ap}}\,(l_{\mathrm{pre}} + l_{\mathrm{tp}})\,l_{\mathrm{pre}}^{-1}$ [Sch85, Bol14] [4]. Now, the intrinsic spectrometer resolution, *i.e.* the normalized uncertainty in energy $\Delta\mathcal{E}/\mathcal{E}$, is given by [Jun11]

$$\begin{aligned}\left|\frac{\Delta\mathcal{E}}{\mathcal{E}}\right| &= \frac{\mathrm{d}\mathcal{E}}{\mathrm{d}y_{\mathrm{tp}}}\,\delta_{\mathrm{tp}} \times \frac{1}{\mathcal{E}} \\ &= \frac{2\delta_{\mathrm{tp}}}{y_{\mathrm{tp}}} \propto \sqrt{\mathcal{E}}\,.\end{aligned} \tag{6.20}$$

---

[4] example: in the PHELIX experiment, a 200 µm pinhole was attached in a distance of $l_{\mathrm{pre}} = 430.0\,\mathrm{mm}$ from the TCC. The detector was placed in a distance of $l_{\mathrm{tp}} = 354.7\,\mathrm{mm}$. This leads to a broadening of $\delta_{\mathrm{tp}} \approx 365\,\mu\mathrm{m}$.

Figure 6.29 illustrates the *CST*-simulated $^{\Delta\mathcal{E}}/_{\mathcal{E}}$-energy dependency exemplified for both $^4\text{He}^{1+}$ (red curve) and $^4\text{He}^{2+}$ ions (blue curve), respectively ($\delta_{\text{tp}} = 365\,\mu\text{m}$). With the help of such a plot, the experimentally obtained ion energies directly can be related to their normalized energy uncertainty.

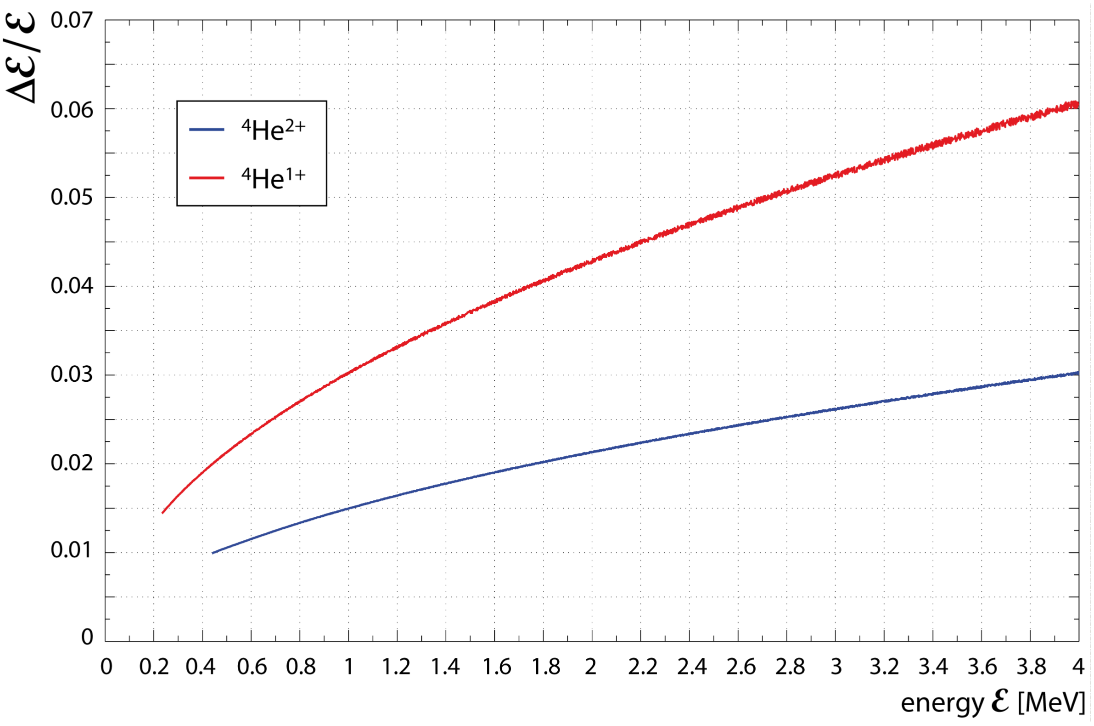

Figure 6.29.: *CST*-simulated $^{\Delta\mathcal{E}}/_{\mathcal{E}}$-energy dependency for $^4\text{He}^{1+,2+}$ ions (red and blue curve) and a Thomson parabola broadening of $\delta_{\text{tp}} = 365\,\mu\text{m}$.

6.2.6. Non-electronic ion detectors

As it is described in the previous Secs., ions are forced on specific Thomson parabolas in the spectrometer according to their $^q/_m$-ratio as well as their initial energies. In order to record helium ion Thomson parabolas within the PHELIX experiments, both *image plates* (IP) and *CR-39 solid-state nuclear track detectors* were applied. Another well-proven detector film in the field of laser-plasma physics is the radiochromic film (RCF). In the following, these non-electronic particle detectors are described in detail.

CR-39 solid-state nuclear track detectors

CR-39 is a poly-allyl diglycol carbonate (PADC, $C_{12}H_{18}O_7$, $\rho_{\text{CR}-39} = 1.3\,^{\text{g}}/_{\text{cm}^3}$) which can serve as a solid-state nuclear track detector (SSNTD). In 1940, it was originally developed by the *Columbia Southern Chemical Company* in order to enhance military technology with modern resin science during World War II. The 39th formula showed the desired properties and the new product therefore was named *Columbia Resin #39* with the well-known abbreviation CR-39. In everyday life, CR-39 often is used as spectacle-lens.

The advantage of using CR-39 as quantitative ion detector in laser-acceleration experiments is its insensitivity for electron and laser light signals and even huge EMPs cannot disturb particle detection. With CR-39 plates, single ion events with ion energies of $\geq 100\,\mathrm{keV}$ per nucleon can be recorded. In the framework of this thesis, *TASTRAK* CR-39 detector plates from *Track Analysis Systems Ltd (TASL)* [Trac] were used in order to detect protons and α-particles.

When CR-39 is irradiated with energetic ions (incidence angle δ on the polymer surface), each massive particle damages the polymer while propagating through the material. The penetration depth $\boldsymbol{R}$ of the energetic particle depends on the incident initial particle energy $\mathcal{E}_i$ and the stopping power ${}^{\mathrm{d}\mathcal{E}}/_{\mathrm{d}x}$ of the CR-39 material.

A uniform explanation for the damage mechanism is not given. In [Fle65, Fle75] the *ion explosion spike mechanism* is explained. Here, the incident irradiation ionizes the material, the left-behind ions repulse which forms the damage in the polymer. In contrast to this explanation, [Hen71] describes the damage process by knock-off electrons which are generated by the incident particles. The restricted energy loss REL is given by a special case of the Bethe formula:

$$\mathrm{REL} = \left(\frac{\mathrm{d}\mathcal{E}}{\mathrm{d}x}\right)_{\mathcal{W} \leq \mathcal{W}_{\mathrm{cut}}} = \frac{Z^2 e^4\, n_{\mathrm{e}}}{4\pi\, \varepsilon_0^2\, m_0 c^2 \beta^2} \left(\ln \frac{2\, m_0 c^2 \beta^2\, \mathcal{W}_{\mathrm{cut}}}{\bar{\mathcal{U}}(1-\beta^2)} - 2\,\beta^2\right) , \tag{6.21}$$

with Ze as the incident particle's charge, m_0 as the rest mass, βc as the velocity of the incident particle, n_{e} as the electron density in units of a unit volume, $\bar{\mathcal{U}}$ as the average ionization energy of the material, and $\mathcal{W}_{\mathrm{cut}}$ as the cut-off energy, *i.e.* the maximal transferred energy from the incident particle to the electrons ($\mathcal{W}_{\mathrm{cut}} \sim \mathcal{O}(100\,\mathrm{eV})$ [Yad95]).

The material damage causes a change of the CR-39's physical properties, namely its density, molecular weight, as well as its solubility [Vir01]. Indeed, directly after irradiating a CR-39 detector plate with energetic ions, the damage within the material is not visible. It can be visualized by, *e.g.*, chemical etching of the irradiated CR-39 detector plates. When being etched in a high-molarity sodium hydroxide solution (NaOH, aqu.) at a certain temperature T, the surface of the CR-39 detector plates, *i.e.* the bulk plastic, is etched at a characteristic bulk etching rate $\boldsymbol{v}_{\mathrm{b}} = \mathrm{const}$ (typically a few µm per h). Along the ion trajectory axis the etching rate $\boldsymbol{v}_{\mathrm{t}}$ is higher than in the surrounding non-irradiated regions. Therefore, single etch tracks (*e.g.* cone-shaped etch pits with an opening angle of θ) are formed with increasing maintenance time in the NaOH solution. $\boldsymbol{v}_{\mathrm{t}}$ is called the characteristic track etching rate which is proportional to the amount of damage in the medium. Therefore, it is dependent on the restricted energy loss ${}^{\mathrm{d}\mathcal{E}}/_{\mathrm{d}x}$.

The relation between the characteristic etching rates determines the track registration efficiency f_{t} which can be calculated by:

$$f_\mathrm{t} = 1 - \frac{v_\mathrm{b}}{v_\mathrm{t}} = 1 - \sin(\theta_\mathrm{cr})\,, \tag{6.22}$$

with $\theta_\mathrm{cr} = \arcsin\left({}^{v_\mathrm{b}}/_{v_\mathrm{t}}\right)$ as the critical angle of the incident particle trajectory relative to the detector surface: θ_cr is the minimal incidence angle δ_min for which particle tracks can be etched and detected [Ran02]. Both etching rates $v_\mathrm{b,t}$ strongly depend on the temperature of the etchant and follow the Arrhenius equation:

$$v_\mathrm{b,t} = c_\mathrm{b,t} \times \exp\left(-\frac{\mathcal{E}_\mathrm{b,t}}{k_\mathrm{B}T}\right) \text{ [Ran02]}\,, \tag{6.23}$$

with $c_\mathrm{b,t}$ as constants, $\mathcal{E}_\mathrm{b,t}$ as the mean values of the specific activation energies of bulk and track etching given with $\mathcal{E}_\mathrm{b} = 0.939\,\mathrm{eV}$ and $\mathcal{E}_\mathrm{t} = 0.310\,\mathrm{eV}$ [Ran02], respectively, and T as the temperature of the NaOH solution.

Hence, also the track registration efficiency f_t depends on the temperature of the etchant: for a 6 N NaOH solution at 60 °C, f_t has a maximum value of 97.6 % and decreases toward higher temperatures. A temperature increase to 70 °C leads to a track registration efficiency of about 95 % [Ran02]. Furthermore, also an increase of the NaOH concentration reduces f_t.

As stated above, CR-39 SSNTD are not sensitive for γ photons and visible light. But it is important to notice, that an irradiation of CR-39 with gammas and light influences the ratio ${}^{v_\mathrm{b}}/_{v_\mathrm{t}}$. [Bla82] showed that additional gamma irradiation increases the bulk etching rate so that particle tracks recorded on CR-39 were etched out much faster. In the framework of this thesis, unshielded CR-39 were placed in different distances next to the laser-plasma interaction zone. After etching those irradiated CR-39, a color change from translucent to cloudy-white could be observed (*cf.* Sec. 7.2.2). Hence, for particle detection and identification the CR-39 were useless. Furthermore, the influence of UV, IR, and laser radiation on the characteristic etching rates were investigated by [AJ91, Kha95, Pra03]: while an exposure to UV and IR light leads to an increase of the etching rates, laser radiation resulted in hardening of the detector material surface, and thus, in decreasing track sizes.

But also the age of the CR-39 SSNTDs has an effect on its response to charged particles [Sin11]. It already drops within the first month after manufacture and with increasing age the achievable track diameters decrease more and more. This aging effect can be inhibited by storing the CR-39 below 0 °C.

Etch track development In Fig. 6.30 the etch track development along the incident particle's damage trail can be regarded [Hen71]. On the trajectory axis as well as within the penetration depth R the degree of damage in the polymer is maximal. With increasing distance from this axis, the damage decreases. Therefore, the track etching rate $\boldsymbol{v}_\mathrm{t}$ increases with the depth and becomes maximal in the region of the particle's Bragg peak.

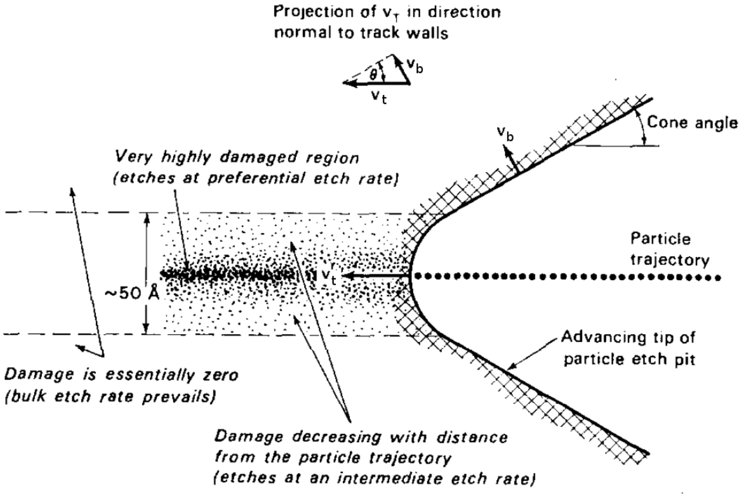

Figure 6.30.: Damage trail and etch track development [Hen71].

The whole etching and track formation process can be characterized by different stages which are illustrated in Fig. 6.31 (adapted from [Hen71]). At the beginning of the etching process (*initial stage* (A) at $t = t_0$), the surface of the CR-39 detector plate is even. It is called the *pre-etch surface*. In the *conical phase* (B) at $t = t_1$, the non-irradiated initial surface has been etched about a distance $|\boldsymbol{v}_\mathrm{b}| \times t_1$. Along the particle trajectory the characteristic track etching rate $\boldsymbol{v}_\mathrm{t} > \boldsymbol{v}_\mathrm{b}$ dominates. The pit depth can be calculated by $|\boldsymbol{v}_\mathrm{t}| \times t_1$. The projection of the track onto the CR-39 surface looks like a cone (*cf.* Figs. 6.31 *"top view"* and 6.32 *"right side"* [Trac]). Its axis and the particle trajectory coincide. The cone angle θ can be calculated by $\theta = \arcsin({}^{v_\mathrm{b}}/_{v_\mathrm{t}})$ (*cf.* Fig. 6.31: vector diagram including $\boldsymbol{v}_\mathrm{b,t}$). On the etched surface, the entrance into the track pit is an ellipse with the minor and major axes $M_\mathrm{min}(t_1)$ and $M_\mathrm{maj}(t_1)$, respectively. Both axes together with the length of the cone $X_t(t_1)$ serve as track parameters in order to characterize the incident particles. When at $t = t_2$ the track has been fully etched, the *transient stage* (C) is introduced. The particle penetration depth can be calculated by $|\boldsymbol{R}| = |\boldsymbol{v}_\mathrm{t}| \times t_2$. Since $\boldsymbol{v}_\mathrm{t}$ is dependent on the restricted energy loss, it has a maximal value in the region of the particle's Bragg peak. On the pit walls, etching continues with the bulk etching rate $\boldsymbol{v}_\mathrm{b}$ in all directions. After having passed the particle's Bragg peak depth at $t > t_2$, the track is etched out and $\boldsymbol{v}_\mathrm{t}$ decreases (*spherical stage* (D)). Since the bulk etching rate $\boldsymbol{v}_\mathrm{b}$ dominates in this stage, the track is still growing in diameter, but its depth decreases while its shape becomes more and more spherical (*cf.* Fig. 6.32 left side [Trac]). In the beginning of this stage, the originally pointed track vertex becomes more and more rounded. Finally, it becomes a sphere with a radius of $r = v_\mathrm{b}(t - t_2)$.

Figure 6.32 illustrates examples of α-particle tracks for different etch times [Trac]. The photographic picture is taken by a microscope scanner. The tracks on the right were developed after being etched in a 6.25 M NaOH solution at 95 °C for a maintenance time of 1 h. The characteristic cone-shaped structure can be regarded. With increasing

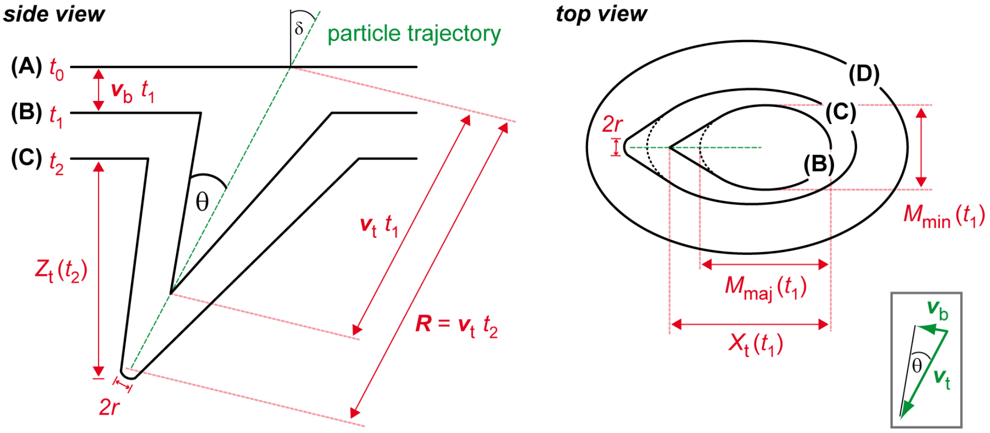

Figure 6.31.: Stages of etch track development (adapted from [Hen71]).

maintenance time the track structure will vanish and the track diameter grows. The track on the left is etched for 5 h.

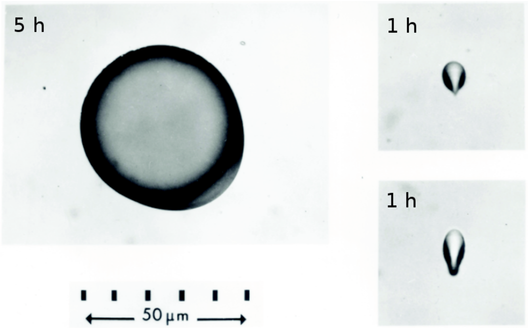

Figure 6.32.: Example for α-particle etch tracks for different etch times [Trac].

Image plates (IP)

Image or *imaging plates* (IPs) are reusable non-electronic detector films for ionizing radiation [Row02, Mea08, Pat08, Leb11]. In the 1980s, the commercial use of IPs was initiated by the *Fujifilm Holdings Corporation (Fujifilm)*.

In the framework of this thesis, *Agfa MD4.0 Image Plates* (without protection layer) were used in order to detect laser-accelerated helium ions. Their active layer with a thickness of 210 µm is coated on a PET layer (coating weight of 75 $^{\mathrm{mg}}/_{\mathrm{cm}^2}$). Since laser-accelerated helium ions had to be detected, it was important to use IPs without any protective layer as top-coat. Due to the small range of helium ions in various materials, much of the signal (or in the worst case even the whole signal) would be blocked. For *Agfa MD4.0* the active layer consists of the photo-stimulable storage phosphor BaSrFBrI:Eu^{2+}. The phosphorescence utilizing storage phosphor chemical composition is $Ba_{0.924}Sr_{0.074}Eu_{0.002}F_{1.05}Br_{0.80}I_{0.15}$ ([Dep15]: email correspondence with *Agfa*). The dilute contamination with Eu^{2+} serves as an activator which determines the spectrum of emitted light [Row02].

The physical principle of this 2D detector film is photo-stimulated luminescence (PSL). If ionizing radiation like γ photons, laser light, or also laser-accelerated charged particle beams impinge on the IP, energy is deposited in the active layer. As a result, electrons from Eu^{2+} are excited into a metastable state where they stay trapped into lattice defects for a certain time [Pat08, Leb11]. Since these lattice defects are important, they are inserted into the storage phosphor on purpose. By illuminating the irradiated IPs with HeNe-laser light at 632.8 nm within an IP scanner (*e.g.* a *FLA-7000* by *FujiFilm&GE Healthcare* [GE]), the excited metastable states are stimulated, and thus, they decay. UV Eu^{2+} luminescence ($\lambda_{\mathrm{lum}} = 400\,\mathrm{nm}$), *i.e.* PSL, is emitted and processed with the attached scanner. The intensity of the emitted PSL is dependent on the dose of the incident ionizing radiation. In the scanning device, a photo-multiplier converts this light into an electronic signal which is digitized and stored in a 16 bit grayscale image. Now, a spatial distribution of gray scale values is given. In order to calculate the PSL out of the grayscales, the following Eq. by *FujiFilm* applies [Fuj]

$$\mathrm{PSL} = \left(\frac{s_{\mathrm{pix}}}{100\,\mu\mathrm{m}}\right)^2 \times \frac{4000}{S} \times 10^{L\left({QL}/{G} - 1/2\right)}\,, \tag{6.24}$$

where PSL is the quantified PSL value in linear scale, $s_{\mathrm{pix}} = 25\,\mu\mathrm{m}$ is the scanner resolution (*i.e.* the size of each pixel), $S = 10^4$ is the scanning sensitivity, $L = 5$ is the exposure latitude, G is the digitization-dependent gradation (in case of a 16 bit image, in total $2^{16} - 1 = 65535$ gray scale values are available), and QL is the quantum level input[5] from the raw-data image, *i.e.* a certain gray scale value grabbed from the TP image.

After the experimental data is stored, the IP can be erased by exposure with intense white light for about 15 min. Now, the IP can be used again in the TP. It is important to note that during the experiments, *i.e.* between the irradiation with laser-accelerated ions and the scanning readout, the IP has to be handled with care regarding undesired light exposure. Thus, a light-sealed cassette or bag for transporting irradiated IPs to the scanner is mandatory. If *e.g.* high-energy protons are investigated, then the IPs can be wrapped in 5 μm Al foil in order to protect the IP signal. Indeed, one has to consider the energy loss of the protons within the aluminum when analyzing the PSL values. But, in case of few-MeV helium ions an aluminum layer of such a thickness corresponds to a range of 1.6 MeV α-particles in Al. Hence, helium ions with energies $< 1.6\,\mathrm{MeV}$ are completely stopped and cannot reach the IP. Therefore, in order to ensure that all signal is detected and no signal is lost until the information is stored, the best solution for handling irradiated IPs between laser shots is to turn off the ambient light in the laboratory when changing the detectors.

---

[5] Note: "if $QL = 0$ then PSL defines as $\mathrm{PSL} = 0$" [Fuj].

Fading Another important issue is the elapsed time between IP irradiation and the scanning readout. As stated above, the excited metastable states in the active IP layer decay spontaneously with increasing time even without illuminating the IP: the so-called *dark-decay* or *fading* [Leb11]. Fading can be described by rates of decay which may vary between different IP types and which can be dependent on the given IP temperatures, the PSL signal strength at the time of exposure, etc. [Mor94, Pat08, Ale14]. Since published fading characteristics cannot ensure a desired accuracy for the own data analysis, the fading has to be investigated experimentally for the own IPs. In case of *Agfa MD4.0* IPs, an exponential decay of the PSL signal with a fading constant ($^1/_e$-value) of $\tau = 200 - 300\,\text{min}$ was determined: $\text{PSL}(t) = \text{PSL}_0\ \exp(-^t/_\tau)$ [Dep15, Bar15]. Regarding the time needed to vent the vacuum chamber after a laser shot and to transport the irradiated IP to the scanner (usually $t = 20 - 30\,\text{min}$), a PSL signal of $85 - 90\,\%$ of the original PSL will be extracted.

IP calibration There are several possibilities to calibrate IPs for TP measurements. A well-proven calibration method would, *e.g.*, involve slitted CR-39 which are positioned directly in front of the IP [Pra10, Ale14]. The inter-slit distance as well as the slit diameter have to be chosen according to the desired energy resolution (energy dispersion: in contrast to the lower-energy case the corresponding deflections are closely spaced for higher energies). Deflected ions will alternately hit on the CR-39 detector plate or on the IP. Afterwards, both data sets will complement one another. By analyzing the border regions "CR-39-IP" for several energy intervals, a CR-39-obtained real ion number can be related to a specific gray scale value (or PSL value) from the IP scans. For further information regarding several calibration methods *cf.* [Har08, Pra10, Fre11, Ale14]. Unfortunately, for the PHELIX beamtime i009 no slitted CR-39 was available due to unforeseen technical issues.

Radiochromic films (RCF)

Radiochromic dye films (RCF) are self-developing non-electronic detectors for ionizing radiation. Basically, they consist of an active layer with a dye precursor coated on a clear PET host substrate. Since the active layer can be easily scratched, a protective cover layer is often added. But similar to the demands on the used IPs, such a protective layer is not useful if low-energy helium ions need to be detected. Therefore, RCF without any cover layer, *GAFCHROMIC® HD-V2* RCF [6], were used in the PHELIX experiments [ISPb, ISP10].

According to [McL77], ionizing radiation, *i.e.* the radiation dose, leads to a polymerization process which subsequently causes changes in optical density (OD) and color of the active layer: the absorbance in the active layer increases. Directly after exposure to radiation with a certain dose, a color change is visible. This characteristic is useful in laser-plasma experiments: an immediate qualitative result is given after a laser shot which is not usual if non-electronic detectors are used. The color formation within the active RCF layer continues. A quantitative analysis of the deposited dose usually is possible after a post-exposure time of 24 h since the self-development of the RCF has

---

[6] note: the well-known precursor RCF was *GAFCHROMIC® HD-810*

not been fully completed, yet: within 24 h after exposure, the absorbance can increase by about 16 %, and in the following two weeks slightly by about 4 % (these values vary depending on the absorbed dose and on the attached RCF) [NR98]. According to [Che05], at least 6 h shall be passed after exposure in order to provide a high level of accuracy for RCF analysis.

For RCF readout, the irradiated RCF can be scanned with commercial flatbed color scanners in transmission mode. For the PHELIX experiments, a resolution of 900 dpi was chosen and the RCF information was digitized as 64 bit RGB HDRi raw *.tif*-data. Next to irradiated RCF also unexposed RCF have to be scanned in order to subtract the original color values from the experimental data. It is important to note that RCF have to be scanned in their preferred orientation (landscape or portrait, respectively) since the RCF response is influenced by this small detail. This is due to the fact, that the alignment of the formed polymers in the active layer is preferentially parallel to the coating direction. Hence, for landscape or portrait orientation light is scattered differently and the scanning output changes accordingly. For various scans the same scanning direction has always to be chosen regarding maintaining comparability.

In the field of laser-acceleration physics, a quantitative RCF-analysis of the particle flux and the particle energies is possible with more or less high accuracy if primarily one ion species is present and if the RCF are calibrated[7] with exactly this particle species and comparable energies. But as soon as more particle species are being detected, the changes in absorbance cannot be related to exactly one and the same particle flux and energy (the same color change can be caused by different species only by varying particle number and energy). For a proper calibration *e.g.* for protons or helium ions, a monoenergetic particle beam with known flux is directed on the RCF for a certain time. The resulting absorbancies can be transferred to the experimental data. A proven method to investigate the whole energy spectrum of high-energy laser-accelerated particles is to take a stack of several RCF (also possible are additional degrader layers). From the RCF analysis the particle energy can be deduced. Near the Bragg peak most of the particle energy is deposited. When the experimental dose D as well as an average deposited energy $\mathcal{E}_{\mathrm{avg}}$ per particle are known, the deposited energy $\mathcal{E}_{\mathrm{dep}}$ per area A_{act} of the active layer with density ρ_{act} and thickness d_{act} can be deduced. Subsequently, the number n_{p} of incident particles per area unit can be estimated by

$$n_{\mathrm{p}} = \frac{\mathcal{E}_{\mathrm{dep}}}{A_{\mathrm{act}}\,\mathcal{E}_{\mathrm{avg}}} = \frac{D\,\rho_{\mathrm{act}}\,d_{\mathrm{act}}}{\mathcal{E}_{\mathrm{avg}}}\ \text{[Raa11]}\,. \tag{6.25}$$

Handling of RCF RCF have to be stored at temperatures below 40 − 50 °C in order to minimize effects of temperature and time dependent development [NR98, Che05]. Furthermore, RCF have to be protected from water since the active layer is easily soluble. Especially *GAFCHROMIC® HD-V2* RCF do not have any protective layer

---

[7] note: a calibration has to be performed with every new RCF charge. This is due to the fact that the manufacturer often improves its product or that the chemical composition might vary from time to time.

on top of their sensitive side. Therefore, gloves have to be worn when handling RCF and for storage a waterproof lightproof cassette or bag is recommended. Within a laser-acceleration experiment, it is important to wrap RCF in 5 µm Al foil in order to shield the detector from side-scattered laser light. Of course, this additional degrader foil filters incoming ions. In case of $^4\mathrm{He}^{2+}$ ions, a range of 5 µm corresponds to an energy loss of 1.6 MeV in aluminum. This issue has to be considered in the analysis of the experimental data.

Properties of the used RCF Within the PHELIX experiments, *GAFCHROMIC®* *HD-V2* RCF were used in order to detect both laser-accelerated $\mathrm{He}^{1+,2+}$ simultaneously. The sensitive layer has a thickness of 8 µm and it is coated on a 97 µm thick polyester substrate [ISPb, ISP10]. A yellow marker-dye is used. *HD-V2* RCF have a dynamic dose range of $10 - 1000$ Gy. In order to detect much lower doses, *GAFCHROMIC®* *EBT2* RCF can be used [ISPa, ISP10]. They provide a wide dose range of $0.1 - 40$ Gy and are composed of in total five layers: (*top* to *bottom*) a clear polyester protection of 50 µm, an adhesive layer of 25 µm, a top coat of 5 µm on the active substrate layer of 30 µm, and finally a clear polyester layer of 175 µm. Indeed, a total thickness of 285 µm is not suitable for detecting few-MeV helium ions. But within the PHELIX experiment, also the forward direction had to be investigated in terms of a small high-energy helium ion signal.

7. Studies on Laser-accelerated Helium Ions

Within the current doctoral studies, two laser-acceleration experiments were performed at two laser facilities, the Arcturus laser and the PHELIX laser. In the following parts of this chapter, the experimental setups as well as the obtained results are presented and discussed.

7.1. Arcturus experiment

In Feb. 2014, a first experiment with ^{4}He gas as underdense plasma target was carried out at the Arcturus laser facility at Heinrich-Heine-University Düsseldorf (for the technical details of the laser, *cf.* Sec. 2.2.2 on p. 8).

The scientific goal of this beamtime was to detect helium ions mainly in forward direction, *i.e.* in laser propagation direction. Differently to [Kru99, Wei04, Wil06] (*cf.* Sec. 3.2.5), a thin gas jet out of a supersonic de Laval nozzle (minimal nozzle diameter of 167 µm) served as plasma target. Former EPOCH simulations as well as preliminary experimental data from a preceding Faraday cup measurement on laser axis predicted a sharp ion-emission angle of 0°. This beamtime was scheduled in order to verify the predictions and to investigate the laser-induced ion-acceleration mechanism by both plasma diagnosis and ion energy measurements.

7.1.1. Experimental setup

The experiment was performed in the target chamber TC-1 (*cf.* p. 9). The enlarged compressed laser beam (circular shape, beam diameter of 80 mm, beam energy after compression $\mathcal{E}_\mathrm{L} = 2 - 4\,\mathrm{J}$, pulse duration $\tau = 25\,\mathrm{fs}$, wavelength $\lambda_\mathrm{L} = 800\,\mathrm{nm}$) is guided into TC-1 via a deviation pot within the beam line. Inside TC-1, a turning mirror directs the laser beam on an off-axis parabolic mirror or off-axis parabola (OAP) with a focal length of 1000 mm, *i.e.* an f-number of $F = 1000 : 80 = 12.5$. Theoretically, the minimal focus diameter achievable with this OAP can be calculated to

$$d_\mathrm{foc} = \frac{4}{\pi}\,\lambda_\mathrm{L} \times F \approx 12.7\,\mu\mathrm{m}\,. \tag{7.1}$$

Focus adjustment

The focus adjustment right before the laser shots is necessary to ensure a nearly perfectly shaped focus with minimal diameter in a pre-defined shooting position. The focus shape and its actual position could be monitored with the *focus-diagnostics line*: a retractable 1” mirror behind the focal spot directs the diverging laser beam through a 2” magnifying lens (magnification of 12) from where the parallelized beam propagates onto the chip of a *Basler scout* CCD camera (resolution 659 × 494 pixel, pixel size 7.4 µm × 7.4 µm, frame rate 71 fps, 12 bit). In the following, the laser propagation direction (optical axis) will be denoted as z-axis, the horizontal and vertical directions are x- and y-axis, respectively.

For a proper focus adjustment, the OAP as well as the turning mirror have to be aligned thus, that astigmatism[1] is minimized. An easy test for astigmatism is a translation of the OAP along the z-axis, *i.e.* a translation of the focal plane. While the beam diameter w is minimized at the focus position (beam waist $2w_0$), before and behind this location the beam diameter increases (focusing and diverging around the focus position). A perfectly adjusted focus does not change its shape when "traveling" through the focal plane, *i.e.* its circular shape will remain untouched. Every single light ray from the incoming parallel laser beam is focused to the same point by the OAP, *i.e.* the rays have the same focal distance. But, in case of a misaligned OAP, focal distances vary which leads to an elliptical shape of the monitored focus.

The adjustment procedure has to be split into the vertical and the horizontal adjustment. First of all, the OAP has to be translated along the optical axis, *i.e.* the focus-diagnostics camera images not the focal region ("out of focus") and the light spot is enlarged. The given ellipse can be tilted in one dimension so that it is oriented horizontally or vertically, respectively. This is done by (horizontal or respectively vertical) tip&tilt of turning mirror and OAP. After having cleared one dimension, the procedure has to be conducted in the opposite direction. The shape of the defocused laser spot becomes more and more circular until a minimal beam diameter is reached. When translating the OAP around the focal position in z, the beam should expand and close symmetrically with a circular shape. It is important to mark the focus position on the screen (focus-diagnostics camera) in order to define a reference regarding future re-alignments: *e.g.* the center of the camera image on the monitor. After aligning the OAP, during the experiment the best focus diameter could be set to a FWHM-value of 15 µm.

Defining the TCC

Since with the focus position a nominal target position was defined, it was necessary to adjust the gas jet accordingly. Therefore, the gas-jet source, the *Parker Hannifin series 9* solenoid valve mounted on an (x, y, z) translation stage, was positioned beneath the TCC.

In order to precisely define the spatial position of the nozzle tip relative to the laser focus, a thin vertically oriented wire (known diameter of 50 µm) was glued on the nozzle surface. During the experiments, the position of the wire tip served as the reference for the shooting position of the valve, and hence, it was handled with care. For a proper alignment of the wire tip, the laser beam diameter was decreased (iris in front of the compressor) and the shadow of the illuminated wire could be imaged by the focus-diagnostics camera. By translation of the valve in x- and y-direction, the wire tip sidewisely could be positioned in the predefined focus position (center of the camera image). With the z-translation, the shadow image of the wire tip could be sharpened, *i.e.* the wire tip was brought in focus. The actual coordinates could be monitored by

---

[1] note: in this context, *astigmatism* denotes an aberration in off-axis imaging and has not to be confused with the biological eye defect due to an amorphic eye lens

Heidenhain length gauges: one Heidenhain-unit corresponded to 100 µm in x and y, while in z it was 200 µm. The defined wire tip position was set to zero which, thus, characterized the TCC.

The given offset in x, y, z between wire tip and the center of the cylindrical nozzle tip could be determined by introducing a second imaging line perpendicular to the focus-diagnostics line: the *side view*. With both the focus-diagnostics and the side-view camera the nozzle tip could be aligned such, that the vertical nozzle edges were imaged sharply on both cameras. The center of the horizontally oriented nozzle edge was positioned in the predefined focus position. The shooting position for the experimental laser shots could be reached by translating the valve downwards (typically 500 µm) in order not to clip the focusing laser beam or not to endanger the attached nozzle. The wire had two important functions: on the one hand, its position clearly defined the TCC, and on the other hand, it served as a calibration tool for the camera imaging: with the known wire diameter, the pixel information from the camera pictures could be translated into a unit of length.

Probe and plasma diagnostics

In order to gain an insight into physical processes inside the plasma region at a certain time after the first laser-target interaction, a *probe (beam)* can be used. The probe is a small portion of the main laser pulse which is temporally delayed when illuminating the interaction region. The delay can be defined by a slightly different propagation length of probe and main pulse[2]. Important for a proper alignment of the probe line is to mainly avoid "funny angles" (*i.e.* angles $\neq 90°$). In the Arcturus experiments, a 0.5" pickup mirror in front of the turning mirror coupled a beamlet out into the *delay stage*. The delay stage consisted of a motorized linear translation stage. Two (1") mirrors were mounted on the moving carriage thus, that the optical paths of incoming and outgoing light were oriented parallely.

After having passed through the laser-target interaction region perpendicularly to the main pulse, the probe exited TC-1 through an AR-coated window ($\lambda_{\mathrm{L}} = 800\,\mathrm{nm}$, for minimizing undesired chirps within the glass medium). Outside the chamber, the probe was split into three beamlets for three individual diagnostics lines: the polarimetry (two Glan-Laser Calcite polarizers), the shadowgraphy line, and the interferometry (Nomarski interferometer with a Wollaston prism).

Polarimetry line In order to avoid dispensable disturbing glass media in the polarimetry line (additional beamsplitter cubes, for instance), the investigation directly starts outside TC-1. With a 50:50 non-polarizing beam splitter cube the beamlet was split again. Each secondary beamlet had to propagate through a Glan-Laser Calcite polarizer before being imaged by a *Basler scout* CCD camera (magnification factor of 10). A Glan-Laser Calcite polarizer (polarization purity of 100 000 : 1, high damage threshold, AR-coating for 800 nm) is a modified Glan-Taylor Calcite polarizer for high-energy laser pulses. The prism splits the incoming light in an escaping ordinary ray (scattered and nearly

---

[2] note: in vacuum a propagation length of 3 mm corresponds to a delay time of approximately 10 ps

unpolarized portions of light) and an extraordinary output ray (highly polarized), which is detected by the CCD. In front of each camera a filter stack (ND, CF color filter BG 39, and IF interference filter for 2ω) was put. The polarizers were adjusted at $\pm\theta_{\mathrm{GL}}$ (detune in opposite direction). When electrons are accelerated by the laser pulse, the resulting electron current inside the plasma induces azimuthal magnetic fields B_φ which can be measured by Faraday rotation of the probe polarization along a path l [Sta75, Kal10]: $\phi_{\mathrm{rot}} = {}^{e}\!/\!{}_{(2m_{\mathrm{e}}c\,n_{\mathrm{c}})} \int_l n_{\mathrm{e}}(r)\, \boldsymbol{B}_\varphi(r) \cdot d\boldsymbol{s}$. Only B_φ-components parallel to the probe axis will contribute to the Faraday rotation. Both CCD cameras will measure an intensity which is dependent on θ_{GL} and ϕ_{rot}. The relation between both intensities will result in a ϕ_{rot} distribution which is due to the electron movement inside the plasma.

Shadowgraphy line The shadowgraphy line also served as the above mentioned side-view line. An *Allied Vision Pike F-1100* 14 bit 11 MP camera with a resolution of 4008 × 2672 pixel, a cell size of 9 µm, and a frame rate of 5 fps was attached in order to grab a time-resolved image of side-scattered light from the interaction region. A filter stack (ND, CF color filter BG 39, and IF interference filter for 2ω) was put in front of the camera.

Interferometry line The third plasma diagnostics line was the interferometry line. Here, a Nomarski interferometer with a Wollaston prism (separation angle of 7°) was set up. The Wollaston was mounted close to the focus of a focusing lens ($f = 200\,\mathrm{mm}$). Similar to the Mach-Zehnder interferometer, the Nomarksi interferometer is based on superposition of two beamlets. In this case, the beamsplit of the probe (beam) occurs after passing the interaction region. Thus, the beamlets propagate through the same optical devices. The Wollaston prism basically is built up by two cuneiform birefringent crystals combined at a coplanar area. The incoming light ray is separated into an ordinary and an extraordinary beamlet within the first crystal. Due to the different propagation velocities of the two beamlets, their refraction indices $\eta_{\mathrm{o,e}}$ are not equal. Hence, at the boundary surface the refraction angles differ so that both beams are refracted in different directions. Now, two angular separated beams with vertical and horizontal polarization are given, which can be projected to two virtual foci in front of the Wollaston prism. Two partially overlapping images of the plasma region are given. The overlap range, *i.e.* the interference region, is characterized by fringes. For a proper plasma diagnosis it is important to overlap vacuum regions with plasma regions. Thus, changes in particle density due to laser-induced particle acceleration become visible by local fringe shifts. A filter stack (ND, CF color filter BG 39, and IF interference filter for 2ω) was put in front of the *Basler scout* camera.

Ion diagnostics

For the first laser shots, a Faraday cup battery (FC) was mounted in order to reproduce the experimental data from a preceding measurement [Hol14]. The battery consisted of eight vertically oriented Faraday cups with 10 mm in diameter each and an immediate-neighbor distance of 25 mm. The FC was aligned on laser axis in a distance of 233 mm from the laser-target interaction region so that the on-axis cup covered a divergence angle of approximately 1.2°. The FC was read out with two 4-channel *LeCroy WaveRunner 6 Zi GHz* oscilloscopes with a sampling rate of up to 20 $^{\mathrm{GS}}/_{\mathrm{s}}$. The FC only served as a pre-diagnostics tool for ion detection.

In addition, a TP with attached Microchannel Plate detector (MCP) as particle detector [3] was mounted on laser axis (0°). In a distance of 650 mm from the focus a pinhole with 500 µm in diameter served as entrance into the differentially pumped vacuum chamber (10^{-6} mbar). Thus, a solid angle of 0.465 µSr was covered. The size of the pinhole was chosen in order to ensure that during the first laser shots enough helium ions enter the TP. Finally, when a constant ion signal would be given, the diameter should be decreased (to 100 − 200 µm) to increase the energy resolution. Directly behind the pinhole, a vertically oriented homogeneous electric field was built up by a high voltage of −1430 V and +3300 V followed by a magnetic dipole ($B_{\mathrm{max}} = 0.6\,\mathrm{T}$) in front of the MCP detector. The resolution on the MCP camera was 13.7 pixel per mm.

Timing

The Arcturus laser was used in two different shot modes: in one-shot mode during the experiments and in 10 Hz mode for the general alignment. First of all, it was important to adjust the timing between the main pulse and the probe. For this purpose, a simple thin glass plate was put in the focus. It was tilted about 45° relative to the laser axis. Therefore, the main pulse was partly reflected sideways and superimposed with the transmitted parts of the probe. With a photo diode the incoming light could be monitored on an oscilloscope. By manipulation of the delay stage, both signals temporally could be put on top of each other. For this setting, the delay between both pulses was 0 ps. Now, the desired delay could be defined by enlarging the propagation path with the delay stage.

Next to the probe beam timing, it was important to define the temporal behavior of the other devices relative to the main pulse. This adjustment is crucial for a successful realization of a laser-acceleration experiment. If the laser is focused "too early", *i.e.* before the valve could be opened, then no laser-target interaction can occur. Furthermore, the valve cannot be opened for very long time durations in order not to destroy the necessary vacuum inside the chamber. The laser trigger served as input for a *Stanford Research Systems Inc. Digital Delay and Pulse Generator*. With this device, individual delay times for the *Parker IOTA ONE Pulse Driver* of the valve [Para] as well as for the cameras could be set. The valve opened 5 ms before the main pulse was focused. The total opening time of the valve was 10 ms which could be adjusted using the *IOTA ONE* controller box. Thus, a stable gas jet could be built up for the laser-target interaction. The delay of each plasma diagnostics camera was defined according to the actual probe timing in order to grab an image of the plasma region at the "right" time.

7.1.2. Results

During the first laser shots, the FC was applied. The oscilloscopes grabbed a similar signal shape like in the preceding measurements [Hol14]. At a time of around 100 ns

---

[3] for further information on MCPs as particle detector in TPs *cf.* [Wiz79, Bol14]

after the first laser-target interaction, the spectrum showed a sharp negative amplitude going down to approximately −10 V. It was followed by a wide positive amplitude (peak value of ∼ 1 V) between 120 and 210 ns. The former interpretation of this signal was that a bunch of fast electrons arriving at the FC before helium ions which form the positive part of the signal. A zero-measurement, *i.e.* a vacuum shot without any gas-jet target, yielded the same oscilloscope signal. Subsequent tests with decreasing laser energy (100 %, 50 %, 10 %) proved that the grabbed signal from the FC scaled with the given laser parameters. Therefore, it could be concluded that the preceding measurements did not represent a laser-accelerated helium ion signal. The laser intensity on the copper mesh of the FC ionized the FC material which caused the measured signal. Finally, this conclusion was also drawn in [Hol14].

The Arcturus beamtime continued with the TP at 0° as ion diagnostics. During the first shots no high voltage was applied, *i.e.* only the horizontal magnetic field was present in order to deflect charged particles in the vertical direction. Apart from a measured electron signal on the MCP (electron energy range of 40 − 60 MeV), no ion signal could be measured on laser axis. Figure 7.1 illustrates a recorded MCP image[4]: the zero order, *i.e.* the position of the pinhole, clearly can be regarded in the center of the screen. Since the magnetic field was aligned horizontally, negative charges are deflected upwards. The signal above the pinhole position is due to deflected electrons which entered the MCP in forward direction. The white spot next to the electron signal is not a signal from incoming particles. Either it was originated from side-scattered incident laser light (the TP was mounted on laser axis), or it was a damaged section on the CCD or the MCP.

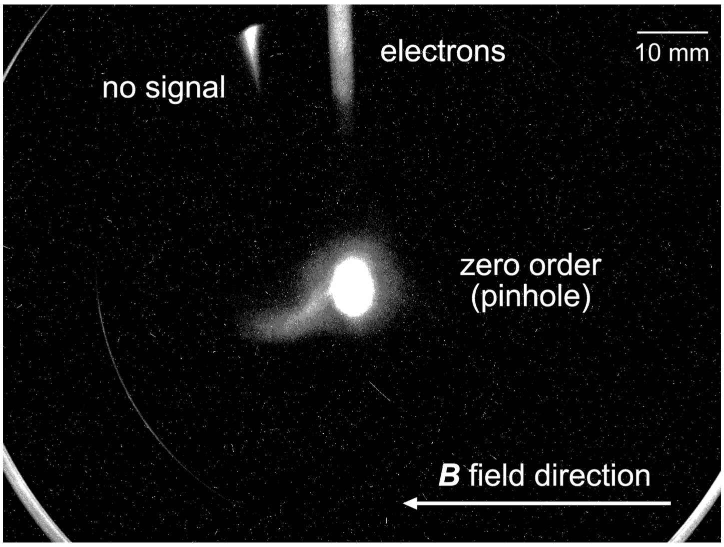

Figure 7.1.: Deflected electrons on the MCP screen (the arrow indicates the orientation of the $\boldsymbol{B}$ field).

Several attempts to extract an ion signal in forward direction, like *e.g.* variation the laser parameters (preferential the pulse duration), changing the focus position relative to the gas-jet dimensions, variation of the gas-jet densities by attaching different backing

---

[4] The image was taken from the back of the MCP. The laser axis is pointing out of the image plane.

pressures, attaching a razor blade close to the nozzle in order to improve the particle-density distribution ramp at the border gas-vacuum, stood fruitless. Also with an array of CR-39 detector plates which covered an angular range of −8° to 24° in forward direction a helium ion signal could not be extracted. Either the achieved ion energies were below the detection threshold of CR-39, or the number of laser-accelerated helium ions in forward direction was too small to get a significant measurable signal in forward direction. This result is in agreement with [Lif14] (*cf.* Sec. 3.2.5 on p. 31) as well as with subsequently conducted EPOCH simulations (*cf.* Sec. 5.3.2 on p. 56). But, in order to fully investigate laser-induced ion acceleration out of a helium gas jet at the Arcturus laser, a wider angular range (especially 80° to 100° relative to the laser direction) is highly recommended to be investigated in future experiments at Arcturus.

Since the search for an ion signal in forward direction was time consuming and did not yield positive results in this angular range, the investigation of plasma processes could not be deepened. The only tool to directly recognize that laser-plasma interaction had occurred was the shadowgraphy. Images similar to the one given in Fig. 7.2 helped to optimize the defined laser/target parameters: a channel in plasma density and filaments are visible above the nozzle edge. The position of the nozzle relative to the laser focus as well as the probe delay were optimized in order to image the laser-plasma interaction fully.

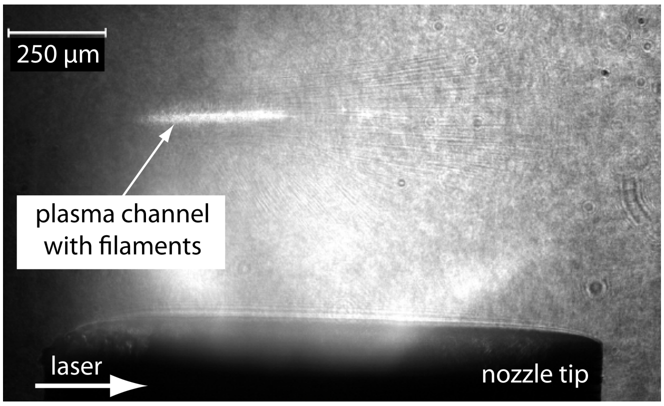

Figure 7.2.: Shadowgraphy image of a channel in plasma density above the nozzle edge (the laser propagation direction is indicated by the white arrow).

7.2. PHELIX experiment

In Jan. 2015, a second experiment with ^{4}He as well as unpolarized ^{3}He gas as underdense plasma target was conducted at the PHELIX laser facility at GSI Darmstadt: PHELIX experiment i009. For the technical details of the laser, *cf.* Sec. 2.2.1 on p. 6.

The scientific goal of this beamtime was to determine the angular distribution of laser-accelerated ions and to measure the energy spectra for three specific angles relative to the laser direction: 80°, 90°, and 100°. EPOCH simulations predicted a wide angular ion-emission range around ±90° (*cf.* Fig. 5.7 on p. 63, Sec. 5.3.2), comparable to

[Kru99, Wei04]. A gas jet out of a supersonic de Laval nozzle (minimal nozzle diameter of 0.5 mm, different attached backing pressures) served as plasma target. This beamtime was scheduled in order to demonstrate the feasibility of helium-ion acceleration at the PHELIX laser and to determine the best laser/target parameters for the future experiment with pre-polarized ^{3}He gas as plasma target.

7.2.1. Experimental setup

The experiment was performed within the PHELIX target chamber (*cf.* p. 7). The enlarged compressed laser beam (elliptical shape, beam diameter of 220 mm, beam energy after compression $\mathcal{E}_\mathrm{L} \approx 40 - 120\,\mathrm{J}$, pulse duration $\tau = 0.4 - 1.1\,\mathrm{ps}$, wavelength $\lambda_\mathrm{L} = 1053\,\mathrm{nm}$) is guided into the chamber via a deviation pot within the beam line. Inside this deviation pot a 90° OAP with a focal length of 1500 mm, *i.e.* an f-number of $F = 1500 : 220 = 6.8$, was aligned thus, that the focus had a minimal spot size of about $11 \times 15\,\mathrm{\mu m}$ (the focus adjustment procedure was similar to the one described on p. 105).

Defining the TCC

The general target alignment regarding the TCC is similar to the one described on p. 106: the *Parker Hannifin series 9* valve with attached 0.5 mm supersonic de Laval nozzle was mounted on an (x, y, z) translation stage beneath the focus location. In contrast to the previous alignment, a fine wolfram needle served as a reference for the shooting position. Figure 7.3 illustrates the needle position relative to the nozzle tip. The needle holder was mounted on a magnetic base being attached to the valve holder. Hence, it could be positioned if needed for various alignments, *e.g.* of the used TPs. By checking both the focus-diagnostics as well as the side-view line, the tip of the needle was positioned in the predefined laser focus. Here, the needle position was set to zero which defined the TCC. A *Basler A622f* served as focus-diagnostics camera (on the image, 1 pixel corresponded to 2.195 µm), and a *Basler A601f* as side-view camera (on the image, 1 pixel corresponded to 3.194 µm), respectively. In Fig. 7.4, an image of the side-view camera illustrating the needle tip in the TCC can be regarded. Subsequently, the offset between the needle and the nozzle tip was determined. The desired shooting position was set to a height of 500 µm above the nozzle edge.

Ion diagnostics

Several ion diagnostics were aligned in order to gain information about the angular distribution of the laser-accelerated helium ions, their energies as well as their ionization stages. With the help of an RCF wrap-around detector close to the target, the EPOCH predictions regarding the angular ion distribution shall be proved qualitatively. In order to investigate the acceleration process quantitatively, three TPs were mounted at three specific angles relative to the laser axis. Thus, regarding the propagation direction of the laser, the TPs covered the right side of the interaction zone. On the other side, CR-39 detector plates were positioned around the target in order to additionally detect

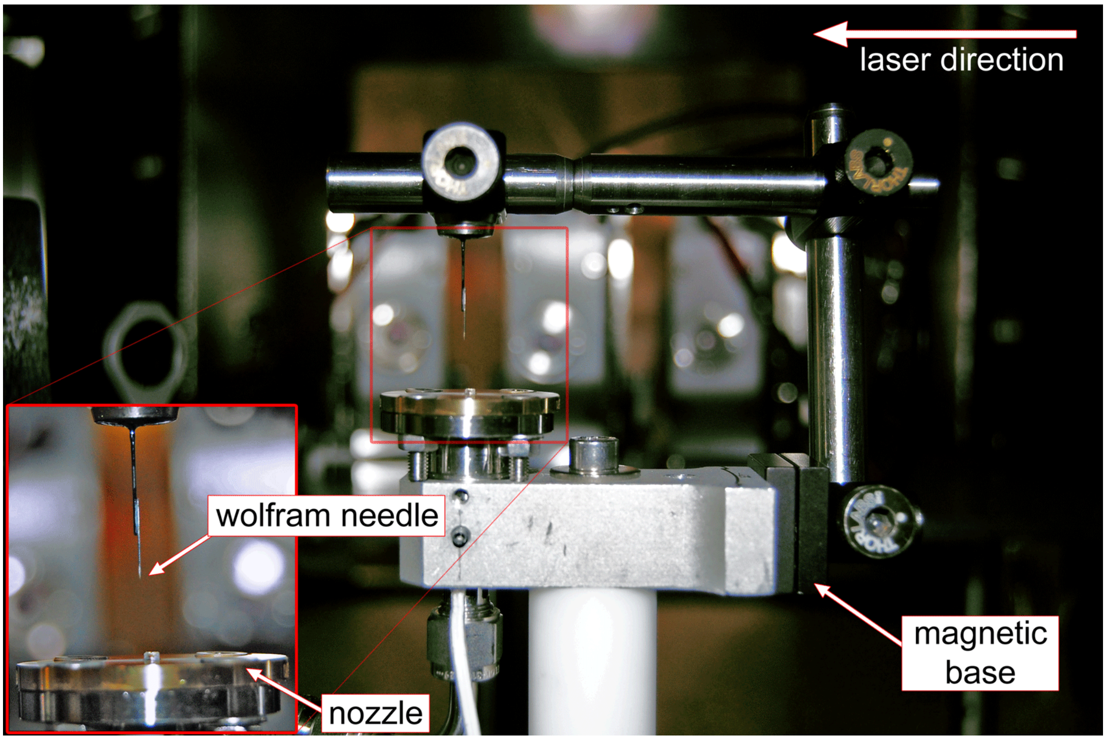

Figure 7.3.: Needle position relative to the nozzle tip (the laser propagation direction is indicated by the white arrow). *Additional information:* in the background of this picture right behind the nozzle location, three TPs can be regarded (blurred shape). They are aligned at three angles relative to the laser axis (*cf.* p. 115).

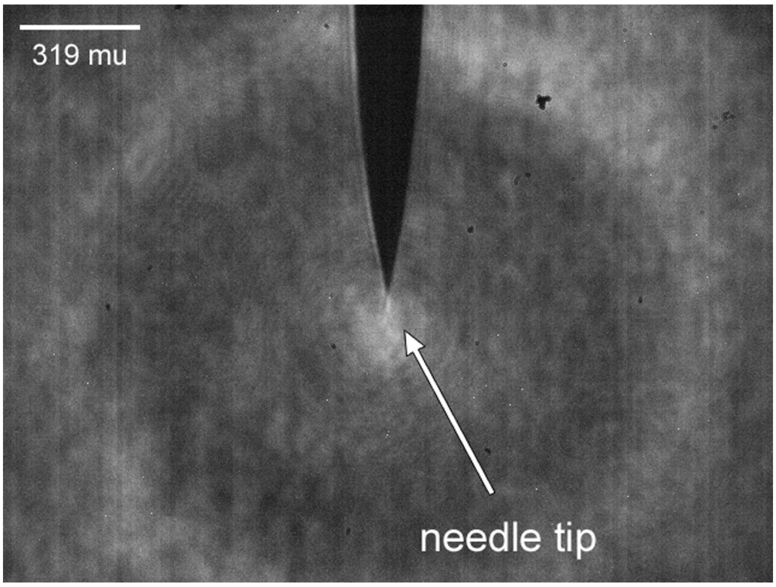

Figure 7.4.: Side-view camera image of the needle tip in the TCC.

the pure undeflected ion signal. In the following, the adjustment of each diagnostics will be described in detail.

RCF wrap-around detector An RCF wrap-around detector was used in order to cover a wide angular range around the plasma target. The self-made wrap-around holder was built of aluminum. Rolled endwalls were welded on a ground plate with circular cross-section area (diameter of 104 mm). In order not to clip the focusing/diverging laser beam, an entrance/exit gap is given between the endwalls: $s_{\mathrm{entr}} = 26.2\,\mathrm{mm}$ (entrance), and $s_{\mathrm{exit}} = 20\,\mathrm{mm}$ (exit). Hence, at each side an angular range of 11.1° to 165.4° could be covered relative to the laser axis. The RCF wrap-around holder could be mounted directly on the valve holder without disassembling the setup. This is important since the previously defined nozzle position has not to be lost in any case. The mounted RCF wrap-around holder is illustrated in Fig. 7.5. As it can be regarded in the picture, at the right side with respect to the laser axis, a borehole in the well wall allows to simultaneously operate the −90°-TP during the wrap-around RCF measurements. *GAFCHROMIC® HD-V2* RCF wrapped in 5 µm thick Al foil were used. Note: according to *SRIM*, 5.09 µm corresponds to the range of 1.6 MeV $^{4}\mathrm{He}^{2+}$ ions in aluminum. Thus, ions with an energy > 1.6 MeV could reach the RCF. The Al shielding is important in order to block side-scattered laser light and to protect the RCF from arising plasma temperatures. For the sake of convenience, the RCF were fixed with paper-clips at the endwalls.

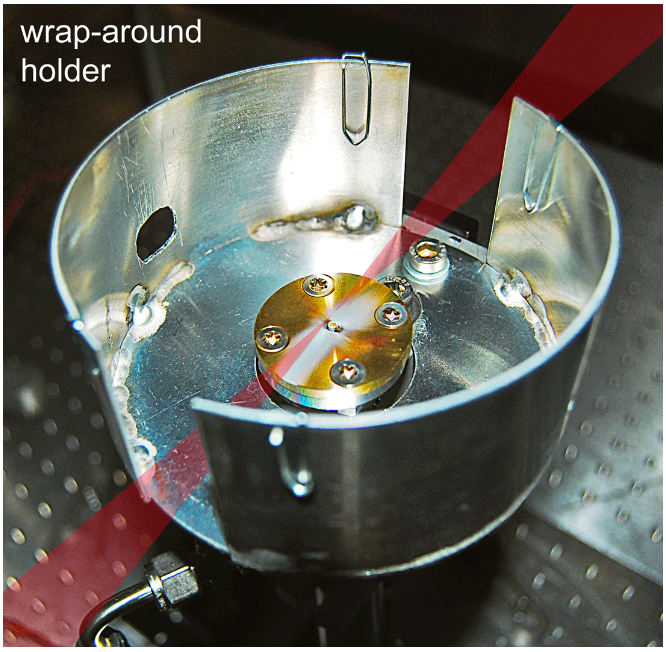

Figure 7.5.: Wrap-around holder for RCF mounted on the valve holder (the red semi transparent arrows indicate the focusing/diverging laser beam; the laser propagates from the upper right to the lower left image section).

TPs at 80°, 90°, and 100° In total, three TPs were aligned at three angles relative to the laser propagation direction: −80°, −90°, and −100°. In the further course of this thesis, the TPs are denoted as follows: TP-80, TP-90, and TP-100, respectively. The pinhole diameters for the TPs were chosen according to the experimental results in [Kru99], *cf.* Figs. 3.4 (a) and (b) on p. 29: here, the main acceleration direction was determined to be at 90° relative to the laser axis and the relative ion number decreased rapidly for angles $< 80°$. Therefore, within the PHELIX experiment, TP-90 was equipped with a 200 µm pinhole, TP-80 got a 650 µm pinhole in order to catch as many ions as possible during the first shots (it was changed to a diameter of 350 µm afterwards), and a 350 µm pinhole served as entrance into TP-100. The fine adjustment of the TPs was performed with an alignment diode which was coupled in the side-view line by a 1" mirror in front of the TCC. Furthermore, the wolfram needle was positioned in the TCC. The 1" mirror was mounted on a translation stage with additional rotation stage (fine pitch worm gear). First of all, TP-90 was aligned. The alignment diode propagated at an angle of 90° relative to the laser axis and illuminated the needle tip. The TP was positioned thus, that the diode beam propagated through the 200 µm pinhole into the spectrometer. A distance of approximately 1 mm to the positively charged electric field plate was set in order to ensure that incoming ions do not get lost by hitting onto the hardware. Considering the inter-capacitor distance of 2.3 mm, the ion beam was centrally arranged between the capacitor plates. The other two TPs could be aligned by adjusting the rotation stage by an angle of ±5° (relative to the prior defined 90° setting) which corresponds to a total angle of ±10°, *i.e.* the desired 80° and 100°. Since the diode beam was misaligned after the mirror rotation, the needle tip could be re-illuminated by translating the mirror along the laser axis. Both TPs were positioned like TP-90: diode beam passing through the pinhole with 1 mm space to the anode. Figure 7.6 illustrates the TP arrangement. As it can be regarded in the upper picture, the distances between the TCC and the particular TP (to be more precise: the pinhole as entrance into the spectrometer) had to be varied. This is due to the geometry of the TP housing and its base plates. In order to make the distance for each TP equal, the distance would have been increased too much and the covered solid angle would have become smaller. Therefore, TP-90 was positioned closer to the TCC than the other spectrometers. A high voltage (HV) of 3 kV was applied for building up the electric field between the capacitor plates. In order to protect the attached particle detectors inside the TPs from disturbing radiation (mainly gammas and side-scattered laser light), a lead shielding was attached: in the beginning, 2 mm thick lead plates covered the TPs. During the measurements, it turned out that the amount of lead was inappropriate (with regard to the background on the IPs) so that the lead thickness was doubled to 4 mm in total. The TP parameters, like distance to the TCC or pinhole size, *e.g.*, are listed in Tab. 7.1.

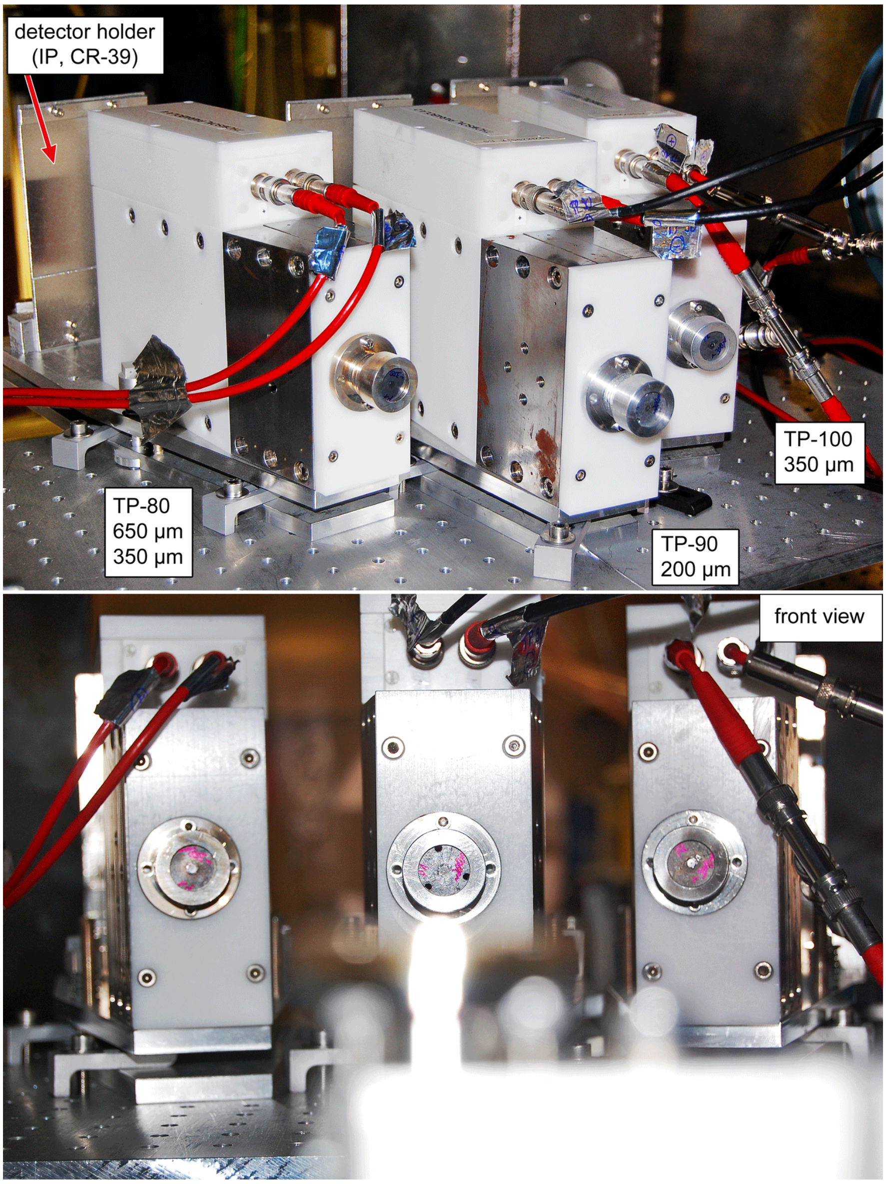

Figure 7.6.: Mounted TPs at 80°, 90°, and 100° relative to the laser axis. *Top:* perspective view, *bottom:* front view, *i.e.* from the TCC's point of view (in the foreground of the picture, the blurred shape of the valve with attached nozzle can be regarded). *Additional information:* for the sake of an unobstructed view on the TPs, the lead shielding was removed.

TP-#	pinhole size [µm]	distance to TCC [cm]	solid angle [nSr]	HV [kV]
TP-80	650 and 350	52	1227.2 and 355.8	3
TP-90	200	43	169.9	3
TP-100	350	51	369.9	3

Table 7.1.: TP parameters in the PHELIX experiment

Additional ion detectors Since all three TPs were mounted at the right side of the target with respect to the laser propagation direction, on the other side three CR-39 plates (feed size of 5 cm) were placed in a distance of 6 cm around the TCC. During the experiments, the distance was doubled to 12 cm. This was due to the fact that the plasma temperatures in this distance caused black residues on the translucent plastic detectors. The CR-39 were mounted in common filter holders. A honeycomb grid made of stainless steel (thickness of 1.2 mm) was positioned in front of the CR-39 in order to get a specific "shadow" pattern after developing the tracks.

Additionally to the side detectors, one CR-39 covered the forward direction. It was wrapped in 5 µm thick Al foil in order to protect the detector from direct laser light. This CR-39 was replaced by a *GAFCHROMIC® EBT2* RCF as well as by a stack of 4 *HD-V2* RCF, both for one laser shot.

Polarimetry tests

A first calibration test of the polarimetry method for laser-accelerated ^{3}He ions was planned for the PHELIX beamtime. Unpolarized ^{3}He gas served as plasma target. The polarimetry cage with a CD_2 foil as secondary scattering target was placed at −90° relative to the laser axis. The distance between the TCC and the first entrance aperture was 89 mm. Laser-accelerated ^{3}He ions entered the cage through a stack of apertures with diameters of (outside to inside) 5 mm, 2 mm, and 1 mm, respectively. CR-39 plates as well as *HD-V2* RCF served as proton detectors. A lead shielding protected the detectors from undesired gamma and laser radiation. Figure 7.7 illustrates the mounted polarimetry cage in front of the TCC. For the sake of an unobstructed view inside the cage, the lead shielding was removed.

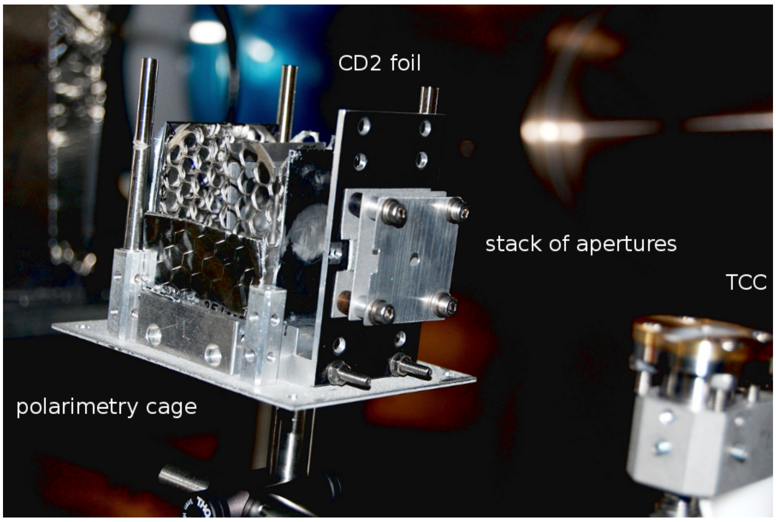

Figure 7.7.: The polarimetry cage aligned at −90° in a distance of 89 mm from the TCC. A stack of apertures (diameters of 5 mm, 2 mm, and 1 mm) served as entrance into the cage. In the cage's center, a CD_2 foil was placed as secondary scattering target for laser-accelerated ^{3}He ions. The protons out of the D-^{3}He fusion reaction should be detected with CR-39 and RCF detectors.

Timing

Within the PHELIX experiment i009, two trigger times were available for temporally matching the incoming laser pulse and the opening of the valve: a "ms"-trigger and a "s"-trigger signal. An individual temporal delay of 4 ms between the valve's opening and the laser pulse was chosen. It had to be ensured that on the one hand the gas jet will be built up fully when the laser pulse is focused. And on the other hand the vacuum inside the PHELIX target chamber had not to be destroyed which would cause the interlock shutters in front of the compressor to be closed. Thus, a delay time of 4 ms was a good compromise for the experimental demands. Therefore, the 2 s PHELIX trigger served as input signal for the *IOTA ONE pulse driver*.

7.2.2. Results

In Tab. A.1, App. A.4 on p. 168, the laser-shot parameters for the PHELIX experiment i009 are summarized. In total, 19 laser shots could be fired which are consecutively numbered from 11159 (first laser shot) to 11203 (last laser shot). In the following, when denoting a specific laser shot next to the official PHELIX laser shot-# also the individual shot number will be placed in parentheses.

Within the first laser shots (# 11159 (01) to 11166 (05)) the optimal laser parameters for the whole experiment could be determined. ^{4}He gas served as plasma target. This was due to the fact that ^{4}He is (in comparison to the rare ^{3}He with similar properties) a more or less inexpensive gas. Due to safety regulation issues, the first laser shot was performed with about one-third of the maximal available laser energy (in the PHELIX experiment i009 it was given with $\mathcal{E}_{\text{max}} = 120\,\text{J}$): 43.8 J. The RCF wrap-around measurement directly delivered a clear helium ion signal (*cf.* the next paragraph: *Angular ion distribution*). The simultaneously performed TP measurement with *Agfa MD4.0* IPs in TP-90 yielded, as expected, two helium-ion Thomson parabolas for both ion species.

For the second and third laser shot the laser energy was set to 112 J and 120 J, respectively. Helium ions could be accelerated and were detected in all TPs, but the high laser energy caused several problems. On the one hand, next to both helium parabolas a third parabola appeared: a proton signal with an energy range of $0.6\,\text{MeV} \leq \mathcal{E}_{\text{p}} \leq 1.4\,\text{MeV}$. On the other hand, the tip of the 0.5 mm de Laval nozzle was damaged after the first shot day and had to be changed. Figure 7.8 illustrates the damaged nozzle tip. In the next laser shots several parameters were changed: the laser energy was decreased (to 99.5 J and finally to 58.3 J) and the focus height above the nozzle tip was increased (up to a height of 1100 µm). Due to a strict time schedule, the proton acceleration mechanism could not be investigated. Most likely, the detected protons were originated from the surface of the nozzle. Before the experiments, all hardware was cleaned with acetone which leaves hydrocarbon impurities on the nozzle material. The laser pulse did not hit on the nozzle itself (otherwise also higher-Z ions from brass would have been detected within the TP). The increase of the focal height did not have any significant effect on the parasitic proton signal. Probably the plasma temperatures from the laser-target interaction zone affected the proton acceleration. Only the decrease in laser energy to values below 60 J ensured a clean helium ion signal from the spectrometer measurements and also the safety for the attached hardware. Therefore, for the following laser shots the laser energy was set to values around $40 - 50\,\mathrm{J}$ and the focus height was chosen to be $500 - 650\,\mu\mathrm{m}$ above the nozzle tip.

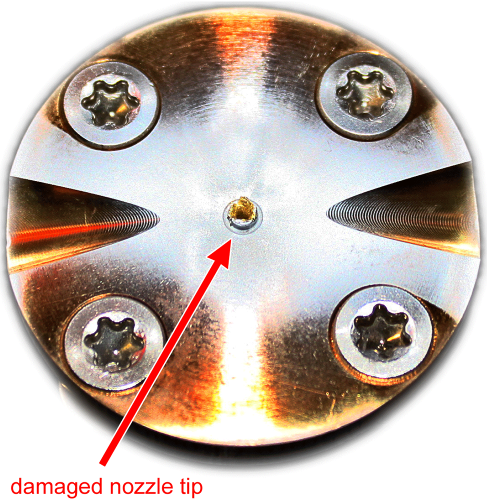

Figure 7.8.: Damaged nozzle tip after maximum-energy laser shots on ^{4}He gas. The laser propagated from the left to the right.

Angular ion distribution

The RCF wrap-around measurements were conducted for laser shots-# 11159 (01) and 11169 (06): laser beam energies after compression 43.8 J and 46.7 J, pulse durations 3191 fs and 1176 fs, respectively. The huge pulse duration of $\sim 3.2\,\mathrm{ps}$ (first shot) is due to the fact that the laser system had to be fine-tuned at the beginning of the beamtime. Afterwards, the pulse duration could be set in a mean range of $\sim 0.6 - 0.8\,\mathrm{ps}$. The wrap-around RCF holder was armed with *GAFCHROMIC® HD-V2* RCF being wrapped in $5\,\mu\mathrm{m}$ Al foil. In both cases, ^{4}He gas at a backing pressure of 30 bar served as plasma target. The 0.5 mm de Laval nozzle was attached to the valve. The maximum particle density at this backing pressure is $n_{\mathrm{max}} \approx 6 \times 10^{19}\,\mathrm{cm}^{-3}$ (in a height of $500\,\mu\mathrm{m}$ above the nozzle edge) which corresponds to $0.06\,n_{\mathrm{c}}$.

Figure 7.9 illustrates irradiated RCF from the right and left side with regard to the laser propagation direction for laser shot-# 11159 (01). The RCF were labeled before each laser shot: after the beamtime, it is important to correctly assign the shot number as well as the laser direction to each set of exposed detectors. Next to exposed RCF also a non-irradiated *HD-V2* RCF can be regarded in the bottom part of the image. The original yellow dye color turns green when exposing the RCF to ionizing radiation. Due to the Al shielding, only gammas and laser-accelerated ^{4}He ions with energies $> 1.6\,\mathrm{MeV}$ could reach the active RCF layer, but no side-scattered laser light. Hence, the color change is due to ions and gammas. It becomes obvious that a nearly homogeneous color change is present (exposure to gammas) which is interspersed with more intense regions (laser-accelerated ^{4}He ions). *Additional information:* the "shadows" of the paper-clips for fixing the RCF at the wrap-around holder can clearly be recognized (nearly no radiation could pass the paper clips). The dimensions of the RCF were $l_{\mathrm{RCF}} = 140\,\mathrm{mm}$ and $h_{\mathrm{RCF}} = 40\,\mathrm{mm}$.

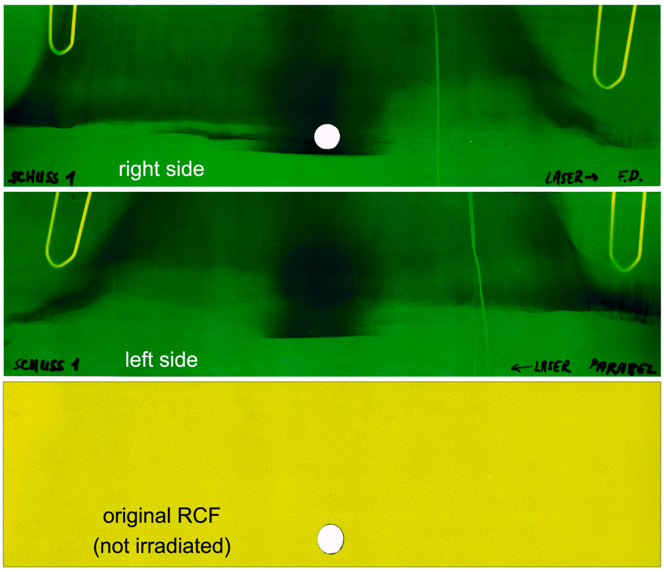

Figure 7.9.: Irradiated RCF from shot-# 11159 (01). *Top:* right side, *center:* left side, *bottom:* original RCF, *i.e.* not irradiated. Length: $l_{\mathrm{RCF}} = 140\,\mathrm{mm}$, height: $h_{\mathrm{RCF}} = 40\,\mathrm{mm}$.

In order to analyze the RCF signals, it is important to define a coordinate system for the RCF wrap-around measurements: in Fig. 7.10 (a) and (b) a cylindrical coordinate system as well as the dimensions regarding the RCF wrap-around detectors are illustrated. A point P on the RCF surface can be defined by $x_{\mathrm{RCF}} = r_{\mathrm{RCF}} \cos\varphi$, $y_{\mathrm{RCF}} = r_{\mathrm{RCF}} \sin\varphi$, and $z_{\mathrm{RCF}} = z$. Here, r_{RCF} is the (constant) radius of the RCF holder, φ is the azimuth angle relative to the x_{RCF}-axis in the x_{RCF}-y_{RCF}-plane, and z is the height. The origin of the coordinate system is placed within the TCC. The RCF detectors are mounted circularly around the TCC (radius $r_{\mathrm{RCF}} = 52\,\mathrm{mm}$). For the focusing/diverging laser beam an entrance/exit gap of 26.2 mm and 20 mm is given. Thus, an angular range of $11.1^\circ \leq \varphi \leq 165.4^\circ$ was covered at each side of the TCC. The laser pulse propagates in $+x_{\mathrm{RCF}}$-direction. The RCF longitudinal is equal to the length of the arc of the RCF circle b_{RCF}. With the relation

$$\frac{b_{\mathrm{RCF}}}{2\pi\, r_{\mathrm{RCF}}} = \frac{\varphi - \varphi_{\mathrm{exit}}}{360^\circ}\,, \tag{7.2}$$

the length of the arc of the circle b_{RCF} can be related to a specific angle φ relative to the laser axis, and vice versa. With the given setup, an angle of *e.g.* $\varphi = 90^\circ$ corresponds to a distance of $b_{\mathrm{RCF}} = 71.61\,\mathrm{mm}$ from the forward RCF boundary in Fig. 7.9.

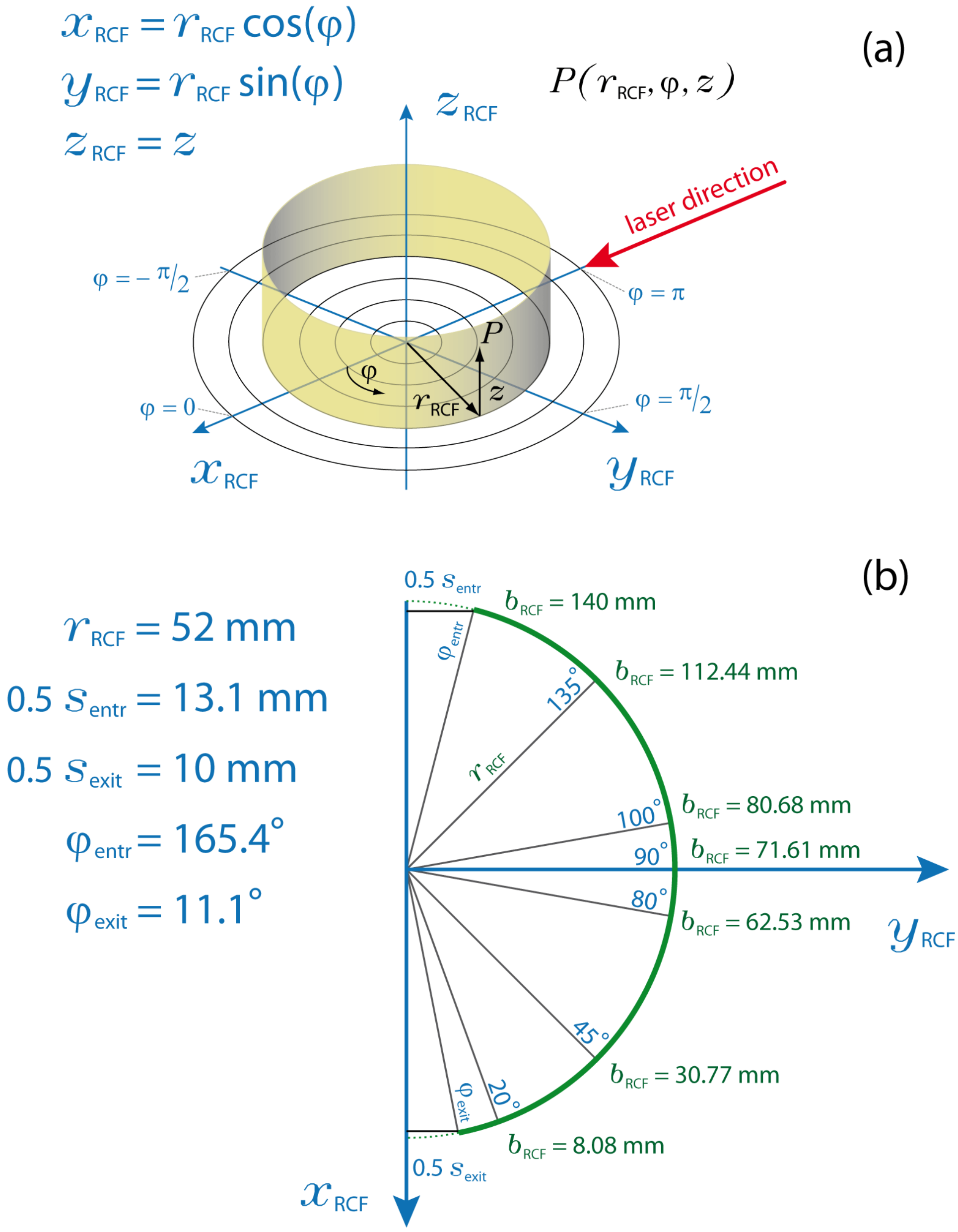

Figure 7.10.: (a) Cylindrical coordinates and (b) dimensions regarding the RCF wrap-around detector. The distance from the TCC (here: the origin of the coordinate system) to the RCF detectors is $r_{\mathrm{RCF}} = 52\,\mathrm{mm}$. The laser propagates in $+x_{\mathrm{RCF}}$-direction. The lengths of specific arcs of the RCF circle b_{RCF}, *i.e.* the specific RCF lengths at fix angles relative to the laser axis, are marked.

The RCF images were analyzed with *ImageJ*. A 3D surface plot converts the gray scale values into a vertical data information which arises from the RCF plane. Additionally, pseudo colors help to identify color gradations. Figure 7.11 illustrates such a pseudo-color surface plot for laser shot-# 11159 (01).

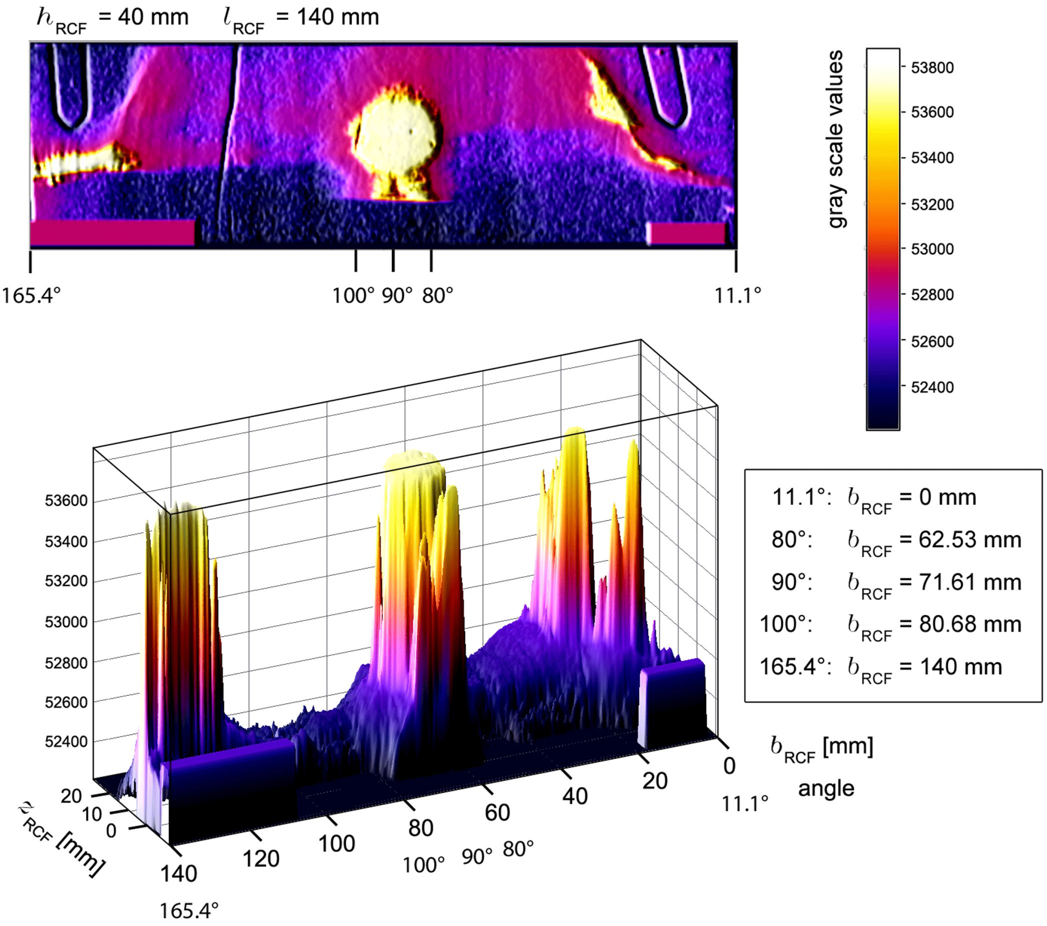

Figure 7.11.: Irradiated RCF (left side) from shot-# 11159 (01): 3D surface plot. *Top:* top view, *bottom:* perspective view. The gray scale values are defined by pseudo colors. The angles relative to the laser axis are marked on the abscissae and the corresponding circular arc lengths b_{RCF} are listed in the inset.

In the upper half of the image, a top view of the RCF (left side) is given. The determined angles relative to the laser direction are marked on the abscissa. The huge ion signal around 90° can be regarded. In the lower half of the image, a perspective view of the same image is illustrated. The b_{RCF}-axis with the corresponding angles φ as well as the RCF height z_{RCF} are drawn. It is important to note that the TCC height was taken as a reference for the signal height z_{RCF}: the height of 11 mm from the lower RCF boundary was set to zero. This is due to the fact that all TPs were aligned in the same height in order to catch laser-accelerated helium ions in the focal plane. Regarding the 3D surface plot, it becomes obvious that the angular distribution of $^{4}\mathrm{He}^{1+,2+}$ ions in the transverse direction is concentrated around 90° relative to the laser propagation direction and extends to about $z_{\mathrm{RCF}} = 20\,\mathrm{mm}$ above the TCC (in terms of spherical coordinates, this vertical displacement corresponds to a polar angle ϑ of about 21°). A lineout along the RCF longitudinal for $z_{\mathrm{RCF}} = 0$ (TCC height) is illustrated in Fig. 7.12. The background-corrected gray scale values are plotted against φ. The angular FWHM of the transversal peak in ion signal is $\varphi_{\mathrm{fwhm}} = 23°$ (from 80.7° to 103.7°). The angular RCF-obtained ion distribution is in line with the corresponding EPOCH simulations (*cf.* Fig. 5.7 on p. 63, Sec. 5.3.2).

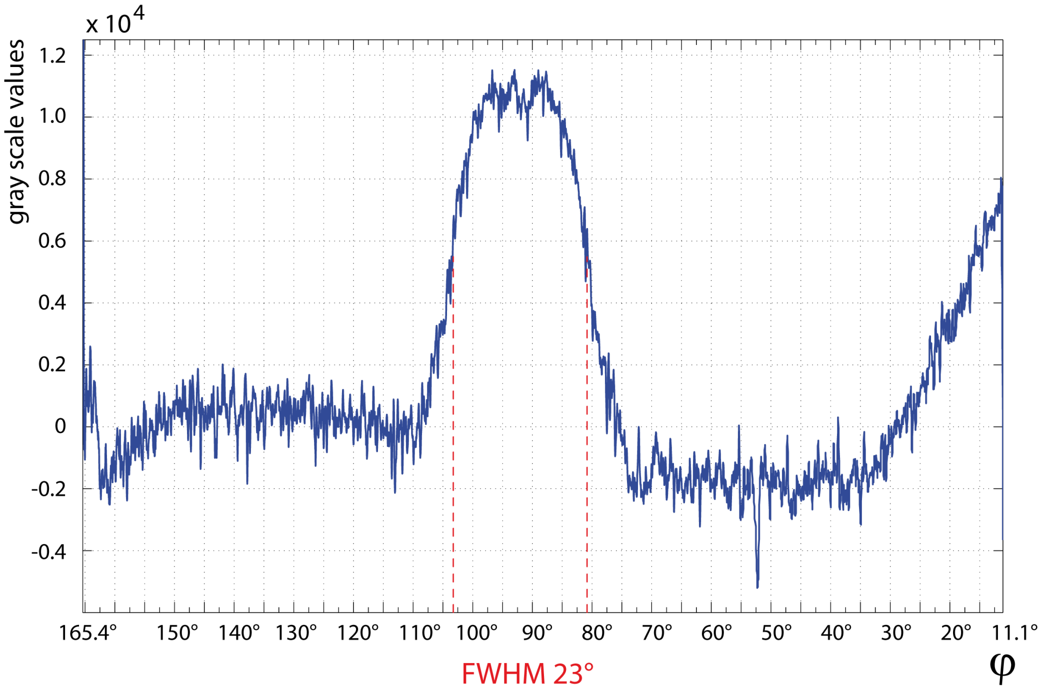

Figure 7.12.: BG-corrected lineout along the RCF longitudinal in the focal height (shot-# 11159 (01)). The angles relative to the laser axis are marked on the abscissa. Around 90° a peak in ion signal was detected. The FWHM has a value of 23°.

Furthermore, both in forward and in reverse direction intense ion signals could be detected in the angular ranges of $23.4° \leq \varphi \leq 42.9°$ and $143.4° \leq \varphi \leq 165.4°$, respectively. In both cases, the helium ions got a vertical momentum component, *i.e.* the signals are detected above the focal plane. Moving from both RCF boundaries to the RCF center, the ion distribution narrows with increasing height. In order to investigate the ion distribution also in larger heights above the TCC, a second RCF wrap-around measurement was conducted with *HD-V2* RCF. The new RCF height was 100 mm, the length was not changed. Figure 7.13 illustrates the laser-accelerated helium ion signal up to $z_{\mathrm{RCF}} = 100\,\mathrm{mm}$ for laser shot-# 11169 (06). The basic shape of the angular distribution is comparable to the prior data. It becomes obvious, that with increasing z_{RCF} the narrowing in ion signal continues but peters out, *i.e.* the RCF are exposed to less dose. Either the number of laser-accelerated $^4\mathrm{He}^{1+,2+}$ ions decreases for these angular ranges, or the particle energies. And since the 5 µm Al shielding filters low-energy ions, less dose will be absorbed by the RCF.

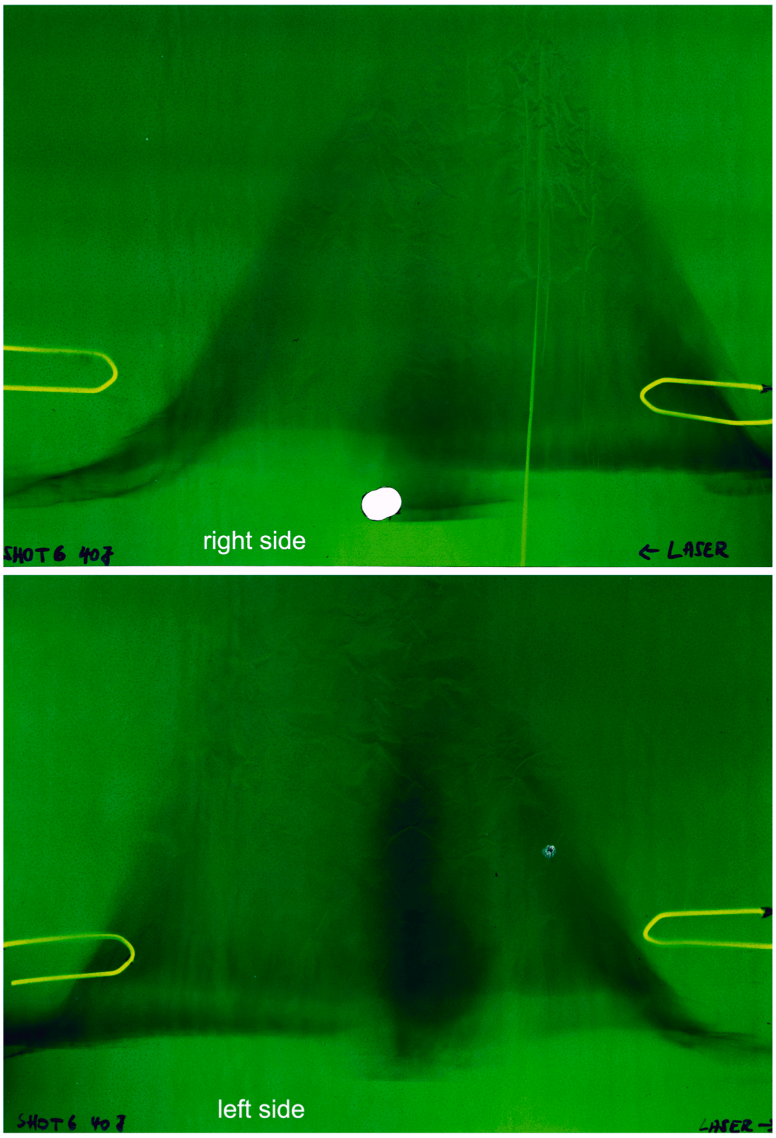

Figure 7.13.: Irradiated RCF from shot-# 11169 (06). *Top:* right side, *bottom:* left side. Length: $l_{\mathrm{RCF}} = 140\,\mathrm{mm}$, height: $h_{\mathrm{RCF}} = 100\,\mathrm{mm}$.

The RCF wrap-around measurements allow only a qualitative analysis of the angular ion distribution. The ion species as well as specific ion energies cannot be extracted from the raw data. Therefore, attendant TP measurements were conducted around 90° relative to the laser direction. As described in Sec. 7.2.1 on p. 115, the TPs were aligned in the height of the TCC. In order to analyze ion signals above the TCC height quantitatively with a TP, the spectrometer has to be aligned inclined, *i.e.* at a specific polar angle ϑ relative to the ion source. Thus, it can be ensured that laser-accelerated helium ions enter the TP parallely to the z_{tp}-axis without clipping at the hardware, and furthermore, only one intrinsic momentum component ($\boldsymbol{p}_z$) is present.

Ion energy spectra

The TP measurements for extracting the energy spectra for both helium-ion species were performed with *Agfa MD4.0* IPs. As stated in Sec. 6.2.6, these IPs could not be calibrated with $^{3,4}\mathrm{He}^{1+,2+}$ ions. Therefore, the obtained IP signals do not yield any credible quantitative information about the real ion number, but the achieved ion energies could be determined for various laser-target parameters. The ion-energy spectra, *i.e.* the normalized signal intensity (per MeV and Sr, $\log_{10}$-scale) against the ion energy (in MeV, lin. scale), could be extracted from the IP scans. A TP-analysis *Matlab* code was used for this purpose [Swa15]. The IP raw data serves as input for the code. The zero order has to be defined manually (oversaturated single pixels). The ion-species properties (charge, mass) as well as the field parameters (length, strength) have to be set. According to these input parameters, the code simulates the corresponding particle parabola along which the image data, *i.e.* the gray scale values, are extracted, and henceforward, related to the particle energies. Furthermore, the background values instantly are subtracted. In addition, the obtained ion energies can also be compared to the *CST*-simulated data regarding the energy-deflection dependencies (*cf.* Sec. 6.2.4 on p. 92). The *CST*-simulated energy-deflection fit parameters a and b in Eq. (6.19) on p. 95 for all $^{3,4}\mathrm{He}$ ion species as well as for all TP configurations are listed in Tab. 7.2. With the help of these fit parameters, any desired deflection in y_{tp}-direction (on the ion parabola within the IP raw image) of a specific helium ion species in a particular TP directly can be transformed into the corresponding ion energy: $\mathcal{E}_{\mathrm{ion}} = a y_{\mathrm{tp}}^{-2} + b$.

TP-#	*ion species*	a [keV m^2]	b [keV]
TP-90	$^4\mathrm{He}^{2+}$	2.3170	24.570
	$^4\mathrm{He}^{1+}$	0.5790	6.819
	$^3\mathrm{He}^{2+}$	3.0880	34.390
	$^3\mathrm{He}^{1+}$	0.7719	9.577
TP-80 & TP-100	$^4\mathrm{He}^{2+}$	2.2680	24.570
	$^4\mathrm{He}^{1+}$	0.5669	6.812
	$^3\mathrm{He}^{2+}$	3.0230	34.370
	$^3\mathrm{He}^{1+}$	0.7556	9.576

Table 7.2.: *CST*-simulated energy-deflection fit parameters a and b for $^{3,4}\mathrm{He}$ ion species for all TP configurations, according to Eq. (6.19) on p. 95.

In order to gain knowledge about the real ion number, TP-80 was armed with a CR-39 detector during laser shot-# 11174 (09). In order not to run the risk of oversaturating the SSNTDs, TP-80 was chosen according to the aforegoing own EPOCH simulations (*cf.* Sec.5.3.2 on p. 61). Furthermore, within laser shot-# 11174 (09) a decreased He backing pressure should also ensure a decreased number of laser-accelerated helium ions.

He ion signal for shot-# 11159 (01) Simultaneously to the described RCF wrap-around measurement during laser shot-# 11159 (01), TP-90 was armed with an IP detector. 23 min after exposure, the IP was scanned. Two sharp Thomson parabolas were recorded. Directly after having extracted the scanned data, the signals, *i.e.* the deflection parameters in x_{tp}- and y_{tp}-direction, were roughly analyzed and cross-checked with the *CST*-simulated data for $^4\text{He}^{1+,2+}$ ions in order to verify the experimental outcome regarding the accelerated ion species. Figure 7.14 illustrates the IP scan in pseudo colors (originally, the 16 bit *.tif*-files are saved in gray scale values, *cf.* Fig. 7.17). One pixel corresponds to 25 µm. The $\{x, y\}_{\text{tp}}$-axes, *i.e.* the E- and B-deflection directions, were added to the plot (units in cm).

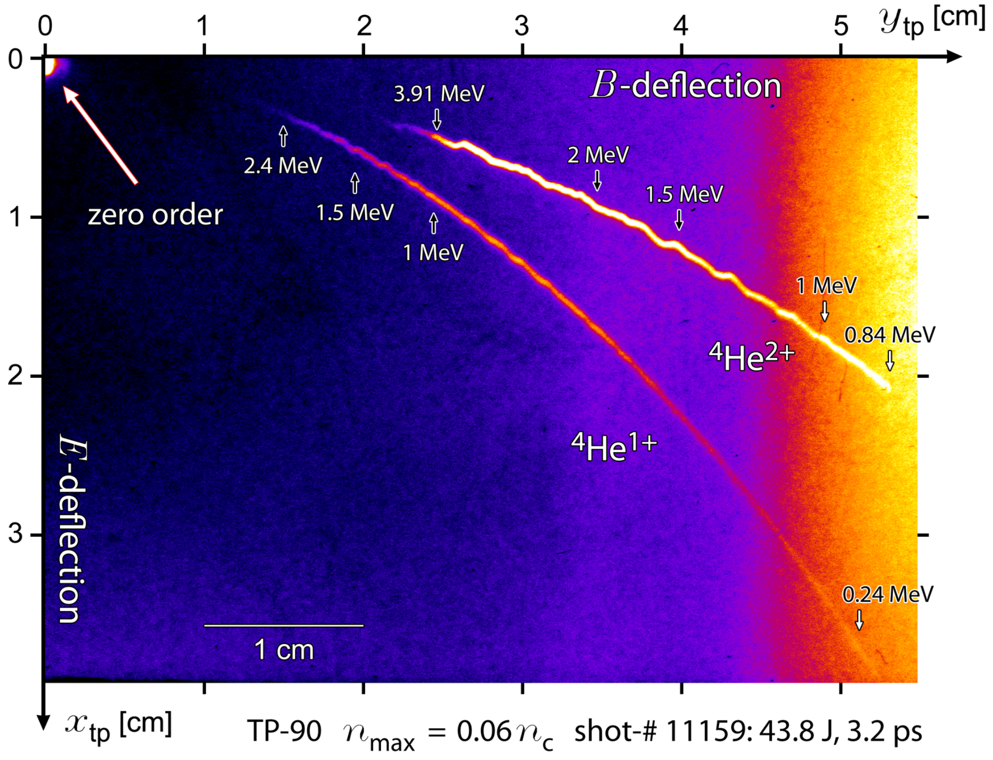

Figure 7.14.: $^4\text{He}^{1+,2+}$ Thomson parabolas from TP-90 for laser shot-# 11159 (01). The maximal particle density inside the gas jet was $0.06\,n_{\text{c}}$. Exemplarily, some y_{tp} values were transformed into the corresponding *CST*-simulated ion energies.

In the origin of the coordinate system, the *zero order* can be regarded. It is mainly due to gamma radiation from the laser-target interaction, and possibly also from side-scattered laser light. Physically, it is a gamma image of the plasma region (the pinhole in the specific distance to the TCC functions as a pinhole camera). The zero order is very important for the IP analysis, since it serves as a reference on the detector plane. With the current brightness/contrast settings it might look oversaturated, but indeed only a few of the inner pixels are so. Exemplarily, some y_{tp} values were transformed into the corresponding *CST*-simulated ion energies using the fit function for $^4\text{He}^{1+,2+}$ in TP-90 in Tab. 7.2. The Thomson parabola width δ_{tp90} can be determined to (360 ± 5) µm. Taking Eq. (6.20) and Fig. 6.29 on p. 95 *f.* into account, this leads to a normalized energy uncertainty $\Delta\mathcal{E}\mathcal{E}^{-1}$ of about ~ 0.030 for $\mathcal{E} = 3.91\,\text{MeV}$ and about ~ 0.014 for $\mathcal{E} = 0.84\,\text{MeV}$ ($^4\text{He}^{2+}$ parabola).

The right side of the image actually is the top side of the IP. The decreasing background signal is represented by the color gradient from the right (yellow) to the left (deep blue to black). It is maximal about 1 cm from the right (*i.e.* upper) IP boundary and overlies the low-energy tails of the ion parabolas. This disturbing background is due to less lead shielding, and thus, transmitted gamma radiation. As stated above, for the first laser shots only 2 mm lead shielding was applied. Later on, the shielding was doubled to 4 mm. The background signal could be suppressed.

In Fig. 7.15 the corresponding ^{4}He$^{1+,2+}$ ion-energy spectra are illustrated (blue line: ^{4}He^{2+}, red line: ^{4}He^{1+}). The normalized gray scale values from the Thomson parabolas (units in MeV^{-1} Sr^{-1}) are plotted against the ion energies.

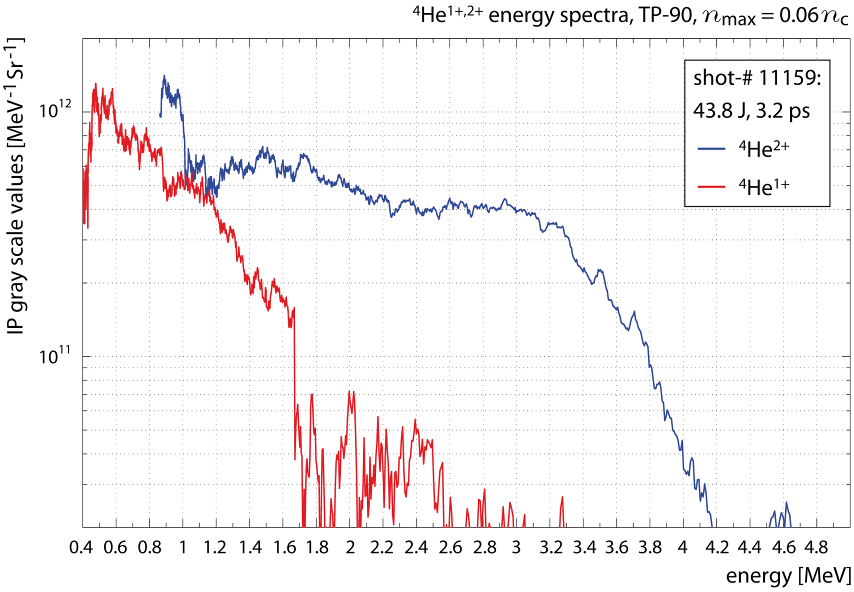

Figure 7.15.: ^{4}He$^{1+,2+}$ ion-energy spectra from TP-90 for laser shot-# 11159 (01): in blue ^{4}He^{2+}, in red ^{4}He^{1+}. The maximal particle density inside the gas jet was $0.06\,n_c$. The obtained IP gray scale values were standardized to 1 Sr^{-1}.

It might be conspicuous that in case of ^{4}He^{1+} the minimal ion energies in Fig. 7.14 are not plotted. This is due to the fact that the ^{4}He^{1+} parabola became almost indistinct with the gamma background for the low energy range. Therefore, energies between 0.24 and about 0.5 MeV had to be cut. In case of ^{4}He^{2+} ions, the signal was much stronger so that it was distinguishable from the disturbing gamma signal.

Taking into account that the gray scale values of the IP scans depend on the incident ion dose (energy, ion number), then *roughly speaking* a larger gray scale value corresponds to a larger ion number at constant energy. When regarding the energy spectra for the first laser shot, it can be concluded that the recorded ^{4}He^{1+} signal is smaller in intensity (compared to ^{4}He^{2+} a factor of ~ 4 less at 1.6 MeV, *e.g.*) and furthermore ^{4}He^{1+} were accelerated to lower energies. The high-energy and low-energy cut-offs for ^{4}He^{2+} are 4.6 MeV and 0.84 MeV, while for ^{4}He^{1+} the energy spectrum yields a small peak discriminable from background noise around 3.27 MeV. It has to be noted that by manually manipulating the brightness/contrast parameters of the raw IP data, a high-energy cut-off of 3.4 MeV can hardly be determined by eye.

The energy spectra for both ion species basically look quite familiar regarding thermal energy spectra: a peak in ion number (or signal intensity) at low energies and a decrease in signal for higher energies. For ${}^4\mathrm{He}^{1+}$, the signal decreases nearly one order of magnitude in the energy range of 0.5 and 1.65 MeV. The sharp saltus at 1.65 MeV is striking. For the ${}^4\mathrm{He}^{2+}$ spectrum, a peak in signal intensity is given between 0.9 and 1 MeV. A nearly plateau-like saddle in signal intensity is given till an energy of about 3.2 MeV. For higher energies, the signal decreases to the zero baseline at 4.17 MeV. A small peak between 4.5 and 4.65 MeV terminates the signal.

Angular energy measurement In Fig. 7.16 (a) and (b) the energy spectra for both ${}^4\mathrm{He}$ ion species are plotted for laser shot-# 11173 (08) (dependent on the emission angle). The laser beam energy after compression was 38.3 J at a pulse duration of 0.8 ps. Regarding the beam energy, this shot can be compared to the first laser shot (the pulse durations differ a lot: 3.2 ps and 0.8 ps). The maximum particle density in focal height was about $0.06\,n_c$. The line-color code in the plots is: blue for TP-90, red for TP-100, and brown for TP-80. The first plot, (a), represents the extracted ${}^4\mathrm{He}^{1+}$ ion-energy spectra. The basic shape of the spectra with regard to the emission angle is similar to each other. The maximal energy cut-offs were reached in TP-90 (~ 3 MeV), followed by TP-100 (~ 2.75 MeV) and finally TP-80 (~ 2.25 MeV). Regarding the normalized signal intensities and the shape of the spectrum, similarities for TP-90 and -100 can be regarded, while for TP-80 the decrease in signal develops rapidly. A difference between the TP-90 and -100 signal is the formation of a saddle in the TP-100 signal (from 0.8 to 1.3 MeV). For higher energies, the signal shape is similar to the TP-90 data again. Regarding all TP data, less ${}^4\mathrm{He}^{1+}$ ions were emitted at $-80°$. This partial result is in good agreement with the RCF wrap-around measurements, where the FWHM of the signal peak in focus height was ranged between 80.7° and 103.7° relative to the laser direction (*cf.* Fig. 7.12).

In Fig. 7.16 (b), the ${}^4\mathrm{He}^{2+}$ energy spectra are plotted. As it could be concluded for the ${}^4\mathrm{He}^{1+}$ spectra in (a), TP-80 recorded the smallest signal and the high-energy cut-offs are maximal for TP-90: ~ 4.06 MeV at $-90°$, ~ 3.52 MeV at $-100°$, and ~ 3.4 MeV at $-80°$. A difference to the ${}^4\mathrm{He}^{1+}$ case is the spectrum shape: saddle structures are stretched out over longer energy ranges. The rapid decrease in the TP-90 signal intensity starts at 3.4 MeV and for TP-100 it is more sharp at 2.8 MeV (followed by a second plateau to 3 MeV). For TP-80, a saddle between 2.2 and 3 MeV is given. Regarding the TP-100 signal, the huge peak in normalized signal intensity in the low-energy region is striking. When having a look into the IP raw images, it becomes obvious that *doubled parabolas*, *i.e.* secondary "parallel" ion traces slightly shifted in side, were recorded.

Figure 7.17 illustrates this phenomenon. From the left to the right of the image, the TP-100 to TP-80 data can be regarded. The ion species for both doubled parabolic branches is the same, but the incidence angle of the laser-accelerated ions of the same species varies. Therefore, the trajectories inside the TP fields are slightly changed which causes the separation on the detector plane. [TA08, TA10, Sok11] reported on these

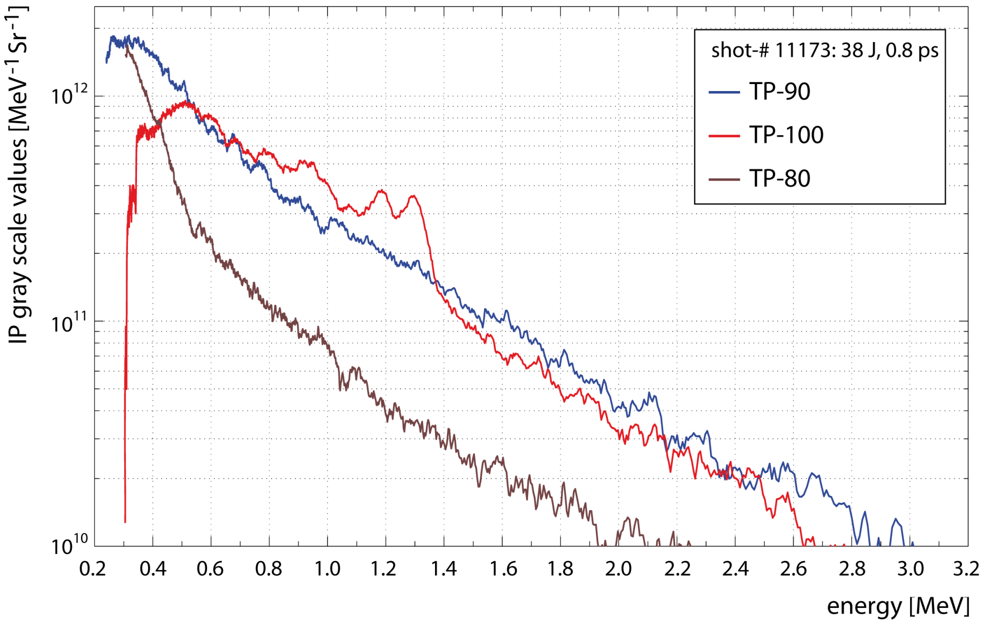

(a) ^{4}He^{1+} energy spectra, $n_{\mathrm{max}} = 0.06\,n_{\mathrm{c}}$

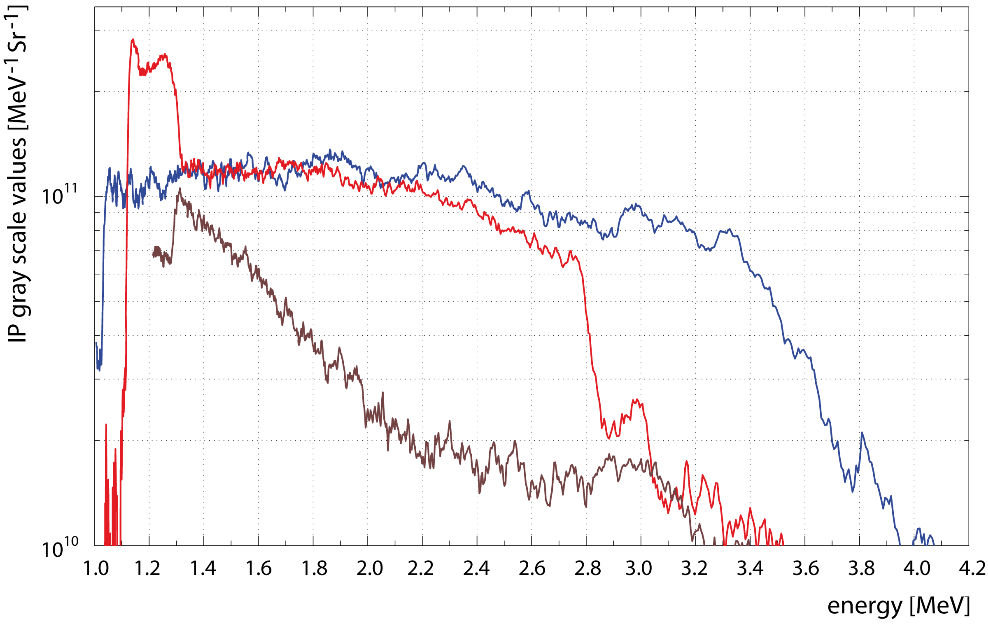

(b) ^{4}He^{2+} energy spectra, $n_{\mathrm{max}} = 0.06\,n_{\mathrm{c}}$

Figure 7.16.: ^{4}He$^{1+,2+}$ ion-energy spectra for laser shot-# 11173 (08): in blue TP-90, in red TP-100, in brown TP-80.

Thomson parabola fluctuations or "irregularities" effects for laser-accelerated protons from foil targets. Here, the two spatially separated proton sources were due to different absorption mechanisms inside the plasma region: ponderomotively-driven electrons and resonance absorption. Both electron "species" can boost proton acceleration by building up (spatially separated) secondary electrostatic fields. The ASE level of the laser pulse influences which absorption mechanism will dominate. This effect can be investigated by manipulating the contrast and conducting a Čerenkov emission measurement in order to gain information about the specific electron dynamics. According to [TA10], a laser contrast ratio of $10^7 - 10^8$ will promote spatially separated particle sources (in case of laser-foil interaction and with the used laser parameters, of course). In the PHELIX experiment, a laser contrast of 10^7 was used. The origin of the measured irregularities could not be investigated since a flexible reaction on an unforeseen data output is hardly possible within laser beamtime.

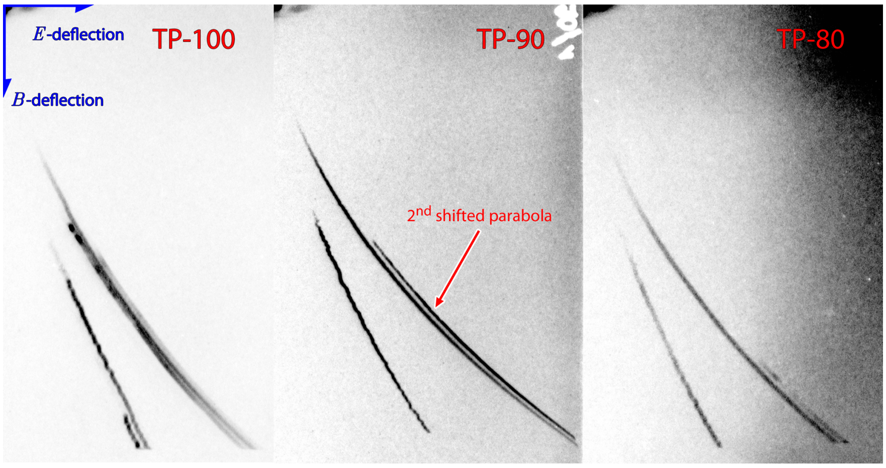

Figure 7.17.: Irregularities of the Thomson parabolas in laser shot-# 11173 (08): *from the left to the right*: raw IP scans for TP-100, TP-90, and TP-80 (the brightness/contrast settings as well as the image sizes vary).

Laser energy The influence of the attached laser energy on the achievable ion energies is exemplified in Fig. 7.18 for laser shot-# 11163 (03) and 11173 (08): 119.1 J (after compression) at 0.4 ps and 38.3 J at 0.8 ps. The ion spectra for both ^{4}He ion species were extracted from the TP-90 data. The color code indicates the ion species and the line width represents the specific laser shot (*cf.* the inset). It becomes obvious that the $^4\text{He}^{2+}$ high-energy cut-off is enlarged to $\sim 10.9\,\text{MeV}$, *i.e.* a factor of about $\times 2.7 \approx \times 3$ in comparison to laser shot-# 11173 (08)[5]. In contrast to $^4\text{He}^{2+}$, the $^4\text{He}^{1+}$ high-energy cut-off is constant ($\sim 3\,\text{MeV}$). The basic shape of the spectra for the same species is comparable. But, the normalized signal intensities for low ion energies are approximately one order of magnitude larger than in the low-energy laser shot (regarding the same ion species).

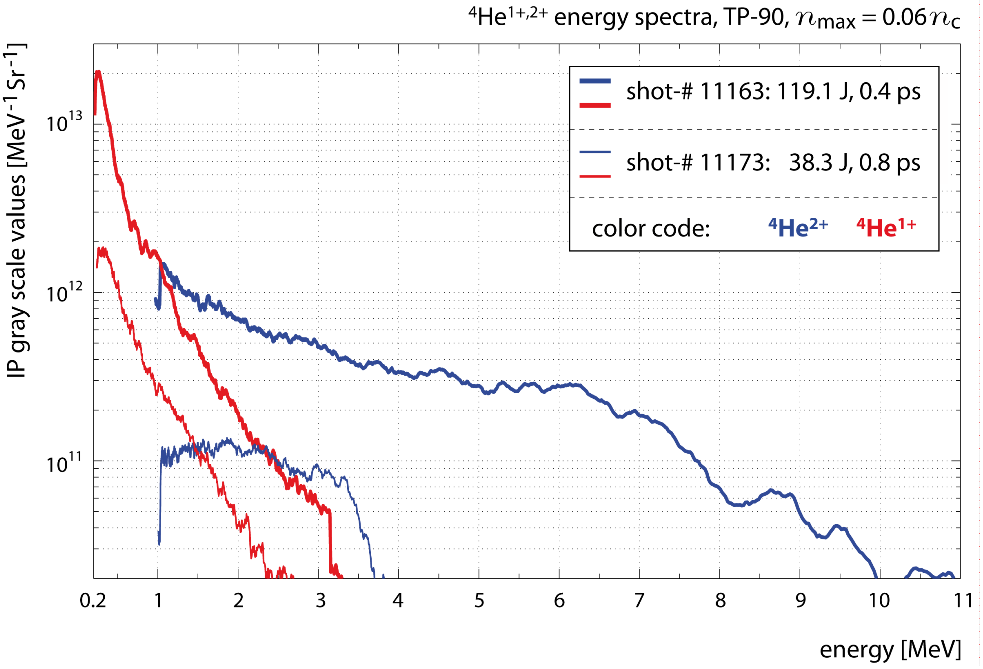

Figure 7.18.: $^4\text{He}^{1+,2+}$ ion-energy spectra from TP-90 for laser shot-# 11163 (03) and 11173 (08): in blue $^4\text{He}^{2+}$, in red $^4\text{He}^{1+}$. The thicker line width is assigned to the maximum-energy laser shot. The maximal particle density was $0.06\,n_c$.

---

[5] note: the limit of the normalized signal-intensity axis was changed according to the high-energy data. Therefore, the data from Fig. 7.16 is cut to smaller values.

Particle-density dependency During the measurements, two different helium-4 gas pressures were attached: 30 bar ($n_{\mathrm{max}} = 0.06\,n_{\mathrm{c}}$ in 500 µm above the nozzle edge) and 14 bar ($n_{\mathrm{max}} = 3.25 \times 10^{19}\,\mathrm{cm}^{-3} \approx 0.03\,n_{\mathrm{c}}$ in a height of 500 µm). Figure 7.19 (a) and (b) illustrate the ion-energy spectra for both density regimes.

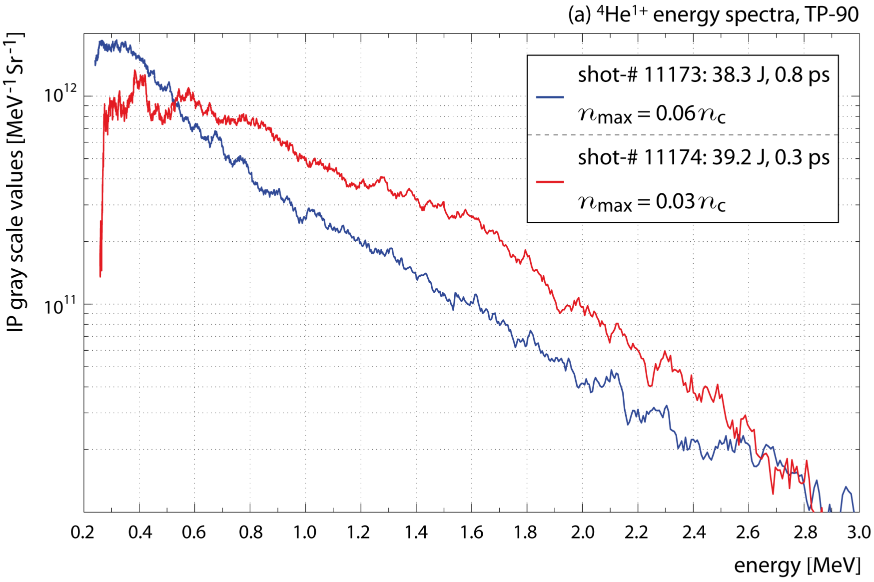

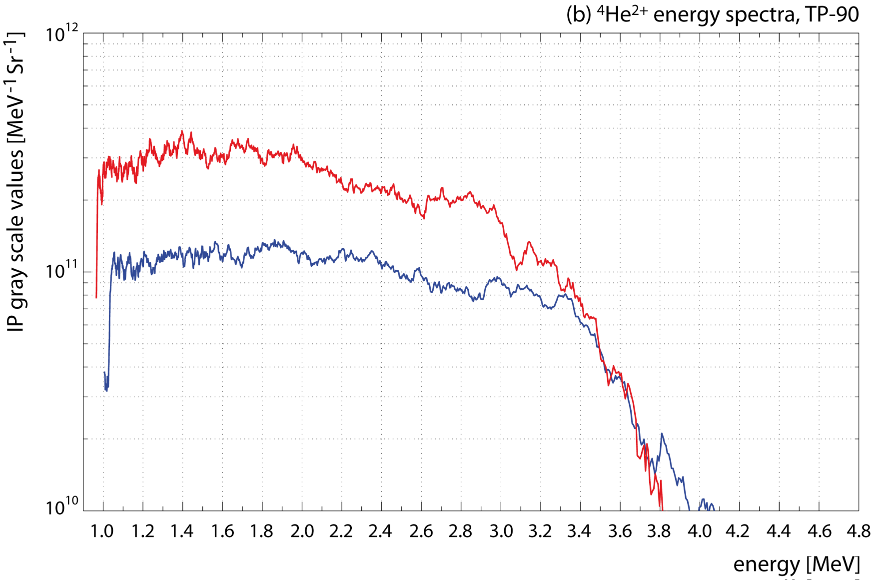

Figure 7.19.: ^{4}He$^{1+,2+}$ ion-energy spectra from TP-90 for laser shot-# 11173 (08) and 11174 (09): in blue $0.06\,n_{\mathrm{c}}$, in red $\sim 0.03\,n_{\mathrm{c}}$. (a) ^{4}He^{1+}, (a) ^{4}He^{1+}

The line-color code is blue for $0.06\,n_{\mathrm{c}}$, and red for $0.03\,n_{\mathrm{c}}$. The inset is valid for both sub-figures. It can be regarded that the shapes of the spectra (for the same ion species) as well as the maximal achieved high-energy cut-offs do not differ much (mean difference of 0.2 MeV in both cases). But, in case of the lower-dense gas-jet target, the normalized signal intensity is larger for both ion species. This result is interesting since, as published in [Wei04] (*cf.* Sec. 3.2.5 on p. 28), an about one order of magnitude higher particle density leaded to higher $^{4}\mathrm{He}^{2+}$ energies ($\sim \times 6$). Basically, it can be assumed that with a higher particle density inside the neutral helium gas *more* plasma constituents are present after ionizing the medium. Hence, also *more* ions could have been accelerated to *higher* energies since the acting forces are stronger. Within the PHELIX experiment i009, a decrease in density by a factor of two does not result in significant changes (in comparison to a factor of 10 in [Wei04]). Unfortunately, the laser parameters regarding the pulse duration have changed during both laser shots: a difference of $\Delta\tau_{\mathrm{L}} = 0.5\,\mathrm{ps}$ is present. It cannot be concluded if the larger signal intensity is due to the decreased pulse duration or to the decreased maximum helium density.

Acceleration of ^{3}He ions from unpolarized gas Since the first part of the experimental studies at PHELIX demonstrated the feasibility of ^{4}He-ion acceleration out of underdense gas-jet targets, for the following beamtime unpolarized ^{3}He gas was attached as plasma target.

3 bar l of ^{3}He gas was given in a 0.2 l gas bottle, leading to an intrinsic pressure of 15 bar. Due to the additional volume of the tube connection to the valve, the backing pressure in front of the nozzle throat will be declined. Before the experiment, a decreased backing pressure of 13 bar was calculated for a given amount of tubes with known inner diameter. But finally during the beamtime, the internal volume necessarily had to be increased by using different tubes with a larger inner diameter. Therefore, after attaching the gas to the valve, the backing pressure was decreased to 8 bar. At 8 bar the maximal particle density in a height of 500 µm above the nozzle edge is $n_{\mathrm{max}} \approx 1.67 \times 10^{19}\,\mathrm{cm}^{-3} \approx 0.02\,n_{\mathrm{c}}$. The first laser shots on ^{3}He were conducted with these density parameters. $^{3}\mathrm{He}^{1+,2+}$ ions could be successfully accelerated. But in order to reach a higher backing pressure, additional ^{3}He gas was borrowed from the Mainz study group *Helium-3* [Hei]: 7.5 bar l ^{3}He (17 bar in a 0.44 l gas bottle). Now, a backing pressure of 14 bar was reached in front of the nozzle throat: a pressure comparable to the second density setting with ^{4}He gas. However, *Murphy's law* struck again: the valve had a malfunction and could not be operated anymore. Of course, the valve problem could have been fixed during the beamtime. But the whole precious ^{3}He filling (14 bar) would have been lost when opening the gas system. And since the "new" Mainz gas pressure was also decreased to 14 bar (nearly the same pressure as the intrinsic ^{3}He filling right in the beginning), a refilling of the tube system would have been yielded a backing pressure below 8 bar. Hence, fixing the valve would not have been of enormous (or even of *any*) benefit. Therefore, the beamtime was shut down at this point. *"Whatever can go wrong will go wrong."*

The last sentence in the previous paragraph is only partially true: in Fig. 7.20 the scanned IP images from laser shot-# 11188 (14) can be regarded. From this raw data, three conclusions can be drawn. Firstly, next to ^{3}He-ion Thomson parabolas also weak ^{4}He traces were recorded (primarily in TP-90). They are due to small portions of ^{4}He rest gas inside the tube system. Of course, the supply pipes were evacuated before filling the system with pure ^{3}He gas, but the remaining amount of ^{4}He inside the pressure reducer unit apparently was large enough for a detectable signal on the IPs. This is an indirect proof for the sensitivity of the applied spectrometer and the used IPs. Secondly, at −80° only ^{3}He^{1+} ions were accelerated. The visible second Thomson parabola in TP-80 is a ^{4}He^{2+} ion signal. This can easily be verified by laying scans with each a ^{4}He- and a ^{3}He-ion signal on top of another and adjusting the transparency of the upper image. And finally, the ^{3}He^{2+} Thomson parabola in TP-90 is uncontinuous for "higher" energies, *i.e.* the trace is interrupted. This is also visible in the corresponding ion-energy spectrum.

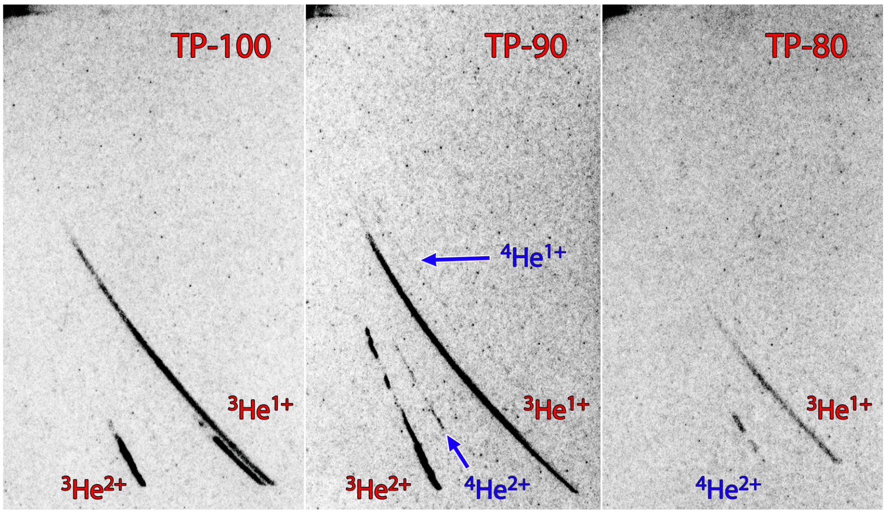

Figure 7.20.: ^{3}He ion Thomson parabolas for all TPs. Next to ^{3}He ions, also a small amount of ^{4}He$^{1+,2+}$ ions was laser-accelerated and detected within the spectrometer.

In the following Fig. 7.21 (a) and (b), the ^{3}He$^{1+,2+}$ ion-energy spectra are illustrated. The laser/target parameters were defined as: 57 J (after compression), 0.6 ps, and 0.01 n_c. In (a), the ^{3}He^{1+} spectra are plotted. The high-energy cut-off energies in TP-90 and -100 are a factor of about ∼ ×0.33 (TP-90 and TP-80) and ∼ ×0.43 (TP-100) smaller than the ones extracted from laser shot-# 11173 (08) (with a maximal ^{4}He density of 0.06 n_c, 38 J, 0.8 ps): for TP-90 it is ∼ 1.07 MeV, for TP-100 the high-energy cut-off is ∼ 1.18 MeV, and for TP-80 it is ∼ 0.7 MeV. Compared to shot-# 11173 (08), also the normalized signal intensities for lower energies are reduced.

Comparing the ^{3}He^{2+} ion spectra in Fig. 7.21 (b) to the corresponding TP data from shot-# 11173 (08), it becomes obvious that for TP-90 and -100 the high-energy cut-offs are nearly halved: 2.16 MeV (TP-90) and 1.64 MeV (TP-100), respectively. As it could be concluded from the raw data, the ^{3}He^{2+} spectrum for TP-90 exhibits several interruptions, and thus, peaks are formed. The normalized signal intensity decreases to zero in the energy ranges 1.45 − 1.54 MeV, 1.67 − 1.7 MeV, and 1.73 − 1.79 MeV. Considering the ion propagation through the TP fields, it can be concluded that the incident ^{3}He^{2+} ion beam consisted of several energy "bunches" at −90° relative to the laser axis. In contrast to the TP-90 data, the TP-100 spectrum is continuous and shows a rapid decrease in signal intensity between 1.45 MeV and 1.55 MeV.

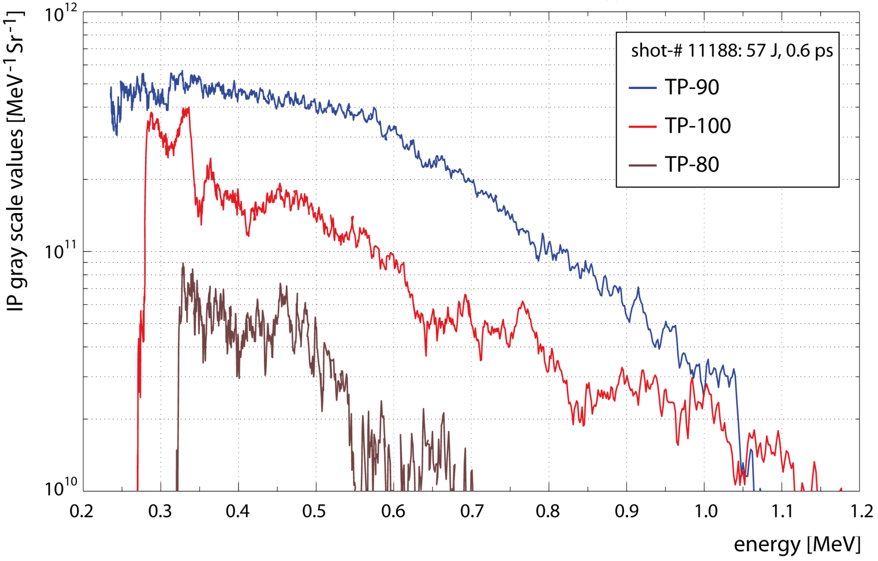

(a) ^{3}He^{1+} energy spectra, $n_{\text{max}} = 0.02 n_c$

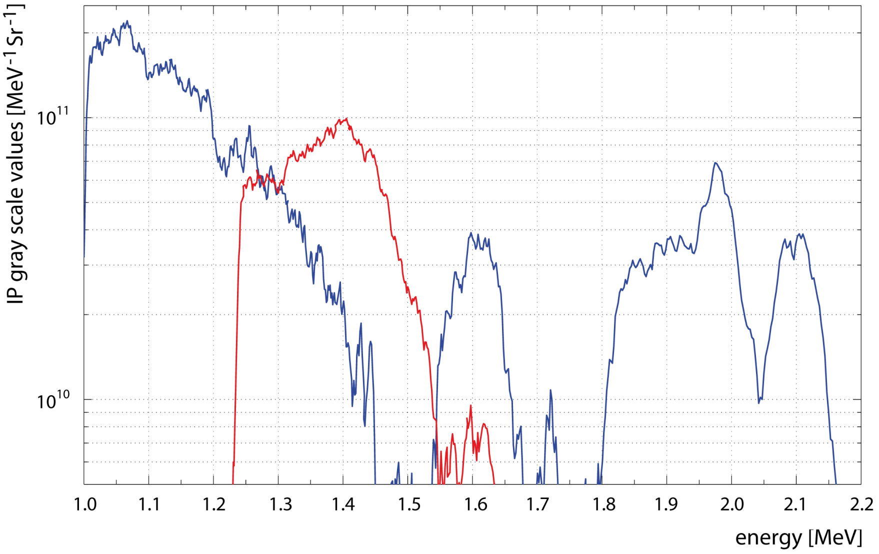

(b) ^{3}He^{2+} energy spectra, $n_{\text{max}} = 0.02 n_c$

Figure 7.21.: ^{3}He$^{1+,2+}$ ion-energy spectra for laser shot-# 11188 (14): in blue TP-90, in red TP-100, in brown TP-80.

^{4}He ion-energy spectra from CR-39

In order to gain knowledge about the number of laser-accelerated helium ions, TP-80 was armed with two CR-39 detector plates (feed size of 5 cm) for laser shot-# 11174 (09) (39.2 J, 0.3 ps, $\sim 0.03\,n_\mathrm{c}$). The extracted ion number cannot serve as a valid IP calibration due to shot-to-shot fluctuations. But, it is a reference for getting a good impression of the order of magnitude in ion number.

Preparations for data extraction Before the beamtime, the CR-39 SSNTDs were pre-etched for 10 h in a 6.25 M NaOH (aqu.) solution at 85 °C, neutralized in acetic acid and washed in pure water. For preparing x l NaOH solution of concentration c the following calculations have to be made. The desired concentration is $c = 6.25\,\mathrm{mol\,l^{-1}}$, the volume is $V = 3\,\mathrm{l}$. With $c = n\,V^{-1}$ the amount of substance n can be calculated to $n = 18.75\,\mathrm{mol}$. This amount of substance is related to a mass m of sodium hydroxide pellets via $m = n\,M = 750\,\mathrm{g}$, with $M = 40\,\mathrm{g\,mol^{-1}}$ as the formula mass of NaOH. Hence, accurately weighed 750 g of pure sodium hydroxide has to be solved in pure water and the solution has to be filled up to 3 l. ATTENTION! When solving NaOH pellets in water, the solution is heated (exothermic reaction!). After the solution has cooled down to room ambient temperature, the concentration has to be checked by measuring the density ρ in $\mathrm{g\,cm^{-3}}$ with a hydrometer. With the help of the online *Sodium Hydroxide Density-Concentration* calculator [han], the density at a given temperature is calculated into a concentration $c\,[\%]$ which can be converted into $\mathrm{mol\,l^{-1}}$ via $c\,[\mathrm{mol\,l^{-1}}] = \rho\,M^{-1} \times c\,[\%]$. It is important to always determine the concentration of the prepared NaOH solution at the same temperature in order to have the same conditions for all CR-39 etching iterations.

The NaOH solution was heated with an *IKA HBR 4 digital Heating Bath* [IKA]. The heater has two main functions: heating and stirring. The magnetic stirrer is advantageous for etching CR-39 because it ensures a homogeneous NaOH concentration, *i.e.* less density gradients due to temperature fluctuations. The temperature remains nearly constant over time: measured fluctuation of ±0.5 °C at a nominal value of 75 °C (obtained in the center of the etchant). A self-made glass lid with a sealed feedthrough for a thermometer was prepared. Furthermore, the lid has a radiused internal side so that condensed water can drop back into the etchant. Thus, the adjusted desired concentration stays constant for long time durations. When etching CR-39, it is important to always etch some "empty" CR-39 plates together with the irradiated ones. These so-called sacrifice plates can be used in order to measure the loss in bulk material after each etching iteration. The thickness of each plate can be measured at various locations of a single detector with micron-accuracy. The difference in thickness (divided by 2!) leads to the bulk etching rate (units in micron per hour). Within the PHELIX CR-39 analysis, a typical etch rate (in 6.25 M NaOH at 75 °C) was about $4 - 5\,\mathrm{\mu m\,h^{-1}}$.

After exposure to ^{4}He ions within the PHELIX experiment i009, the detectors were etched, neutralized and washed in three iterations. Since the range of low-energy α-particles in CR-39 is small, a careless handling (regarding the etching process) endangers the stored data: if the maintenance time of the irradiated CR-39 is too long or if the parameters of the etchant are chosen imprudently, then too much bulk will be etched away and the desired information is lost forever. Thus, the PHELIX CR-39 were etched for 1 h in total: the 1st etching interval was set to 10 min (plus additionally 60 min for neutralizing and washing), the 2nd one was 20 min, and the final interval was set to 30 min. It has to be noted, that after the 2nd interval the $^4\mathrm{He}^{1+,2+}$ ion tracks already were developed and became visible. The important data could be extracted. Therefore, for the final etching period the maintenance time in NaOH courageously was doubled. The track development continued and the visibility of the ion traces improved. Thus, the data extraction was performed again.

Data extraction A *TASLimage* microscope scanning system was used for data extraction [Trab, Traa]. The scanner consists of a vertically adjustable monochrome 25 fps CCD with a pixel size of 8 $\mu\mathrm{m}^2$. A revolver for attaching several microscope objectives is given. Beneath the camera, a 2-axes translation stage is mounted which carries a metal frame for holding CR-39 plates. All stages can be translated with micron-accuracy. A green light source illuminates the translucent SSNTDs from the bottom up. With the camera-control tool the camera settings (like gain, gamma correction, or the shutter speed) can be adjusted individually. The software is able to detect specific pre-defined track parameters (*e.g.* the pit diameter, the track depth, the cone angle, or the minor and major axes) within a split second and filters disturbing background features like dirt, fluffs, hair, etc.

Actually, the device shall simplify the scanning procedure especially when processing a huge amount of irradiated CR-39 or large SSNTD surfaces. But, during the automated scans several problems can occur. The automatic focus is functioning properly if the surface of the CR-39 is even. If a CR-39 plate bends within the hot NaOH solution and gets a rounded shape, the scanning routine is not able to find the best focus when scanning. Before the scan starts, in total four to five locations are characterized regarding the best focus. Now, the scanning software interpolates a plane through these spots. If, due to the bended surface, the interesting regions are below this plane, they are out of focus, of course. The scanner will continue with the scanning routine without detecting important data. Even if the live-focus setting is chosen it might happen that instead of focusing the front side of the detector the rear side is focused randomly. A second problem can occur regarding the detection efficiency of desired pits. It is dependent on the adjusted camera settings. For testing the best set of adjustments, a region with many known particles can be selected and the automatic particle detection routine for a fix image section can be started. But even if the optimal parameters are found, the filtering of desired/undesired tracks is not reproducible.

Since the PHELIX CR-39 were bent after etching and the automatic scanning routine did not yield any credible reproducible output, the CR-39 plates were scanned manually. After the final etching routine, the Thomson parabolas as well as the zero order (due to gamma radiation) became visible by eye. Figure 7.22 illustrates the irradiated CR-39 detector plate beneath the microscope objective. Fortunately, the zero order developed during the etching procedure so that a fix reference for the origin of the x_{tp}-y_{tp} coordinate system was defined. Before the PHELIX experiment, it was not obvious that exposure of CR-39 to gamma radiation leads to a color change from translucent to cloudy/milky white. In fact, a surface analysis and data extraction from these locations is not possible since the light of the scanner is not transmitted through the (dis-)colored regions.

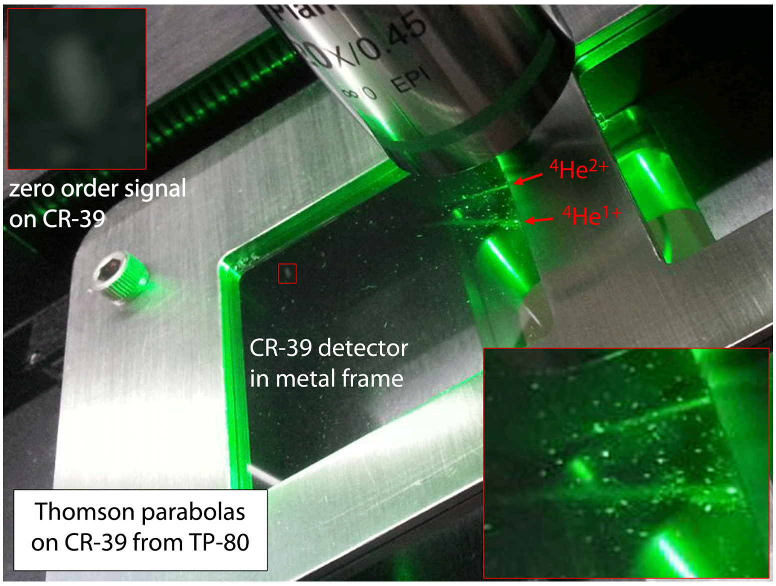

Figure 7.22.: Visible $^{4}\mathrm{He}^{1+,2+}$ Thomson parabolas on CR-39. The detector plate is illuminated with green light of the *TASLimage* microscope scanner. Also the zero-order signal from gamma radiation on pinhole height became visible after etching.

Figure 7.23 illustrates the CR-39 analysis procedure. On the left side, the outcome of an automated scan is illustrated. This specific scan was split into three single scanning sections. This was due to the fact that when scanning the whole area the automatic focus was completely lost before one third of the scan could be completed. But also in the sectioned scans the problem of a lost focus becomes obvious (shown by the red arrows at the doubled $^{4}\mathrm{He}^{1+}$ parabola). It could be assumed that the interruptions of the parabolas were real experimental data. But further automated scans yielded completely different track distributions.

For the manual scanning of both irradiated CR-39, the location of the zero order was set to zero. From here, the CR-39 was translated (in y_{tp}-direction) until the beginning of the $^{4}\mathrm{He}^{1+}$ Thomson parabola, *i.e.* the high-energy cut-off, was visible in the microscope camera. The CCD image has a size of $\Delta x = 622\,\mu\mathrm{m}$ and $\Delta y = 450\,\mu\mathrm{m}$ (*cf.* Fig. 7.23). In the specific distance $y_{\mathrm{tp},i}$ (with i as a "height" index), the parabolas were scanned sidewise in x_{tp}-direction, image-frame per image-frame. For each single image, the focus was adjusted manually and each image was saved. This time-consuming procedure was repeated in y_{tp}-steps of $450\,\mu\mathrm{m}$. In case of the $^{4}\mathrm{He}^{1+}$ Thomson parabola, for one parabola height-profile up to six single images had to be stored. This was due to the presence of a doubled parabola.

After the scanning was finalized, the raw data had to be processed and purified. Each single image was individually purged from dirt. Furthermore, if two or more helium-ion tracks were merging, *i.e.* the pits are positioned so close to each other that the track pixels overlap, then the overlap-region was manually deleted by slightly cutting the disturbing pixels. Thus, the tracks could be separated. This procedure is very important in order to finally correctly count the single ion tracks for each parabola section.

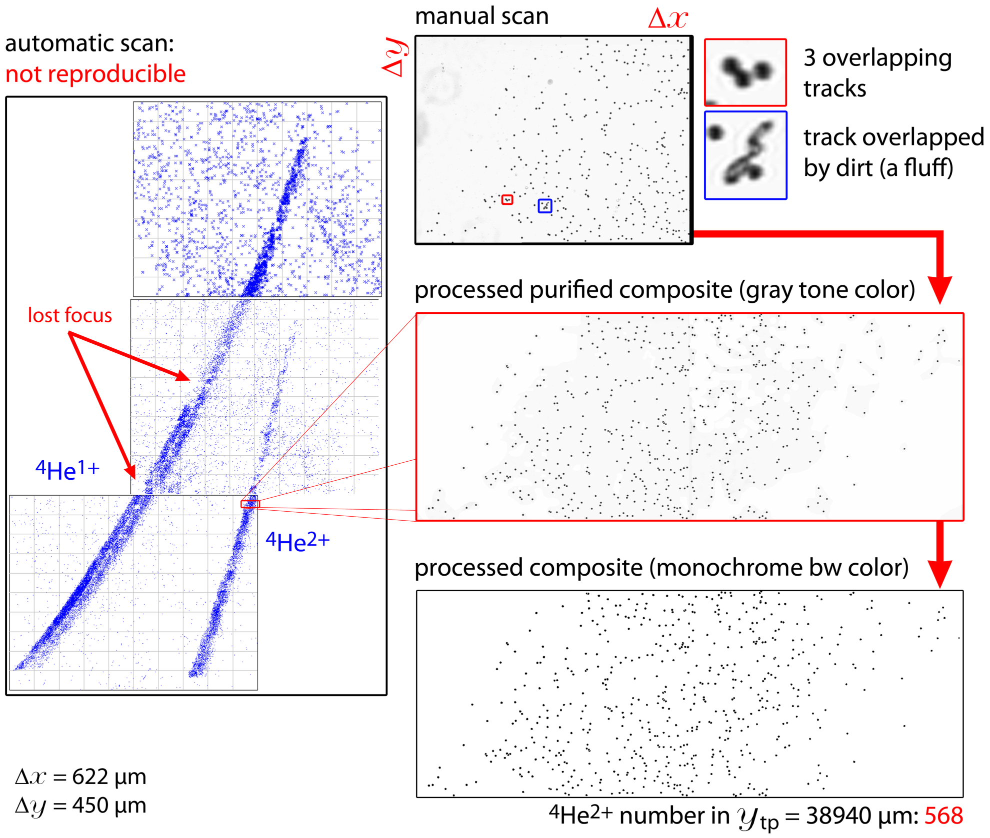

Figure 7.23.: CR-39 analysis procedure for extracting the real ion number exemplified for ^{4}He^{2+} ions in a "height" of $y_{\mathrm{tp}} = 38\,940\,\mu\mathrm{m}$. *Left*: outcome of an automated scan. *Top*: original single raw image of a ^{4}He^{2+} parabola section and examples for disturbing dirt and merging ion tracks. *Center*: processed purified composite in gray tone colors. *Bottom*: the same processed purified composite in monochrome black&white colors for analysis with *ImageJ*.

The processed and purified single images were assembled and all composites were transformed into a monochrome black&white image by adjusting the threshold values carefully. Now, each composite represents a slice through the specific parabola for a given height y_{tp}. Data analysis was performed with *ImageJ*. A special plug-in for counting cells in biology was used in order to count particles on CR-39. It has to be ensured that after adjusting the threshold settings only helium ion tracks are visible since each additional black pixel within the composite would have been treated as an ion pit. The obtained ion numbers together with the corresponding y_{tp}-values (B-deflection) were stored in a *.txt*-file.

The deflection values were transformed into the ion energies using the *CST*-simulated fit-parameters in Tab. 7.2 on p. 125. Furthermore, the extracted ion numbers were normalized to the ion energy and to the solid angle (TP-80, pinhole diameter $d_{\mathrm{ap}} = 350\,\mu\mathrm{m}$, distance to TCC $l_{\mathrm{pre}} = 520\,\mathrm{mm}$, distance between pinhole and CR-39 detector plane $l_{\mathrm{tp}} = 351.7\,\mathrm{mm}$). Figure 7.24 (a) and (b) illustrate the plotted CR-39 data for the $^4\mathrm{He}^{1+,2+}$ ion-energy spectra as well as for the normalized energy uncertainty $\Delta\mathcal{E}\,\mathcal{E}^{-1}$ over the ion energy $\mathcal{E}$ (the experimental width of the Thomson parabolas was $\delta_{\mathrm{tp80}} = 590\,\mu\mathrm{m}$).

From the $^4\mathrm{He}^{1+,2+}$ ion-energy spectra for laser shot-# 11174 (09) the high-energy cut-offs can be determined to $\sim 3.28\,\mathrm{MeV}$ ($\Delta\mathcal{E}\,\mathcal{E}^{-1}(3.28\,\mathrm{MeV}) \approx 0.045$) for $^4\mathrm{He}^{2+}$ ions and to $\sim 2.48\,\mathrm{MeV}$ ($\Delta\mathcal{E}\,\mathcal{E}^{-1}(2.48\,\mathrm{MeV}) \approx 0.077$) for $^4\mathrm{He}^{1+}$. The corresponding low-energy cut-offs are $1\,\mathrm{MeV}$ ($\Delta\mathcal{E}\,\mathcal{E}^{-1}(1\,\mathrm{MeV}) \approx 0.025$) and $0.25\,\mathrm{MeV}$ ($\Delta\mathcal{E}\,\mathcal{E}^{-1}(0.25\,\mathrm{MeV}) \approx 0.025$), respectively. The shape of both spectra is comparable to the prior discussed IP-obtained energy spectra. The total number of both laser-accelerated ion species could be determined to 2.02×10^4 ($^4\mathrm{He}^{2+}$) and 4.92×10^4 ($^4\mathrm{He}^{1+}$).

Polarimetry tests and additional measurements

Additional CR-39 detectors (left side) and in forward direction Simultaneously to the TP-measurements, an array of three angled CR-39 detector plates (behind a 1.2 mm thick honeycomb mesh made of stainless steel) was mounted on the left side of the target with respect to the laser axis. During the first shots, the distance to the TCC amounted to 6 cm. Due to dark color changes on the CR-39 front surfaces, the distance was doubled for a new set of CR-39. Furthermore, one CR-39 detector (wrapped in $5\,\mu\mathrm{m}$ Al foil) was placed at 0° in order to detect high-energy helium ions in forward direction. Later on, it was replaced by an *EBT2* RCF.

After etching all of the additional CR-39, a color change from translucent to milky/cloudy white became apparent. It has to be noted that the color change only took place on the front side of the CR-39, *i.e.* on the TCC-facing surface. The intensity or "strength" of the white staining was dependent on the experimental distances between the plastic detectors and the TCC: close to the TCC, the color was a strong white which bleached out a little bit for the doubled distance (12 cm). In a distance of 50 cm from the TCC with the thin Al-shielding, the milky color change was even weaker. Furthermore, the 1.2 mm thick honeycomb grid caused a shadow pattern on the CR-39, *i.e.* the cloudy areas on the CR-39 surface were bordered by the translucent sections beneath the honeycomb grid pattern. Due to the distance dependency as well as due to the fact that the 0° CR-39 was wrapped in lightproof Al foil, it can be concluded that the color change is not due to side-scattered laser light. But rather the gamma signal might have caused changes in the CR-39 polymer structure which result in such a color change during the etching process. An increased area-wide etching rate might be a plausible explanation. Another indication for this consideration is the visible zero order on the CR-39 surface inside TP-80.

All of the etched colored CR-39 were examined with the microscope scanner: none could be analyzed since a clear transmission of light was not possible. If naked CR-39 around the laser-target interaction region would have been the only diagnostics within the PHELIX experiment, then no experimental output (except the author's new knowledge about *CR-39 and gamma radiation*) would have been extracted out of the whole beamtime.

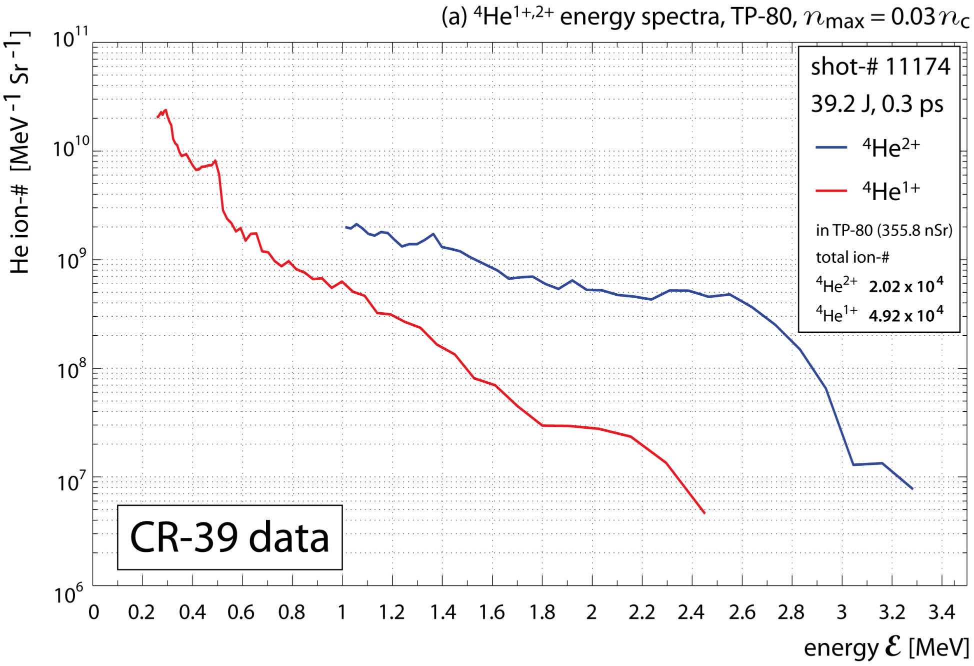
(a) ^{4}He$^{1+,2+}$ energy spectra, TP-80, $n_{\max} = 0.03\, n_c$

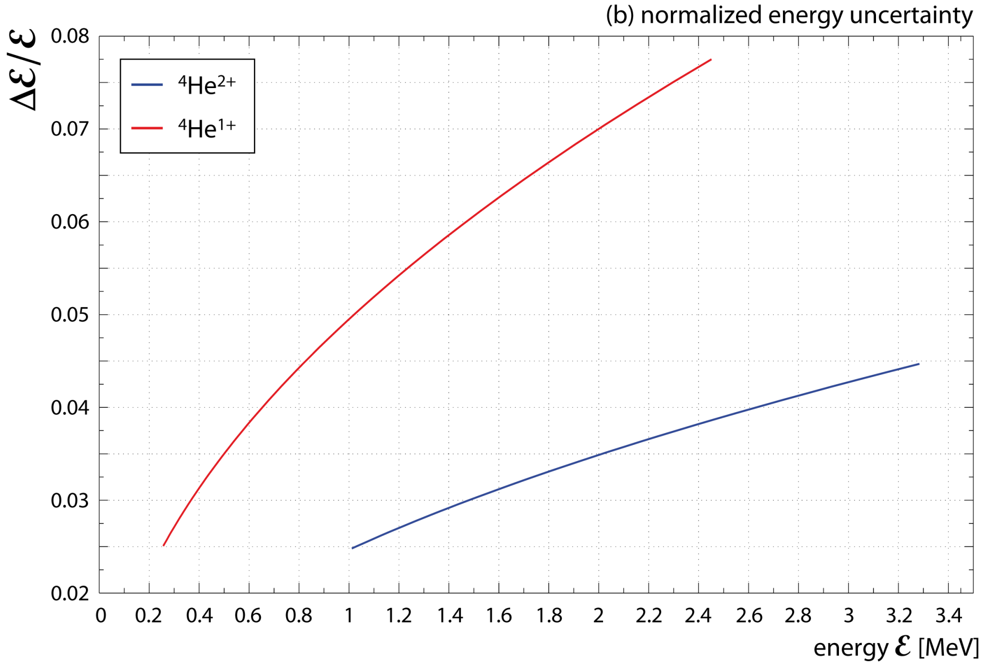
(b) normalized energy uncertainty

Figure 7.24.: (a) ^{4}He$^{1+,2+}$ ion-energy spectra from TP-80 for laser shot-# 11174 (09): in blue ^{4}He^{2+}, in red ^{4}He^{1+}. (b) Normalized energy uncertainty for both ion species ($\delta_{\mathrm{tp80}} = 590\,\mu\mathrm{m}$). The data is obtained from a CR-39 measurement. The total number of ^{4}He^{2+} was 2.02×10^4 and the one of ^{4}He^{1+} was 4.92×10^4.

The *EBT2* as well as the stack of 4 *HD-V2* RCF detectors at 0° (both wrapped in 5 µm Al foil) did not yield any significant signal. The *EBT2* was homogeneously colored. No striking signal was apparent. And none of the *HD-V2* layers from the RCF stack did not show any color change. Hence, the ion dose of possible forward-accelerated helium ions was too small (or equal to zero) to cause a measurable signal in *HD-V2* and also in the thick protected *EBT2* RCF (in case of high-energy ions).

^{3}He measurements Since the measurements with unpolarized ^{3}He gas had to be aborted due to technical problems with the valve, no polarimetry measurement could be conducted with a higher ^{3}He-gas pressure.

Reference measurement A reference measurement, the so-called *zero-shot*, was performed for the last laser shot (# 11203 (19)). Here, the valve was not triggered, *i.e.* no gas jet was built up. This measurement was done in order to get an impression of the detector behavior when no laser-target interaction occurs. The expectable result: no signal could be extracted from the IP detectors. A second reference measurement, the *zero-zero-shot*, was also planned but could not be conducted (malfunction of the valve). For this measurement, the helium-gas target would have been replaced by a different gas (nitrogen or argon) in order to investigate the detector behavior for the changed laser target.

In general, a zero-shot is important because it helps to falsify (not prove) experimentally obtained data. When a detector signal misleadingly is interpreted as experimental data, but in practice it is originated from a totally different process, then a zero shot increases the probability to uncover the *truth*. With the zero-zero-shot this probability is increased again. During the first reference measurement, no plasma target is given: the focused laser pulse diverges in vacuum and hits on the beam dump. But, if a different gas target is attached and laser-target interaction takes place, then it would be interesting how the diagnostics behave.

8. Layout of the polarized ^{3}He target

The experimental results in Chap. 7 proved the general feasibility of laser-driven ^{3,4}He-ion acceleration out of unpolarized gas-jet targets at PHELIX. With this *sine qua non* for a spin-polarization measurement of laser-accelerated ^{3}He^{2+} ions, an appropriate layout of a polarized ^{3}He gas-jet target has to be developed, planned, and constructed. This chapter contains the essential components of such a layout: the magnetic holding field for storing pre-polarized ^{3}He gas for long time durations within the PHELIX target chamber, the gas-jet source for providing the desired laser target, and finally a polarimetry setup for measuring the spin-polarization degree of laser-accelerated ^{3}He^{2+} ions.

8.1. Magnetic holding field

When planning a homogeneous magnetic field for maintaining the spin-polarization of pre-polarized ^{3}He gas for long time durations one of the most important issues to be contemplated is the available amount of space. Adequate field gradients require a well-considered design of the magnetic field source.

A Helmholtz-coil arrangement would always be the first idea to establish homogeneous magnetic fields. An advantage of electrically originated fields is the (limited) freedom in the achievable field strength. Furthermore, the field direction can easily, *i.e.* "non-invasively", be inverted by a pole change. Indeed, when operating Helmholtz coils in vacuum, a proper cooling system has to be realized. An unsolved question with regard to high-intensity laser-plasma interaction is the influence of huge EMP signals on the Helmholtz-generated magnetic field, or precisely speaking, on the field gradients around the stored spin-polarized ^{3}He gas.

In contrast to electric coils, permanent magnets do not need to be cooled in vacuum and their field is constantly present, even in presence of huge EMP signals. If several permanent magnets are combined in a specific array, the resulting field distribution can be shaped. In a Halbach array [Sol10], multiple permanent magnets are circularly arranged and form a ring. The magnetization direction of each magnet is aligned thus, that within the ring plane the magnetization is rotated by $4\,\pi$, *i.e.* opposing magnets are magnetized in the same direction. Nowadays, neodymium magnets (NdFeB) are the strongest commercial permanent magnets.

For the future laser-acceleration experiment with spin-polarized ^{3}He gas at PHELIX, the magnetic holding field will be built up by a combination of both concepts: an outer Halbach array composed of an upper and lower ring of 48 NdFeB permanent magnets together with an inner Helmholtz-coil array consisting of four single Helmholtz coils. The whole system was planned according to the given dimensions of the PHELIX target chamber (TC). First considerations involved concepts of a holding field outside the TC. But due to its outer dimensions, the magnetic holding field would have been of large size which causes collisions with fix TC equipment (like the deviation pots for housing the OAP or vacuum tubes). The best solution was to install the magnetic system inside the PHELIX TC as it is illustrated in Fig. 8.1 [Pfe14b]: 3D model of the constructed holding field. From (a) to (d): perspective view of the fully mounted magnetic system inside the PHELIX target chamber, top view, front view, and side view.

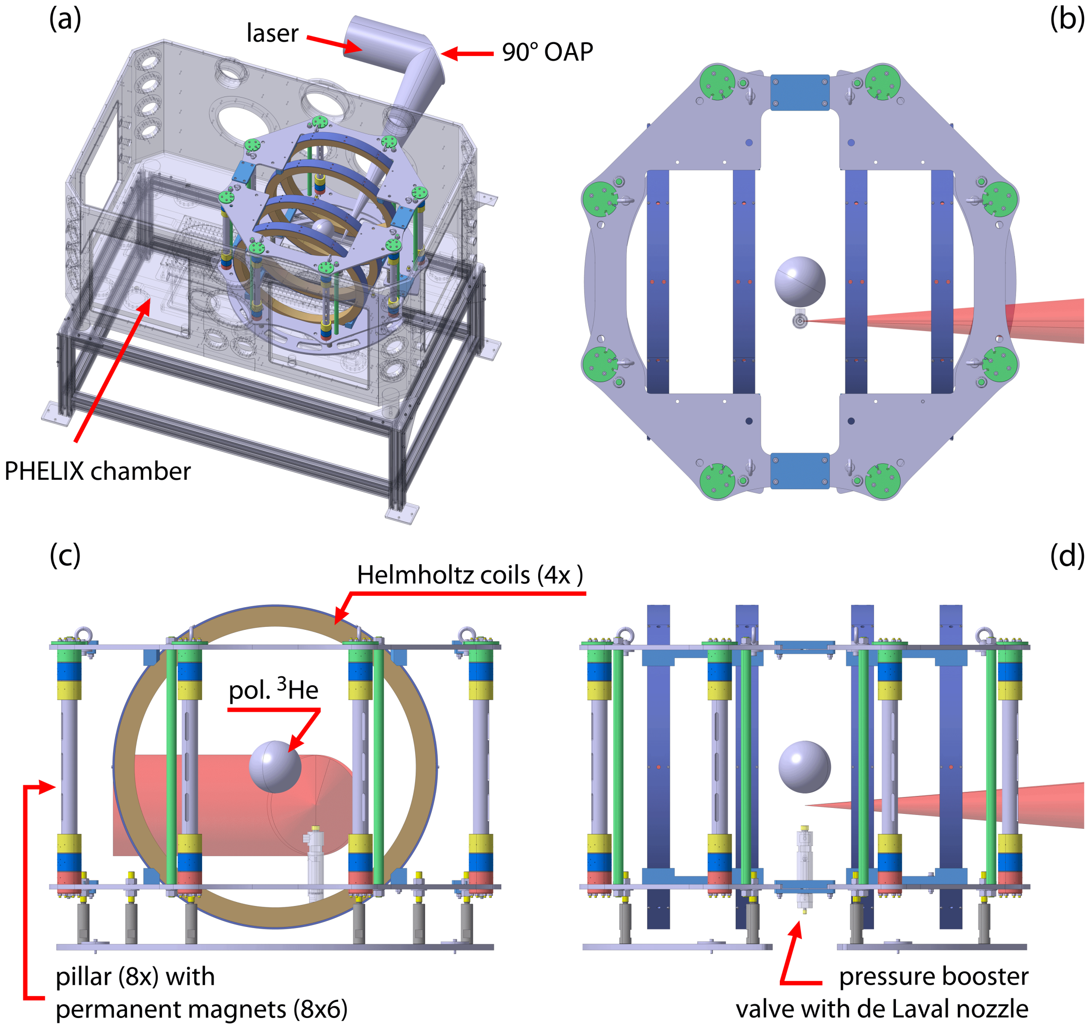

Figure 8.1.: 3D model of the magnetic holding field for the PHELIX target chamber [Pfe14b]. (a) Perspective view of the fully mounted magnetic system inside the PHELIX chamber, (b) top view, (c) front view, (d) side view.

For getting a better orientation, the storage vessel for pre-polarized ^{3}He gas, the laser beam (which is focused by the 90° OAP), as well as the valve with attached de Laval nozzle are included in the 3D model.

Halbach array The Halbach array is composed of eight vertical pillars arranged in a circle with 1100 mm in diameter. The inter-pillar distance (immediate neighbors) is 420.95 mm. Each pillar contains in total six NdFeB permanent magnets. Here, three vertically stacked magnets form a unit. The distance between two magnets is 5 mm. Both units are located in the top and bottom of the pillar, respectively. In the Fig., the magnets are included in housings which are colored differently: the bottom components are red, blue, yellow, and the top ones are yellow, blue, green. Between the centers of the upper and lower blue magnet housings a distance of 471.71 mm is given. A single NdFeB magnet has an octagonal cross-section area with a feed size (front to rear side) of 38.4 mm and a height of 40 mm. The magnetic energy density is 320 $^{\mathrm{kJ}}/_{\mathrm{m}^3}$. In the center of the Halbach array a magnetic field strength of 1.4 mT is reached. In total, the Halbach array has a (preliminary) mass of 160 kg.

Helmholtz-coil array The Helmholtz-coil array is composed of four single Helmholtz coils which are oriented thus that their magnetic field is aligned parallel to the laser direction. The two single front/rearward coils (with respect to the laser propagation direction) form a unit, a Helmholtz pair. The distance between both coils in one unit is 218.95 mm and the distance between both inner coils is 285.75 mm. A single coil consists of coiled Cu sheet with a width and thickness of 40 mm. The outer and inner diameters of the naked Cu coil are 789 mm and 709 mm. The housing for the coiled Cu has the dimensions of: 56 mm (width and thickness), 803 mm and 695 mm (outer and inner diameter). The whole Helmholtz-coil array has a (preliminary) mass of 160 kg

The complete assembly is bulky and heavy (320 kg). A manual mounting of the single field components inside the chamber is not possible. Therefore, the chamber cover flange has to be removed and the magnetic system has to be lifted into the TC with a hoisting crane. With the constructed magnetic holding field inside the chamber the alignment of the field can be adjusted by either switching the poles of the Helmholtz array or manually rotating the Halbach pillars.

A first test-Halbach array successfully was built up and characterized at ZEA-1, FZJ [Bur14]. A relative field gradient of $\partial_r B = 1.465 \times 10^{-3}\,\mathrm{mT\,cm^{-1}}$ with a maximal magnetic field strength of $B_{\mathrm{max}} = 1.43\,\mathrm{mT}$ could be reached. Furthermore, the relaxation times of spin-polarized ^{3}He inside the Halbach field could be determined with a gradiometer measurement. For this purpose, four *Fluxmaster* fluxgate magnetometers with a resolution of 0.1 nT were applied [Ste]. The experimentally obtained relaxation time of spin-polarized ^{3}He was 21.4 h [Nau14].

8.2. Pressure booster and valve

The second essential component for the layout of a polarized ^{3}He gas-jet target is the gas source. The pre-polarized ^{3}He gas is delivered at an intrinsic pressure of 3 bar. Such a backing pressure in front of the de Laval-nozzle throat does not provide an adequate particle density for an efficient laser-driven ion acceleration. But, as stated in Sec. 4.5 on p. 37, the pressure cannot easily be increased without rapidly decreasing the relaxation times of the nuclear spin-polarization. Therefore, the pre-polarized gas will remain in its vessel at 3 bar.

Pressure booster A solution for the above described dilemma is a pressure booster which will extract a specific amount of spin-polarized ^{3}He (at 3 bar) and will compact this defined volume. Thus, a desired final pressure can be reached (*e.g.* 15 bar or 30 bar). This procedure has to be performed quickly and immediately *i.e.* within split seconds before the laser shot. The amount of gas (low pressure) depends on the nozzle geometry. In Sec.6.1.2, the intrinsic ^{3}He volume to be boosted from 3 bar to 30 bar (0.5 mm de Laval throat) was calculated to about 13 ml (*cf.* p. 71).

The pressure booster has to be built of non-magnetic materials since the whole system will be mounted within the external magnetic holding field. Even a small amount of magnetizable components will cause local field gradients which affect the spin-polarization negatively. Figure 8.2 illustrates a 3D model of the planned device [Lei15] (top: perspective view, bottom: side view). In the center of the booster body, a piston with two different cross-section areas is given. The boundary surface piston-housing is sealed with O-rings. The piston can be translated by applying a gas pressure to the gas supply (industrial gas, *e.g.* N_2 or also ^{4}He). In the beginning, the piston is positioned on the left side and pre-polarized ^{3}He (3 bar) is let into the predefined volume of 13 ml. By translating the piston to the right side, the volume is compacted. When the desired pressure of *e.g.* 30 bar is reached, the gas exits the pressure booster through the gas outlet. With the male thread at the bottom (left side of the picture) the pressure booster can directly be mounted on a 2” post inside the PHELIX chamber. *Additional information:* the bumper sealing shall suppress most of the vibrations when the piston hits on the rear/front side of the booster body.

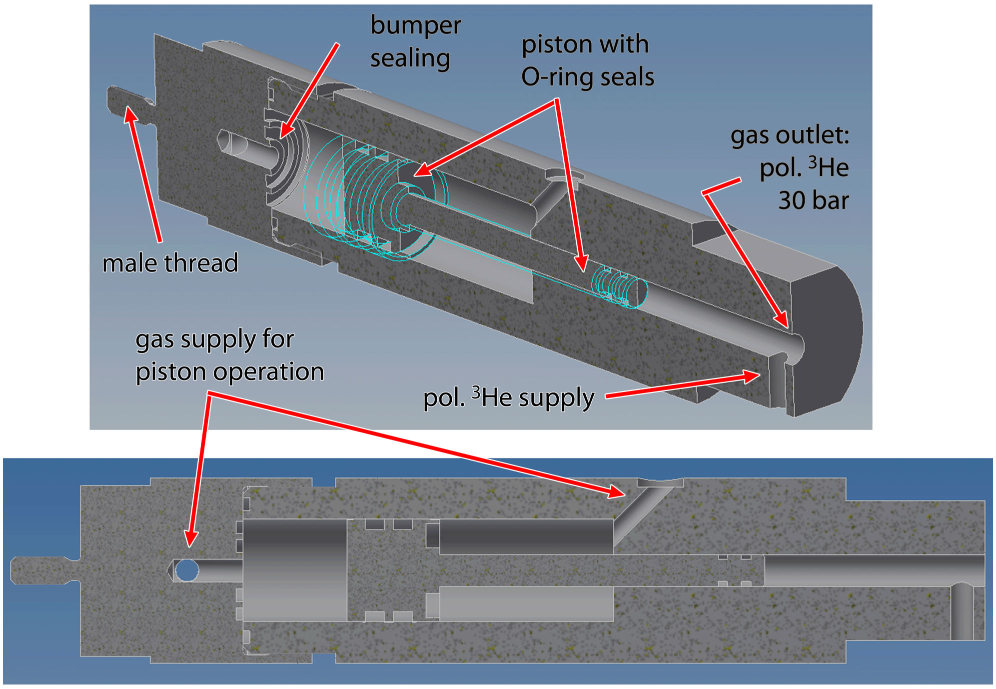

Figure 8.2.: 3D model of the pressure booster [Lei15].

Valve Until now, the pre-polarized ^{3}He gas was only compacted. But for a laser-acceleration experiment it is very important to have a manageable target which can be timed with the incoming laser pulse: an adequate valve has to be constructed. The commercial *Parker Hannifin series 9* valve cannot be operated with spin-polarized ^{3}He gas since the gradient fields of the solenoid endanger the polarization. Other commercial possibilities for the tight requirements are not available: standard piezo-driven valves operate in low-pressure regimes (up to 12 bar) and hydraulic-driven valves are too slow for laser-acceleration experiments in vacuum. Therefore, the valve had to be self-constructed.

Two general opening mechanisms were considered for the valve: a piezo-driven solution and a gas-pressure driven mechanism. Regarding the first one, piezo actuators like the *PI P-602.800* with a maximal travel range of 1 mm and a pushing forces of 100 N are commercially available [PI] and can be manufactured of non-magnetic materials (for extra charge, of course). A possibility to translate the linear displacement of the piezo actuator into an opening mechanism of a valve is given: an armature with attached poppet has to be screwed to the moving part of the piezo actuator. The poppet will close the orifice of the gas outlet. When the actuator is supplied with voltage, the orifice is unblocked and gas can leave the valve.

The second general opening mechanism involves a driving industrial gas which operates the valve. In Fig. 8.3 (a) to (c), three possible solutions are presented [Pfe14a]. All of these possibilities involve a bushing beneath the de Laval nozzle with cone-shaped pockets. The bushing is built up thus, that a metal tip, *i.e.* the poppet, can be pulled/pushed by applying industrial gas at the gas supply. If the valve is operated, the metal tip is pulled backwards and unblocks the connection between the installed pressure booster and the mounted de Laval nozzle on top of the central component. The closure is performed by pushing the metal tip back to its original position. A massive metal block (soft metal, *e.g.* Cu) serves as a sealing. The moveable metal tip is pressed into the sealing block. In (a), an offset between the nozzle axis and the outlet of the pressure booster is given. The unblocking of the inner passage can be realized with *e.g.* a hollow metal tip. In (b), the nozzle center is positioned directly above the pressure-booster outlet so that the back-pulled metal tip immediately opens the valve. In the last image section, in (c), the pressure booster (or maybe two of them) is installed sidewise from the central component. The poppet is oriented vertically and unblocks the booster's outlet by being pulled downwards. Every single concept has its individual advantages regarding *e.g.* the suppression of disturbing vibrations or the response times. Both the pressure booster and the valve are currently being in developing and construction stage. In near future, they can be manufactured and tested.

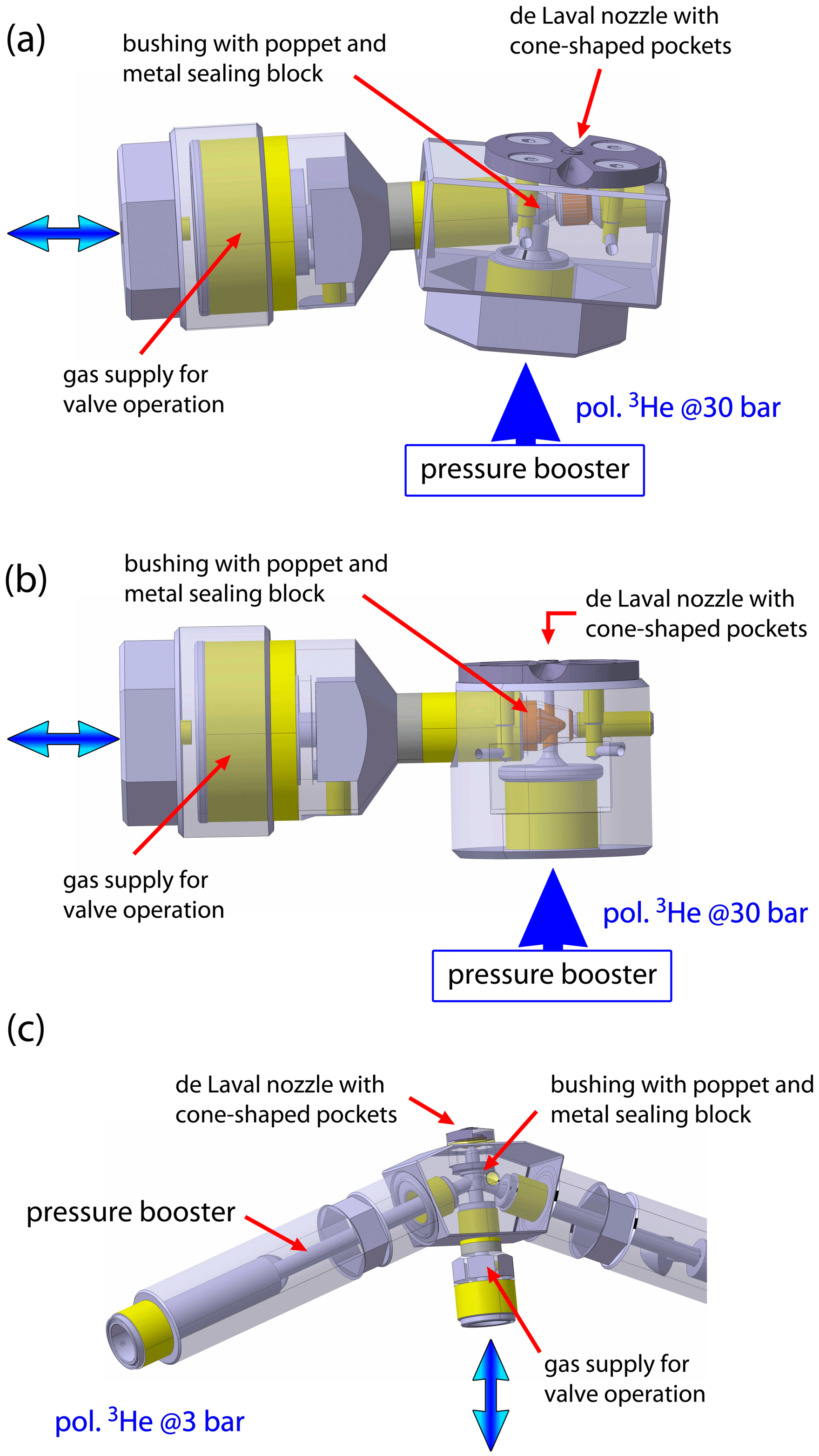

Figure 8.3.: 3D model of different valve concepts [Pfe14a].

8.3. Ion-polarization measurement setup

In order to measure the polarization degree of laser-accelerated $^3He^{2+}$ ions from a pre-polarized ^3He gas-jet target, the polarimetry setup requires a secondary scattering target. As it is described in Sec. 4.5.3, a CD_2 foil will be attached for this purpose. A first prototype of the polarimetry cage was assembled for the PHELIX beamtime (*cf.* Sec. 7.2.1). Figure 8.4 illustrates the preliminary setup. The entrance into the cage is established with a stack of apertures. In the center, a CD_2 foil is mounted. Incoming $^3He^{2+}$ ions will propagate through the apertures and hit on the CD_2 foil. The given setup was planned with CR-39 detector plates as fusion-proton detectors. The SSNTDs can be inserted into the slotted CR-39 holders. Additional Al degrader foil can be put in front of the CR-39 detectors in order to block low-energy protons from reactions with carbon.

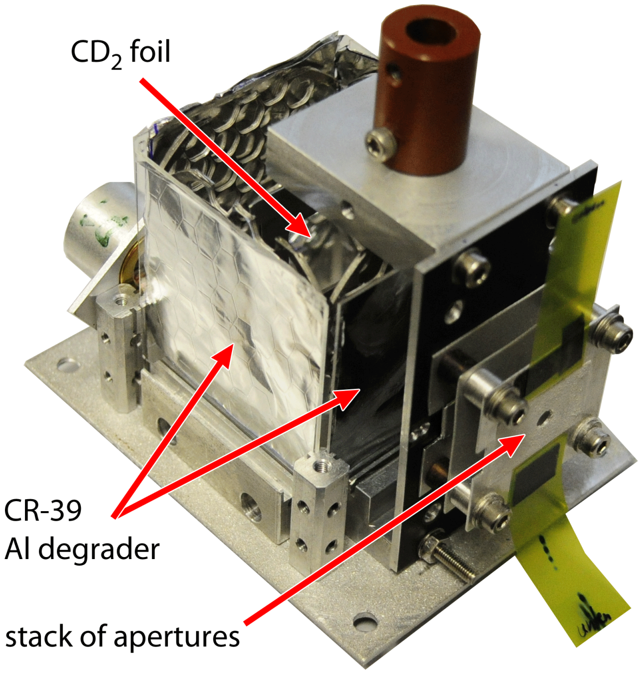

Figure 8.4.: Prototype of the polarimetry cage.

The polarimetry procedure has to be calibrated before manufacturing the final version of the cage. A calibration can be conducted at the Jülich Tandetron accelerator. The Tandetron provides monoenergetic $^3He^{2+}$ ion beams with energies between 0.89 and 2 MeV and beam currents up to 100 pA (in case of an energy of 0.89 MeV).

For calibration of the polarimeter, different $^3He^{2+}$ ion energies as well as different exposure times have to be chosen. If CR-39 is used as proton detector, then the thickness of the plastic detectors has to be set slightly larger than the Bragg peak of the maximum-energy fusion protons in CR-39. According to *SRIM*, the ranges of 10 MeV, 13 MeV, 15 MeV, and 17 MeV protons in CR-39 are 966.34 µm, 1.55 mm, 2 mm, and

2.5 mm. Therefore, the CR-39 thickness should be set to 3 mm in total to ensure that all fusion protons are stopped within the plastic. It is highly recommended to use a stack of *e.g.* six single CR-39 detectors with a thickness of 500 µm. Such a configuration has several advantages. On the one hand, more energy ranges can be investigated after only one etching procedure. This important fact saves a lot of time: assuming an average bulk etch rate of $\sim 10\,\mu\mathrm{m\,h^{-1}}$, for an etched bulk of 100 µm a time of 10 h has to be planned. Possible inaccuracies due to changed NaOH concentrations are not considered in this example. A minimization of the maintenance time of the detectors inside the hot etchant furthermore minimizes the probability of data loss if an unforeseen problem occurs (*e.g.* a malfunction of the heater, completely bended CR-39).

Estimation of the fusion proton yield With the experimentally obtained $^4\mathrm{He}^{2+}$ ion number at −80° relative to the laser direction (*cf.* Fig. 7.24 on p. 141), it is possible to improve the "rough" prior estimations of the fusion proton yield from Sec. 4.5.3. In the following, the ^{4}He ion number is transferred to the future $^3\mathrm{He}^{2+}$ ion number from a pre-polarized gas target.

The total number of $^4\mathrm{He}^{2+}$ ions (from a gas-jet target with $n_\mathrm{max} = 0.03\,n_\mathrm{c}$) being detected in TP-80, *i.e.* in 355.8 nSr, was 2.02×10^4 per laser shot (including all of the achieved ion energies). Normalized to the whole solid angle, this number is identical to $5.68 \times 10^{10}\,\mathrm{Sr}^{-1}$ per laser shot. For sure, with an attached higher density ($n_\mathrm{max} = 0.06\,n_\mathrm{c}$) and for an emission angle of ±90°, this number is even higher. But the following estimation will be performed with the TP-80 data, and thus, it can be regarded as a lower limit for the proton yield.

The entrance into the polarimetry cage is a 1 mm aperture (radius of $r = 0.5\,\mathrm{mm}$) in a distance of $l_\mathrm{pre} = 50\,\mathrm{mm}$ from the TCC. The covered solid angle is equal to $\pi r^2/l_\mathrm{pre}^2 \approx 314.16\,\mu\mathrm{Sr}$. Hence, approximately $N_{^3\mathrm{He}^{2+}} \approx 17.84 \times 10^6$ ions will enter the polarization measurement setup and impinge on the CD_2 foil.

With the following Eq. the proton yield per detector can be calculated:

$$\begin{aligned} n_\mathrm{p} &= \mathcal{L} \times \frac{\mathrm{d}\sigma}{\mathrm{d}\Omega}\Delta\Omega \\ &= N_{^3\mathrm{He}^{2+}} \times \rho_{A,\mathrm{CD}_2} \times \frac{\mathrm{d}\sigma}{\mathrm{d}\Omega}\Delta\Omega\,. \end{aligned} \tag{8.1}$$

Here, $\mathcal{L} = N_{^3\mathrm{He}^{2+}} \times \rho_{A,\mathrm{CD}_2}$ is the luminosity, *i.e.* the ion number (per laser shot) times the areal CD_2 density $\rho_{A,\mathrm{CD}_2} = 2.7 \times 10^{20}\,\mathrm{cm}^{-2}$, $\mathrm{d}\sigma/\mathrm{d}\Omega = 60\ \mathrm{mb/Sr}$ is the resonance value of the differential cross section for the D-^{3}He fusion reaction at an incident ion energy of 500 keV, and $\Delta\Omega = 6.25\,\mathrm{Sr}$ is the covered solid angle inside the polarimetry cage (detector area of $2500\,\mathrm{mm}^2$ in a distance of 20 mm from the CD_2 foil).

With the given parameters, the *lower limit* of the fusion proton number per detector per laser shot can be estimated to about $n_\mathrm{p} \approx 1800$. By choosing a different emission angle of the laser-accelerated $^3\mathrm{He}^{2+}$ ions (±90°), this number might be increased further.

9. Concluding Remarks and Recommendations

9.1. Laser-induced ion acceleration from ^{4}He and ^{3}He gas jets

In the framework of this thesis, preparatory investigations for the spin-polarization measurement of laser-accelerated $^3\mathrm{He}^{2+}$ ions from a pre-polarized ^{3}He gas-jet target were conducted.

The key issues of the recent studies contained the proof of the general feasibility of laser-driven ion acceleration out of unpolarized ^{3,4}He gas jets as well as extensive Particle-in-Cell simulations to support the experimental parts of this work. Furthermore, a layout of the polarized ^{3}He target available for laser-acceleration experiments had to be designed.

For the first key issue, two experiments were carried out at two high-intensity laser facilities: the Arcturus laser at the institute for laser and plasma physics at Heinrich-Heine-University Düsseldorf as well as PHELIX at GSI Darmstadt.

The first experiment at Arcturus was scheduled in order to verify former EPOCH predictions as well as former preliminary experimental results regarding laser-driven helium-ion acceleration exclusively in forward direction, *i.e.* precisely on laser axis. The experiments were performed with a laser energy of $2-4\,\mathrm{J}$ (after compression), a pulse duration of 26 fs, and a wavelength of 800 nm. The laser pulse was focused to a 15 µm (FWHM) spot using an off-axis parabola (OAP) with an f-number of 12.5. The peak intensity was about $4.4 \times 10^{19}\ \mathrm{W/cm^2}$. Helium-4 gas was applied as laser target. The gas jet was built up by a commercial solenoid valve with a thin de Laval nozzle attached (nozzle throat of 167 µm). With a backing pressure of 25 bar, in the focal height a particle density of $10^{19}\,\mathrm{cm}^{-3} \approx 0.006\,n_\mathrm{c}$ was reached. Several plasma diagnostics were prepared (interferometry, polarimetry, shadowgraphy). For the first laser shots, the same ion diagnostics like in the former experiments was applied: a Faraday-cup detector on laser axis. Later on, a Thomson parabola spectrometer (TP) aligned at 0° served as main ion diagnostics.

The Arcturus experiment in Feb. 2014 did not yield any measurable ion signal in forward direction. All attempts to improve the experimental conditions by varying the laser and gas-jet parameters could not improve the experimental outcome. However, the former experimentally obtained data could be reproduced and identified as a pure laser-induced signal inside the Faraday-cup detector. After the beamtime, EPOCH simulations were performed on the Jülich Supercomputers in order to investigate the ion-emission angles for the given experimental parameters. As laser target, a neutral ^{4}He gas jet was defined in a $1.5\,\mathrm{mm} \times 0.25\,\mathrm{mm}$ simulation box with a spatial resolution of $\Delta x = \Delta y = 0.04\,\mu\mathrm{m}$. The simulated particle-density profile was implemented according to interferometrical characterizations of the gas flow through the particular 167 µm de Laval nozzle. Indeed, the simulations predict a thin forward peak in ion signal with a small current density. But, as main ion-emission direction sharp angular ranges around ±90° relative to the laser direction could be ascertained. Therefore, it is highly recommended to further experimentally investigate helium-ion emission in the transversal direction around the gaseous target within a future experiment at Arcturus.

For the second laser-acceleration experiment at PHELIX, the corresponding EPOCH simulations were performed before scheduling the beamtime. Again, a neutral ^{4}He gas jet was set in a 2 mm × 0.25 mm box with a spatial resolution of $\Delta x = \Delta y = 0.04\,\mu\text{m}$. Now, the interferometrical data from a larger de Laval nozzle (0.5 mm nozzle throat) were taken into account in order to define the simulated density distribution. The simulated main ion-emission angles were located around ±90° relative to the laser direction. No forward peak in ion signal could be extracted from the simulated data. With this knowledge, the corresponding PHELIX experiment i009 was planned, and finally, carried out in Jan. 2015.

The optimal laser parameters for the whole experiment could be determined within the first laser shots. The laser energy was set to $40 - 50\,\text{J}$ (after compression), the pulse duration (which could not be controlled by the experimenter) was $0.4 - 1.1\,\text{ps}$, the wavelength was $1.053\,\mu\text{m}$. The laser beam was focused using a 90° OAP with an f-number of 6.8. Before each shot, the laser focus was aligned to a minimal spot size of $\pi\, 11 \times 15\,\mu\text{m}^2$. Peak intensities of about $1.4 \times 10^{19}\ ^{\text{W}}/_{\text{cm}^2}$ were reached. As laser target, both helium-4 gas and unpolarized helium-3 gas was used. A de Laval nozzle with a minimal diameter of 0.5 mm was attached in order to shape an adequate density profile for the laser-target interaction. Different backing pressures were applied during the experimental beamtime: in case of helium-4 gas, the pressures were 30 bar and $14 - 15\,\text{bar}$, and in case of helium-3 gas a maximal backing pressure of 8 bar was available. The maximal particle densities for these pressure regimes in the focus height were $6 \times 10^{19}\,\text{cm}^{-3} \approx 0.06\, n_\text{c}$, $3.25 \times 10^{19}\,\text{cm}^{-3} \approx 0.03\, n_\text{c}$, and $1.67 \times 10^{19}\,\text{cm}^{-3} \approx 0.02\, n_\text{c}$, respectively. As main ion diagnostics, a removable RCF wrap-around detector was mounted close to the laser-target interaction region cylindrically around the gas source. In addition, in total three Thomson parabola spectrometers were placed at −80°, −90°, and −100° relative to the laser direction. Within the current thesis, these spectrometers were denominated as TP-80 to TP-100. The TPs were armed with image plates (IP) and for one laser shot with CR-39 SSNTDs. Appropriate *CST* simulations for the TP setup were conducted in order to gain information about the energy-deflection dependencies of all ion species inside the TP fields. Thus, the experimental data for the deflection parameters for each species directly could be related to the corresponding ion energies.

Within the PHELIX experiment i009, $^{4,3}\text{He}^{1+,2+}$ ions could successfully be accelerated to MeV energies. The ion-angular distribution as well as the energy spectra for all ion species could be extracted. The results are in line with the corresponding EPOCH simulations. Indeed, high-energy laser shots (laser energy of up to 120 J, after compression) yielded a maximal $^4\text{He}^{2+}$ ion high-energy cut-off of up to 10.9 MeV with a normalized energy uncertainty of $\Delta\mathcal{E}\,\mathcal{E}^{-1} = 0.05$ (maximal gas-jet density: $0.06\, n_\text{c}$, emission angle: −90°). However, applying high laser energies caused several problems especially concerning the applied hardware (like the de Laval nozzle beneath the plasma regions). Therefore, for the following shots, the laser energy was decreased to about one third of the maximal available value ($40 - 50\,\text{J}$). With this parameter setting, the high-energy cut-off for $^4\text{He}^{2+}$ at −90° was determined to 4.6 MeV ($\Delta\mathcal{E}\,\mathcal{E}^{-1} = 0.02$). The TP-obtained data was in line with the angular-distribution data from the RCF wrap-around measurement. Here, the measured ion signal showed a peak in transversal direction with a FWHM of 23° ranging from 80.7° to 103.7°. In comparison, the strongest signals were recorded with TP-90, followed by TP-100 and finally TP-80. The measurements with unpolarized ^{3}He gas as laser target yielded lower ion energies (for both ion species). The high-energy cut-off in case of $^3\text{He}^{2+}$ ions could be determined to about 2.2 MeV ($\Delta\mathcal{E}\,\mathcal{E}^{-1} = 0.04$). Unfortunately, the given ^{3}He backing pressure could not be increased in order to investigate the ion yield for higher density regimes. The TP data was recorded with IPs which could not be calibrated with $^{3,4}\text{He}^{1+,2+}$ ions. Therefore, the energy spectra were plotted as a normalized signal intensity (per MeV per Sr) dependent on the incident ion energy (in MeV). For one laser shot, TP-80 was equipped with CR-39 SSNTDs. The particle numbers of both ^{4}He ion species in a covered solid angle of 355.8 nSr and for an emission angle of −80° could be determined to 2.02×10^4 $^4\text{He}^{2+}$ ions and 4.92×10^4 $^4\text{He}^{1+}$ ions.

The second key issue of the current doctoral studies involved the design of a layout for the polarized ^{3}He gas target for a near-future laser-acceleration experiment at PHELIX. Such a layout includes a magnetic holding field with adequate field gradients for storing pre-polarized ^{3}He gas for long time durations inside the target chamber. Furthermore, a proper gas source is needed to ensure appropriate gas-density distributions for an efficient laser-driven ion acceleration from gaseous targets. And finally, a polarimetry setup has to be planned which is used to measure the polarization degree of laser-accelerated $^3\text{He}^{2+}$ ions from a pre-polarized gas.

For the magnetic holding field, a combination of a Halbach-array and a Helmholtz-coil system was planned, constructed and partially manufactured. The first component, the Halbach-array, consists of 48 NdFeB permanent magnets which were aligned in two vertically oriented rings with a diameter of 1100 mm. The field contribution from the Helmholtz-coil array is built up by four Helmholtz coils with an outer diameter of 803 mm. The maximal field strength at the location of the stored pre-polarized ^{3}He gas is 1.4 mT. For testing the theoretical considerations, a first Halbach-array was manufactured and characterized. Also the relaxation times of the spin polarization of pre-polarized ^{3}He gas inside this field could be measured to about 20 h. Regarding the preliminary Halbach-array field, a relative field gradient of $\partial_r B = 1.465 \times 10^{-3}\,\text{mT}\,\text{cm}^{-1}$ and a a maximal magnetic field strength of $B_{\text{max}} = 1.43\,\text{mT}$ could be reached. The whole magnetic system was designed according to the available amount of space within the PHELIX target chamber. Since the pre-polarized ^{3}He gas is delivered at a maximal backing pressure of 3 bar which does not provide an adequate particle density for an efficient laser-driven ion acceleration, a pressure booster for increasing tenfold the pressure of a specified gas volume was designed. Due to the fact, that the gas source will be operated within the external magnetic holding field, only non-magnetizable materials have to be used in order not to create local inhomogeneities which worsen the magnetic field gradients. Thus, the ^{3}He spin-polarization degree would be decreased rapidly. Next to the pressure booster, a valve with a non-magnetic opening mechanism is necessary for controlling the gas flow into vacuum. Conventional solenoid valves obviously do not fulfill these requirements for the use with polarized ^{3}He gas. For this purpose, a piezo-driven as well as a pressure-driven valve were designed. Finally, an ion-polarimetry setup was constructed and built. Laser-accelerated $^3\text{He}^{2+}$ ions from the pre-polarized

^{3}He gas-jet target will enter the polarimetry cage through a stack of apertures with different diameters. This leads to a reduction of undesired scattering effects at the aperture boundaries. Inside the cage, a CD_2 foil is positioned in the center of the ion polarimeter and serves as a secondary-scattering target for the incoming ion bunches. The angular distribution of the fusion protons out of the D(^{3}He,p)^{4}He nuclear reaction can be measured with detectors which are aligned around the CD_2 foil. CR-39 SSNTDs were planned as proton detectors. It is highly recommended to use stacks of *e.g.* six CR-39 with a thickness of 500 µm in order to develop the proton tracks for various energy ranges. With the help of the experimentally obtained ^{4}He^{2+} ion number from the PHELIX beamtime, a *lower limit* for the fusion proton yield could be estimated with high accuracy. In total, 1800 protons are expected on each detector.

9.2. Future work

Since the experimental as well as the simulated results within the current doctoral studies are promising and the feasibility of laser-driven ion acceleration from helium-gas jets was demonstrated at PHELIX, a proposal for PHELIX beamtime will be submitted at the end of Aug. 2015. The beamtime period will be scheduled from 2016 to 2017. Independently from the decision of the PHELIX committee, the further work on the layout for the polarized ^{3}He target will be continued. This includes the manufacturing, assembling and testing of the whole magnetic field system, the pressure booster as well as the valve. The knowledge about the final field gradients as well as the relaxation times of the ^{3}He spin polarization inside this field is of great importance. Moreover, the behavior of the nuclear spins after compaction has to be investigated. Such a measurement has to be conducted within the magnetic holding field. A possible technique would be to compact a specific amount of pre-polarized gas and to store it in an empty storage vessel. The amount of high-pressure gas should be chosen thus, that a measurement of the relaxing spin polarization is possible, of course. Furthermore, the polarimetry cage has to be calibrated. This can be done with monoenergetic ^{3}He^{2+} ions with energies up to 2 MeV at the Jülich Tandetron accelerator. The fusion proton yield can be measured dependent on the incident ion dose. Another issue regarding the polarization measurement would be to replace the planned CR-39 SSNTDs as fusion proton detectors with scintillators and photo-multipliers. In comparison to CR-39, an online detection of the fusion protons within the PHELIX experiment would have enormous advantages since the results can be analyzed directly after each laser shot without breaking vacuum. But, the realization of such a detection technique is challenging. One has to consider the huge EMP signals as well as the gamma background. The latter can be suppressed by proper lead shielding. Regarding the EMP, a possible solution would involve a thick copper housing for the whole polarimetry cage. All of the electric supply cables have to be shielded.

As it was concluded within this thesis, based on the present EPOCH simulations, a further investigation of the helium-ion yield at an angular range around ±90° relative to the laser direction, *i.e.* in the transversal direction, is highly recommended for a future beamtime at Arcturus. A setup which includes Thomson parabola spectrometers aligned at two or three angles close to ±90° would be the best solution for extracting a possible ion signal.

Appendix

A. Appendix

A.1. Nuclear Spin Polarization

A.1.1. Polarization of a particle beam

The density matrix ρ includes the statistical properties of a particle beam. Every pure quantum state $|\psi_i\rangle$ of each single particle is related with its occupation probability p_i, *i.e.* the probability to find the i^{th} quantum state in the ensemble with n pure quantum states. The density matrix is given by

$$\rho = \sum_{i=1}^{n} p_i \, |\psi_i\rangle \, \langle\psi_i| \; . \tag{A.1}$$

The expected value of an operator A can be defined with the help of Eq. (A.1):

$$\langle A \rangle = \sum_{i=1}^{n} p_i \, \langle\psi_i| \, A \, |\psi_i\rangle = \operatorname{tr}(\rho A) \; , \tag{A.2}$$

and due to the fact that the corresponding polarization operator P has real eigenvalues, the density matrix has to be Hermitian and positive definite. With $|\psi\rangle = a\,|{}^1\!/\!_2, +{}^1\!/\!_2\rangle + b\,|{}^1\!/\!_2, -{}^1\!/\!_2\rangle$ the density matrix for spin-${}^1\!/\!_2$ particles can be written as

$$\rho = \begin{pmatrix} |a|^2 & ab^* \\ a^*b & |b|^2 \end{pmatrix} \qquad \text{, with } \; \operatorname{tr}(\rho) = \; |a|^2 + |b|^2 \; = 1 \, . \tag{A.3}$$

The basis matrices are the identity matrix $\mathbb{1}$ as well as the three Pauli matrices σ_i ($i = x, y, z$), with

$$\sigma_x = \begin{pmatrix} 0 & 1 \\ 1 & 0 \end{pmatrix} \; , \; \sigma_y = \begin{pmatrix} 0 & \mathrm{i} \\ -\mathrm{i} & 0 \end{pmatrix} \; , \; \sigma_z = \begin{pmatrix} 1 & 0 \\ 0 & -1 \end{pmatrix} \; . \tag{A.4}$$

The matrices have the following properties: $\operatorname{tr}(\rho) = 1$, $\operatorname{tr}(\mathbb{1}) = 2$, $\operatorname{tr}(\sigma_i) = 0$ and $\operatorname{tr}(\sigma_i\sigma_k) = 2\delta_{ik}$. Hence, the density matrix ρ can be expanded to

$$\rho = \alpha\mathbb{1} + \sum_{i=1}^{3} \beta_i \sigma_i \, , \tag{A.5}$$

Thus, α can be calculated as $\alpha = {}^1\!/_2$.

With the help of Eq. (A.4), the polarization $\boldsymbol{P} = (P_x, P_y, P_z)$ can be defined as the expected value of the Pauli matrices: $P_i = \langle \sigma_i \rangle = \mathrm{tr}(\rho\sigma_i)$ $(i = x, y, z)$. Along the z-axis, the polarization P_z is given by $P_z = \mathrm{tr}(\rho\sigma_z)$. β_i can be calculated as follows:

$$P_i = \mathrm{tr}(\rho\sigma_i) = \mathrm{tr}(\alpha \mathbb{1} \sigma_i + \sum_{i=1}^{3} \beta_i \sigma_j \sigma_i) = 2\beta_i\,. \tag{A.6}$$

Now, the density matrix is given by

$$\rho = \frac{1}{2} \begin{pmatrix} 1 + P_z & P_x + \mathrm{i}P_y \\ P_x - \mathrm{i}P_y & 1 - P_z \end{pmatrix}\,. \tag{A.7}$$

The probability $p_\pm$ for beam particles with $m = \pm{}^1\!/_2$ is given by $p_\pm = {}^{N_\pm}\!/_{N}$. Here $N_\pm$ is the occupation number for particles with up and down state, respectively, and the number of all particles $N = N_+ + N_-$ is proportional to the intensity I of the incoming particle beam. With the help of this relation, the polarization P_z of such an ensemble can be defined as:

$$\begin{aligned} P_z = \langle \sigma_z \rangle &= \sum_{i=1}^{n} p_i \left\langle \psi_i \left| \sigma_z \right| \psi_i \right\rangle\,, \quad \text{with } \left|\psi_i\right\rangle = \left|m\right\rangle \\ &= \sum_m p_i \left\langle m \left| \sigma_z \right| m \right\rangle = \sum_m 2mp_m \\ &= p_+ - p_- = \frac{N_+ - N_-}{N_+ + N_-}\,. \end{aligned} \tag{A.8}$$

A.1.2. Measurement of spin polarization

An incoming particle beam can be seen as a particle wave ψ. In a large distance from the interaction point, the wave function is given by

$$\psi_{\text{out}} \propto \overbrace{\mathrm{e}^{\mathrm{i}\boldsymbol{k}_{\text{in}}\cdot\boldsymbol{z}}}^{\text{(I)}} + \underbrace{f\left(\boldsymbol{k}_{\text{out}}, \boldsymbol{k}_{\text{in}}\right) \cdot \frac{\mathrm{e}^{\mathrm{i}k_{\text{out}}r}}{r}}_{\text{(II)}}\,. \tag{A.9}$$

The first term (I) in Eq. (A.9) represents the particle wave of outgoing unscattered particles, while (II) stands for the outgoing spherical wave of particles which interacted with the atomic nuclei. Here, $f\left(\boldsymbol{k}_{\text{out}}, \boldsymbol{k}_{\text{in}}\right)$ is the scattering amplitude, a scalar form factor applicable for the special case of an unpolarized incoming particle beam. Some spin-spin interactions do not cancel out which enforces to replace the amplitude $f\left(\boldsymbol{k}_{\text{out}}, \boldsymbol{k}_{\text{in}}\right)$ by a matrix $M\left(\boldsymbol{k}_{\text{out}}, \boldsymbol{k}_{\text{in}}\right)$:

$$\psi_{\text{out}} = \mathrm{e}^{\mathrm{i}\boldsymbol{k}_{\text{in}}\cdot\boldsymbol{z}} + M\left(\boldsymbol{k}_{\text{out}}, \boldsymbol{k}_{\text{in}}\right) \times \frac{\mathrm{e}^{\mathrm{i}k_{\text{out}}r}}{r} \; . \tag{A.10}$$

Now, the deflected state $|\psi\rangle_{\text{out}}$ can be defined as

$$|\psi\rangle_{\text{out}} = M\left(\boldsymbol{k}_{\text{out}}, \boldsymbol{k}_{\text{in}}\right)|\psi\rangle_{\text{in}} \; , \tag{A.11}$$

and the resulting density matrix of the outgoing particle wave is given by

$$\rho_{\text{out}} = M\rho_{\text{in}}M^{\dagger} \, , \tag{A.12}$$

with the density matrix $\rho_{\text{in}} = \sum\limits_{n} p_i \, |\psi\rangle_{\text{in}} \, \langle\psi|_{\text{in}}$ of the incoming polarized beam.

The cross section for this reaction can be written as

$$\left(\frac{d\sigma}{d\Omega}\right)_{\text{in-out}} = \frac{k_{\text{out}}}{k_{\text{in}}} \times \operatorname{tr}(\rho_{\text{out}}) = \frac{k_{\text{out}}}{k_{\text{in}}} \times \operatorname{tr}(M\rho_{\text{in}}M^{\dagger}) \, . \tag{A.13}$$

The influence of polarization of the incoming polarized particles on the deflected particles are summarized in the analyzing powers $A_i = A_i(\mathcal{E}, \vartheta)$ $(i = x, y, z)$, with $\mathcal{E}$ as the beam energy and ϑ as the angle between incoming ($\boldsymbol{k}_{\text{in}}$) and scattered particles ($\boldsymbol{k}_{\text{out}}$). The analyzing powers are defined by

$$A_i = A_i(\mathcal{E}, \vartheta) = \frac{\operatorname{tr}\left(M\sigma_i M^{\dagger}\right)}{\operatorname{tr}\left(MM^{\dagger}\right)} \; . \tag{A.14}$$

This allows a compact form of the differential cross section of polarized spin-$1/2$ particles:

$$\left(\frac{d\sigma}{d\Omega}\right)_{\text{pol}} = \left(\frac{d\sigma}{d\Omega}\right)_{\text{unpol}} \left(1 + P_x A_x + P_y A_y + P_z A_z\right) \, . \tag{A.15}$$

A.2. Metastable exchange optical pumping

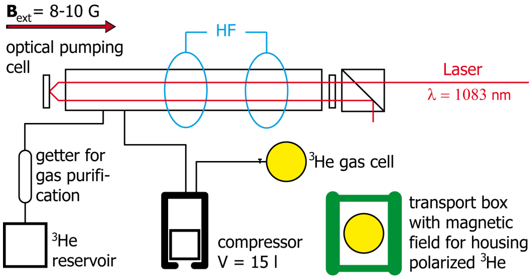

Figure A.1.: Schematic: the ^{3}He polarizer [Eng11].

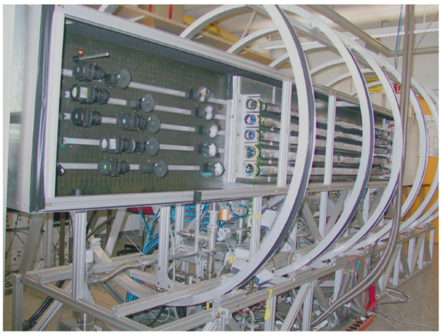

Figure A.2.: The ^{3}He polarizer [Hei].

At Mainz University the ^{3}He gas is polarized by metastable exchange optical pumping. Figure A.1 illustrates the schematic of the polarizer [Eng11]. In an optical pumping cell (cylindric design with a radius of $r = 2.5\,\mathrm{cm}$), located in an external homogeneous magnetic field $B_\mathrm{ext} \approx 8 - 10\,\mathrm{G}$ (*cf.* the big Helmholtz coils in Fig. A.2 [Hei]), pure ^{3}He gas with a pressure of approximately 1 mbar is deployed. MEOP is mostly efficient for ^{3}He pressures of $\leq 1\,\mathrm{mbar}$. If the pressure arises, the density of the 2^3S_1 atoms is too low and the relaxation processes occur too fast. After the polarization process the ^{3}He gas is compressed with an adequate compressor developed at Mainz for a better applicability and for the transport [Sur95, Ebe00].

A gas discharge (high frequency of about $2-4\,\mathrm{MHz}$) excites the electrons of approximately 1 ppm of the ^{3}He atoms from the ground state 1^1S_0 into the 2^3S_1 metastable state (*cf.* Fig. A.3).

The ground state 1^1S_0 with $F = {}^1\!/_2$ has two Zeeman sublevels $G_{1,2}$ with $m_F = \pm{}^1\!/_2$. The number of all particles n_g in the ground state is given by:

$$n_\mathrm{g} = g_1 + g_2 = \frac{p}{k_\mathrm{B}T} = 2.47 \cdot 10^{22}\,\frac{p}{\mathrm{m}^3}\ , \tag{A.16}$$

with $g_i = {}^{n_\mathrm{g}}\!/_2\,(1 \pm P)$ $(i = 1,\,2)$ as the particle number in the G_i sublevels, P as the polarization, p (in mbar) as the gas pressure and $T = 293.15\,\mathrm{K}$ as the temperature. Because only 1 ppm of the ^{3}He is excited into the metastable state, n_g approximately is constant after the excitation by the gas discharge.

The metastable 2^3S_1 state has two hyperfine levels $F = {}^3\!/_2$ (with states $m_F = {}^3\!/_2$, ${}^1\!/_2$, $-{}^1\!/_2$, $-{}^3\!/_2$, written as A_{1-4}) and $F = {}^1\!/_2$ (with states $m_F = {}^1\!/_2$, $-{}^1\!/_2$, written as $A_{5,6}$) [Nac85]. For the metastable states A_i the number of all particles n_m is given by the sum of the particle numbers a_i:

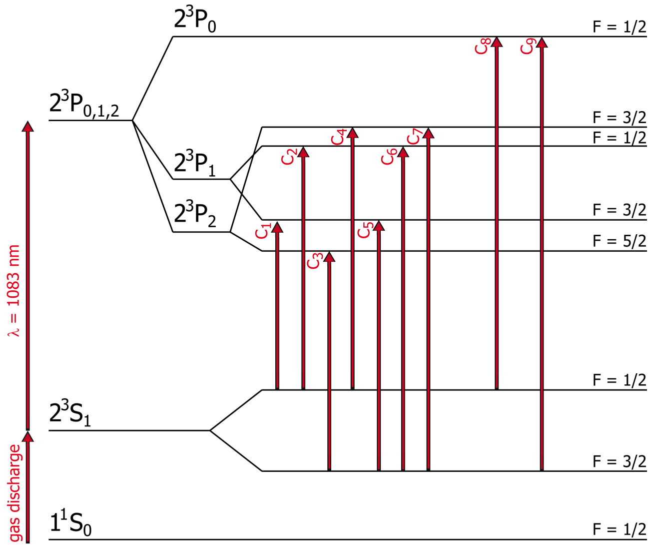

Figure A.3.: Metastable optical pumping (MEOP) of ^{3}He atoms: After an excitation from the ground state into the 2^3S_1 metastable state by a gas discharge, a circular polarized Laser pulse excites the ^{3}He* atoms into the 2^3P_J state. Nine transmissions $C_1 - C_9$ are possible [Eng11].

$$n_{\mathrm{m}} = \sum_{i=1}^{6} a_i \ . \tag{A.17}$$

The supressed probability of more photon transitions prohibits a radiation decay from the metastable into the ground state. Due to the interaction with the walls of the reservoir, the mean lifetime is $\tau_{\mathrm{He}^*} \approx 1\,\mathrm{ms}$.

The incoming resonant σ^+ circular polarized Laser pulse ($\lambda = 1083\,\mathrm{nm}$, propagating in the direction of B_{ext}) pumps these ^{3}He* atoms into the 2^3P_0 state (*cf.* Fig. A.3). Because of the σ^+-polarity of the Laser, transfers with a $\Delta m_F = 1$ are excited, so that the angular momentum of the absorbed photons is transferred to the ^{3}He.

The 2^3P_J state has five levels P_0, P_x, P_1, P_y, P_2. 18 Zeeman sublevels B_j are possible. For the metastable states B_j the number of particles n_{p} is given by:

$$n_{\mathrm{p}} = \sum_{j=1}^{18} b_j \ . \tag{A.18}$$

Figure A.4 illustrates the Zeeman sublevels for ^{3}He: The states 1^1S_0, 2^3S_1 and 2^3P_J with quantum numbers F, m_F are occupied by G_i, A_i and B_j.

The absorption rate, or absorbed photon rate, Γ_{ij} for a transfer from the Zeeman levels A_i to B_j can be defined as:

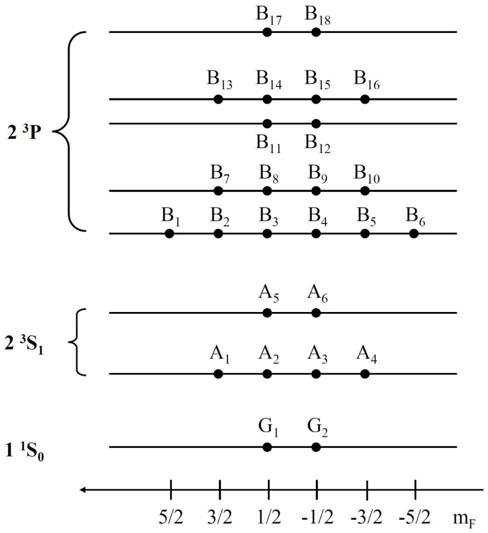

Figure A.4.: Zeeman sublevels for ^{3}He: The G_i, A_i, B_j states are illustrated [Wol04].

$$\Gamma_{ij} = \frac{1}{\tau_{ij}} = \gamma_{ij} \cdot T_{ij} \ , \tag{A.19}$$

where γ_{ij} represent the Laser parameters, characteristics of the transfer (like the oscillating power for helium or frequencies for the transfer from 2^3S_1 to 2^3P_J) and constants (like the fine structure constant α or the mass of the electrons), while the T_{ij} are matrix elements for the transfer from A_i to B_j. As it can be regarded in Fig. A.3, nine hyperfine transfers C_1 to C_9 from both 2^3S_1 hyperfine states into the five hyperfine states of the 2^3P_J multiplet are possible. A pumping on the C_1 and C_3 transfers generates a contrarious polarization [Nac85], which mixes with the other transfers. The transfers $C_1 - C_7$ are very close and cannot be pumped separately, so they mix. The contributions to the polarization degree from these transfers is very low. Only C_8 and C_9, which transfer to the 2^3P_0 states $B_{17,18}$, are clearly separated from the other ones and do not overlap, so that these transfers can be used for MOEP [Sch04].

The external magnetic field induces a splitting of the hyperfine states into the Zeeman levels with the quantum number m_F. The single 2^3P_J Zeeman states with a mean lifetime of $\tau_{P_J} \approx 97.8\,\text{ns}$ mix due to gas kinetic collisions (radiation-free collisional mixing) and decay back with equal probabilities isotropicly to all 2^3S_1 sublevels. The cross section has a value of $\sigma_{\text{cm}} = 68 \cdot 10^{-20}\,\text{m}^2$ [Sch67, Sch68], so that the time constant τ_{cm} for collisional mixing at a pressure of 1 mbar is given by $\tau_{\text{cm}} = 30\,\text{ns}$. While decaying back, no net angular momentum is transferred to the atoms. The electron spin is solely oriented by the Laser pulse.

A nuclear spin-polarization is induced because of the hyperfine interaction. The interaction time for the coupling of the nuclear spins with the spin of the electrons in the shell can be calculated with the help of the hyperfine constant $A = 4.4931\,\text{GHz}$ of the

2^3S_1 state of ^{3}He: $\tau_{\mathrm{HF}} = A^{-1} = 2.23 \cdot 10^{-10}\,\mathrm{s}$ [Cou02]. Because of $\tau_{\mathrm{HF}} \ll \tau_{P_J}$, the m_J and m_I quantum numbers of the m_F basis change completely during the excitation and disexcitation of the atoms [Wol04]. Thus, the nuclear spin aligns along the quantization axis given by the external magnetic field.

If atoms of the metastable state collide with those of the ground state (metastability exchange collisions with a collision time of approxiamtely $\tau_{\mathrm{coll}} \approx 10^{-12}\,\mathrm{s}$), an energy transfer results and the spin of the electron shell is transferred from the excited metastable atom to the one of the ground state [Col64, Gre64, DR71, DR73]. For the collision rate Γ for gaskinetic collisions the following Eq. applies:

$$\Gamma = \frac{1}{\langle\tau\rangle} = \sqrt{2}\sigma \,\langle v\rangle\, n \ , \tag{A.20}$$

$$\begin{aligned} \text{with} \quad \frac{1}{\tau_{\mathrm{me,g}}} &= \sqrt{2}\sigma_{\mathrm{me}} \,\langle v\rangle\, n_{\mathrm{g}} \\ \text{and} \quad \frac{1}{\tau_{\mathrm{me,m}}} &= \sqrt{2}\sigma_{\mathrm{me}} \,\langle v\rangle\, n_{\mathrm{m}} \ , \end{aligned} \tag{A.21}$$

with the average collision time $\langle\tau\rangle$, the cross section σ_{me}, the average velocity of the atoms $\langle v\rangle$ and the particle density n. $1/\tau_{\mathrm{me},i}$ ($i = \mathrm{g,m}$) are the collision rates for atoms in the ground state (n_{g}) and for those of the metastable 2^3S_1 state (n_{m}), respectively. For ^{3}He and room ambient temperature the average velocity $\langle v\rangle_{^3\mathrm{He}}$ is given by:

$$\langle v\rangle_{^3\mathrm{He}} = \sqrt{\frac{8k_{\mathrm{B}}T}{\pi m}} = 1434\,\frac{\mathrm{m}}{\mathrm{s}} \ , \tag{A.22}$$

The cross section for the metastable atoms is $\sigma_{\mathrm{He}^*} \approx 1.2 \cdot 10^{-18}\,\mathrm{m}^2$. At a pressure of 1 mbar and for room ambient temperature about 10^5 collisions occur during $\tau_{\mathrm{He}^*} = 1\,\mathrm{ms}$ [Eva69]. However, a change of the orientation of the nuclear spins does not occur, because the interaction time of the hyperfine interaction is about two magnitudes larger than the collision time: $\tau_{\mathrm{HF}} > \tau_{\mathrm{coll}}$.

The reaction for the collisions involving metastability exchange is given by:

$$^3\mathrm{He}^*_{(\mathrm{I},m_F)} + {}^3\mathrm{He}_{(\mathrm{II},\downarrow)} \rightleftharpoons {}^3\mathrm{He}_{(\mathrm{I},\uparrow)} + {}^3\mathrm{He}^*_{(\mathrm{II},m'_F = m_F - 1)} \ \text{[Eck92]} \ . \tag{A.23}$$

Here ^{3}He* is the excited atom and ^{3}He is the atom being in the ground state, while I and II represent the nuclei of the atoms with a nuclear spin up (↑) or down (↓). After the impact an excited ^{3}He* with spin down is present, which can be pumped again, while the other ^{3}He being in the ground state has a spin up. Hence, the orientation of the metastable state is transferred to the nuclear spin of the ground state atoms [Eck92], and the occupation number of the ground state is enlarged.

Metastability exchange collisions result an energy transfer from polarized metastable ^{3}He to the ones in the ground state. The cross section is given by $\sigma_{\mathrm{me}} = (7.6 \pm 0.4) \cdot 10^{-20}\,\mathrm{m}^2$ [DR71]. From 10^5 collisions only every 15th collision will cause an energy transfer.

Relaxation mechanisms referring to MEOP

Orientation of the metastable ^{3}He* Not only metastability exchange collisions between ^{3}He* and ^{3}He have an effect on the spin alignment of the atoms, but also collisions, which induce a change from A_i to A_j, or collisions with the walls, which mainly disexcite the atoms, influence the orientation. For given pressures of 1 mbar the wall-interaction is the dominant relaxation mechanism. However, the number of ^{3}He* is constant, because the disexcited atoms are directly replaced by other excited, but disoriented, atoms with a rate $1/\tau_{\mathrm{r}}$. For the rate equation the following Eq. applies:

$$\dot{a}_i^{\mathrm{coll}} = \frac{1}{\tau_{\mathrm{r}}} \left(\sum_{j=1}^{6} \frac{a_j}{6} - a_i \right) \text{ [Wol04] .} \tag{A.24}$$

The average time for diffusion of the ^{3}He* with values of several 1 ms is much larger than the other time constants, so that in general, this relaxation has small effects on the polarization.

Collisional mixing Collisional mixing results a change from B_j to B_i states of the atoms in the 2^3P_J states. For the rate equation the following Eq. applies:

$$\dot{b}_i^{\mathrm{coll}} = \frac{1}{\tau_{\mathrm{cm}}} \left(\sum_{j=1}^{18} \frac{b_j}{18} - b_i \right) \text{ [Wol04] ,} \tag{A.25}$$

with $\tau_{\mathrm{cm}} = 30\,\mathrm{ns}$ as the time constant of the collisional mixing at a pressure of 1 mbar. Because of $1/\tau_{\mathrm{cm}} > 1/\tau_{\mathrm{me,g}}$ as the exchange rate of the metastable atoms with the ones of the ground state, and also $1/\tau_{\mathrm{cm}} > 1/\tau_{ij}$ as the absorption rate, the 2^3P_J states B_{1-16} are occupied equally by collisional mixing.

Relaxation by gas discharge Inside the pumping cell the strongest relaxation rate comes from the gas discharge, which excites allready polarized ^{3}He. Thereby, circular polarized fluorescent light is emitted and thus, the nuclear spins disorient.

A.3. Input deck

In order to get an impression of the structure of an input deck, the following code exemplifies the parameter setting for the simulated PHELIX laser interacting with a neutral charged ^{4}He gas jet:

Listing A.1: input.deck with simulation parameters

```
#neutral 4He gas target, ionized by laser, 0.5 mm nozzle, 26 bar
#actual 2014 PHELIX laser param.: 50 J, 0.8 ps, 11x15 mu^2 FWHM, 1.38 W/cm^2
#------------------------------------------------------------
#control block
begin:control
  #global number of grid points
  nx = 50000             #in x
  ny = 5000              #in y
  #final time of simulation
  t_end = 15.0e-12       #simulation time 15 ps
  #size of domain
  x_min = 0.0            #minimum grid position of the domain
  x_max = 2.5e-3         #maximum grid position of the domain,
                         # total width 2500 mu
  y_min = 0.0            #minimum grid position of the domain
  y_max = 0.25e-3        #maximum grid position of the domain,
                         # total height 250 mu
  #ionization mechanism
  field_ionisation = T
end:control
#------------------------------------------------------------
#boundary block
begin:boundaries
  bc_x_min_field = simple_laser          #em wave source attachable,
  # min reflection of impinging em waves, particles fully transmitted
  bc_x_min_particle = simple_outflow
  bc_x_max = simple_outflow     #no em waves attachable, inflowing
                                # characteristics set to zero, i.e.
                                # particles are removed when reaching
                                # the boundary
  bc_y_min = simple_outflow
  bc_y_max = simple_outflow
end:boundaries
#------------------------------------------------------------
#constants block
begin:constant
  #gas jet borders
  xl = 0.12e-3                  #left edge of the gas jet
  xr = xl + 1.6e-3              #right edge of the gas jet
  xm = (xl + xr)/2.0            #x-position of central axis
  xgrid = (x_max - x_min)/nx    #length per grid points in x
  ygrid = (y_max - y_min)/ny    #length per grid points in y
  xleft = x_min + xgrid/2.0
  xright = x_max - xgrid/2.0
  yup = y_max - ygrid/2.0
  ydown = y_min + ygrid/2.0
  #c{1,2} constants for superGaussian density distribution
  c1 = 0.502e-3
  c2 = 0.8e-3
  #laser's incidence angle: degr< 90degr, and rad
  incidence_deg = 0.0
  incidence_rad = incidence_deg*pi/180.0
  #focus position in x
  xf = xm - 0.1e-3              #here: 100 mu before central gas jet axis
  #center of laser beam in y
  ym = (yup + ydown)/2.0 - (xf - xleft)*tan(incidence_rad)
  #number of grid points inside borders of gas jet in x
  ngridx = (nx/(x_max - x_min))*(xr - xl)
  #number of particles per cell
  part = 1.0
  #gas jet param.: 0.5 mm nozzle, 20 bar
  xfwhm = 1000 * micron                         #gas jet width FWHM = 1000 mu
  wxfwhm = xfwhm/(2.0 * sqrt(loge(2.0)))        #xFWHM = wxfwhm 2 sqrt(ln2)
  densitymax = 5.55e25                          #max. density [1/m^3] at xm
```

```
  #laser parameters for PHELIX
  lambda = 1.053 * micron                      #wavelength = 1053 nm
  intensity_w_cm2 = 1.38e19                    #calculated intensity
  omega = 2.0*pi*c/lambda                      #laser frequency omega_L
  den_crit = critical(omega)                   #critical density n_c
  tlaser = 0.8*pico                            #laser pulse duration FWHM
  wtlaser = tlaser/(2.0 * sqrt(loge(2.0)))     #1/e^2 pulse length of FWHM
  dfocus = 25.7*micron                         #focus diameter dFWHM 25.7 mu
                                               # original: 11x15 mu^2 (eliptical)
  waist = (dfocus)/2.0                         #focus radius rFWHM = 12.85 mu
  wwaist = waist/(2.0*sqrt(loge(2.0)))         #1/e^2 width of beam waist:
                                               # rFWHM = 2 wwaist sqrt(ln2)
  xrayleigh = pi*(wwaist)^2/lambda             #Rayleigh length
  #laser beam radius at left edge of the box, beam spot size evolution
  ylaser0 = wwaist * sqrt(1 + ((xf-xleft)/(xrayleigh))^2)
  #radius of curvature
  rcurv = (xf - xleft) * (1 + (xrayleigh / (xf-xleft))^2)
  #Gouy phase
  gouy = atan((xf-xleft)/xrayleigh)
  #normalization of the intensity
  norm = wwaist/ylaser0 /(sqrt(cos(gouy)))
end:constant
#-------------------------------------------------------------
#species blocks
begin:species
  name = Helium                       #neutral 4He gas
  charge = 0.0                        #neutral charged
  mass = 2*1836.2 + 2*1838.7 + 2.0    #2p&2n (nucl.), 2e (shell)
  #num. gas jet grids in x,y*partcl/grid
  npart = ngridx * ny * part
  #2 superGauss distr. in x (6th order), centered on xm, charac. width c1 and c2
  density = (4.75e25 * supergauss(x,xm,c1,6) + 8e24 * supergauss(x,xm,c2,6))
  density = if((x lt xl) or (x gt xr), 1e-11, density(Helium))
  density_min = 1e-12
  density_max = densitymax
  #ionization energies for 4He
  ionisation_energies = (54.4*ev,24.6*ev)
  electron = (Electron1,Electron2)
end:species
#-------------------------------------------------------------
begin:species
  name = Electron1
  charge = -1.0
  mass = 1.0
  rho = 0.0
end:species
#-------------------------------------------------------------
begin:species
  name = Electron2
  charge = -1.0
  mass = 1.0
  rho = 0.0
end:species
#-------------------------------------------------------------
#laser block
begin:laser
  boundary = x_min
  lambda = lambda
  intensity_w_cm2 = intensity_w_cm2
  #temporal gauss profile
  t_profile = gauss(time,3*wtlaser,wtlaser)
  #spatial gauss profile
  profile = norm*gauss(y,ym,ylaser0)
  #phase, thanks to Oliver Deppert @TUD ;)
  phase = 2.0*pi/lambda*((y-ym)^2/(2.0*rcurv)-y*sin(incidence_rad))
end:laser
```

```
#----------------------------------------------------------------
#output block
begin:output
  #number of time steps between output dumps
  dt_snapshot = 0.5 * pico
  #number of snapshots between full dumps
  full_dump_every = 10
  restart_dump_every = -1
  force_last_to_be_restartable = F
  #particle properties
  particles = alwaxs
  particle_grid = always
  px = always
  py = always
  pz = always
  particle_weight = always
  particle_energy = always
  #grid properties
  grid = always
  ex = always
  ey = always
  bz = always
  #derived variables
  number_density = always + species
  charge_density = always + species
  distribution_functions = always + species
  absorption = always
end:output
#----------------------------------------------------------------
begin:dist_fn
  name=angle_en
  ndims=2
  dumpmask=always
  direction1=dir_xy_angle
  resolution1 = 1000
  direction2 = dir_en
  range2 = (1e-10*mev, 30*mev)
  resolution2 = 500
  include_species:Helium2
end:dist_fn
begin:dist_fn
  name=angle_en
  ndims=2
  dumpmask=always
  direction1=dir_xy_angle
  resolution1 = 1000
  direction2=dir_en
  range2 = (1e-10*mev, 120*mev)
  resolution2 = 500
  include_species:Electron1
  include_species:Electron2
end:dist_fn
```

A.4. PHELIX experiment i009: shot parameters

shot-#	PHELIX shot-#	date, time	energy [J]	pulse length [fs]	gas	pressure [bar]
01	11159	2015-01-23, 09:13	43.8	3191	^{4}He	30
02	11161	2015-01-23, 10:55	112.0	612		
03	11163	2015-01-23, 12:57	119.1	400		
04	11165	2015-01-23, 14:48	99.5	771		
05	11166	2015-01-23, 17:51	58.3	1001		
06	11169	2015-01-26, 09:56	46.7	1176	^{4}He	30
07	11172	2015-01-26, 11:26	36.9	780		
08	11173	2015-01-26, 13:04	38.3	804		
09	11174	2015-01-26, 15:40	39.2	300		14
10	11176	2015-01-26, 17:50	42.7	n.a.		
11	11178	2015-01-27, 10:16	42.3	n.a.	^{3}He	8
12	11186	2015-01-27, 11:48	50.3	n.a.		
13	11187	2015-01-27, 13:15	51.0	n.a.		
14	11188	2015-01-27, 14:51	57.0	610		
15	11191	2015-01-27, 16:24	49.9	5000		
16	11194	2015-01-27, 17:55	43.9	n.a.		
17	11198	2015-01-28, 09:33	38.7	916	^{3}He	14
18	11201	2015-01-28, 11:23	54.1	547		
19	11203	2015-01-28, 15:53	52.7	n.a.	no gas	–

Table A.1.: Laser-shot parameters in the PHELIX experiment i009.

List of Abbreviations

ASE	amplified spontaneous emission
ATI	above-threshold ionization
BG	background
BSI	barrier suppression ionization
CCD	charged couple device
CPA	chirped pulse amplification
CR-39	Columbia Resin #39
CW	continuous wave
EMP	electromagnetic pulse
EPOCH	Extendable PIC Open Collaboration (silent H)
FLOPS	floating point operations per second
FWHM	full width at half maximum
FZJ	Forschungszentrum Jülich - GmbH
GPFS	general parallel file system
GSI	Gesellschaft für Schwerionenforschung - GmbH
IKP	Institut für Kernphysik
ILPP	Institut für Laser- und Plasmaphysik
IP	image plate *or* imaging plate
IR	infrared
JSC	Jülich Supercomputing Centre
JUQUEEN	JUelich Blue Gene/Q
JURECA	JUelich Research on Exascale Cluster Architectures
JUROPA	JUelich Research On Petaflop Architectures
*Ju*SPARC	Juelich Short-pulse Particle and Radiation Centre (in planning stage, 2014/2015)
laser	light amplification by stimulated emission of radiation
MCP	multi channel plate
MEOP	metastable exchange optical pumping
MPI	multi-photon ionization *and* message passing interface
OAP	off-axis parabola *or* off-axis parabolic mirror
OTBI	over-the-barrier ionization
PADC	poly-allyl diglycol carbonate
PHELIX	Petawatt High-Energy Laser for heavy Ion eXperiments
PIC	particle-in-cell
PSL	photo-stimulated luminescence
RCF	radiochromic film
RF	radio frequency
RHIC	Relativistic Heavy Ion Collider
SDF	structure-data file
SSNTD	solid-state nuclear track detector
TCC	target-chamber center
TI	tunneling ionization
TNSA	target normal sheath acceleration
TP	Thomson parabola spectrometer
UV	ultraviolet

Bibliography

[Ago68] P. Agostini, G. Barjot, J. Bonnal, G. Mainfray, C. Manus, and J. Morellec. *Multiphoton ionization of hydrogen and rare gases.* Quantum Electronics, IEEE Journal of, vol. 4, no. 10:pp. 667–669, 1968. ISSN 0018-9197. URL http://dx.doi.org/10.1109/JQE.1968.1074955.

[Ago79] P. Agostini, F. Fabre, G. Mainfray, G. Petite, and N. K. Rahman. *Free-free transitions following six-photon ionization of xenon atoms.* Phys. Rev. Lett., vol. 42:pp. 1127–1130, 1979. URL http://dx.doi.org/10.1103/PhysRevLett.42.1127.

[AJ91] F. Abu-Jarad, M. A. Islam, I. Abu-Abdoun, and M. A. Khan. *Ultraviolet and laser irradiation effects on various batches of CR-39.* International Journal of Radiation Applications and Instrumentation. Part D. Nuclear Tracks and Radiation Measurements, vol. 19, no. 1–4:pp. 135 – 138, 1991. ISSN 1359-0189. URL http://dx.doi.org/10.1016/1359-0189(91)90158-E.

[Ale14] A. Alejo, S. Kar, H. Ahmed, A. G. Krygier, D. Doria, R. Clarke, J. Fernandez, R. R. Freeman, J. Fuchs, A. Green, J. S. Green, D. Jung, A. Kleinschmidt, C. L. S. Lewis, J. T. Morrison, Z. Najmudin, H. Nakamura, G. Nersisyan, P. Norreys, M. Notley, M. Oliver, M. Roth, J. A. Ruiz, L. Vassura, M. Zepf, and M. Borghesi. *Characterisation of deuterium spectra from laser driven multi-species sources by employing differentially filtered image plate detectors in Thomson spectrometers.* Review of Scientific Instruments, vol. 85, no. 9:093303, 2014. URL http://dx.doi.org/10.1063/1.4893780.

[Ali05] V. K. Alimov, M. Mayer, and J. Roth. *Differential cross-section of the D(^{3}He,p)^{4}He nuclear reaction and depth profiling of deuterium up to large depths.* Nuclear Instruments and Methods in Physics Research Section B: Beam Interactions with Materials and Atoms, vol. 234, no. 3:pp. 169 – 175, 2005. ISSN 0168-583X. URL http://dx.doi.org/10.1016/j.nimb.2005.01.009.

[Amm86] M. V. Ammosov, N. B. Delone, and V. P. Krainov. *Tunnel ionization of complex atoms and of atomic ions in an alternating electromagnetic field.* Soviet Physics - JETP, vol. 64, no. 6:pp. 1191–1194, 1986. URL http://www.jetp.ac.ru/cgi-bin/e/index/e/64/6/p1191?a=list.

[And67] J. H. B. Anderson. *An experimental determination of the Gladstone-Dale constants for dissociating oxygen.* University of Toronto, Institute for Aerospace Studies (UTIAS), Toronto, USA, pp. 1–103, 1967. Technical Report: UTIAS Technical Note No. 105, AFOSR 67-0336, URL http://oai.dtic.mil/oai/oai?verb=getRecord&metadataPrefix=html&identifier=AD0650162.

[Aur15] B. Aurand. 2015-03-20: personal communication, 2015. Institute for Laser and Plasma Physics, Heinrich-Heine-University Düsseldorf, Germany.

[Ban06] S. Bandyopadhyay, M. Borghesi, D. C. Carroll, G. Gregori, F. Lindau, O. Lundh, P. McKenna, D. Neely, C.-G. Wahlström, and A. Higginbotham. *Analysis on a Wedge-shaped Thomson spectrometer for ion studies*, 2006. Central Laser Facility Annual Report 2005/2006: Short Pulse Plasma Physics, URL http://www.clf.stfc.ac.uk/CLF/Publications/Annual%20Reports/2005-06/18146.aspx.

[Bar89] J. N. Bardsley, B. M. Penetrante, and M. H. Mittleman. *Relativistic dynamics of electrons in intense laser fields.* Phys. Rev. A, vol. 40:pp. 3823–3835, 1989. URL http://dx.doi.org/10.1103/PhysRevA.40.3823.

[Bar00] H. C. Barr, P. Mason, and D. M. Parr. *Electron parametric instabilities of relativistically intense laser light in under and overdense plasma.* Physics of Plasmas (1994-present), vol. 7, no. 6:pp. 2604–2615, 2000. URL http://dx.doi.org/10.1063/1.874102.

[Bar15] A. W. Barasa. *Absolute Calibration of Agfa MD4.0 Image Plate.* Bachelor thesis, TU Darmstadt, 2015.

[Bau95] D. Bauer, P. Mulser, and W. H. Steeb. *Relativistic ponderomotive force, uphill acceleration, and transition to chaos.* Phys. Rev. Lett., vol. 75:pp. 4622–4625, 1995. URL http://dx.doi.org/10.1103/PhysRevLett.75.4622.

[Ber04] L. Bergmann, C. Schaefer, H. Niedrig, and H.-J. Eichler. *Lehrbuch der Experimentalphysik; Bd. 3: Optik.* Walter de Gruyter, Berlin, New York, 2004.

[Bet77] H. A. Bethe and E. E. Salpeter. *Quantum mechanics of one- and two-electron atoms.* Plenum, New York, NY, 1977. URL http://dx.doi.org/10.1007/978-1-4613-4104-8.

[Bir85] C. K. Birdsall and A. B. Langdon. *Plasma physics via computer simulation.* New York: McGraw-Hill, 1985. ISBN 0-07-005371-5.

[Bla82] C. Blatchley, P. D. Zimmerman, O. Pruet, P. Sioshansi, and F. Wittel. *Anomalous track development in CR-39: Effects of gamma irradiation.* Nuclear Instruments and Methods in Physics Research, vol. 201, no. 2–3:pp. 535 – 537, 1982. ISSN 0167-5087. URL http://dx.doi.org/10.1016/0167-5087(82)90595-6.

[Bol14] P. Bolton, M. Borghesi, C. Brenner, D. Carroll, C. D. Martinis, F. Fiorini, A. Flacco, V. Floquet, J. Fuchs, P. Gallegos, D. Giove, J. Green, S. Green, B. Jones, D. Kirby, P. McKenna, D. Neely, F. Nuesslin, R. Prasad, S. Reinhardt, M. Roth, U. Schramm, G. Scott, S. Ter-Avetisyan, M. Tolley, G. Turchetti, and J. Wilkens. *Instrumentation for diagnostics and control of laser-accelerated proton (ion) beams.* Physica Medica, vol. 30, no. 3:pp. 255–270, 2014. ISSN 1120-1797. URL http://dx.doi.org/10.1016/j.ejmp.2013.09.002.

[Bon99] R. Bonetti, C. Broggini, L. Campajola, P. Corvisiero, A. D'Alessandro, M. Dessalvi, A. D'Onofrio, A. Fubini, G. Gervino, L. Gialanella, U. Greife, A. Guglielmetti, C. Gustavino, G. Imbriani, M. Junker, P. Prati, V. Roca, C. Rolfs, M. Romano, F. Schuemann, F. Strieder, F. Terrasi, H. P. Trautvetter, and S. Zavatarelli ((LUNA Collaboration)). *First Measurement of the $^{3}He(^{3}He,2p)^{4}He$ Cross Section down to the Lower Edge of the Solar Gamow Peak.* Phys. Rev. Lett., vol. 82:pp. 5205–5208, 1999. Information taken from the arXiv version, available at http://arxiv.org/pdf/nucl-ex/9902004.pdf, accessed: 2014-12-01, URL http://dx.doi.org/10.1103/PhysRevLett.82.5205.

[Bor70] J. P. Boris. *Relativistic plasma simulation-optimization of a hybrid code.* Proceeding of Fourth Conference on Numerical Simulations of Plasmas, 1970. URL http://www.dtic.mil/dtic/tr/fulltext/u2/a023511.pdf.

[Bor92] A. B. Borisov, A. V. Borovskiy, O. B. Shiryaev, V. V. Korobkin, A. M. Prokhorov, J. C. Solem, T. S. Luk, K. Boyer, and C. K. Rhodes. *Relativistic and charge-displacement self-channeling of intense ultrashort laser pulses in plasmas.* Phys. Rev. A, vol. 45:pp. 5830–5845, 1992. URL http://dx.doi.org/10.1103/PhysRevA.45.5830.

[Bos92] H.-S. Bosch and G. Hale. *Improved formulas for fusion cross-sections and thermal reactivities.* Nuclear Fusion, vol. 32, no. 4:p. 611, 1992. URL http://dx.doi.org/10.1088/0029-5515/32/4/I07.

[Bra13] C. Brady, K. Bennett, H. Schmitz, C. Ridgers, T. Arber, R. Evans, and T. Bell. *Developers Manual for the EPOCH PIC codes.* University of Warwick, 2013. For EPOCH version 4.0 (code and manual are available after registration on ccpforge.cse.rl.ac.uk, project: EPOCH), URL http://ccpforge.cse.rl.ac.uk/gf/download/docmanfileversion/663/3620/%65%70%6f%63%68%5f%64%65%76%2d%34%2e%30%2e%70%64%66.

[Bra14] C. Brady, K. Bennett, H. Schmitz, C. Ridgers, T. Arber, R. Evans, and T. Bell. *Users Manual for the EPOCH PIC codes.* University of Warwick, 2014. For EPOCH version 4.3 (code and manual are available after registration on ccpforge.cse.rl.ac.uk, project: EPOCH), URL http://ccpforge.cse.rl.ac.uk/gf/download/docmanfileversion/1014/4591/%65%70%6f%63%68%5f%75%73%65%72%2d%34%2e%33%2e%70%64%66.

[Bur74] W. E. Burcham, O. Karban, S. Oh, and W. B. Powell. *A source of polarized ^{3}He ions.* Nuclear Instruments and Methods, 1974. URL http://dx.doi.org/10.1016/0029-554X(74)90569-2.

[Bur93] K. Burnett, V. C. Reed, and P. L. Knight. *Atoms in ultra-intense laser fields.* Journal of Physics B: Atomic, Molecular and Optical Physics, vol. 26, no. 4:p. 561, 1993. URL http://dx.doi.org/10.1088/0953-4075/26/4/003.

[Bur14] P. Burgmer. *Auslegung und Bau eines magnestischen Systems für die Erhaltung der Polarisation von ^{3}He bei Laser-induzierter Teilchenbeschleunigung.* Bachelor thesis, FH Aachen, Campus Jülich, FB 10 Energietechnik, Physikingenieurwesen, and Peter Grünberg Institut, Forschungszentrum Jülich GmbH, 2014. URL http://juser.fz-juelich.de/record/187556.

[Car10] D. Carroll, P. Brummitt, D. Neely, F. Lindau, O. Lundh, C.-G. Wahlström, and P. McKenna. *A modified Thomson parabola spectrometer for high resolution multi-MeV ion measurements - Application to laser-driven ion acceleration.* Nuclear Instruments and Methods in Physics Research Section A: Accelerators, Spectrometers, Detectors and Associated Equipment, vol. 620, no. 1:pp. 23–27, 2010. ISSN 0168-9002. URL http://dx.doi.org/10.1016/j.nima.2010.01.054.

[Cat88a] G. D. Cates, S. R. Schaefer, and W. Happer. *Relaxation of spins due to field inhomogeneities in gaseous samples at low magnetic fields and low pressures.* Phys. Rev. A, vol. 37:pp. 2877–2885, 1988. URL http://dx.doi.org/10.1103/PhysRevA.37.2877.

[Cat88b] G. D. Cates, D. J. White, T.-R. Chien, S. R. Schaefer, and W. Happer. *Spin relaxation in gases due to inhomogeneous static and oscillating magnetic fields.* Phys. Rev. A, vol. 38:pp. 5092–5106, 1988. URL http://dx.doi.org/10.1103/PhysRevA.38.5092.

[Che05] T. Cheung, M. J. Butson, and K. Peter. *Post-irradiation colouration of Gafchromic EBT radiochromic film.* Physics in medicine and biology, vol. 50, no. 20:p. N281, 2005. URL http://dx.doi.org/10.1088/0031-9155/50/20/N04.

[Chi11] H. Childs, E. Brugger, B. Whitlock, J. Meredith, S. Ahern, K. Bonnell, M. Miller, G. H. Weber, C. Harrison, D. Pugmire, T. Fogal, C. Garth, A. Sanderson, E. W. Bethel, M. Durant, D. Camp, J. M. Favre, O. Rübel, P. Navrátil, M. Wheeler, P. Selby, and F. Vivodtzev. *VisIt: An End-User Tool For Visualizing and Analyzing Very Large Data.* In *In Proceedings of SciDAC.* 2011. Accessed: 2014-11-18, URL http://citeseerx.ist.psu.edu/viewdoc/summary?doi=10.1.1.393.8134.

[Col60] F. D. Colegrove and P. A. Franken. *Optical Pumping of Helium in the $^3S_1$ Metastable State.* Phys. Rev., vol. 119:pp. 680–690, 1960. URL http://dx.doi.org/10.1103/PhysRev.119.680.

[Col63] F. D. Colegrove, L. D. Schearer, and G. K. Walters. *Polarization of He^3 Gas by Optical Pumping.* Phys. Rev., vol. 132:pp. 2561–2572, 1963. URL http://dx.doi.org/10.1103/PhysRev.132.2561.

[Col64] F. D. Colegrove, L. D. Schearer, and G. K. Walters. *Temperature Dependence of Helium Metastability Exchange Cross Section.* Phys. Rev., vol. 135:pp. A353–A357, 1964. URL http://dx.doi.org/10.1103/PhysRev.135.A353.

[Cou02] E. Courtade, F. Marion, P.-J. Nacher, G. Tastevin, K. Kiersnowski, and T. Dohnalik. *Magnetic field effects on the 1083 nm atomic line of helium.* The European Physical Journal D - Atomic, Molecular, Optical and Plasma Physics, vol. 21, no. 1:pp. 25–55, 2002. ISSN 1434-6060. URL http://dx.doi.org/10.1140/epjd/e2002-00176-1.

[Cou07] A. Couairon and A. Mysyrowicz. *Femtosecond filamentation in transparent media.* Physics Reports, vol. 441, no. 2–4:pp. 47 – 189, 2007. URL http://dx.doi.org/10.1016/j.physrep.2006.12.005.

[cst] *CST-Computer Simulation Technology: Particle Studio.* Accessed: 2015-07-27, URL https://www.cst.com/products/cstps.

[Cum70] E. Cumberbatch. *Self-focusing in Non-linear Optics.* IMA Journal of Applied Mathematics, vol. 6, no. 3:pp. 250–262, 1970. URL http://dx.doi.org/10.1093/imamat/6.3.250.

[Dai12] H. Daido, M. Nishiuchi, and A. S. Pirozhkov. *Review of laser-driven ion sources and their applications.* Reports on Progress in Physics, vol. 75, no. 5:p. 056401, 2012. URL http://dx.doi.org/10.1088/0034-4885/75/5/056401.

[Den99] A. Deninger, B. Eberle, M. Ebert, T. Großmann, W. Heil, H.-U. Kauczor, L. Lauer, K. Markstaller, E. Otten, J. Schmiedeskamp, W. Schreiber, R. Surkau, M. Thelen, and N. Weiler. *Quantification of Regional Intrapulmonary Oxygen Partial Pressure Evolution during Apnea by ^{3}He MRI.* Journal of Magnetic Resonance, vol. 141, no. 2:pp. 207 – 216, 1999. ISSN 1090-7807. URL http://dx.doi.org/10.1006/jmre.1999.1902.

[Den00] A. J. Deninger, B. Eberle, M. Ebert, T. Grossmann, G. Hanisch, W. Heil, H.-U. Kauczor, K. Markstaller, E. Otten, W. Schreiber, R. Surkau, and N. Weiler. *^{3}He-MRI-based measurements of intrapulmonary p_{O2} and its time course during apnea in healthy volunteers: first results, reproducibility, and technical limitations.* NMR in Biomedicine, vol. 13, no. 4:pp. 194–201, 2000. ISSN 1099-1492. URL http://dx.doi.org/10.1002/1099-1492(200006)13:4⟨194::AID-NBM643⟩3.0.CO;2-D.

[Den06] A. Deninger, W. Heil, E. W. Otten, M. Wolf, R. K. Kremer, and A. Simon. *Paramagnetic relaxation of spin polarized ^3He at coated glass walls.* The European Physical Journal D - Atomic, Molecular, Optical and Plasma Physics, vol. 38, no. 3:pp. 439–443, 2006. ISSN 1434-6060. URL http://dx.doi.org/10.1140/epjd/e2006-00051-1.

[Dep15] O. Deppert. 2015-01-09: personal communication, 2015. Plasma Physics PHELIX, GSI Darmstadt, Germany.

[DR71] J. Dupont-Roc, M. Leduc, and F. Laloë. *New value for the metastability exchange cross section in helium.* Phys. Rev. Lett., vol. 27:pp. 467–470, 1971. URL http://dx.doi.org/10.1103/PhysRevLett.27.467.

[DR73] J. Dupont-Roc, M. Leduc, and F. Laloë. *Contribution à l'étude du pompage optique par échange de métastabilité dans ^3He. - Deuxième Partie.* Journal de Physique, vol. 34, no. 11-12:pp. 977–987, 1973. URL http://dx.doi.org/10.1051/jphys:019730034011-12097700.

[Dud99] B. J. Duda, R. G. Hemker, K. C. Tzeng, and W. B. Mori. *A Long-Wavelength Hosing Instability in Laser-Plasma Interactions.* Phys. Rev. Lett., vol. 83:pp. 1978–1981, 1999. URL http://dx.doi.org/10.1103/PhysRevLett.83.1978.

[Dwa71] M. R. Dwarakanath and H. Winkler. *$^3He(^3He,2p)^4He$ Total Cross-Section Measurements Below the Coulomb Barrier.* Phys. Rev. C, vol. 4:pp. 1532–1540, 1971. URL http://dx.doi.org/10.1103/PhysRevC.4.1532.

[Ebe68] J. H. Eberly and A. Sleeper. *Trajectory and Mass Shift of a Classical Electron in a Radiation Pulse.* Phys. Rev., vol. 176:pp. 1570–1573, 1968. URL http://dx.doi.org/10.1103/PhysRev.176.1570.

[Ebe00] M. Ebert. *Entwicklung eines leistungsstarken Polarisators und Kompressors für $^3\vec{He}$ für medizinische MR Tomographie.* Ph.D. thesis, Johannes Gutenberg University Mainz, 2000. Accessed: 2014-11-24, URL http://archimed.uni-mainz.de/pub/2000/0122/diss.pdf.

[Eck92] G. Eckert, W. Heil, M. Meyerhoff, E. Otten, R. Surkau, M. Werner, M. Leduc, P. Nacher, and L. Schearer. *A dense polarized ^3He target based on compression of optically pumped gas.* Nuclear Instruments and Methods in Physics Research Section A: Accelerators, Spectrometers, Detectors and Associated Equipment, vol. 320, no. 1–2:pp. 53 – 65, 1992. URL http://dx.doi.org/10.1016/0168-9002(92)90769-Z.

[Ein17] A. Einstein. *Zur Quantentheorie der Strahlung.* Physikalische Zeitschrift, vol. 18:pp. 121–128, 1917.

[Eng11] I. Engin. *Preparations for the Polarization Measurement of ^3He Ions from Laser-induced Plasmas.* Diploma thesis, RWTH Aachen University and FZJ, 2011. (not uploaded), URL http://juser.fz-juelich.de/record/127933.

[Eng14] I. Engin. *Lecturer at the Hadron Physics Summer School 2014 (Conference Venue Schloss Rauischholzhausen, Germany), exclusive author of the abstract for the "Laser-Plasma" working group: Polarization Measurement of laser-accelerated ^3He Ions*, 2014. Accessed: 2015-06-30, URL http://collaborations.fz-juelich.de/ikp/hpss2014/program.shtml.

[Eva69] S. A. Evans and N. F. Lane. *Total and Excitation-Transfer Cross Sections for Collisions between 2^3S Metastable and Ground-State Helium Atoms.* Phys. Rev., vol. 188:pp. 268–279, 1969. URL http://dx.doi.org/10.1103/PhysRev.188.268.

[Fen11] L. Feng. 2011-05-10: personal communication, 2011. Institute for Laser and Plasma Physics, Heinrich-Heine-University Düsseldorf, Germany.

[Fic91] D. Fick. *Einführung in die Kernphysik mit polarisierten Teilchen (1. Auflage 1971).* Erlangen - Nürnberg, 1991.

[Fin69] D. O. Findley, S. D. Baker, E. B. Carter, and N. D. Stockwell. *A polarized $^3He^+$ ion source.* Nuclear Instruments and Methods, vol. 71, no. 2:pp. 125 – 132, 1969. ISSN 0029-554X. URL http://dx.doi.org/10.1016/0029-554X(69)90001-9.

[Fle65] R. L. Fleischer, P. B. Price, and R. M. Walker. *Ion Explosion Spike Mechanism for Formation of Charged - Particle Tracks in Solids.* Journal of Applied Physics, vol. 36, no. 11:pp. 3645–3652, 1965. URL http://dx.doi.org/10.1063/1.1703059.

[Fle75] R. L. Fleischer, P. B. Price, and R. M. Walker. *Nuclear Tracks in Solids: Principles and Applications*. University of California Press, Berkeley, California, USA, 1975.

[Flo93] J. L. Flowers, B. W. Petley, and M. G. Richards. *A measurement of the nuclear magnetic moment of the helium-3 atom in terms of that of the proton*. Metrologia, vol. 30, no. 2:p. 75, 1993. URL http://dx.doi.org/10.1088/0026-1394/30/2/004.

[Fre11] C. G. Freeman, G. Fiksel, C. Stoeckl, N. Sinenian, M. J. Canfield, G. B. Graeper, A. T. Lombardo, C. R. Stillman, S. J. Padalino, C. Mileham, T. C. Sangster, and J. A. Frenje. *Calibration of a Thomson parabola ion spectrometer and Fujifilm imaging plate detectors for protons, deuterons, and alpha particles*. Review of Scientific Instruments, vol. 82, no. 7:073301, 2011. URL http://dx.doi.org/10.1063/1.3606446.

[Fuj] Fuji Photo Film Co., LTD., Industrial Materials & Products Division, Science Systems, Tokyo, Japan, 2003. *Image Format Description, BAS2500 system*. Accessed: 2015-05-17, URL http://beamline.harima.riken.jp/bl45xu/web_old/Info/BAS2500imgSpec.pdf.

[Gab04] E. Gabriel, G. E. Fagg, G. Bosilca, T. Angskun, J. J. Dongarra, J. M. Squyres, V. Sahay, P. Kambadur, B. Barrett, A. Lumsdaine, R. H. Castain, D. J. Daniel, R. L. Graham, and T. S. Woodall. *Open MPI: Goals, Concept, and Design of a Next Generation MPI Implementation*. In *Proceedings, 11th European PVM/MPI Users' Group Meeting*, pp. 97–104. Budapest, Hungary, 2004. URL http://www.open-mpi.org/papers/euro-pvmmpi-2004-overview/euro-pvmmpi-2004-overview.pdf.

[GE] GE Healthcare Bio-Sciences AB, Uppsala, Sweden. *Typhoon FLA 7000 and 7000 IP biomolecular imager, data file 28-9610-73 AC*. Accessed: 2015-08-02, URL https://www.gelifesciences.com/gehcls_images/GELS/Related%20Content/Files/1314807262343/litdoc28961073_20130110133703.pdf.

[Gib05] P. Gibbon. *Short Pulse Laser Interactions with Matter: An Introduction*. Imperial College Press, London, 2005. ISBN 1-86094-135-4. URL http://juser.fz-juelich.de/record/47943.

[Gol95] R. J. Goldston and P. H. Rutherford. *Introduction to plasma physics*. Plasma Physics Series. Institute of Physics Pub., 1995. ISBN 0 7503 0325 5.

[Gre64] R. C. Greenhow. *Optical pumping in he^3*. Phys. Rev., vol. 136:pp. A660–A662, 1964. URL http://dx.doi.org/10.1103/PhysRev.136.A660.

[han] *handymath.com - solution for technicians: The Complete Sodium Hydroxide Density-Concentration Table Calculator*. Accessed: 2015-08-23, URL http://www.handymath.com/cgi-bin/naohtble3.cgi?submit=Entry.

[Har08] K. Harres, M. Schollmeier, E. Brambrink, P. Audebert, A. Blazevic, K. Flippo, D. C. Gautier, M. Geißel, B. M. Hegelich, F. Nürnberg, J. Schreiber, H. Wahl, and M. Roth. *Development and calibration of a Thomson parabola with microchannel plate for the detection of laser-accelerated MeV ions*. Review of Scientific Instruments, vol. 79, no. 9:093306, 2008. URL http://dx.doi.org/10.1063/1.2987687.

[Has90] K. C. Hasson, G. D. Cates, K. Lerman, P. Bogorad, and W. Happer. *Spin relaxation due to magnetic-field inhomogeneities: Quartic dependence and diffusion-constant measurements*. Phys. Rev. A, vol. 41:pp. 3672–3688, 1990. URL http://dx.doi.org/10.1103/PhysRevA.41.3672.

[Hei] W. Heil. *Helium-3 study group, Prof. W. Heil, Johannes Gutenberg University Mainz*. Accessed: 2014-12-13, URL http://www.ag-heil.physik.uni-mainz.de/38_ENG_HTML.php.

[Hen71] R. P. Henke and E. V. Benton. *On geometry of tracks in dielectric nuclear track detectors*. Nuclear Instruments and Methods, vol. 97, no. 3:pp. 483 – 489, 1971. ISSN 0029-554X. URL http://dx.doi.org/10.1016/0029-554X(71)90250-3.

[Hie06] S. Hiebel. *Methodische und technische Weiterentwicklung der $^3\vec{H}e$-MRT im Hinblick auf erweiterte lungendiagnostische Anwendungsmöglichkeiten*. Ph.D. thesis, Johannes Gutenberg University Mainz, 2006. Accessed: 2014-11-30, URL http://ubm.opus.hbz-nrw.de/volltexte/2007/1250/pdf/diss.pdf.

[Hie10] S. Hiebel, T. Großmann, D. Kiselev, J. Schmiedeskamp, Y. Gusev, W. Heil, S. Karpuk, J. Krimmer, E. Otten, and Z. Salhi. *Magnetized boxes for housing polarized spins in homogeneous fields*. Journal of Magnetic Resonance, vol. 204, no. 1:pp. 37 – 49, 2010. URL http://dx.doi.org/http://dx.doi.org/10.1016/j.jmr.2010.01.017.

[Hig] High Speed Vision GmbH, Ettlingen, Germany. *SpeedCam MegaVis product information.* Accessed: 2015-07-01, URL http://www.hsvision.de/images/pdf/en/flyer_MegaVis_engl.pdf.

[Hol14] A. Holler. *Machbarkeitsstudie einer polarisierten ^{3}He-Ionenquelle mit Hilfe laserinduzierter Teilchenbeschleunigung.* Ph.D. thesis, University of Cologne, 2014. Accessed: 2015-06-28, URL http://kups.ub.uni-koeln.de/5752/.

[Hon91] T. Honda, Y. Nakao, Y. Honda, K. Kudo, and H. Nakashima. *Burn characteristics of inertially confined D-^{3}He fuel.* Nuclear Fusion, vol. 31, no. 5:p. 851, 1991. URL http://dx.doi.org/10.1088/0029-5515/31/5/004.

[IKA] IKA Werke Staufen, Germany. *HBR 4 digital Heating Bath, data sheet.* Accessed: 2015-08-23, URL http://www.ika.com/ika/datasheet/datasheet.php?iProduct=2602300&iLang=1&iCountry=276&filename=DataSheet_HBR_4_digital_Heating_bath.pdf.

[ISPa] ISP International Specialty Products, Wayne, New Jersey, USA. *GAFCHROMIC® Dosimetry Media, Type EBT2 Dosimetry Film.* Accessed: 2015-08-02, URL http://www.ashland.com/Ashland/Static/Documents/ASI/Advanced%20Materials/ebt2.pdf.

[ISPb] ISP International Specialty Products, Wayne, New Jersey, USA. *GAFCHROMIC® Dosimetry Media, Type HD-V2 Dosimetry Film.* Accessed: 2015-08-02, URL http://www.ashland.com/Ashland/Static/Documents/ASI/Advanced%20Materials/gafchromic-hdv2.pdf.

[ISP10] ISP International Specialty Products, Wayne, New Jersey, USA. Author: D. F. Lewis. *GAFCHROMIC® Radiochromic Film*, 2010. Accessed: 2015-08-02, URL http://www.ashland.com/Ashland/Static/Documents/ASI/Advanced%20Materials/lewis-radiochromic-film.pdf.

[Jun98] M. Junker, A. D'Alessandro, S. Zavatarelli, C. Arpesella, E. Bellotti, C. Broggini, P. Corvisiero, G. Fiorentini, A. Fubini, G. Gervino, U. Greife, C. Gustavino, J. Lambert, P. Prati, W. S. Rodney, C. Rolfs, F. Strieder, H. P. Trautvetter, and D. Zahnow (The Luna Collaboration). *Cross section of ^{3}He(^{3}He,2p)^{4}He measured at solar energies.* Phys. Rev. C, vol. 57:pp. 2700–2710, 1998. URL http://dx.doi.org/10.1103/PhysRevC.57.2700.

[Jun07] R. Jung. *Laser-plasma interaction with ultrashort laser pulses.* Ph.D. thesis, Heinrich-Heine-University Düsseldorf, 2007. Accessed: 2014-11-24, URL http://www.uni-duesseldorf.de/HHU/math_nat_fak/WE/physik/laserphy/GRK/Dissertationen/Jung.

[Jun11] D. Jung, R. Hörlein, D. Kiefer, S. Letzring, D. C. Gautier, U. Schramm, C. Hübsch, R. Öhm, B. J. Albright, J. C. Fernandez, D. Habs, and B. M. Hegelich. *Development of a high resolution and high dispersion Thomson parabola.* Review of Scientific Instruments, vol. 82, no. 1:013306, 2011. URL http://dx.doi.org/10.1063/1.3523428.

[Kal10] M. C. Kaluza, H.-P. Schlenvoigt, S. P. D. Mangles, A. G. R. Thomas, A. E. Dangor, H. Schwoerer, W. B. Mori, Z. Najmudin, and K. M. Krushelnick. *Measurement of Magnetic-Field Structures in a Laser-Wakefield Accelerator.* Phys. Rev. Lett., vol. 105:p. 115002, 2010. URL http://dx.doi.org/10.1103/PhysRevLett.105.115002.

[Kel65] L. V. Keldysh. *Ionization in the field of a strong electromagnetic wave.* Soviet Physics JETP, vol. 20:pp. 1307–1314, 1965. URL http://www.jetp.ac.ru/cgi-bin/e/index/e/20/5/p1307?a=list.

[Kha95] A. H. Khayrat and S. A. Durrani. *The effect of UV exposure on the track and bulk etching rates in different CR-39 plastics.* Radiation Measurements, vol. 25, no. 1–4:pp. 163 – 164, 1995. ISSN 1350-4487. Nuclear Tracks in Solids, URL http://dx.doi.org/10.1016/1350-4487(95)00061-I.

[Kla14] M. Klaiber, E. Yakaboylu, C. Müller, H. Bauke, G. G. Paulus, and K. Z. Hatsagortsyan. *Spin dynamics in relativistic ionization with highly charged ions in super-strong laser fields.* Journal of Physics B: Atomic, Molecular and Optical Physics, vol. 47, no. 6:p. 065603, 2014. URL http://dx.doi.org/10.1088/0953-4075/47/6/065603.

[Kle14] F. Klehr, K. Dahlhoff, I. Engin, P. Jansen, and E. Wiebe. 2014-12-10: personal communication, 2014. Planning, construction, fabrication, assembly, testing. Central Institute for Engineering, Electronics and Analytics (ZEA), Forschungszentrum Juelich GmbH, Germany.

[KLO05] T. N. P. L. Kaye & Laby Online, Version 1.0. *Tables of Physical & Chemical Constants (16th edition 1995). Chapter 4, Section 4.7, Subsect. 4.7.4: Nuclear Fusion (online version)*, 2005. Accessed: 2014-12-01, URL http://www.kayelaby.npl.co.uk/atomic_and_nuclear_physics/4_7/4_7_4.html.

[Kog66] H. Kogelnik and T. Li. *Laser Beams and Resonators.* Appl. Opt., vol. 5, no. 10:pp. 1550–1567, 1966. URL http://dx.doi.org/10.1364/AO.5.001550.

[Kri09] J. Krimmer, M. Distler, W. Heil, S. Karpuk, D. Kiselev, Z. Salhi, and E. W. Otten. *A highly polarized target for the electron beam at MAMI.* Nuclear Instruments and Methods in Physics Research Section A: Accelerators, Spectrometers, Detectors and Associated Equipment, vol. 611, no. 1:pp. 18 – 24, 2009. ISSN 0168-9002. URL http://dx.doi.org/10.1016/j.nima.2009.09.064.

[Kru99] K. Krushelnick, E. L. Clark, Z. Najmudin, M. Salvati, M. I. K. Santala, M. Tatarakis, A. E. Dangor, V. Malka, D. Neely, R. Allott, and C. Danson. *Multi-MeV Ion Production from High-Intensity Laser Interactions with Underdense Plasmas.* Phys. Rev. Lett., vol. 83:pp. 737–740, 1999. URL http://dx.doi.org/10.1103/PhysRevLett.83.737.

[Kul11] H. J. Kull. *Laserphysik: Physikalische Grundlagen des Laserlichts und seine Wechselwirkung mit Materie.* Oldenbourg Wissenschaftsverlag GmbH, 2011. ISBN 978-3-486-58023-5.

[Kum06] N. Kumar, V. K. Tripathi, and B. K. Sawhney. *Filamentation of a relativistic short pulse laser in a plasma.* Physica Scripta, vol. 73, no. 6:p. 659, 2006. URL http://dx.doi.org/10.1088/0031-8949/73/6/021.

[Lan28] I. Langmuir. *Oscillations in Ionized Gases.* In *Proceedings of the National Academy of Science*, pp. 627–637. 1928. URL http://dx.doi.org/10.1073/pnas.14.8.627.

[Leb11] P. Leblans, D. Vandenbroucke, and P. Willems. *Storage Phosphors for Medical Imaging.* Materials, vol. 4, no. 6:pp. 1034–1086, 2011. ISSN 1996-1944. URL http://dx.doi.org/10.3390/ma4061034.

[Lei15] T. Leipold. 2015-04-02: personal communication, 2015. Peter Gruenberg Institut, Forschungszentrum Juelich GmbH, Germany.

[Lif14] A. Lifschitz, F. Sylla, S. Kahaly, A. Flacco, M. Veltcheva, G. Sanchez-Arriaga, E. Lefebvre, and V. Malka. *Ion acceleration in underdense plasmas by ultra-short laser pulses.* New Journal of Physics, vol. 16, no. 3:p. 033031, 2014. URL http://dx.doi.org/10.1088/1367-2630/16/3/033031.

[Mad71] Madison. *3rd International Symposium on polarization phenomena in nuclear reactions.* In H. H. Barshall and W. Haeberli (eds.), *Polarization phenomena in nuclear reactions: Proceedings.* University of Wisconsin Press, 1971.

[Mai60] T. H. Maiman. *Stimulated optical radiation in ruby.* Nature, vol. 187:pp. 493–494, 1960. URL http://dx.doi.org/10.1038/187493a0.

[Mai91] G. Mainfray and G. Manus. *Multiphoton ionization of atoms.* Reports on Progress in Physics, vol. 54, no. 10:p. 1333, 1991. URL http://dx.doi.org/10.1088/0034-4885/54/10/002.

[Mal00] V. Malka, C. Coulaud, J. Geindre, V. Lopez, Z. Najmudin, D. Neely, and F. Amiranoff. *Characterization of neutral density profile in a wide range of pressure of cylindrical pulsed gas jets.* Review of Scientific Instruments, vol. 71, no. 6:pp. 2329–2333, 2000. URL http://dx.doi.org/10.1063/1.1150619.

[Mar75] J. H. Marburger. *Self-focusing: Theory.* Progress in Quantum Electronics, vol. 4, Part 1, no. 0:pp. 35 – 110, 1975. ISSN 0079-6727. URL http://dx.doi.org/10.1016/0079-6727(75)90003-8.

[Max74] C. E. Max, J. Arons, and A. B. Langdon. *Self-modulation and self-focusing of electromagnetic waves in plasmas.* Phys. Rev. Lett., vol. 33:pp. 209–212, 1974. URL http://dx.doi.org/10.1103/PhysRevLett.33.209.

[Max14] J. Maxwell, R. Milner, and C. Epstein. *Development of a polarized ^3He ion source for RHIC.* Physics of Particles and Nuclei, vol. 45, no. 1:pp. 301–302, 2014. ISSN 1063-7796. URL http://dx.doi.org/10.1134/S1063779614010651.

[McK11] P. McKenna, A. P. L. Robinson, D. Neely, M. P. Desjarlais, D. C. Carroll, M. N. Quinn, X. H. Yuan, C. M. Brenner, M. Burza, M. Coury, P. Gallegos, R. J. Gray, K. L. Lancaster, Y. T. Li, X. X. Lin, O. Tresca, and C.-G. Wahlström. *Effect of lattice structure on energetic electron transport in solids irradiated by ultraintense laser pulses.* Phys. Rev. Lett., vol. 106:p. 185004, 2011. URL http://dx.doi.org/10.1103/PhysRevLett.106.185004.

[McL77] W. McLaughlin, A. Miller, S. Fidan, K. Pejtersen, and W. B. Pedersen. *Radiochromic plastic films for accurate measurement of radiation absorbed dose and dose distributions.* Radiation Physics and Chemistry (1977), vol. 10, no. 2:pp. 119–127, 1977. ISSN 0146-5724. URL http://dx.doi.org/10.1016/0146-5724(77)90017-6.

[Mea04] M. J. Mead, D. Neely, J. Gauoin, R. Heathcote, and P. Patel. *Electromagnetic pulse generation within a petawatt laser target chamber.* Review of Scientific Instruments, vol. 75, no. 10:pp. 4225–4227, 2004. URL http://dx.doi.org/10.1063/1.1787606.

[Mea08] A. L. Meadowcroft, C. D. Bentley, and E. N. Stott. *Evaluation of the sensitivity and fading characteristics of an image plate system for x-ray diagnostics.* Review of Scientific Instruments, vol. 79, no. 11:113102, 2008. URL http://dx.doi.org/10.1063/1.3013123.

[Mon95] P. Monot, T. Auguste, P. Gibbon, F. Jakober, G. Mainfray, A. Dulieu, M. Louis-Jacquet, G. Malka, and J. L. Miquel. *Experimental demonstration of relativistic self-channeling of a multiterawatt laser pulse in an underdense plasma.* Phys. Rev. Lett., vol. 74:pp. 2953–2956, 1995. URL http://dx.doi.org/10.1103/PhysRevLett.74.2953.

[Mor94] C. Mori, A. Matsumura, T. Suzuki, H. Miyahara, T. Aoyama, and K. Nishizawa. *Detection of extremely low level radioactivity with imaging plate.* Nuclear Instruments and Methods in Physics Research Section A: Accelerators, Spectrometers, Detectors and Associated Equipment, vol. 339:pp. 278–281, 1994. URL http://dx.doi.org/10.1016/0168-9002(94)91816-3.

[Mor11] J. T. Morrison, C. Willis, R. R. Freeman, and L. Van Woerkom. *Design of and data reduction from compact Thomson parabola spectrometers.* Review of Scientific Instruments, vol. 82, no. 3:033506, 2011. URL http://dx.doi.org/10.1063/1.3556444.

[Nac85] P. Nacher and M. Leduc. *Optical pumping in ^3He with a laser.* Journal de Physique, vol. 46, no. 12:pp. 2057–2073, 1985. URL http://dx.doi.org/10.1051/jphys:0198500460120205700.

[Nak12] K. Nakayama and M. Tanaka. *Simulation analysis of triboplasma generation using the particle-in-cell/Monte Carlo collision (PIC/MCC) method.* Journal of Physics D: Applied Physics, vol. 45, no. 49:p. 495203, 2012. URL http://dx.doi.org/10.1088/0022-3727/45/49/495203.

[Nau14] B. T. Nauschütt. *Messung der Polarisation von ^3He und Bestimmung der Relaxationszeit.* Bachelor thesis, FH Aachen, Campus Jülich, FB 10 Energietechnik, Physikingenieurwesen, and Peter Grünberg Institut, Forschungszentrum Jülich GmbH, 2014. URL http://juser.fz-juelich.de/record/187558.

[New93] N. R. Newbury, A. S. Barton, G. D. Cates, W. Happer, and H. Middleton. *Gaseous $^3He-^3He$ magnetic dipolar spin relaxation.* Phys. Rev. A, vol. 48:pp. 4411–4420, 1993. URL http://dx.doi.org/10.1103/PhysRevA.48.4411.

[Nol06] W. Nolting. *Gundkurs Theoretische Physik 5/2: Quantenmechanik - Methoden und Anwendungen, 6. Auflage.* Springer, Braunschweig/Wiesbaden, 2006.

[NR98] A. Niroomand-Rad, C. Blackwell, B. Coursey, K. Gall, J. Galvin, W. McLaughlin, A. Meigooni, R. Nath, J. Rodgers, and C. Soares. *Radiochromic film dosimetry: Recommendations of AAPM Radiation Therapy Committee Task Group 55.* Medical Physics, vol. 25, no. 11:pp. 2093–2115, 1998. URL http://dx.doi.org/10.1118/1.598407.

[Para] Parker Automation, Parker Hannifin Corporation, New Jersey Operation, USA. *IOTA ONE operating manual and setup instructions.* Accessed: 2015-06-28, URL http://www.parker.com/portal/site/PARKER/menuitem.de7b26ee6a659c147cf26710237ad1ca/?vgnextoid=fcc9b5bbec622110VgnVCM10000032a71dacRCRD&vgnextfmt=EP&vgnextdiv=&vgnextcatid=2946271&vgnextcat=IOTA+ONE+VALVE+DRIVER&Wtky=.

[Parb] Parker Hannifin, Precision Fluidics Division, Hollis, USA. *Pulse Valves Series 9 - Ultra Low Leak Extreme Performance Valve (Datasheet).* Accessed: 2015-06-29, URL http://ph.parker.com/us/12051/en/pulse-valves-miniature-high-speed-high-vacuum-dispense-valve.

[Pat08] I. J. Paterson, R. J. Clarke, N. C. Woolsey, and G. Gregori. *Image plate response for conditions relevant to laser–plasma interaction experiments.* Measurement Science and Technology, vol. 19, no. 9:p. 095301, 2008. URL http://dx.doi.org/10.1088/0957-0233/19/9/095301.

[Per66] A. M. Perelomov, V. S. Popov, and M. V. Terentev. *Ionization of atoms in an alternating electric field.* Soviet Physics JETP, vol. 23, no. 5:pp. 924+, 1966. URL http://www.jetp.ac.ru/cgi-bin/e/index/e/23/5/p924?a=list.

[Per67] A. M. Perelomov, V. S. Popov, and M. V. Terent'ev. *Ionization of atoms in an alternating electric field: II.* Soviet Physics JETP, vol. 24:p. 207, 1967. URL http://www.jetp.ac.ru/cgi-bin/e/index/e/24/1/p207?a=list.

[Pfe14a] J. Pfennings, I. Engin, H. Glückler, and M. Schmitt. 2015-08-18: personal communication, 2014. Planning, construction, fabrication, assembly, testing. Central Institute for Engineering, Electronics and Analytics (ZEA), Forschungszentrum Juelich GmbH, Germany.

[Pfe14b] J. Pfennings, I. Engin, H. Glückler, M. Schmitt, and H. Soltner. 2015-07-10: personal communication, 2014. Planning, construction, fabrication, assembly, testing. Central Institute for Engineering, Electronics and Analytics (ZEA), Forschungszentrum Juelich GmbH, Germany.

[PHE] PHELIX. *PHELIX laser facility, Plasma Physics, GSI Darmstadt, Germany, homepage with sub-link: "Target Chamber".* Accessed: 2014-12-22, URL https://www.gsi.de/en/start/research/forschungsgebiete_und_experimente/appa_pni_gesundheit/plasma_physicsphelix/phelix.htm?nr=%2Fproc%2Fself%2Fenv%27.

[PI] PI Physik Instrumente GmbH und Co. KG, Karlsruhe, Germany. *PiezoMove High-Stiffness Linear Piezo Actuator P-602.* Accessed: 2015-08-24, URL http://www.physikinstrumente.com/download/PI_Datasheet_P-602_20150122.pdf.

[Pol] M. N. Polyanskiy. *Refractive index database.* Accessed: 2015-07-02, URL http://refractiveindex.info.

[Pra03] S. Prasher and S. Singh. *The effect of infrared radiation on etching characteristics of CR-39 plastic track recorder.* Radiation Measurements, vol. 36, no. 1–6:pp. 105 – 106, 2003. ISSN 1350-4487. Proceedings of the 21st International Conference on Nuclear Tracks in Solids, URL http://dx.doi.org/10.1016/S1350-4487(03)00103-3.

[Pra10] R. Prasad, D. Doria, S. Ter-Avetisyan, P. Foster, K. Quinn, L. Romagnani, C. Brenner, J. Green, P. Gallegos, M. Streeter, D. Carroll, O. Tresca, N. Dover, C. Palmer, J. Schreiber, D. Neely, Z. Najmudin, P. McKenna, M. Zepf, and M. Borghesi. *Calibration of Thomson parabola—MCP assembly for multi-MeV ion spectroscopy.* Nuclear Instruments and Methods in Physics Research Section A: Accelerators, Spectrometers, Detectors and Associated Equipment, vol. 623, no. 2:pp. 712–715, 2010. ISSN 0168-9002. 1rs International Conference on Frontiers in Diagnostics Technologies, URL http://dx.doi.org/10.1016/j.nima.2010.02.078.

[Puk99] A. Pukhov, Z.-M. Sheng, and J. Meyer-ter Vehn. *Particle acceleration in relativistic laser channels.* Physics of Plasmas, vol. 6, no. 7:pp. 2847–2854, 1999. URL http://dx.doi.org/10.1063/1.873242.

[Puk03] A. Pukhov. *Strong field interaction of laser radiation.* Reports on Progress in Physics, vol. 66, no. 1:p. 47, 2003. URL http://dx.doi.org/10.1088/0034-4885/66/1/202.

[Que98] B. Quesnel and P. Mora. *Theory and simulation of the interaction of ultraintense laser pulses with electrons in vacuum.* Phys. Rev. E, vol. 58:pp. 3719–3732, 1998. URL http://dx.doi.org/10.1103/PhysRevE.58.3719.

[Raa11] N. Raab. *Development of a method to measure the polarization of laseraccelerated protons.* Ph.D. thesis, University of Cologne, 2011. Accessed: 2014-11-24, URL http://kups.ub.uni-koeln.de/4232/1/diss_raab.pdf.

[Raa14] N. Raab, M. Büscher, M. Cerchez, R. W. Engels, I. Engin, P. Gibbon, P. Greven, A. Holler, A. Karmakar, A. Lehrach, R. Maier, M. Swantusch, M. Toncian, T. Toncian, and O. Willi. *Polarization measurement of laser-accelerated protons.* Physics of Plasmas (1994-present), vol. 21, no. 2:023104, 2014. URL http://dx.doi.org/10.1063/1.4865096.

[Ran02] M. A. Rana and I. E. Qureshi. *Studies of CR-39 etch rates.* Nuclear Instruments and Methods in Physics Research Section B: Beam Interactions with Materials and Atoms, vol. 198, no. 3–4:pp. 129 – 134, 2002. ISSN 0168-583X. URL http://dx.doi.org/10.1016/S0168-583X(02)01526-4.

[Ric02] D. R. Rich, T. R. Gentile, T. B. Smith, A. K. Thompson, and G. L. Jones. *Spin exchange optical pumping at pressures near 1 bar for neutron spin filters.* Applied Physics Letters, vol. 80, no. 12:pp. 2210–2212, 2002. URL http://dx.doi.org/10.1063/1.1461424.

[Row02] J. A. Rowlands. *The physics of computed radiography.* Physics in Medicine and Biology, vol. 47, no. 23:p. R123, 2002. URL http://dx.doi.org/10.1088/0031-9155/47/23/201.

[Ruh] H. Ruhl. *Classical Particle Simulations with the PSC code - An introduction into the PSC.* H. Ruhl's lecture notes at Ludwig-Maximilians-Universität München. Accessed: 2014-11-18, URL https://www.physik.uni-muenchen.de/lehre/vorlesungen/wise_09_10/tvi_mas_compphys/vorlesung/Lecturescript.pdf.

[Saa95] B. Saam, W. Happer, and H. Middleton. *Nuclear relaxation of ^{3}He in the presence of O_2.* Phys. Rev. A, vol. 52:pp. 862–865, 1995. URL http://dx.doi.org/10.1103/PhysRevA.52.862.

[San65] J. Sanderson. *Corrections to Thompson scattering for intense laser beams.* Physics Letters, vol. 18, no. 2:pp. 114 – 115, 1965. URL http://dx.doi.org/10.1016/0031-9163(65)90674-8.

[Sar99] G. S. Sarkisov, V. Y. Bychenkov, V. N. Novikov, V. T. Tikhonchuk, A. Maksimchuk, S.-Y. Chen, R. Wagner, G. Mourou, and D. Umstadter. *Self-focusing, channel formation, and high-energy ion generation in interaction of an intense short laser pulse with a He jet.* Phys. Rev. E, vol. 59:pp. 7042–7054, 1999. URL http://dx.doi.org/10.1103/PhysRevE.59.7042.

[Sch65] L. D. Schearer and G. K. Walters. *Nuclear spin-lattice relaxation in the presence of magnetic-field gradients.* Phys. Rev., vol. 139:pp. A1398–A1402, 1965. URL http://dx.doi.org/10.1103/PhysRev.139.A1398.

[Sch67] L. D. Schearer. *Collision-Induced Mixing in the 2^3P Levels of Helium.* Phys. Rev., vol. 160:pp. 76–80, 1967. URL http://dx.doi.org/10.1103/PhysRev.160.76.

[Sch68] L. D. Schearer. *Depolarization of Light Scattered by Aligned 2^3S and 2^3P Helium Atoms at Resonance.* Phys. Rev., vol. 166:pp. 30–33, 1968. URL http://dx.doi.org/10.1103/PhysRev.166.30.

[Sch85] R. F. Schneider, C. M. Luo, and M. J. Rhee. *Resolution of the Thomson spectrometer.* Journal of Applied Physics, vol. 57, no. 1:pp. 1–5, 1985. URL http://dx.doi.org/10.1063/1.335389.

[Sch04] J. Schmiedeskamp. *Weiterentwicklung einer Produktionsanlage und der Speicherungs- bzw. Transportkonzepte für hochpolarisiertes ^{3}He.* Ph.D. thesis, Johannes Gutenberg University Mainz, 2004.

[Sch06] J. Schmiedeskamp, W. Heil, E. W. Otten, R. K. Kremer, A. Simon, and J. Zimmer. *Paramagnetic relaxation of spin polarized ^{3}He at bare glass surfaces.* The European Physical Journal D - Atomic, Molecular, Optical and Plasma Physics, vol. 38, no. 3:pp. 427–438, 2006. ISSN 1434-6060. URL http://dx.doi.org/10.1140/epjd/e2006-00050-2.

[Sch12] K. Schmid and L. Veisz. *Supersonic gas jets for laser-plasma experiments.* Review of Scientific Instruments, vol. 83, no. 5:pp. –, 2012. URL http://dx.doi.org/10.1063/1.4719915.

[Sch15] V. Schanz. 2015-01-09: personal communication, 2015. Plasma Physics PHELIX, GSI Darmstadt, Germany.

[Sem01] S. Semushin and V. Malka. *High density gas jet nozzle design for laser target production.* Review of Scientific Instruments, vol. 72, no. 7:pp. 2961–2965, 2001. URL http://dx.doi.org/10.1063/1.1380393.

[Sin11] N. Sinenian, M. J. Rosenberg, M. Manuel, S. C. McDuffee, D. T. Casey, A. B. Zylstra, H. G. Rinderknecht, M. Gatu Johnson, F. H. Séguin, J. A. Frenje, C. K. Li, and R. D. Petrasso. *The response of CR-39 nuclear track detector to 1–9 MeV protons.* Review of Scientific Instruments, vol. 82, no. 10:103303, 2011. URL http://dx.doi.org/10.1063/1.3653549.

[Slo81] R. J. Slobodrian. *New method for the production of polarized ^{3}He ions based on the 2^3S_1 state of ^{3}He.* Nuclear Instruments and Methods in Physics Research, vol. 185, no. 1–3:pp. 581 – 583, 1981. ISSN 0167-5087. URL http://dx.doi.org/10.1016/0029-554X(81)91257-X.

[Sok11] T. Sokollik. *Characterisation and Manipulation of Proton Beams Accelerated by Ultra-Short and High-Contrast Laser Pulses.* Springer-Verlag Berlin Heidelberg, 2011. ISBN 9783642150395. Springer Theses, URL http://dx.doi.org/10.1007/978-3-642-15040-1.

[Sol10] H. Soltner and P. Blümler. *Dipolar Halbach magnet stacks made from identically shaped permanent magnets for magnetic resonance.* Concepts in Magnetic Resonance Part A, vol. 36A, no. 4:pp. 211–222, 2010. ISSN 1552-5023. URL http://dx.doi.org/10.1002/cmr.a.20165.

[Spr87] P. Sprangle, C.-M. Tang, and E. Esarey. *Relativistic self-focusing of short-pulse radiation beams in plasmas.* Plasma Science, IEEE Transactions on, vol. 15, no. 2:pp. 145–153, 1987. ISSN 0093-3813. URL http://dx.doi.org/10.1109/TPS.1987.4316677.

[Spr92] P. Sprangle, E. Esarey, J. Krall, and G. Joyce. *Propagation and guiding of intense laser pulses in plasmas.* Phys. Rev. Lett., vol. 69:pp. 2200–2203, 1992. URL http://dx.doi.org/10.1103/PhysRevLett.69.2200.

[Sta75] J. A. Stamper and B. H. Ripin. *Faraday-Rotation Measurements of Megagauss Magnetic Fields in Laser-Produced Plasmas.* Phys. Rev. Lett., vol. 34:pp. 138–141, 1975. URL http://dx.doi.org/10.1103/PhysRevLett.34.138.

[Sta97] E. A. Startsev and C. J. McKinstrie. *Multiple scale derivation of the relativistic ponderomotive force.* Phys. Rev. E, vol. 55:pp. 7527–7535, 1997. URL http://dx.doi.org/10.1103/PhysRevE.55.7527.

[Ste] Stefan Mayer Instruments, Dinslaken, Germany. *Magnetfeldmessgerät FLUXMASTER.* Accessed: 2015-08-24, URL http://www.stefan-mayer.com/images/datenblaetter/Datenblatt_Fluxmaster.pdf.

[Ste22] O. Stern and W. Gerlach. *Der experimentelle Nachweis der Richtungsquantelung im Magnetfeld.* Zeitschrift für Physik, vol. 9, no. 1:pp. 349–352, 1922. URL http://dx.doi.org/10.1007/BF01326983.

[Sto06] C. Stoeckl, V. Y. Glebov, P. A. Jaanimagi, J. P. Knauer, D. D. Meyerhofer, T. C. Sangster, M. Storm, S. Sublett, W. Theobald, M. H. Key, A. J. MacKinnon, P. Patel, D. Neely, and P. A. Norreys. *Operation of target diagnostics in a petawatt laser environment (invited).* Review of Scientific Instruments, vol. 77, no. 10:10F506, 2006. URL http://dx.doi.org/10.1063/1.2217922.

[Str85] D. Strickland and G. Mourou. *Compression of amplified chirped optical pulses.* Optics Communications, vol. 56, no. 3:pp. 219 – 221, 1985. ISSN 0030-4018. URL http://dx.doi.org/10.1016/0030-4018(85)90120-8.

[Sur95] R. Surkau. *Entwicklung und Test eines ^{3}He-Neutronen-Spinfilters.* Ph.D. thesis, Johannes Gutenberg University Mainz, 1995.

[Swa15] M. Swantusch. 2015-05-25: personal communication, 2015. Institute for Laser and Plasma Physics, Heinrich-Heine-University Düsseldorf, Germany.

[TA08] S. Ter-Avetisyan, M. Schnürer, T. Sokollik, P. V. Nickles, W. Sandner, H. R. Reiss, J. Stein, D. Habs, T. Nakamura, and K. Mima. *Proton acceleration in the electrostatic sheaths of hot electrons governed by strongly relativistic laser-absorption processes.* Phys. Rev. E, vol. 77:p. 016403, 2008. URL http://dx.doi.org/10.1103/PhysRevE.77.016403.

[TA10] S. Ter-Avetisyan, M. Schnürer, and P. V. Nickles. *Characterisation and Manipulation of Proton Beams Accelerated by Ultra-Short and High-Contrast Laser Pulses.* INTECH Open Access Publisher, 2010. ISBN 9789533072425. In "Coherence and Ultrashort Pulse Laser Emission", Chapter 18, F. J. Duarte (Ed.), URL http://dx.doi.org/10.5772/13266.

[Taj79] T. Tajima and J. M. Dawson. *Laser Electron Accelerator.* Phys. Rev. Lett., vol. 43:pp. 267–270, 1979. URL http://dx.doi.org/10.1103/PhysRevLett.43.267.

[Tan98] M. Tanaka. *Review from experimentalists: The role of polarized ^{3}He in the next century.* Nuclear Instruments and Methods in Physics Research Section A: Accelerators, Spectrometers, Detectors and Associated Equipment, vol. 402, no. 2–3:pp. 492 – 498, 1998. ISSN 0168-9002. Proceedings of the 7th {RCNP} International Workshop on Polarized He Beams and Gas Targets and Their Application, URL http://dx.doi.org/10.1016/S0168-9002(97)00896-6.

[Tem12] M. Temporal, V. Brandon, B. Canaud, J. P. Didelez, R. Fedosejevs, and R. Ramis. *Ignition conditions for inertial confinement fusion targets with a nuclear spin-polarized DT fuel.* Nuclear Fusion, vol. 52, no. 10:p. 103011, 2012. URL http://dx.doi.org/10.1088/0029-5515/52/10/103011.

[Tho11] Sir J. J. Thomson. *XXVI. Rays of Positive Electricity.* Philosophical Magazine Series 6, vol. 21, no. 122:pp. 225–249, 1911. URL http://dx.doi.org/10.1080/14786440208637024.

[Tik10] V. T. Tikhonchuk. *Physics of laser-assisted ion acceleration.* Nuclear Instruments and Methods in Physics Research Section A: Accelerators, Spectrometers, Detectors and Associated Equipment, vol. 620, no. 1:pp. 1–13, 2010. ISSN 0168-9002. URL http://dx.doi.org/10.1016/j.nima.2010.01.051.

[TOP] *TOP500 Supercomputer Site, TOP 10 List for November 2014*. Accessed: 2014-11-21, URL http://www.top500.org/lists/2014/11/.

[Traa] Track Analysis Systems Ltd, Bristol, UK. *TASLIMAGE Radon Dosimetry System - Info Brochure*. Accessed: 2015-08-23, URL http://www.tasl.co.uk/brochures/radonBrochure.pdf.

[Trab] Track Analysis Systems Ltd, Bristol, UK. *TASLIMAGE Radon Dosimetry System - Technical Specifications*. Accessed: 2015-08-23, URL http://www.tasl.co.uk/brochures/radonSystemSpecifications.pdf.

[Trac] Track Analysis Systems Ltd, Bristol, UK. *TASTRAK performance sheet - Alpha-particles*. Accessed: 2014-11-16, URL http://www.tasl.co.uk/brochures/TASTRAK_specification_sheetAlphaParticles.pdf.

[Tsk07] D. Tskhakaya, K. Matyash, R. Schneider, and F. Taccogna. *The Particle-In-Cell Method*. Contributions to Plasma Physics, vol. 47, no. 8-9:pp. 563–594, 2007. URL http://dx.doi.org/10.1002/ctpp.200710072.

[Uhl25] G. E. Uhlenbeck and S. Goudsmit. *Ersetzung der Hypothese vom unmechanischen Zwang durch eine Forderung bezüglich des inneren Verhaltens jedes einzelnen Elektrons*. Die Naturwissenschaften, vol. 13, no. 47:pp. 953–954, 1925. URL http://dx.doi.org/10.1007/BF01558878.

[Vid96] F. Vidal and T. W. Johnston. *Electromagnetic beam breakup: Multiple filaments, single beam equilibria, and radiation*. Phys. Rev. Lett., vol. 77:pp. 1282–1285, 1996. URL http://dx.doi.org/10.1103/PhysRevLett.77.1282.

[Vir01] H. Virk and A. Srivastava. *Modification of optical, chemical and structural response of CR-39 polymer by 50 MeV lithium ion irradiation*. Radiation Measurements, vol. 34, no. 1–6:pp. 65 – 67, 2001. ISSN 1350-4487. Proceedings of the 20th International Conference on Nuclear Tracks in Solids, URL http://dx.doi.org/10.1016/S1350-4487(01)00122-6.

[Vor65] G. S. Voronov and N. B. Delone. *Ionization of the xenon atom by the electric field of ruby laser emission*. JETP Letters, vol. 1, no. 2:pp. 66–68, 1965. URL http://www.jetpletters.ac.ru/ps/1590/article_24398.shtml.

[Wag13] F. Wagner, C. João, J. Fils, T. Gottschall, J. Hein, J. Körner, J. Limpert, M. Roth, T. Stöhlker, and V. Bagnoud. *Temporal contrast control at the PHELIX petawatt laser facility by means of tunable sub-picosecond optical parametric amplification*. Applied Physics B, vol. 116, no. 2:pp. 429–435, 2013. ISSN 0946-2171. URL http://dx.doi.org/10.1007/s00340-013-5714-9.

[Wei04] M. S. Wei, S. P. D. Mangles, Z. Najmudin, B. Walton, A. Gopal, M. Tatarakis, A. E. Dangor, E. L. Clark, R. G. Evans, S. Fritzler, R. J. Clarke, C. Hernandez-Gomez, D. Neely, W. Mori, M. Tzoufras, and K. Krushelnick. *Ion Acceleration by Collisionless Shocks in High-Intensity-Laser-Underdense-Plasma Interaction*. Phys. Rev. Lett., vol. 93:p. 155003, 2004. URL http://dx.doi.org/10.1103/PhysRevLett.93.155003.

[Wil06] L. Willingale, S. P. D. Mangles, P. M. Nilson, R. J. Clarke, A. E. Dangor, M. C. Kaluza, S. Karsch, K. L. Lancaster, W. B. Mori, Z. Najmudin, J. Schreiber, A. G. R. Thomas, M. S. Wei, and K. Krushelnick. *Collimated Multi-MeV Ion Beams from High-Intensity Laser Interactions with Underdense Plasma*. Phys. Rev. Lett., vol. 96:p. 245002, 2006. URL http://dx.doi.org/10.1103/PhysRevLett.96.245002.

[Wil11] O. Willi. 2011-05-10: personal communication, 2011. Institute for Laser and Plasma Physics, Heinrich-Heine-University Düsseldorf, Germany.

[Wiz79] J. L. Wiza. *Microchannel plate detectors*. Nuclear Instruments and Methods, vol. 162, no. 1–3:pp. 587–601, 1979. ISSN 0029-554X. URL http://dx.doi.org/10.1016/0029-554X(79)90734-1.

[Wol04] M. Wolf. *Erzeugung höchster* $^3\vec{He}$ *Kernspinpolarisation durch metastabiles optisches Pumpen*. Ph.D. thesis, Johannes Gutenberg University Mainz, 2004. Accessed: 2014-11-24, URL http://ubm.opus.hbz-nrw.de/volltexte/2005/655/pdf/DISSERTATION_WOLF_BIBLIOTHEK.pdf.

[Yad95] J. S. Yadav. *Charged particle identification using CR-39(DOP) detectors*. Radiation Measurements, vol. 24, no. 2:pp. 115 – 128, 1995. ISSN 1350-4487. URL http://dx.doi.org/10.1016/1350-4487(94)00092-F.

[Zie14] B. Zielbauer. 2014-08-06: personal communication, 2014. Plasma Physics PHELIX, GSI Darmstadt, Germany.